A multimodal approach to investigate the effects of respiration on Fontan flow to inform strategies for circulatory support

by

Markus Attila Horvath

B.S., Medical Engineering
Technical University Munich, 2012
M.S., Mechanical Engineering
Technical University Munich, 2014

Submitted to the Harvard-MIT Program in Health Sciences and Technology in Partial Fulfillment of the Requirements for the Degree of

Doctor of Philosophy in Medical Engineering and Medical Physics

at the

MASSACHUSETTS INSITITUE OF TECHNOLOGY

May 2022

Signature of Author:
_____
Harvard-MIT Program in Health Sciences and Technology
May 10, 2022

Certified by:
_____
Ellen T. Roche, PhD.
W.M. Keck Career Development Professor in Biomedical Engineering,
Associate Professor, MechE and Institute for Medical Engineering and Science,
Massachusetts Institute of Technology
Thesis Supervisor

Accepted by:
_____
Emery N. Brown, M.D., Ph.D.
Director, Harvard-MIT Program in Health Sciences & Technology
Professor of Computational Neuroscience and Health Sciences & Technology

A multimodal approach to investigate the effects of respiration on Fontan flow to inform strategies for circulatory support

by

Markus Attila Horvath

Submitted to the Harvard-MIT Program of Health Sciences and Technology
On May 11, 2022, in partial fulfillment of the requirements for the degree
of Doctor of Philosophy in Medical Engineering and Medical Physics.

Abstract

The prevalence of single ventricle physiology is estimated to be 1/3000. Fontan physiology is the final palliative stage for a series of congenital heart diseases resulting in a single ventricle. Resulting hemodynamics are not well characterized and remain poorly understood. Hence, mid-term survival rates remain high and suitable circulatory support strategies are undetermined. At the core of this clinical problem lies a limited understanding of the interactions of respiration, hemodynamics, and tissue damage. Respiration has been identified to govern flow fluctuation including retrograde flow in the Fontan IVC but bench top simulators and animal models fail to recreate the interaction of breathing and venous flow adequately.

The goal of this dissertation is to develop and validate a suit of bench top and computational models which recapitulate the interaction of respiratory biomechanics and Fontan flow, to leverage the simulator platform and a clinical study to characterize the respiratory impact on Fontan hemodynamics and retrograde flow, and to design and evaluate promising approaches for the circulatory support.

We develop a biomimetic respiratory simulator with integrated circulatory Fontan flow loop that shows high physiological fidelity. Vascular models with physiological compliance values interact with the respiratory mechanics to recreate characteristic Fontan flow. We characterize the simulator and validate the system with a computational lumped parameter model and a pilot clinical trial. We then extend the platform a computational fluid dynamics model of the Fontan shunt.

We leverage the cardiorespiratory simulator to characterize the impact of breathing and other physiological parameters. We conduct a clinical trial to evaluate respiratory effects Fontan retrograde flow. Thereby, we identify and characterize new physiological drivers. Subsequently, we conduct a retrospective study to evaluate clinical effects this flow reversal.

Finally, we design and test circulatory support strategies and establish the importance to tailor them to the unique flow patterns. We potential benefits of valve implantation in the Fontan IVC and optimize the device design.

In summary, this work provides a multimodal simulator platform paired with a clinical trial to provide deeper understanding of the Fontan physiology. The platform is a valuable tool for circulatory support development as we demonstrate here.

Thesis Supervisor:
Ellen T. Roche, PhD
Associate Professor, MechE and Institute for Medical Engineering and Science,
Massachusetts Institute of Technology

Thesis Chair:
Thomas Heldt, PhD
Associate Professor of Electrical and Biomedical Engineering, Department of Electrical Engineering & Computer Science
Core faculty member, Institute for Medical Engineering and Science,
Massachusetts Institute of Technology

Thesis Committee Member:
Pedro J. del Nido, M.D.
Chairman, Department of Cardiac Surgery, Boston Children's Hospital
William E. Ladd Professor of Child Surgery, Harvard Medical School

Acknowledgments

Firstly, I would like to thank my supervisor, Prof. Ellen Roche, who I have had the pleasure to work with across different institutions, different positions, and projects. She has supported and encouraged me from our earliest research discussions in 2014. Since then, she never stopped to inspire me, and I know I would not be the researcher I am today without her. Thank you for guiding me with your excellence and infusing me with the drive to always look for solutions no matter how big the challenge might seem. You provided me with the tools that I needed to choose the right direction and successfully complete my degree. I admire your kindness and exclusively positive way to motivate people around you which profoundly shaped my understanding of leadership.

I would like to extend my gratitude to my entire thesis committee which also includes Dr. Pedro del Nido and Prof. Thomas Heldt. All your immense knowledge and patience has given me power and spirit to excel in my research. Your positive outreach towards me and the passion for your own patients and research has truly inspired me to overcome challenges and to reach further. Your insightful feedback pushed me to sharpen my thinking and brought my work to a higher level.

I would also like to thank the organization that hosted my research, as well as their staff: The Harvard-MIT Health Science and Technologies program, professors and administrative support who offered me a stimulating academic environment and opportunities to grow.

I would like to thank all of the lab members of the Therapeutic Technologies Design and Development lab at MIT for always providing encouragement and sharing insightful suggestions. You all have played a major role in creating a productive and nourishing environment to enable my research. Particularly I thank all the people who took part in my research, for sharing their experience, energy, and wisdom with me. Without them, there would be no project. I thank you for your wonderful collaboration.

A special thank you goes to all my friends I made throughout my college years in Germany and my time around Boston who supported me throughout my journey thus far. I will always remember the fun times we spent together, sleepless nights that gave us the courage to complete tasks before deadlines and for stimulating the discussions. You are the spice in my life and enrich my path so incredibly much. Thank you for questioning me and supporting me at the right times and for carrying me through the lows and highs of our adventures.

I want to express how incredibly grateful I am for the love and support of my family. You are always there for me, you initiated me in all aspects, and taught me what really matters. This gives me the foundation to draw power from and explore this world as well as science. You said “no roots – no wings” and this achievement speaks to the foundation you provided and encouragement throughout the years. Mom, Dad, Timea, Martin, Johanna, and Marie: You are my rock and the sounding board for my development. I strive to keep growing with you.

All of this would have not been possible without the support and love of my partner, Hannah. Sharing this journey has changed me in a good way. I am delighted to keep changing with you! You supported my late nights and provided more than just nourishment and comfort. You enabled me throughout these years. Thank you for centering me, for your wise counsel and sympathetic ear that allowed me to go beyond where I thought I could. Thank you for your love and support which transformed many challenging situations into adventures. What we create together keeps me alert and curiosity to explore life and my research.

Table of Contents

1. General Introduction

1.1 Overview and Clinical Problem

Fontan surgery is a palliative treatment connects the systemic and pulmonary vasculature in series resulting in abnormal hemodynamics, causing chronic disease in multiple organ systems with fatal outcomes. The surgery is performed for a range of patients with congenital cardiac defects and single ventricle physiology. To date, it is estimated that between 50,000 to 70,000 Fontan patients with completed Fontan circulation life worldwide and that the patient population expected to double over the next twenty years[1], [2]. Due to the complex nature of the surgically created circulation, there has been slow progress in clinical management of failing Fontan circulation and attenuating corresponding mortality rates in the past 50 years[3]. Compromised quality of life and high morbidity rates occur for the lifetime of a Fontan patient. At the core of this clinical problem lies a limited understanding of the underlying interactions of hemodynamics, respiration, and tissue damage. Despite a depth of research, replicating Fontan flow has proven difficult due to the unique physiology and the complexity of the condition. Consequently, there are still no approved circulatory support strategies which address the chronic burden of the inadequate sub-pulmonary pump and mitigate resulting morbidity. Current animal models fail to recreate Fontan flow and its biomechanical drivers so there is a need for research with specific focus on the development of models across different domains to investigate Fontan flow characteristics. Recent clinical studies underscored the importance of respiration in governing the venous flow patterns [4]. The impact of the respiratory mechanics on Fontan flow has not been adequately recreated on the bench top impeding the study of physiological relations and investigations of feasible circulatory support strategies. In this work I aim to (1) establish a platform of Fontan simulators across bench top and computational domains which recapitulates the single ventricle venous hemodynamics and cardiorespiratory coupling, and validate it with 4D MRI of Fontan patients; (2) leverage the benchtop models and clinical imaging to investigate the effects of breathing variations on IVC hemodynamics in the Fontan physiology and explore potential clinical effects and (3) develop and characterize Fontan circulatory support strategies. The structure of the aims is represented graphically in Figure 1.

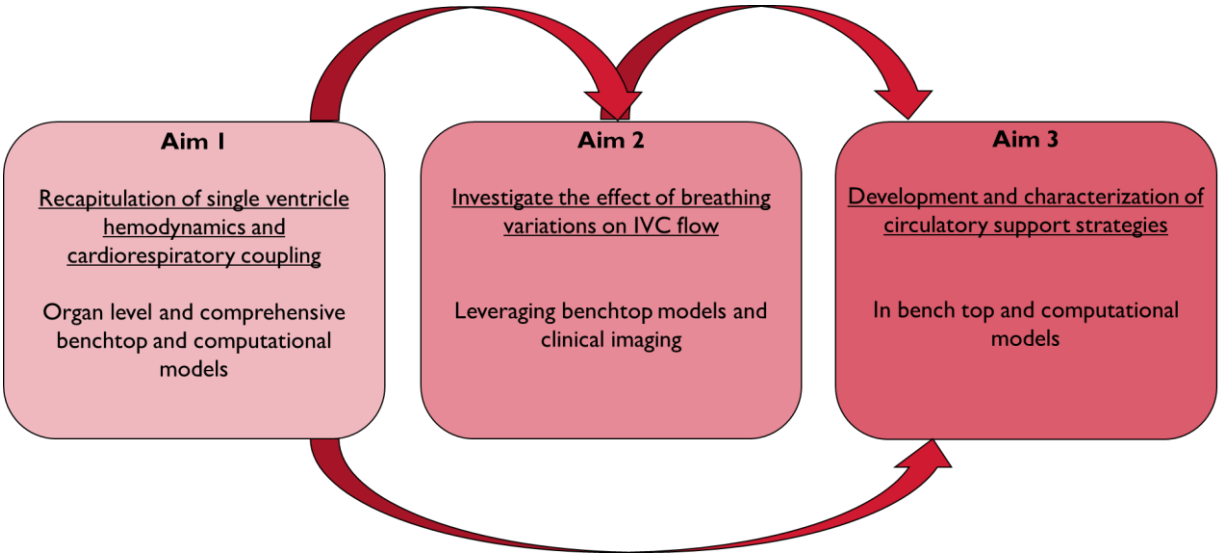

Figure 1: Thesis aim structure

1.1.1 Single Ventricle Disease and Clinical Treatment

The Fontan procedure

The cardiovascular system includes the heart, vasculature throughout the body and blood to enable blood circulation through the body. Efficient blood circulation is essential for human survival because it sustains viability of the entire organism by supplying nutrients and oxygen as well as transporting carbon dioxide and other waste materials. The heart is the major pump of the circulatory system, delivering blood from the right ventricle to the pulmonary circuit for blood oxygenation, and from the left ventricle to the systemic circuit, the rest of the body, as shown in Figure 2A and 2B.

Single ventricle circulation is an encompassing term that covers a wide range of structural cardiac abnormalities in which heart function is impeded, as a single ventricular chamber supports both the pulmonary and systemic circulation. The preferred surgical palliation for single ventricle hearts is the Fontan circulation, whereby the pulmonary and systemic blood flow are in series with the single ventricle, as shown in Figure 2C.

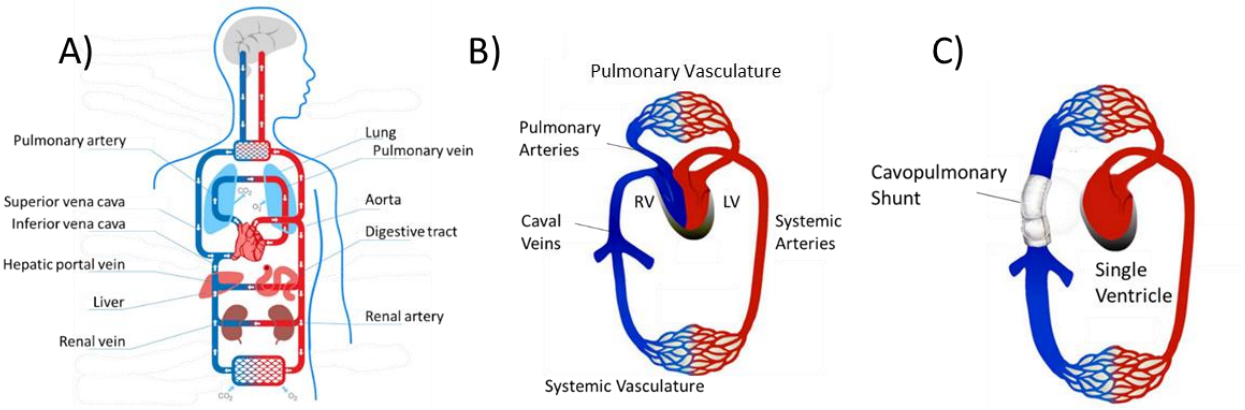

Figure 2: The circulatory system of Normal and Fontan physiologies.(A, B) In normal physiology, the right heart receives blood from the body, and pumps to the lungs. The left heart receives blood from the lungs and pumps to the body. C) In the Fontan physiology, a single ventricle pumps blood in series to the body, where it flows directly to the lungs before returning to the heart.

Underlying pathology and Surgical Intervention

Severe Congenital Heart Defects (CHDs) require early surgical intervention and include: (i) aortic stenosis, whereby aortic flow is restricted; (ii) atrial septal defects, whereby a hole or perforation exists in the walls that separate the atria and ventricles; (iii) bicuspid aortic valve disorders, whereby the normally "trileaflet" aortic valve only has two leaflets, limiting its functionality; (iv) patent ductus arteriosus, whereby blood circulation bypasses the lungs, limiting blood oxygenation; (v) single ventricle disease, whereby one of the ventricles are underdeveloped – this usually affects the left ventricle, which is responsible for pumping blood into the systemic circuit; and (vi) pulmonic stenosis, in which the lumen of the pulmonary artery is narrowed. In cases of congenital cardiac defects that are not suitable for biventricular repair a series of surgical procedures are performed and finalized in the palliative surgery called the "Fontan" procedure. Originally, the Fontan circulation included flow through the right atrial appendage. The contractile properties of the right atrium were used as a sub-pulmonary pump to propel blood, replacing the malformed right ventricle. However, losses in flow power, increases in cardiac arrhythmia, and increased incidents of thrombi contributed to the currently dominant procedure of using an inert conduit to connect the inferior vena cava (IVC) and pulmonary arteries (PAs), creating the total cavo-pulmonary connection (TCPC). This procedure combines three surgical interventions that ultimately result in a TCPC creating a serial coupling of the systemic and pulmonary circuits, with the remaining functional ventricle as the only blood propelling organ. Surgically establishing a working single ventricular physiology in this manner was a great success as it allowed a generation of newborn babies with the most severe forms of congenital heart disease to survive into adulthood. The initial intervention, which is

one of the highest risk procedures in the field of congenital heart surgery[5], is performed in the first weeks of life, while the last one is completed at the age of two or three. Step-wise performance of the interventions is to allow gradual training of the right ventricle to support high pressures of the systemic circulation. Ultimately a shunt connects the superior and inferior vena cava directly to the pulmonary artery, leading to a passive flow of blood to the lungs. The entire procedure is shown in Figure 3. Thus, children with high pulmonary vascular resistance may not tolerate the Fontan procedure[6]. Pulmonary vascular resistance is high *in utero* and takes months to drop. The high resistance means that there is a diminished volume of blood that flows to the lungs. Still, active shunts to increase blood flow to the lungs do not exist. Corrective cardiothoracic surgical procedures in neonates are very complex and carry high risks. The outcomes of surgical interventions for patients with single ventricle physiology have significantly improved over the last decade, but development of treatment methods as well as device development has been stagnant.

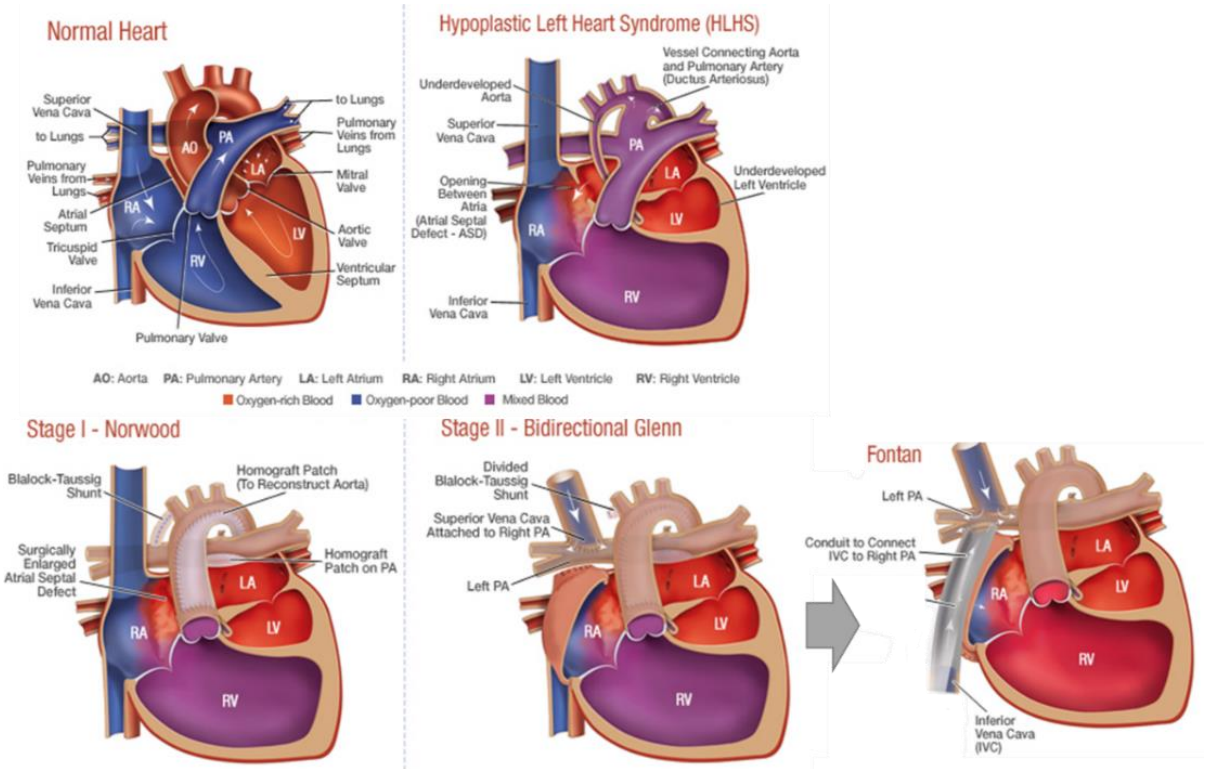

Figure 3: The normal, single ventricle, and Fontan heart anatomies. The Fontan procedure, shown in the bottom three images is a 3-stage palliative procedure that begins a few weeks after birth. The resulting anatomy reroutes blood so that it flows passively to the lungs, bypassing the right side of the heart. The blood flows from the lungs to the left side of the heart where it is pumped to the body (Image rights: Children's Hospital Philadelphia).

Living with Fontan physiology

The persistent burden of elevated venous pressure, reduced pulmonary flow, and impaired cardiac output triggers a cascade of pathophysiological consequences spanning from end organ failure to neurophysiological issue that impede quality of life and raise mortality rates. With surgical and peri-operative advancements, medium-term survival following Fontan operations has improved dramatically since the 1990s, resulting in a growing patient population in their 2nd and 3rd decade. These patients can now survive longer and thus require further treatment [7]. While early postoperative mortality is low in the modern era, the long-term consequences of this unique circulation remain largely unaddressed. Late post-Fontan mortality has not improved significantly over the past several decades [8]–[10]. Multifactorial complications contribute to large variation in midterm survival (40–70% at 25 years) [9], [11]. Recent studies show that the relentless burden of the Fontan hemodynamics heavily impedes quality of life for patients and care givers with 65 % of patients requiring major surgical or catheter-based interventions within 20 years [12]. Heart transplantation remains the only option for patients with failing Fontan physiology, however donors are scarce. This underscores the unmet need for a medical device support strategy for Fontan patients, as stated in a recent executive report by the NIH and FDA[13]. Development of medical devices for Fontan patients has been limited, and thus there is great opportunity to positively impact this patient population.

The failing Fontan Phenotype

Over 50 years after the initial description of the Fontan circulation, we are still not certain about the exact mechanisms of its failure. Clinically, Fontan failure is a condition in which the circulation no longer meets the metabolic demands of the body and is unable to drain the venous blood and/or lymphatics efficiently[14]. This physiology triggers harmful consequences in the entire body including plastic bronchitis, protein losing enteropathy, hepatic and renal dysfunction, ascites, hepatocellular carcinoma, neuropsychological, and neurocognitive deficits[1], [7], [15], [16]. Unsurprisingly, the prevalence of venous insufficiency is high[17]. The myriad of deleterious effects leading to failing Fontan physiologies calls for an adequate treatment option to increase pulmonary flow, reduce retrograde flow, and mitigate venous hypertension.

Fontan failure is a complex syndrome that has a variety of causes, making the management of these patients challenging[14]. This results in highly variable, and inconsistent descriptions of Fontan failure in the literature. Attempt have been made to categorize the different phenotypes of Fontan failure into 4 types as follows; type I: Fontan Failure with Reduced Ejection Fraction, type II: Fontan Failure with Preserved Ejection Fraction, type III: Fontan Failure with Normal Heart, and type IV: Fontan Failure with Abnormal Lymphatics, Plastic Bronchitis, Protein

losing enteropathy [13] but uptake is limited and evaluation as well as treatment in different healthcare centers remains varied. Standardized evaluations for each patient must be coupled with individualized phenotype-specific therapies since complications can vary broadly between patients. Therapies should address the underlying hemodynamics and the causes of Fontan failure [14]. This underscores the importance of phenotype-specific hemodynamic models for the testing of device strategies as well. In this work I aim to overcome this obstacle by developing a Fontan flow model with adjustable components that recreate physiological elements and thereby allows the recapitulation of different hemodynamic conditions.

1.1.2 Hallmarks of Fontan Physiology

Cardiac output and venous flow

Cardiac output in Fontan patients is often compromised but the etiology of diminished cardiac function is multifold. In normal physiology, venous return - the flow of blood from the body back to the heart - flows into the right atrium. In Fontan physiology venous return is rerouted, bypassing the right heart, and flowing directly to the lungs before returning to the single ventricle. Up to 80% of our blood volume is stored on the venous side of our circulation, with up to 60% of that volume in abdominal organs[19]. In normal physiology, venous return is based on the pressure gradient between the mean systemic pressure existing in the circulatory system and right atrial pressure. This driving force is inherently compromised in the Fontan physiology, as blood is shunted directly into the lung vasculature, resulting in systemic venous hypertension and chronic low cardiac output[14]. There are many underlying mechanisms that reduce cardiac output in the Fontan physiology, including the overload of venous capacity and hypertension, passive blood flow through the lungs that relies on low pulmonary vasculature resistance (PVR), the inability to augment heart rate due to sinus node dysfunction, and systolic or diastolic ventricular dysfunction. Recent understanding of the Fontan physiology suggests that the root cause for ventricular dysfunction lies in compromised cardiac return and chronic venous congestion[3]. Increased hepatic portal vein pressures are noted in single ventricle physiology and are associated with Fontan Associated Liver Disease (FALD). There is a clinical need to lower the Hepatic-IVC pressure gradient (suspected decreases of 2-5 mmHg could have profound physiological benefit) as prolonged elevation of this gradient has been associated with FALD progression to hepatocellular carcinoma [20], [21].

Cardiac output: Implications on Fontan modeling and circulatory support

The effects on venous circulation are the focus of this work, which aims to address some of the main challenges of the Fontan flow by creating a physiologically relevant model which emphasizes the recreation of the venous side.

The reduced venous capacitance in Fontan circulation increases flow resistance in the abdomen and lower limbs and makes the venous mechanisms vulnerable to flow path obstructions including prosthetic materials and increased PVR[7]. Hence, this work will focus on support strategies to minimize any causes of such flow obstruction.

Interaction with respiratory biomechanics

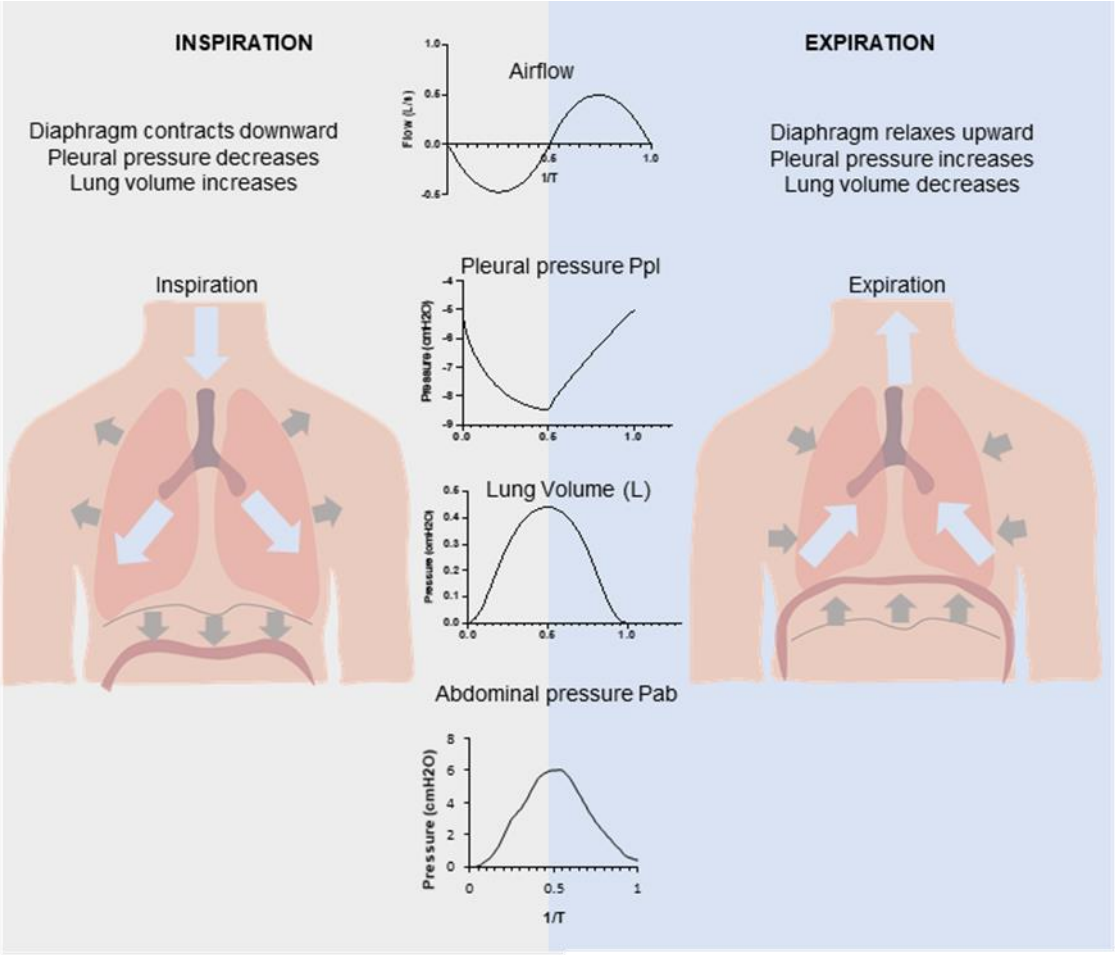

Figure 4: Mechanics of respiration. Diaphragm displacement affects the pressures in the respiratory system, driving airflow, which generates changes in lung volume, resulting in inspiration and expiration.

Respiration plays a large role in blood flow for Fontan patients. Herein, we describe the mechanics of respiration, shown in Figure 4, and its impact on blood flow for Fontan patients. The diaphragm is the major muscle responsible for inspiration, contributing the majority of pump

function within the respiratory system[22]. It separates the negatively pressurized thoracic cavity from the positively pressurized abdominal cavities.

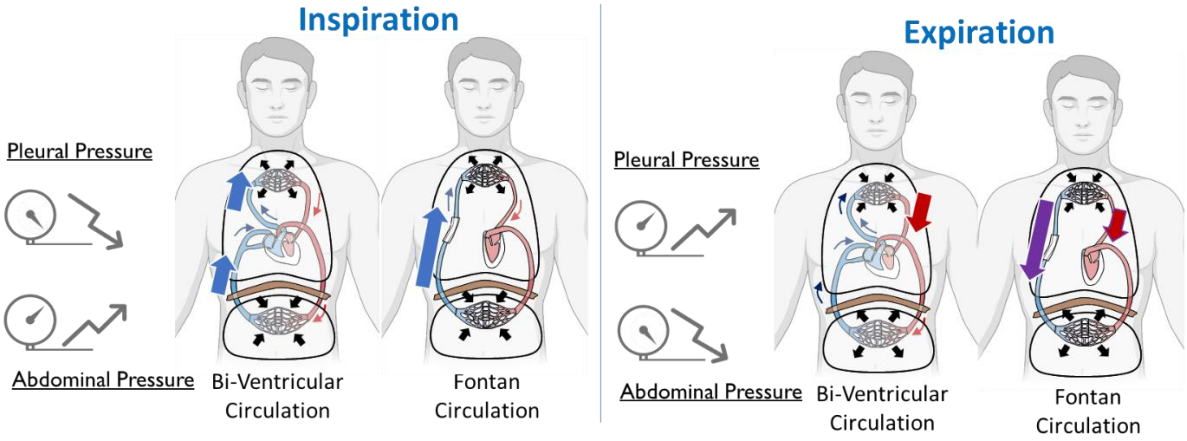

Figure 5: The cardio-respiratory pump in bi-ventricular and Fontan circulation.

The IVC, which ascends from the abdomen to the thorax, as well as the pulmonary vasculature are exposed to pressure variations during the breathing cycle. The negative intrathoracic pressure during inspiration increases the transmural pressure of the vasculature, causing the vasculature to expand. Meanwhile, a concomitant increase in abdominal pressure squeezes the abdominal vasculature, generating a flow of blood from the abdomen through the IVC into the thorax (Figure 5.). This mechanism is also termed the “respiratory pump”. Lung expansion causes its blood volume to increase, which in normal physiology results in elevated IVC flow to the right heart and decreased pulmonary venous return to the left heart through the pulmonary veins. During expiration, the opposite occurs. A pressure gradient squeezes blood from the pulmonary vascular bed causing IVC flow to decrease and left ventricular filling to increase. In biventricular physiology the net effect of increased rate and depth of respiration is an increase in left ventricular stroke volume and cardiac output. The cardiorespiratory mechanism in Fontan physiology is very different. While inspiration also increases IVC return in Fontan patients by up to 140%[23] the major difference occurs during expiration. When blood is pushed from the lung vasculature during expiration it can flow towards the heart or the abdominal vasculature which, in Fontan patients, is directly connected to the lungs (Figure 5). This mechanism can diminish cardiac return during expiration and contributes to retrograde flow in the IVC of up to 30%[4].

Interaction with respiratory biomechanics:
Implications on Fontan modeling and circulatory support

While in normal physiology, increased respiratory effort and rate contribute to increased cardiac return and thus cardiac output, Fontan patients experience an early decrease in ventricular filling volume and stroke volume during exercise[24]. Therefore, a support strategy for Fontan flow that decreases retrograde flow through the IVC holds potential to increase cardiac return and therefore cardiac output. In Fontan patients, flow variations are influenced by changing intrathoracic and intra-abdominal pressure which vary greatly with respiratory effort and rate. The extent to which the extravascular pressures influence hemodynamics depend on patient (and disease state) specific biomechanical tissue characteristics, such as compliance and resistance. Hence, Fontan support strategies must be tested on hemodynamic flow models that incorporate respiration and biomechanical tissue compliances, to accurately mimic physiology. Respiration therapy aiming to use increase breathing efforts to aid Fontan flow has been suggested previously but its effectiveness has been questioned in the light of flow reversal in the IVC [4]. It was suggested that retrograde flow in the IVC increases portal vein pressure [25], [26] which might trigger liver disease. Also, it has been shown that flow reversal due to respiration increases venous pulsatility [4] which in the Fontan physiology is associated with dynamic power loss and less efficient flow [27]. Still, understanding of contributing factors to retrograde flow and potential clinical effects remain unclear.

A flow model which mimics the cardio-respiratory pump will present a platform to investigate the interaction of breathing and venous flow pattern including flow reversal during expiration. This will also allow us to investigate the potentially different impact of respiratory effort and respiratory rate on reverse flow in the IVC which has not been studied so far. Detailed investigation of this relationship may inform respiratory exercises suggested for single ventricle patients. The model platform would need the ability to have adjustable elements representing physiological characteristics to model forementioned highly variable patient phenotypes and explore the impact of potential flow support strategies.

2. Chapter 1:
Recapitulation of single ventricle hemodynamics and cardiorespiratory coupling with benchtop and computational models.

2.1 Introduction

Detailed understanding of the Fontan circulation and its characteristics remain unclear and subject to research. Recent findings have underscored the pronounced impact of respiration on the single ventricle venous flow but still benchtop and computational modeling of the cardiorespiratory pump physiology is limited.

2.1.1 State of the field and current limitations

Clinical measurements of Fontan Hemodynamics

In the clinical setting Fontan hemodynamics can be measured invasively and non-invasively. Invasive measurements are obtained via catheterization often with patients sedated and in the supine position. The invasive nature of these procedures hinders efficient advancements in the exploration of Fontan hemodynamics. Also, the sedative status and positioning of the patient may not be representative of key factors influencing single ventricle circulation. Non-invasive measurements do not record hemodynamics, rather infer the blood flow conditions from respiration and blood pressure measurements on the upper limbs. Hence, imaging studies have become instrumental in overcoming some of these limitations. 2-D doppler ultrasonography has been used to evaluate Fontan flow including the important effects of respiration[25]. Limitations of this kind of ultrasound measurements include its predisposition to errors due to the angle between insonation and flow axis[28]. The IVC is not strictly perpendicular to any plane of the body and ultrasound measurements are performed with handheld devices during which the angle of insonation is subject to the judgment of the user alone. Measurements to quantify IVC flow will incur errors when the insonation angle is not strictly perpendicular to the IVC which can only be estimated by the user. Therefore, real time magnetic resonance imaging (MRI) has become a reliable modality to evaluate Fontan flow including breathing effects[4], [29]–[31]. To segment respiratory phases during hemodynamic analysis of Fontan patients the chest wall motion which was recorded during real time MR imaging has been used previously [30]. Recently, focus shifted towards the quantification of retrograde flow in the IVC during

the expiration phase [4]. While this allows the quantification of flow patterns the assessment of the hemodynamic status remains difficult without any pressure monitoring. Such flow imaging has not been combined with invasive measurements necessary to obtain an accurate picture of the underlying pressures. Additionally, during clinical measurements physiologic parameters cannot be changed during patient analysis and the heterogenous patient population complicates correlating study results between individuals and patient groups.

Preclinical *in vivo* models of Fontan Hemodynamics

Circulatory models aim to simulate the hemodynamics of physiological systems. They can be implemented computationally, on the bench top, or in live animals.

Animal models are established as a critical link to translate research of circulatory support to clinical practice as they often allow for close recapitulation of the patient phenotype[32]. In spite of great efforts to develop comprehensive animal models for the Fontan physiology [33], strategies for their use in evaluating Fontan support devices is limited by (i) low survival rates, (ii) inaccurate anatomical adaptations of Fontan vasculature, (iii) positive pressure ventilation which misrepresents physiological breathing mechanisms, and (iv) a limited variability of physiological and material characteristics to study different hemodynamic conditions. Despite continued efforts to understand and support the Fontan circulation, no animal model is reported to mimic clinical Fontan flow to date.

Bench top and Computational modeling of Fontan Hemodynamics

Lumped parameter networks are used to simulate flow dynamics on an organ level and allow investigation of the global effects of the circulation. *In silico* and *in vitro* flow loops are frequently used in such configurations so that rigid tubes and pumps are combined with elements of specific resistance, compliance and inertance representing physiologically distinct segments of the circulation. Physical and animal models are most suited to evaluate medical devices. Flow loops are commercially available (Medical Implant Testing Lab Inc.) and are used to evaluate VAD systems for adults[34], pediatrics[35], and have been suggested for the Fontan circulation. The most prevalent approach is to simulate compliance with Windkessel vessels (trapped-air chambers). Some efforts to include respiratory impact on Fontan loop hemodynamics involved hybrid flow models which control pumps and Windkessel compliance elements[36]. Over 60% of our blood supply is stored within the liver and digestive tract of the abdomen. These abdominal components are directly impacted by breathing pressures,

especially in Fontan patients. Recapitulating Fontan flow in a physiological manner requires the modeling of compliant vascular beds and respiratory pressures which are interdependent in both the thorax and the abdomen. The most advanced models thus far include segments of the modeled IVC and pulmonary arteries fabricated from compliant materials paired with a rigid case in which a membrane separates fluid from pressurized air. These elements are then subjected to computationally controlled alternating transmural pressures [33], [34]. Due to the large number of variables surrounding respiration and Fontan hemodynamics – including fluctuating volumes, pressures, flow rates, and compliances – mimicking physiological flow patterns in Fontan patients is a complex task. Therefore, the implemented computational control mechanisms run intricate software to carefully synchronize and control flow and compliance of the programmable compliance chambers. While this approach may allow to recreate Fontan flow patterns the interconnected and prescribed variables may impact the hemodynamic response of perturbations of the circulation like devices or changing physiological parameters. Although there exists a variety of simulators in the literature, none capture the extent of biomechanical and biophysical phenomena that govern the hemodynamics of Fontan circulation and recapitulate Fontan flow in a physiological way. Computationally controlled simulators are limited by large numbers of input variables and the interdependence of those input variables. The importance of subdiaphragmatic influence on venous return in Fontan physiology has been emphasized. However, no flow loops have been introduced that consider the pressure variations in the thorax as well as in the abdomen as relatively dependent functions to affect compliant vascular elements and thus hemodynamics. Also, no bench top model has been reported which flow dynamic response to varying breathing patterns has been validated clinically.

Different bench top and computational models can be used to investigate the flow structure of Fontan venous flow in more detail. Numerical simulations like computational fluid dynamics (CFD) and bench top applications like pulse image velocimetry (PIV) allow to (i) investigate velocity and shear stress information which inform hemodynamic performance, (ii) visualize potential risk for thrombogenicity, and (iii) blood damage that may occur as effects of circulatory support. They have been used separately and in combination to investigate flow structures in the Fontan circulation[39]–[41].

2.1.2 Limitations addressed in this chapter

Animal models fail to recreate important hemodynamic changes driven by respiration in the single ventricle physiology. In this light, focus shifts to computational and bench top simulators

to serve as valuable translational tools to investigate circulatory support strategies and surgical approaches.

Limited efforts have been made to recreate respiratory effects on Fontan hemodynamics in benchtop models and none are available which mimic respiratory biomechanics and the interdependent pressure changes between abdominal and thoracic cavities holding compliant vascular beds. We address these shortcomings with a biomimetic simulator of Fontan flow that recapitulates biomechanical influences on flow-dynamics and the interdependence between respiratory pressure and flow in the thorax and abdomen. This has potential to investigate the Fontan hemodynamics on a systems-level in greater detail. Such a tunable simulator can serve as a valuable test bed for the exploration of Fontan circulatory support strategies. Furthermore, it could serve as educational and training tool, to enhance understanding and intuition of complex biological systems, presenting a hands-on learning opportunity while causing no harm to a potential patient or living animal. The proposed bench top simulator will be validated on an organ level with a computational lumped parameter model including all organ systems as well as a prospective clinical trial.

Results from this cardiorespiratory simulator will be validated with a combination of CFD and PIV set ups. This way the technological advancement of the recreation of organ-level Fontan flow will be coupled with state-of-the-art measurement modalities for comprehensive fluid dynamic analysis. This suite of models will provide the ability to investigate physiological characteristics of the Fontan physiology as well as its interaction with potential support strategies bridging systems-level flow dynamics to the detailed evaluation of flow structure, underlying hemodynamics, and blood interaction.

Currently prevailing clinical measurement protocols do not provide a comprehensive picture of Fontan hemodynamics. Also, physiological characteristics in each patient are difficult to manipulate so the exploration of their relationships remains difficult. In this chapter we address these shortcomings with a hemodynamic simulator (Fontan loop) that can simulate the biomechanical interactions between breathing and Fontan flow to permit simultaneous evaluation of flow and pressures giving a more comprehensive picture of this physiology. Elements can be changed to model varying physiologic parameters and even anatomic position. Important vascular geometries can be segmented from patient MRI data and implemented in the physical model to create a tool to provide measurements that cannot be obtained from patients and thereby elucidate important physiological correlations.

2.1.3 Specific aims

A physiological representation of the interaction of Fontan flow with respiratory mechanisms is unavailable so **the goal of this chapter** is to recapitulate single ventricle hemodynamics and cardiorespiratory coupling with benchtop and computational models. To achieve this objective, a biomimetic platform of bench top and computational models will be developed which enables the study of the interaction of respiration and Fontan hemodynamics in more detail and provide a valuable test platform to explore circulatory support strategies for the single ventricle physiology. Bench top and computational models will be validated with a prospective clinical study of five Fontan patients. Towards this end the **specific aims** of this chapter resemble on organ-level flow dynamics and comprehensive flow dynamics:

A.) Organ level flow dynamics:

1. Develop a biomimetic respiratory simulator
2. Develop a biomimetic circulatory simulator with overlaid flow and respiration mechanism for the single ventricle physiology
3. Develop a computational lumped parameter model of the Fontan physiology
4. Validate the *in vitro* and *in silico* models with *in vivo* data.

B.) Comprehensive flow dynamics:

1. Develop a computational fluid dynamic (CFD) model of Fontan flow.

2.2 Methods

Figure 6 shows an overview of the conducted studies including the desired outcomes for chapter 1.

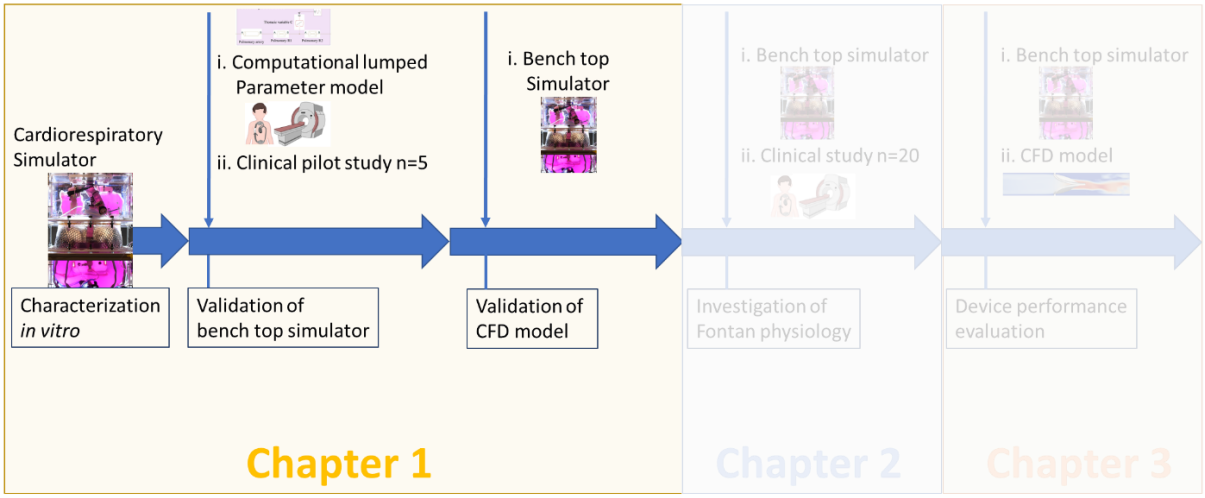

Figure 6 : Schematic showing the sequence of studies for chapter 1.

Organ-level flow dynamics:

2.2.1 Bench top biomimetic respiratory simulator

Approach to mimicking respiratory biomechanics

As described in section 1.1.2 respiration is a governing factor of venous flow pattern in the Fontan IVC. Due to the large number of variables surrounding respiration— including fluctuating volumes, pressures, flow rates, and compliances—mastery of respiratory biomechanics is a complex task. To recreate the relationship between Fontan hemodynamics and respiration in a physiologically meaningful this work aims to mimic the key features of respiration both structurally as well as functionally. This includes the anatomical configuration of the two main respiratory chambers, the thorax and the abdomen, which are separated by the diaphragm, which is the main functional driver of respiratory pressures as can be seen in Figure 7.

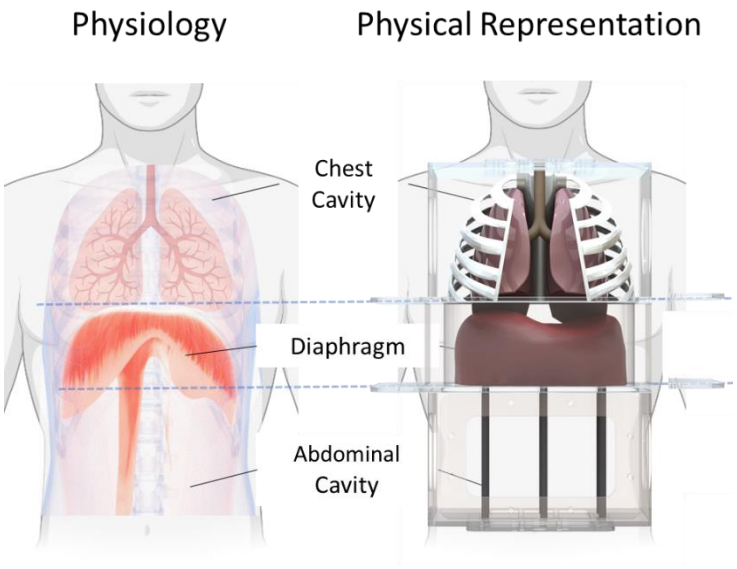

Figure 7: Physiological arrangement of respiratory organs leading the design of the biomimetic respiratory bench top model.

This simulator focuses on replicating physiological pressures and volumes by recreating the mechanical interactions of the lungs, diaphragm, pleural space, and abdomen. The diaphragm is the major muscle responsible for inspiration, contributing the majority of pump function within the respiratory system.16 In normal tidal breathing, downward motion of the diaphragm increases the volume of the thoracic cavity, decreasing pleural pressure (Ppl)—baseline –3 to –5 cm H2O, with quiet breathing efforts generating pleural pressures down to –9 cm H2O17—and alveolar pressure to below the pressure at the airway opening and, thus, driving airflow into the lungs. The diaphragm also couples the thoracic and abdominal cavities together, as its downward motion simultaneously decreases the volume of the abdominal cavity with increasing abdominal pressure (Pab). Clinically, the most relevant pressure outputs are the pleural pressure and the abdominal pressures. The pleural cavity is the potential space between the tissue lining the exterior surface of the lung and the interior surface of the thoracic cavity. In the created system, this corresponds to intrathoracic pressure. This work aims to match the physiologic pressure waveforms for the pleural and abdominal pressures to clinical data for normal breathing. Key to the physiology of the respiratory system is the compliance of different elements. Compliance is defined as the change in the volume of a space due to a change in pressure, dV=dP. This system allows for the tuning of compliance of different elements, such as the lungs or the abdominal cavity, via different soft material mechanisms. As soft robotics are effective in replicating controlled muscle motion, we sought to introduce mechanically programmable soft robotics into a dynamically pressurized system replicating diaphragm displacement.

To monitor physiological breathing pressure in the thorax and abdomen the model was instrumented with pressure sensors. I included real swine lungs to demonstrate how the recapitulated breathing pressures can lead to negative pressure respiration.

Design of the biomimetic respiratory simulator

I constructed the two main cavities simulating the thoracic and abdominal space from acrylic (polymethylmethacrylate) plates of ¼ in. thickness as shown in Figure 7, which were fixed with screws and sealed with chemical adhesive (Clear Weld by JB Weld). The simulated abdomen included a window composed of a silicone sheet that serves as the compliance element (DragonSkin FxPro, Smooth-on, Inc.). To vary the compliance, the silicone window can be covered with a layer of non-extensible polyester which is attached with Velcro around the perimeter; it can be rolled back to various degrees to expose the silicone window and, therefore, increase the compliance as desired.

I formed the shape of the rib cage that borders the modeled diaphragm (the zone of apposition) using a thermal vacuum forming machine (Formech450DT, Formech, Inc.). For this purpose, I segmented computer tomographic images of a ribcage using image processing software (Mimics, Materialise NV). The same data were used to cast a model of the corresponding diaphragm in a composite material of silicone and nylon mesh as shown in Figure 23A (DragonSkin20, Smooth-Sil, Inc.). I selected these silicone elastomers since they were readily available in a range of mechanical properties to match our design requirements and our previous experience with using silicone to mimic dynamic features of dynamic tissue. I 3D printed the upper region of the rib cage that contains the lungs, with geometry derived from physiologic data (Dremel 3D45). To generate the contractile force that displaces the diaphragm down toward the abdominal space, I used McKibben pneumatic artificial muscles. Six of these actuators were equally distributed, sutured, and sealed through the silicone and nylon diaphragm (Silpoxy, Smooth-Sil, Inc.). On the opposite side, the actuators were screwed to the bottom face of the abdominal cavity. I fabricated the McKibben actuators as previously reported [42] and added a latex outer sleeve to facilitate emptying of the pneumatic elements after contraction as shown in the figure below [43].

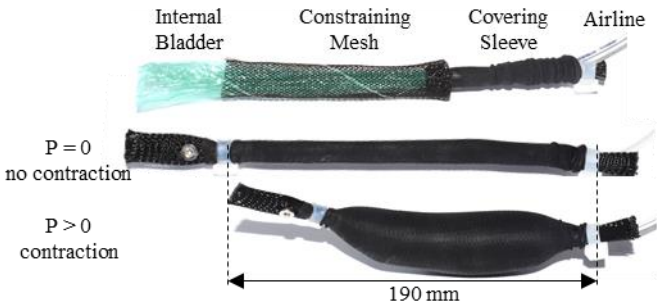

Figure 8: Manufacturing of McKibben PAMs with an internal bladder attached to a supply airline, covered by a nylon mesh, and an elastic liner. Upon pressurization the PAM contracts linearly.

Due to their similarity in size, anatomy and lung tissue resistance and elastance, I used swine lungs to visualize inflation and deflation. Ethics approval for using *ex vivo* swine tissue was obtained from the Committee on Animal Care at the Massachusetts Institute of Technology (Protocol 0121-03-24**)** I used swine lungs fixed in a solution based on propylene glycol to preserve tissue elasticity and used cyanoacrylate-based adhesive to seal any residual tissue defects (AnatomyWarehouse). All measurements were obtained using a mass flow meter and pressure sensors connected to signal conditioning and a custom software interface (SFM3000 by Sensirion AG, ArgoTrans model2 by Argon Medical Devices, NI9237 and Labview software by National Instruments, Inc.).

Electropneumatic control of respiration

We controlled actuation patterns of the diaphragm with a customized pneumatic control system shown in Figure 9.

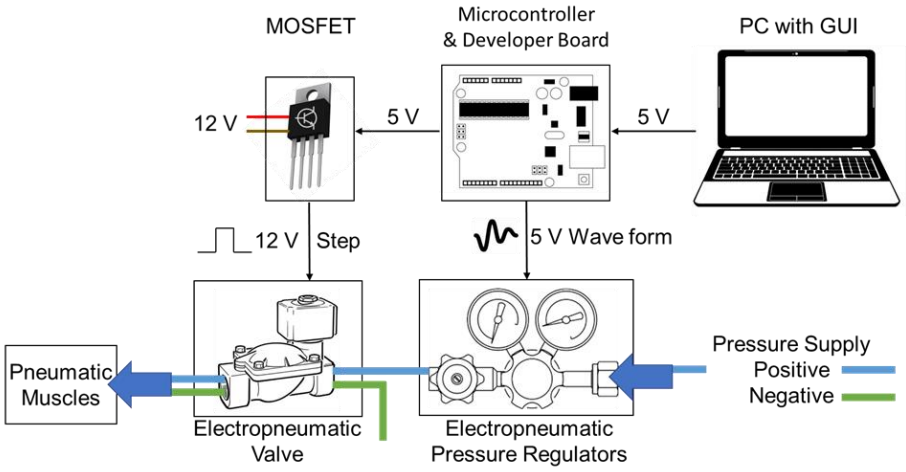

Figure 9: Schematic of the simulator control system. The desired pressure wave form is generated on a PC with a custom GUI. A microcontroller is used to control the pressure regulator and solenoid valve

to deliver the pressure waveforms to the pneumatic artificial muscles actuating the organosynthetic respiratory simulator.

We delivered pressurized air by inputting a pressure waveform to an electropneumatic pressure regulator. We used a laptop with a custom user interface (designed in “Processing” programming language) that communicated input values to the developer board (Arduino Mega). The microcontroller on the developer board inputs the desired pressure waveform to the electropneumatic pressure regulator (ITV1030, SMC, Inc.), which was connected to the wall compressed air supply. We simultaneously used the microcontroller to open and close a solenoid valve (NVKF333, SMC, Inc.) using a 12 V MOSFET that allowed the pressure regulator to provide the desired pressure wave form to actuate the pneumatic artificial muscles and move the diaphragm in our model.

2.2.2 Bench top biomimetic Fontan flow model overlaid with respiratory simulator

Design of the venous Fontan flow loop in respiratory simulator

The concept of an anatomically inspired mock loop includes a respiratory simulator with two main cavities representing the thorax and the abdomen. These cavities are separated by a moving diaphragm to recreate pressure changes similar to breathing. To recapitulate Fontan flow on the bench top I included a (i) lumped parameter flow loop of the venous Fontan hemodynamics into the (ii) biomimetic respiratory simulator. When (i) and (ii) are combined, they mimic the interdependent flow mechanics of Fontan physiology (Figure 10).

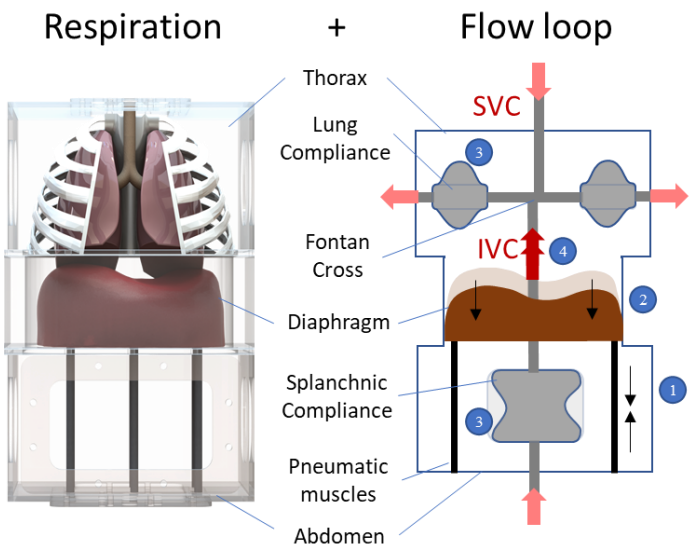

Figure 10: Combining the respiratory simulator with a Fontan flow loop. The mechanism of how breathing mechanics influence the compliant vessels of the circulatory simulator.

As described in section 2.1.1 the focus of the Fontan flow loop is on the venous side of the Fontan circulation where the origins of the pathophysiological effects are concentrated. Hence, the flow system provides constant flow, and includes compliance vessels and resistance valves representing all major vascular reserves. Figure 10 describes the functionality of the proposed system; Pressure waveform are driving the contraction of the Pneumatic Artificial Muscle actuators (PAMs) attached to the diaphragm, using the custom mechatronic control box described in section 2.2.1 (1). During simulated inspiration, the contracting actuators pull the diaphragm into the abdominal cavity (2). This increases the volume of the thoracic cavity, while simultaneously decreasing the volume of the abdominal cavity. This motion causes a pressure drop in the thoracic space, and a pressure increase in the abdominal space. The generated pressure gradient between the two cavities drives fluid from the high-pressure abdominal space to the lower pressure thoracic space (3). This results in an increased forward flow through the mock IVC (4). During expiration this mechanism is reversed resulting in reduced forward flow and even flow reversal.

The anatomical sequence of the Fontan vasculature was replicated in the respiratory flow model as shown in Figure 11. To allow for adequate mixing of the fluid streams we decided to replicate the flow geometry of a patient specific Fontan shunt and Fontan cross. Pressure sensors (Pendotech) and ultrasonic fluid flow sensors (Transonic) were synchronized on a data acquisition platform (Labview, National Instruments) to monitor respiratory and hemodynamic pressure and flows simultaneously. The position of sensors is shown in Figure 11.

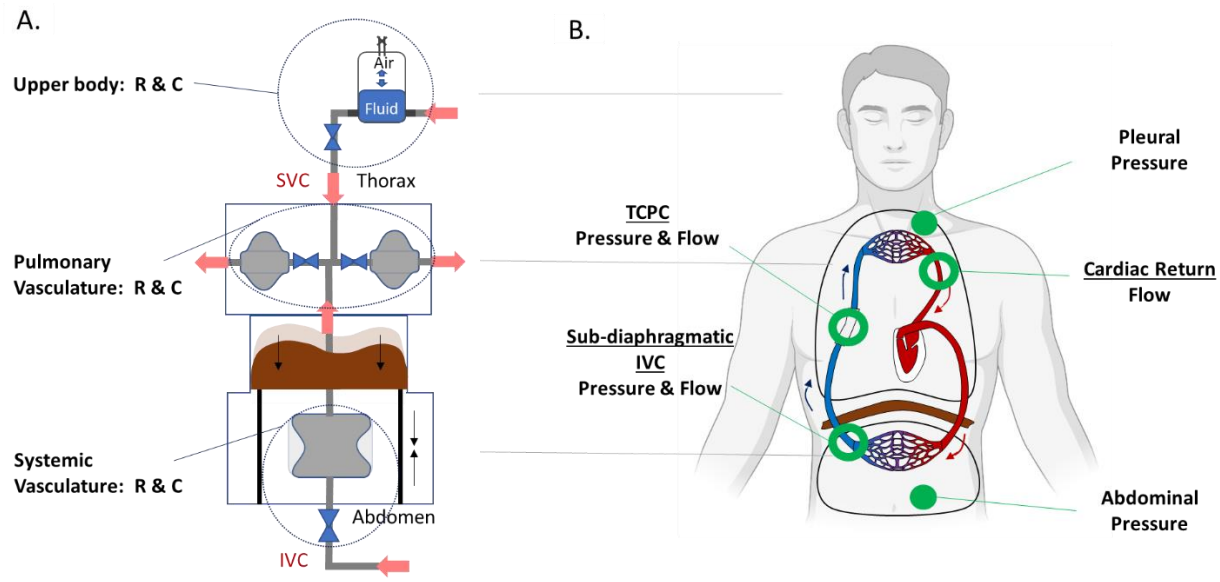

Figure 11: (A) Architecture of lumped parameters for cardiorespiratory simulator: For each segment of the body, upper body, pulmonary vasculature, and systemic vasculature in the abdomen, the vessels consist of a resistance element R and a compliance element C. (B) Schematic drawing of the instrumentation of the breathing and flow model: flow and fluid pressure can be monitored in the locations simulating the hepatic vein in the sub-diaphragmatic IVC, the location of the Fontan shunt (TCPC), and the combined flow and pressures after SVC and IVC reconnect into the cardiac return. Gas pressures are monitored in the abdomen and thoracic compartments.

The venous flow in Fontan patients ranges from 2.3-3 L/min which is the combined IVC flow (from the abdomen) of 1.5-2 L/min, and SVC flow (from the upper body) of 0.8-1 L/min. In Equation 1, volumetric flow, Q, through the cardiovascular system, is defined as [19]:

$$Q = \frac{\Delta P * \pi * r^2}{8 * \mu * l}$$

Equation 1

with pressure gradient ΔP, vessel diameter r, fluid viscosity μ, and length l. In Fontan surgeries shunt diameters are often 20 mm, and so I used 20mm diameter tubing. To generate comparable hemodynamics, the fluid used in the flow loop should have a similar viscosity and density to blood, 3.5 mPa*s and 1055 kg/m^3 respectively. In the mock loop design, I used silicone tubing with a total length of 4 m. The necessary pressure gradient ΔP to drive the desired flow was calculated with Equation 2. This driving pressure ΔP can be generated by the height difference Δh between two constant head reservoirs according to:

$$\Delta P = \rho * g * h$$

Equation 2

with fluid density ρ, and gravitational acceleration g. To generate physiologic IVC pressures of 12-24 mmHg (1.6- 3.2 kPa) the reservoirs which supply the inflow and outflow of the Fontan flow loop are elevated above the relative zero position of the IVC. The height difference between the constant-head reservoirs was calculated to be 40 cm to achieve the maximum desired pressure of 3.2 kPa. The compliance vessels and resistance valves were designed to represent the vascular mechanics of the body. Three main sections of the Fontan circulatory system were reproduced, each with compliance vessels and flow resistors as shown in Figure 11: (i) circulation of the upper body resulting in the SVC flow, (ii) circulation in the abdomen including the liver and the digestive tract, and (iii) the flow through the pulmonary vasculature. The circulation of the upper body is mostly unaffected by breathing efforts, thus, I used a Windkessel design with rigid acrylic walls as a compliance vessel, and a ball valve as a flow resistor (Figure 11). Conversely, the compliance vessels of the simulated abdominal and chest cavity are directly impacted by the surrounding pressure changes. Thus, I designed those vessel wall using extendable silicone membranes. Effective vascular compliance is reported in the range of 2.3-2.7 ml/mmHg/kg with intrathoracic compliance contributing 1-1.2 ml/mmHg/kg [44] to the overall compliance. For an average human (body weight of 62 kg), this results in values of 142.6-167.4 ml/mmHg for total vascular compliance and 62-74.5 ml/mmHg for intrathoracic compliance. The compliance of any cylindric vessel C, shown in the linearized state Equation 3, is dependent on its inner radius r, wall thickness t, and dynamic modulus E [38]:

$$C = \frac{2 * \pi * r^3}{E * t}$$

Equation 3

The available space in the thoracic and abdominal model determined the overall dimensions (length l and radius r) of the abdominal and thoracic compliance vessels. We matched the physiological range for the compliance vessels by using equation 3 to determine the elastic modulus E (DragonSkin 10, Smooth-on Inc) and thickness of the vessel walls as seen in Table 1:

Compliance Vessel	E (kPa)	r (mm)	t (mm)	l (mm)	Estimated Compliance (ml/ml/mmHg)
Chest	152	100	1.5	70	64.4
Abdomen	152	130	1.5	100	101.1

Table 1: Estimated design parameters for chest and abdominal compliance vessels, with resulting estimated compliance values.

Due to space constraints, we split the intrathoracic compliance vessel into two compliance vessels distributed on both sides of the chest cavity similar to the anatomical partitioning of the lung vasculature in the left and right lung. The resulting compliance values $C_{Chest}1$ and $C_{Chest}2$ are connected in parallel and hence add up to the total chest compliance C_{Chest} as in Equation 4:

$$C_{Chest} = C_{Chest}1 + C_{Chest}2$$

Equation 4

Configuration, manufacturing, and integration of flow loop components

Respiratory Effort

The respiratory effort of a Fontan patient changes as they perform daily tasks. Respiratory effort has been reported to have influence on caval blood flow patterns. We varied the respiratory effort in our simulator between shallow and deep breathing, which corresponds to the efforts a patient experiences, and evaluated the change in IVC flow rates. Minimal breathing efforts do not result in flow reversal in the Fontan IVC simulator. Shallow breathing was simulated by providing 52 kPa to the pneumatic muscles actuating the diaphragm. Baseline breathing and heavy breathing efforts were simulated by actuating at 69 kPa and 86 kPa respectively. The shape of the pressure input generating the diaphragm contraction and therefore creating the respiratory pressures remained constant throughout all pressure values. This shape matched the respiratory curves from the literature described in Figure 4. We varied the breathing effort by scaling the amplitude of the input curve only.

Patient specific vasculature from MRI data

To recreate the constant flow observed on the venous side we used two constant-head reservoirs to maintain constant pressure in the mock loop. Each fluid reservoir was fixed on a mechanical lifting stage to control the elevation and, therefore, the pressure generated by the reservoirs. We used silicone tubing Ø19 mm (durometer 50A) for all vasculatures. The Fontan cross was segmented from patient MRI data (Mimics, Materialise NV) as shown in Figure 12, and a hollow shape was subsequently 3D printed (Objet30, Stratasys Ltd) to be included in the flow loop.

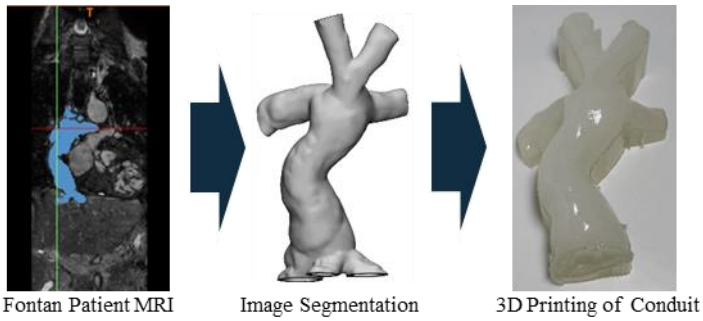

Figure 12: Fabrication of the Fontan cross from patient MRI data.

Compliance vessels simulate vascular beds

In Fontan patients, the upper body is subjected to blood pressures from the heart while the chest and abdominal regions are primarily subjected to respiratory pressures. Thus, two compliance vessel designs were used. The upper body compliance chamber is a trapped air chamber design. We built a rigid acrylic cylinder 70mm*150mm with 3-way stopcock gas port. Air is trapped and compressed inside, controlled by the fluid pressure from the reservoirs. Compliance can be varied using the gas port to inject or remove fluid. The chest and abdominal compliance vessels were designed to be stretchy silicone tubes that respond to diaphragmatic pressures. As respiration occurs the vessels can inflate and deflate causing changes in blood flow, simulating Fontan physiology. Within the abdominal cavity, we fabricated a single compliance vessel and two lung compliance chambers in the thoracic cavity. The compliance vessel frames, made from acrylic, have the following dimensions for the chest; 35mm*35mm*70mm, and for the abdomen; 130mm*40mm*100mm, as shown in Figure 13. Degassing ports and resistance valves were connected to each of the compliance chambers.

Figure 13: Compliance vessels. On the left, the abdominal compliance vessels and on the right, one of the two chest compliance vessels.

The compliant vessels are the components of the vasculature in the mock loop that respond to respiration and are subject to induced changes in flow. Thus, characterizing their function allows us to identify how closely the compliance of these elements match physiological values.

We evaluated the compliance of a stiff, semi-stiff, and compliant configuration. We achieved these changes in compliance by covering the free moving surface area of each compliance vessel with a non-elastic nylon sleeve by 100%, 50%, and 0% respectively. This characterized the range of compliance of our mock vasculature in the thoracic and abdominal space. To measure effective compliance, we injected a volume of fluid into the mock loop in increments of 10 ml, using a syringe pump (PHD ultra, Harvard Apparatus Inc.), and recorded the corresponding IVC pressure at each step. We set the initial IVC pressures in the mock loop to 17 mmHg to match the physiologic use case.

Surrogate fluid mimics blood rheology

As described above the fluid in the cardiorespiratory system should mimic the hemodynamic characteristics of blood at body temperature while being use in room temperature. We used surrogate fluid for the flow loop at room temperature to mimic blood viscosity and density at body temperature. For this purpose, we tested varying concentrations of monoethylene-glycol based coolants (J4D2002 LGC C13, Ravenol LLC). This alcohol-based fluid could be used long-term in the flow loop without fluid fouling. We tested the dynamic viscosity of varying concentrations of the surrogate blood with a Rheometer (Discovery HR-2, TA Instruments) and subsequently tested corresponding fluid densities.

System assembly

To assemble the final cardiorespiratory mock loop, we combined the elements of the respiratory and flow loop systems including the thoracic and abdominal cavities, diaphragm, PAMs, mechatronic control system, the compliance vessels, constant-head tanks, resistance valves, vascular tubing, and Fontan cross. A close-up of the mock loop final assembly is shown in Figure 14A, and the entire system, including upper body (SVC) compliance, constant head reservoirs, and vasculature tubing containing the blood surrogate is shown in Figure 14B.

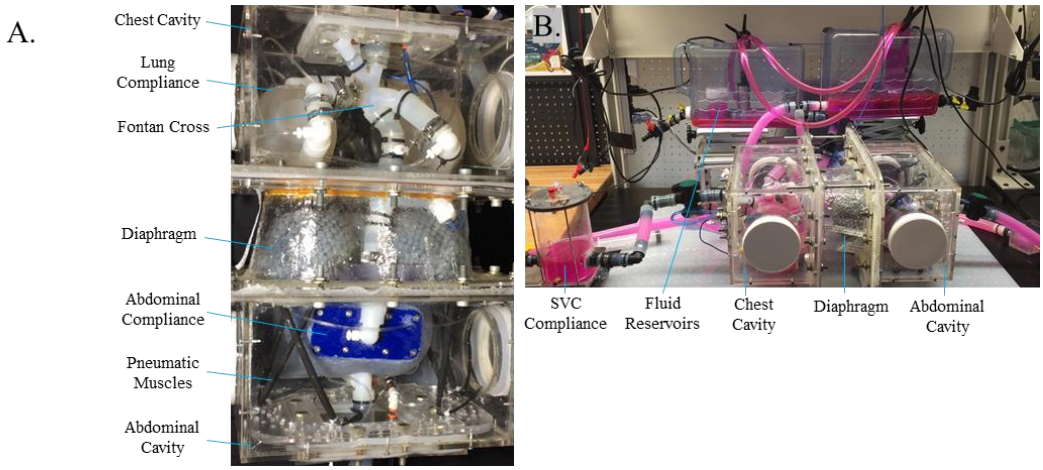

Figure 14: A) An overview of the mock circuit with overlaid respiratory and flow loop components and B) an overview of the whole system.

Simulator Flow-Range and Pressure-Range Characterization

To evaluate whether the mock loop can reach the range of mean physiologic flows relevant in Fontan circulations we varied the height difference between each constant head tank. To investigate possible effective mean pressures in the simulated IVC we incrementally increased the relative height between the two tanks and the IVC in the mock loop itself.

Recapitulation of clinical Fontan IVC flow

Recent studies have emphasized the impact of respiration on the Fontan flow pattern as described in section 1.1.2. Here we aim to adjust the elements of the flow loop to recapitulate published clinical waveforms of Fontan IVC flow during inspiration and IVC flow reversal during expiration [4] as seen in Figure 15.

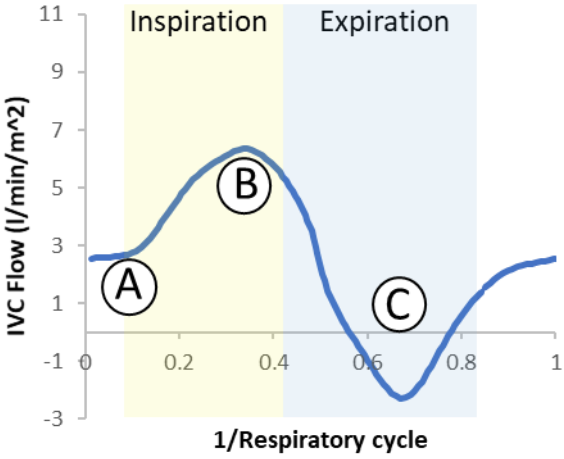

Figure 15: Representative clinical data of IVC flow during respiration from 14 patients with Fontan physiology. With inspiration the venous flow in the IVC increases from baseline A to B. With expiration the IVC flow decreases after B to C and even reverses its flow direction.

The above waveform comprises one respiratory cycle which entails the flow characteristics which respiration elicits in the Fontan IVC flow. We see that during inspiration, the IVC flow increases between (A) and (B) and stops increasing toward the end of the inspiration cycle. With expiration the forward flow in the IVC decreases from (B) to (C) and even reverses its flow direction causing retrograde flow into the abdominal vascular bed. As the respiratory pressure return to baseline, so does the IVC Fontan flow. In this data averaged from 14 patients with Fontan physiology we see that the baseline flow in the IVC was approximately 2.5 L/min which was the baseline flow for our validation experiment. As the SVC flow usually comprises of 1/3 of IVC flow we set the SVC flow in our simulator to 1.25 L/min. The input pressure curves to the PAMs that actuate the diaphragm were taken from the literature [45]. The available clinical data was created with MR imaging techniques and hence no pressure measurements are included. To match physiologically relevant IVC pressure for the Fontan circulation the baseline pressure in the IVC was set to 17 mmHg. After establishing the baseline flow dynamics under constant flow conditions, we initiated the breathing mechanics and monitored IVC fluid flows, IVC pressures in the Fontan shut and in the location of the hepatic vein into the abdominal IVC, and respiratory pressures in the chest and abdomen.

Parameter study to characterize Fontan flow in cardiorespiratory simulator

As described previously the Fontan population displays very heterogeneous physiological parameters and hemodynamics. Therefore, it is important to capture a wide range of hemodynamic conditions a Fontan patient may experience. In our model system we can adjust lumped

parameter elements as well as respiratory mechanics to generate variable Fontan flow conditions and determine which parameters of our flow loop have the highest impact on governing flow patterns. To achieve this objective we varied breathing parameters, baseline fluid dynamic conditions, vessel compliances, and flow resistances. This study served two purposes: (i) to explore what range of physiological input parameters could be simulated with the bench top model, and (ii) characterize the dynamic response of the cardiorespiratory simulator to isolated changes in physiologic parameters. This can then be compared to computational and clinical experiments to validate the functionality and dynamic characteristics of the bench top model.

Baseline conditions were set as follows: caval flow conditions were set to 2 L/min and 1 L/min for the IVC and SVC respectively, which is in the physiologic range of for Fontan patients. The blood pressure at the TCPC was set to 17 mmHg, which is within the physiologic range of Fontan pressures. The respiratory rate at baseline was 12 breaths/min. From these baseline values we conducted a parameter study exploring one of each of the following physiological parameters:

Respiratory Rate

The respiratory rate varies greatly during common daily activities. We explored the impact of respiration rate on IVC flow by altering the respiratory rate in our bench top simulator. Slow, baseline and fast breathing was modeled at 9, 12, and 20 breaths per minute.

Compliance

The compliance of the Fontan vascular beds store fluid and enable the shifting of fluid between them when driven by the respiratory pressures. Lung and abdominal vessel compliances can differ between patients, or within the same patient over time. To model this, we varied vessel compliances from in stiff, semi-stiff, and soft configurations by enclosing the compliant modules 100%, 50%, and 0% respectively. All vessel compliances were varied simultaneously.

Baseline IVC pressure

Mean IVC pressure in Fontan patients can vary based on their disease phenotype. Mean TCPC pressures may vary greatly numbers in the low teens into the high twenties. It has been reported that chronic pressures above 20 are poorly tolerated by the effected organ system of the Fontan physiology. We varied mean TCPC pressure, by changing the difference in height between our

constant-head reservoirs and investigated baseline pressures at 17 mmHg, 23 mmHg, and 26 mmHg.

Baseline IVC flow

Mean IVC flow in Fontan patients can vary based on their physique, and health condition. We aimed to investigate the impact of different amounts of baseline flow in the IVC on the resulting flow reversal in the Fontan shunt. To generate varying baseline flows through the IVC we varied the constant head pressure as described in previous section. We investigated baseline IVC flow of 1.4 l/min, 1.7 l/min and 2.3 l/min, which corresponds to physiological ranges.

2.2.3 Computational organ level lumped parameter model

Bench top models are suitable to simulate specific features of the Fontan physiology. The lumped parameter architecture of the bench top system aggregates functions of physiological elements and simplifies vasculature. As described previously, the biomimetic cardiorespiratory bench top simulator focuses on the recapitulation of the venous Fontan hemodynamics. Therefore, vascular anatomies and elements of the arterial tree, heart itself, and lower limps are not represented. To investigate whether the reduction of vascular elements in the bench top set up oversimplify the Fontan anatomy we developed a computation lumped parameter model which included elements of the entire body of the Fontan circulation to validate the bench approach. By replicating the parameter study to characterize the bench top model with the whole body computational lumped parameter model helps us to identify deviating dynamical behavior of the two system which could indicate oversimplification on the bench top. Conversely, it can validate finding of the hemodynamic impact variables. The object-oriented platform was developed in the MATLAB-based modeling environment SIMSCAPE and computes blood pressures at various sites of the vascular tree. The hydraulic domain allows the determination of cardiovascular hemodynamics intuitively from geometrical and mechanical properties of the system. The model was validated by comparing predicted hemodynamics with normal physiology.

Implementation of the object-oriented lumped parameter model

The object-oriented lumped-parameter model of the cardiovascular network was implemented in the hydraulic domain, where hemodynamics is primarily defined by the geometrical and mechanical characteristics of the human physiology. We adopted the object-oriented platform provided by the MATLAB based modeling environment SIMSCAPE, and utilized the hydraulic

library, which we expanded to mimic cardiac contraction and the effects of respiration on blood flow. General cardiovascular hemodynamics are then presented as a general validation of the proposed model [46]. Using the fluid domain allowed us to implement respiration as mechanical movement of the effected vascular beds to more closely model the biometric approach of the bench top model to recreate respiratory biomechanics.

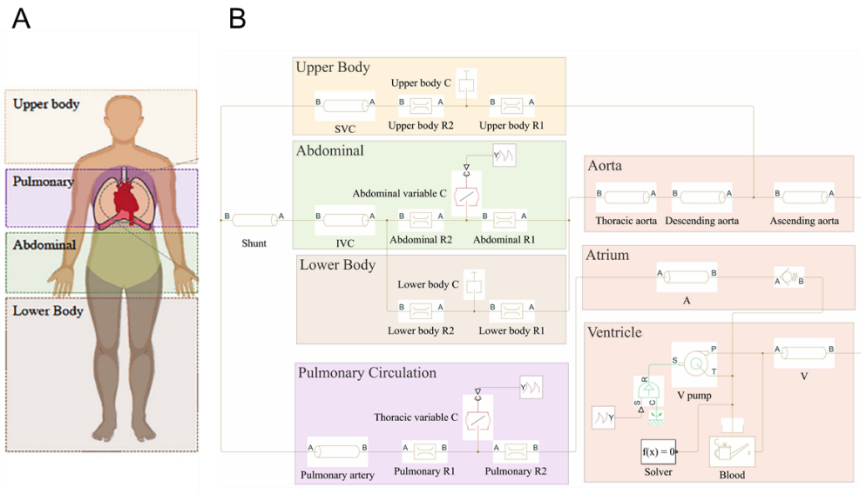

Figure 16: A) Representation of the cardiovascular system of the Fontan anatomy divided into the upper body, pulmonary, abdominal, and lower body circulations. B) Schematic of the simulation based on the human anatomy.

The computational simulation network emulated the Fontan anatomy. As shown in Figure 16, the heart was simulated by one ventricle and one atrium, with a shunt connecting the IVC to the superior vena cava (SVC) and the pulmonary circulation. In this description, breathing was simulated via variable-compliance chambers, in a similar fashion to our previous simulations. Furthermore, a constant input was provided to the centrifugal pump and the heart valves were removed from the model to eliminate any time-dependent effect from the beating of the heart. The geometrical characteristics of the heart chambers were modified from the baseline simulation to more accurately reproduce cardiac anatomy in hypoplastic left heart syndrome. Finally, the thoracic IVC was replaced with a simulated TCPC shunt to mimic that typically implanted during the surgical procedure, and pulmonary resistances were increased to model pulmonary hypertension, which is highly prevalent in Fontan patients. The detailed input parameters of this model and the schematic are described in Rosalia et al.[46]. Respiratory effects of the pulmonary vasculature were implemented by a time dependent variation of the pulmonary vessel compliance. This function followed the respiratory curves that were recorded in the bench top simulator. This allowed the computational model to simulate mechanical deformation of the

lungs to increase and decrease blood volume. Accordingly, the parameter study did not include variations of the baseline compliance of the lung vasculature.

Experimental Setup

We aimed to first recapitulate the published clinical data to show that by matching the average respiratory rate and cardiac output of the patient population in the clinical study, we closely replicated the breathing gating analysis, similar to the bench top model.

We further aimed to validate the hemodynamic characteristics of the benchtop simulator of Fontan hemodynamics described in section 2.2.2. We repeated the parametric study as described in the previous section for the bench top model.

2.2.4 Clinical validation study

To validate the results obtained with the biomimetic cardiorespiratory bench top simulator and the organ level computation model we aimed to conduct a prospective clinical trial. The objective of this pilot study was to evaluate whether the impact of varying respiratory effort and rate, as well as baseline IVC flow which were observed *in vitro* and *in silico* match clinical findings. Other physiological elements which were included in the bench top and computational parameter study described in the previous sections were not included in the clinical validation study as they are impractical to implement in patients. A 4D MRI study was selected as the ideal approach for this study.

Study design

Fontan patients who are scheduled for MRI at Boston Children's Hospital were discussed and screened by the research team. Eligible patients included all patients with a Fontan physiology that were 15 years of age or older and which did not have a Fontan fenestration or lateral tunnel, or which previously had the fenestration closed, and which did not have <85% resting O2 saturation. Once found to be eligible, the patient or family was sent a letter informing them about the study and giving them the opportunity to consent or decline ahead of their visit. The day of the scheduled clinically indicated MR study the patients were approached by the MRI team at patient check-in and prepared for imaging in a private consultation room. At the end of the standard preparations the MRI technologist introduced the research team to those patients who chose to participate. Subsequently, the research team explained the study in detail again, answered outstanding questions, consented the participant, and performed a rehearsal of the

breathing exercise which the participants would perform during MR imaging. Following the patient's routine MRI, the team carried the additional MRI study. During the MRI for research purposes the patient was guided through the breathing exercise using the available headphones and video screen. After the MRI was completed, the team extracted the flow velocities in the IVC and descending aorta from the MRI data, saved the chest wall motion in DICOM format, and reviewed the patient's medical history. The tested variables in breathing pattern which were investigated in this study as well as the measured output variables are summarized in Figure 17B and Figure 17C, respectively. In summary, respiratory effort, respiratory rate was varied and compared with and baseline venous flow in the IVC. Output variables of the IVC flow were forward and reverse flow volumes and forward and reverse flow rates which were used to calculate percent retrograde flow in the IVC as well as the pulsatility index.

The study was approved by the local ethical committee at Boston Children's Hospital (IRB-P00037103), and written informed consent was obtained and stored for all participants.

Study patient population

From April 2021 to June 2021, a total of 5 Fontan patients completed the respiratory study to validate the bench top and computational data. A summary of the patient population is shown in Figure 17A.

A

Patient population	
Age (years)	19.4 (±1.5)
Years post Fontan	17.5 (±2.1)
BSA (m2)	1.8 (±0.3)
BMI (kg/m2)	24.8 (±6.7)
Total patients	n = 5
Male Female	3 2
Fontan types	HLHS (n=3)
	DILV (n=1)
	RdAVC (n=1)

B

Tested variables	
Respiratory effort (RR = 14 = const.)	Shallow breath
	Baseline breath
	Deep breath
Respiratory rate	9
	14
	28
Breath-hold	

C

Output variables	
% retrograde flow	
IVC flow volume	+ / - (ml)
IVC flow rates	+ / - (L/min)
Pulsatility index	$\frac{Amplitude\ of\ flow\ rate}{Mean\ flow}$

Figure 17: Summary of study patient population and tested parameters for the validation study of the computational and bench top data. Characteristics of patient population (A), tested parameters (B), and output variables (C).

The study population consisted of 2 females and 3 males with an average age of 19.4 (+-1.5) years with completed TCPC 17.5. years ago, ± 2.1, a body surface area (BSA) of 1.8 m2 ± 0.3, and body mass index of 24.9 kg/m2 (+-6.7). Congenital heart diseases of the patient population

included hypoplastic left heart syndrome (HLHS, n=3), double inlet left ventricle (DILV, n=1), and right-dominant atrioventricular canal (RdAVC, n=1).

MRI protocol

MRI sequence

All participants performed a breathing exercise while situated in the MRI machine. The breathing exercise consisted of two parts during which the patient was encouraged to synchronize their breathing with an audio-visual guide presented to in the MRI set up. The image from the audio-visual guide for the patient is shown in Figure 18. During inspiration (Figure 18A) the white circle travels down, indicated by the red arrow, circling a violet circle which simultaneously expands as indicated by the white arrows. The inspiratory phase is also marked with red letters on the right side. During the expiratory phase the white circle travels upward on the opposite side of the violet globe, which is not shrinking, and letters indicate breathing out. The video included the five different breathing patterns describe previously and included a simultaneous audio guide for the patient. Following the audio-visual guide was practiced with each participant during a rehearsal study in the MRI preparation room. Respiratory rates were varied in each video section by adjusting the frequency of the circular motions as well as the expansion of the inner globe. Respiratory efforts were classified as shallow, baseline, and deep. The participants were asked to relax their breathing and breath with a respiratory effort comfortable for them which marked the baseline measurement. Subsequently the patient was asked to breath shallowly followed by a section of heavy breathing. We recorded chest wall motion during all phases to monitor how the participants were able to increase the respiratory efforts.

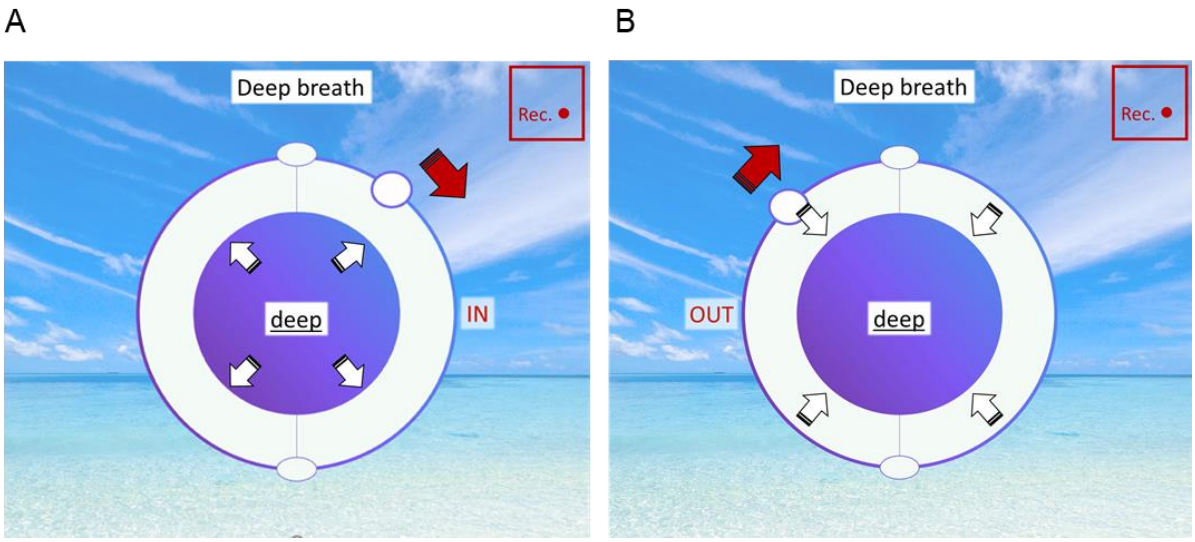

Figure 18: Screenshots of the video guide which lead each participants through varying respiratory rates and efforts; during inspiratory phase (A) and expiratory phase (B).

A schematic of the respiratory study in the MRI which every participant underwent is shown in Figure 19.

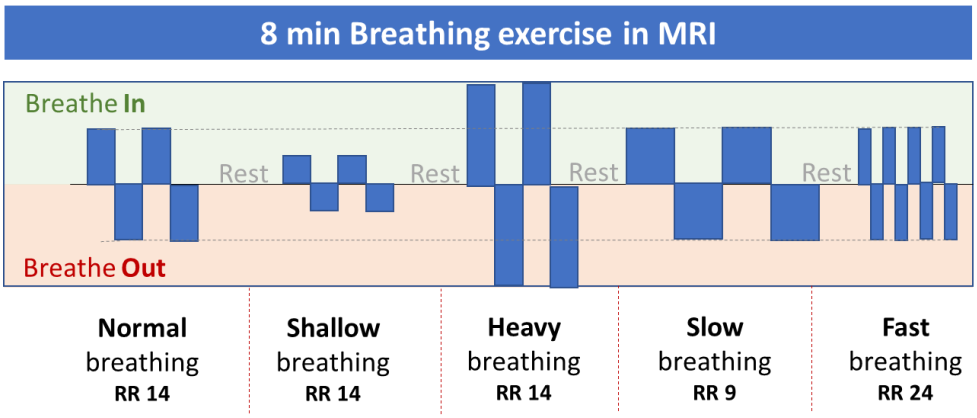

Figure 19 : Schematic workflow of the MRI respiratory study protocol for each participating patient.

During the first part of the breathing exercise the patient kept the respiratory rate constant (approximately 14 breaths/min) and varied the breathing effort. Initially participants breathed at baseline level according to their own comfort (~30s). Subsequently, the participants were encouraged to breathe shallowly (~30s), followed by a relaxation period at baseline effort (~1min) and a period of deep breathing (~30s). In the second part the participant breathed at a comfortable effort and varied the respiratory rate. Initially breathing slowly at approximately 9 breath/min (~30s), then pause with baseline breathing rate (~1 min), and finally a period of fast breathing at approximately 28 breaths/min (~30s). MR recordings during the described respiratory effort and rate exercises were recorded for approximately seven consecutive breaths triggered by the research team. In conclusion, during the real-time MRI study measurements of

five respiratory states were taken: (I) baseline breathing at ~14 breaths/min, (II) shallow breathing at ~14 breaths/min, (III) deep breathing at ~14 breaths/min, (IV) slow breathing at ~9 breaths/min, and (V) fast breathing at ~28 breaths/min. Between each segment of the breathing exercise there was a one-minute break for relaxation and recovery.

Imaging configuration

MR images were performed on a 1.5 Tesla MR system (Philips Medical Systems, Best, Netherlands) using a 28 channel surface coil array. Recordings were made in 2-D phase contrast (PC-MRI) mode to acquire real-time flow measurements at a temporal resolution of 54 ms. Sensitivity encoding (SENSE 5), a velocity encoding (VENC) of 180, and echo planer imaging level 11 were applied during image acquisition. The voxel size was set to 2.5mm x2.73 mm with a slice thickness of 10 mm.

The imaging plane of 300 mm to 300 mm was positioned perpendicular to the IVC 20 mm above entrance of the hepatic veins into the IVC as shown in Figure 20A. The MR image included the IVC, descending aorta, and anterior free moving chest wall.

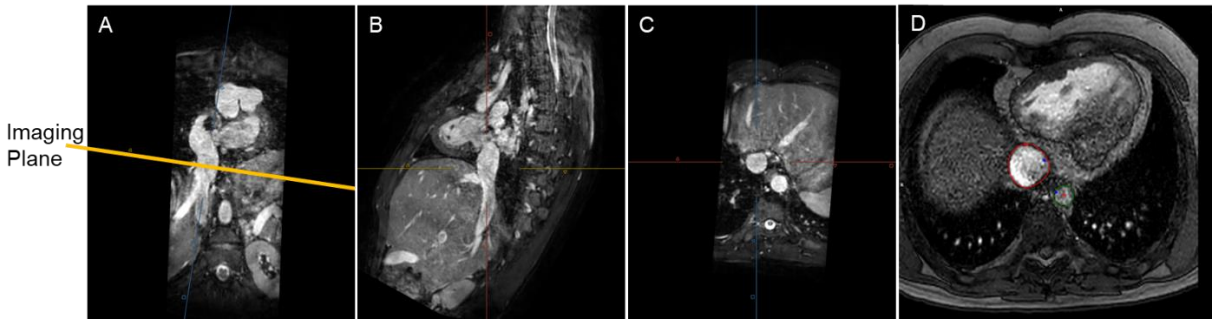

Figure 20 : Imaging plane for the real-time MRI recording of the Fontan IVC. The coronal (A), sagittal (B), and axial (C) axis of the MRI image are used to position the imaging plane axial to the IVC 20 mm above the hepatic veins. The axial view is chosen to segment the IVC (red) and descending aorta (green) for flow quantification.

Data analysis

Respiratory pattern quantification

The recorded MR images served for the quantification of chest wall motion and thus respiratory patterns, as well as for flow quantification which allowed the synchronization of the respiratory cycle and flow measurements on a frame-by-frame basis.

To analyze respiratory motion, we segmented the anterior free chest wall of each participant. For this purpose the recorded MRI data was exported in the DICOM format and a motion tracking software was used to measure the displacement of the chest wall as shown in Figure 21 (Tracker, 2022 Douglas Brown, Wolfgang Christian, Robert M Hanson).

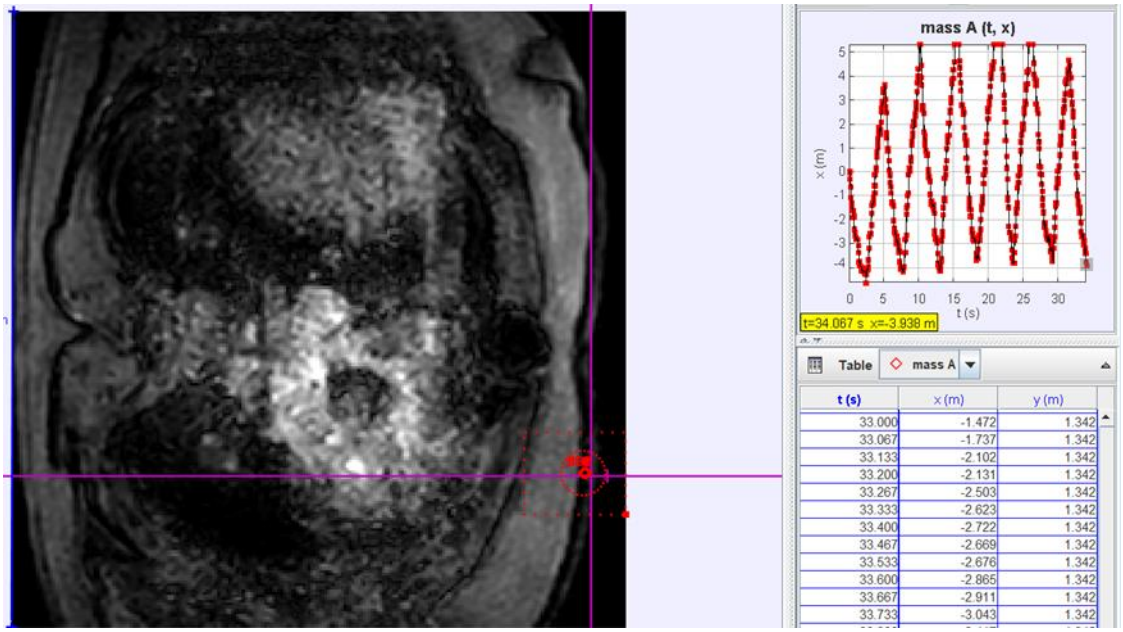

Figure 21 : Segmentation and tracking of the anterior free chest wall to quantify chest wall motion during respiration in the MRI recordings.

Outward motion indicated inspiration while the inward motion of the chest wall indicated expiration. For each patient the displacement data of the chest wall was analyzed (Matlab, MathWorks, USA) and five respiratory cycles of each breathing pattern were averaged. Each peak of the tracked chest wall motion represents the end of inspiration while each trough of the graphs represents the end of expiration. The period of one respiratory cycle is represented by the time between two throughs in the chest wall curve (ends of expiration). The corresponding respiratory rate (RR in 1/min) was calculated with the average period of one respiratory cycle over one minute as shown in Equation 5.

$$RR = \frac{1}{\sum_{i=1}^{n} T_{i+1}^{ex} - T_i^{ex}} * \frac{1}{n}$$

Equation 5

With T^{ex} as the timepoint marked by the end of expiration and $n = 5$ as five respiratory cycles were analyzed for each breathing pattern.

The amplitude between the chest position at the end of expiration (throughs) and the subsequent end of inspiration (peak) was analyzed as the overall chest wall motion and served as a surrogate measurement for the respiratory effort. Chest wall motion analysis from MRI data has been described to track respiratory motion previously [30]. For each participant averages and standard deviates of the chest wall motion amplitude, as well as for the respiratory rate were calculated. The change of respiratory effort during each breathing pattern was calculated as the percentage change of the chest wall amplitude from baseline to shallow and deep breathing resulting in normalized data relative to the baseline chest wall motion. This non-dimensional number could then be compared between all study participants.

IVC Flow quantification

Blood flow quantification was performed in the commercially available software cvi42 (Circle Cardiovascular Imaging Inc., Canada) from velocity maps in the recorded through planes. For this purpose, the area of the IVC and descending aorta were segmented in each frame as shown in Figure 20B. A representative example of the

The quantified flow information was extracted and combined with chest motion data on a frame-by-frame basis in Matlab as described in the previous section. Characteristics of the flow data were interpreted during the five respiratory cycles which were previously segmented. This allowed for a comparison of respiratory patterns and resulting flow. As shown in Figure 17C the following parameters were recorded for each respiratory cycle to then calculate averages and standard deviations over n=5 cycles for each: (i) forward IVC flow rate, (ii) reverse IVC flow rate, (iii) forward IVC flow volume, (iv) reverse IVC flow volume, (v) percent retrograde flow, (vi) pulsatility index. Flow volumes were obtained by integrating the flow rates over the respiratory cycle. Percent retrograde flow was calculated for each respiratory pattern as shown in Equation 6:

$$\%\, retrograde\ flow = \sum_{i=1}^{n} \frac{vol._i^-}{vol._i^+} * \frac{1}{n}$$

Equation 6

With $vol._i^-$ and $vol._i^+$ as the total negative and positive flow measured in the Fontan IVC during one respiratory cycle and n = 5 respiratory cycles.

The pulsatility index was calculated as shown in Equation 7:

$$Pulsatility\ Index = \frac{(maximum\ flow\ rate - minimum\ flow\ rate)}{mean\ flow}$$

Equation 7

Statistical analysis

Statistical analyses were performed to evaluate the significant differences in breathing patterns of each patient and the resulting percentage retrograde flow. Given that the null hypothesis assumed that respiratory chest wall motion, respiratory rate, and percent retrograde flow in the IVC do not change significance of alterations for each patient were determined by a paired, double tailed, t-test with a significance level of 0.05.

Comprehensive flow dynamics:

2.2.5 Computational fluid dynamics model of the Fontan IVC

Bench top and lumped parameter models provide the ability to investigate physiological characteristics of the Fontan physiology. Additional detail is necessary to evaluate flow structures, underlying hemodynamics, and blood interactions. This is particularly important to evaluate potential support strategies. To create a test platform which can bridge systems-level flow dynamics and comprehensive flow studies to allow the exploration on both scales we implemented and validated a computational flow dynamics model of the Fontan IVC.

To validate a CFD model of the Fontan IVC with bench top measurement we chose a double tracked approach. First, we prescribed the pressure boundary conditions observed in the bench top model to the CFD model and compared the resulting flow rates in the IVC. Then we flipped the input parameters, and we prescribed the flow boundary conditions observed in the bench top model to compare the resulting pressure waveforms in the CFD IVC model. Figure 22 shows the location and applied boundary conditions of the CFD Fontan IVC model.

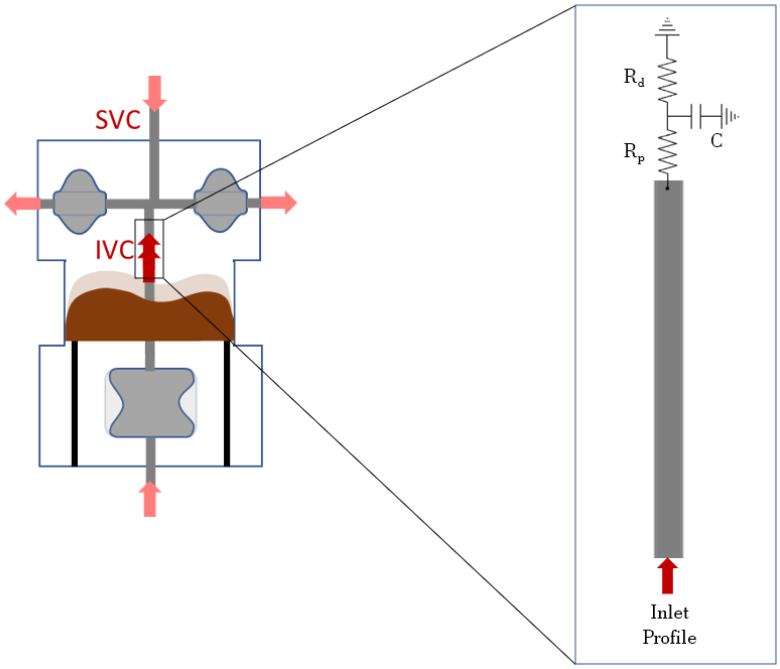

Figure 22 : Schematic of location of CFD model in the Fontan physiology and implemented boundary conditions.

A commercial software (ANSYS Fluent 18.0, ANSYS Inc., Pittsburgh, PA, USA) was used to model the flow pattern inside the IVC. The blood was modeled as an incompressible Newtonian fluid with 1050 kg/m3 density and 0.0035 Pas dynamic viscosity. Experimentally measured pressure profiles were prescribed at the inlet and a three-element Windkessel model consisting of a proximal resistance (R_p), compliance (C), and distal resistance (R_d) was used at the outlet boundary. Pressure at the model outlet is updated at every solver loop according to the 3-element Windkessel model using the flow rate information from the current time step. During the grid generation process, orthogonal quality, aspect ratio, and the skewness were assured to be in the required range. Turbulence was simulated with the k-ω model by considering the mean $\gamma+ < 1$ value with appropriately sized cells near domain walls. The final meshes contained approximately 650,000 cells. The convergence precision was set to 10^{-4} for the scaled residuals, using a uniform time step of 1 ms which allowed time-step size-independent results. The inlet and outlet ports were extended to prevent boundary condition effects on the convergence. Analysis was completed in 6 hours on a desktop PC with a 3.0 GHZ i7-9700 processor with 8 cores and 32 GB RAM.

2.3 Results

Organ-level flow dynamics:

2.3.1 Bench top biomimetic respiratory simulator

Mimicking respiratory biomechanics recapitulates breathing pressures

I realized the described simulator as an *in vitro* benchtop setup equipped with pressure and flow sensors and tunable mechanical properties as shown in Figure 23B

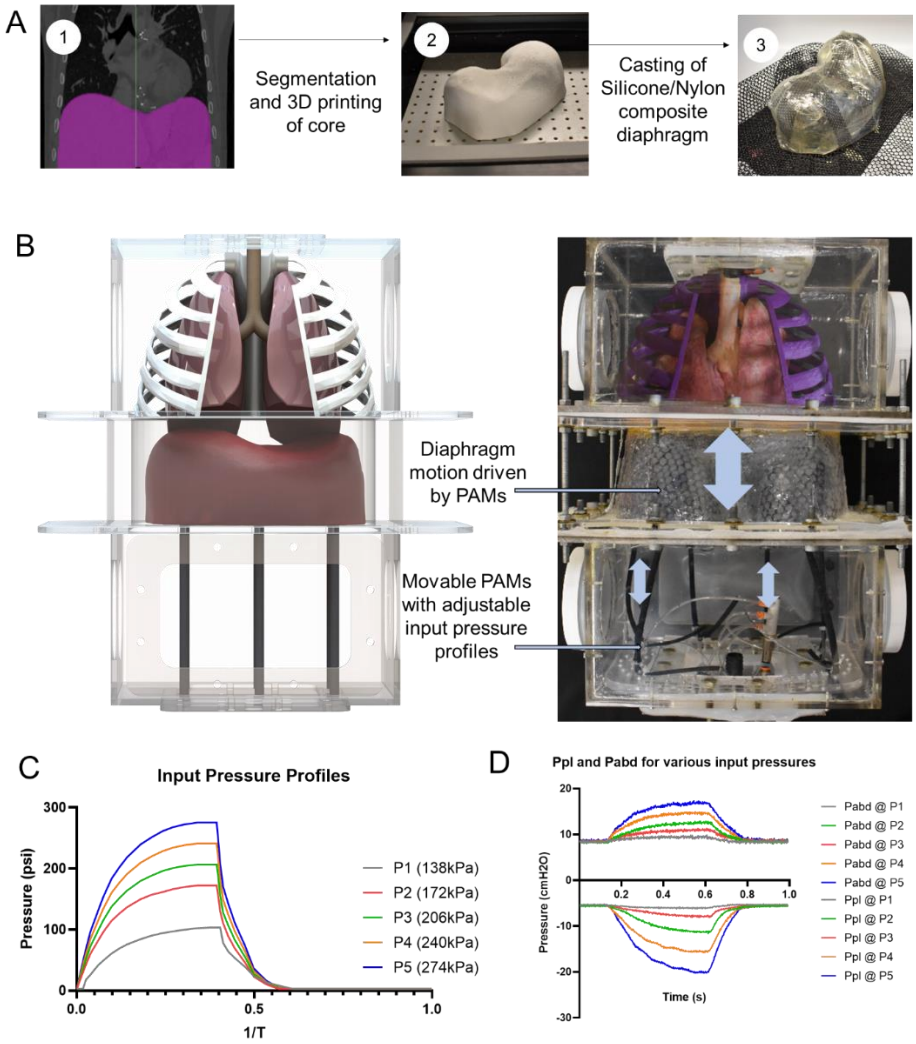

Figure 23: (a) Physical diaphragm insert from 3D data derived from clinical imaging using Mimics software. (b) Rendering and physical realization of the biohybrid respiratory simulator. (c) Pneumatic artificial muscles with different input pressures generate different degrees of diaphragm displacement. (D) Measured outputs of abdominal and pleural pressure in response to varying actuator pressures

I constructed the chassis of the simulator out of optically clear plastics that act as the torso. The chassis encloses the thoracic and abdominal cavities, separated by a diaphragm. This simulator is designed to be modular, and therefore, I included rapid-access ports on the sides of the acrylic boxes. The top and bottom sides of the chassis include modular tubing ports to allow for pressure controls, access to instrumentation and connection ports for the later inclusion of flow loop

components. The simulator assumes a rigid rib cage. The rib cage is broken into two zones: the upper 3D-printed ribs, which act as a boundary between the lungs from the outer thoracic cavity space, and the lower plastic shell, which aims to mimic the zone of apposition (a vertical area of the diaphragm that begins at the insertion point on the inside of the lower ribs and extends to the top of the domes). Because the abdominal cavity is a much more compliant enclosure compared to the rib cage, the abdominal cavity contains a modular compliance window—a critical feature that allows us to tune the relationship between the thoracic and abdominal cavity pressure waveforms. To generate respiration, we drive the motion of the diaphragm. The native diaphragm is a flexible but active muscle that generates up to 70% of the inspiratory tidal respiration via volume changes of the thoracic cavity. As a membrane, it couples the pressures of the thoracic and abdominal cavities together. In this simulator, we represent diaphragm motion via a flexible, passive silicone membrane that is moved via active pulling soft robotic elements located in the abdominal cavity. The diaphragm displacement is driven by pneumatic artificial muscles (PAMs) pulling on the silicone diaphragm. The PAMs are actuated via a custom electro-pneumatic control box that allows us to program specific actuation schemes and is shown in Figure 24.

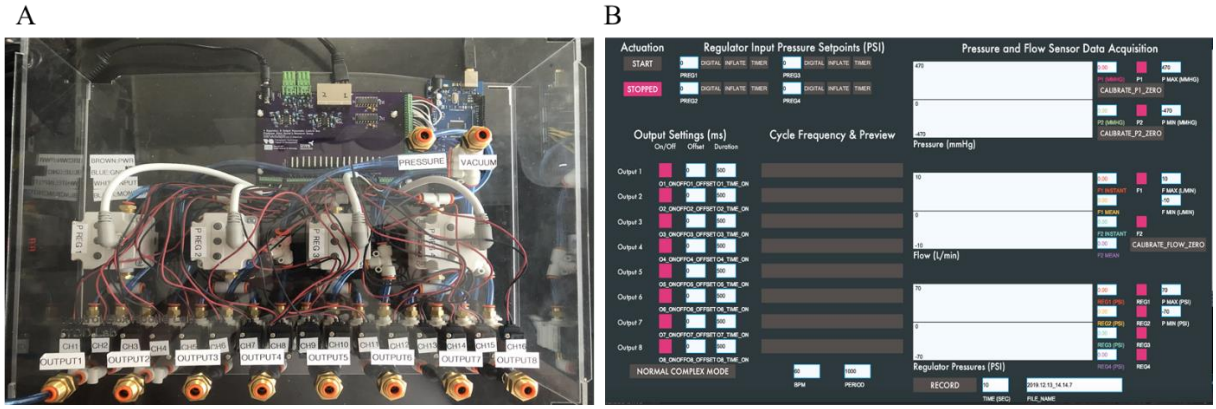

Figure 24: Electropneumatic control box (A) to actuate the respiratory motion of the biomimetic diaphragm in the cardiorespiratory simulator with the custom graphic user interface (B) so control actuation timing, actuation period, negative pressure actuation, and positive pressure amplitudes delivered to the artificial muscles of the modeled diaphragm.

The pneumatic control unit includes 8 outputs with 4 pressure regulators that determine pressure inputs for 2 outputs each. The outputs can be exposed to the pressure from the regulator via one solenoid valve or exposed to a vacuum source via another solenoid valve such that inflation and deflation can be implemented through each output. A custom interface shown in Figure 24 allows for precise configuration of the actuation patterns. This included timing of pressure or vacuum actuation for each individual output as well as relative time offsets between each line.

The pressure which is delivered through each output can be set to a desirable pressure level or pressure profile. The latter allows for the delivery of a pressure curves over a specified time frame such as the curve of respiratory efforts (Figure 23C). By varying the actuation schemes and, thus, the actuator contraction, the system can mimic shallow and deep breaths. It can achieve a range of physiological breathing pressures, generating pleural pressure between –20 and –6 cm H2O, seen in Figure 23D. To characterize the pleural and abdominal pressure ranges of the simulator, no rib cages or lungs were included as they would also not be included in combination with the flow model. As shown in Figure 23D, the contraction of the diaphragm drives the pleural pressure to be more negative and the abdominal pressure to be more positive. This difference is referred to as the transdiaphragmatic pressure and is a metric for diaphragm effort and function.

Recreating negative pressure breathing on the bench top

To show functionality and tunable compliance of the respiratory elements organic lungs were added to the breathing simulator together with instrumentation which allowed for monitoring of respiratory flows and volumes.

Varying the degree of diaphragm effort as described above generates a range of physiological flows, tidal volumes, and pleural pressure as shown in Figure 25.

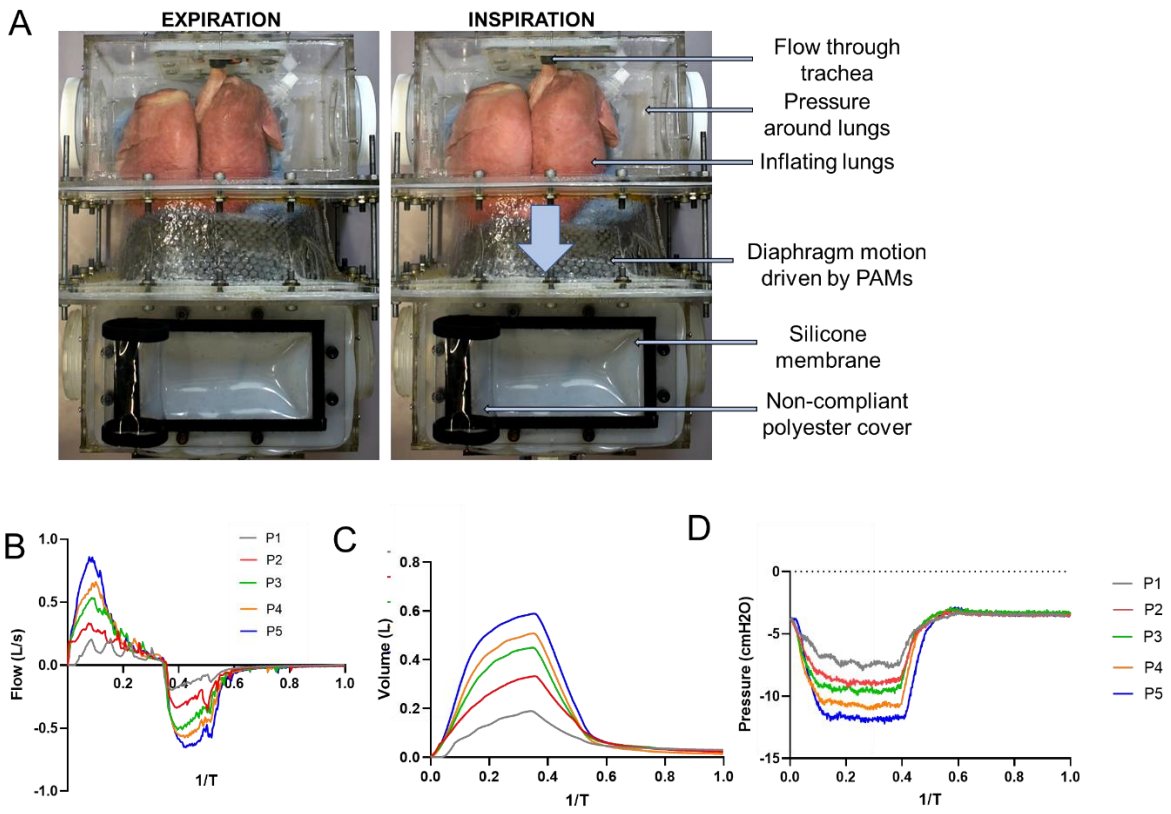

Figure 25: Inclusion of organic lungs to visualize physiological negative pressure respiration. (a) When the artificial muscles are not contracted, the diaphragm is in its resting state. With downward displacement of the diaphragm, inspiration and lung expansion are observed. Spirometry readings replicate physiologic waveforms for flow (b), volume (c), and pleural pressure (d).

We observe how the simulation of different degrees of respiratory effort resulted in corresponding increasing respiratory flows and tidal volumes Figure 25B-D.

Variable compliance impacts respiratory mechanisms

The pressures of the respiratory system interact through various organ and tissue systems, each with unique mechanical properties. The ability to vary compliance of different components in this respiratory simulator allows to tune the performance of the simulator to match both physiologically normal conditions and to examine the mechanical effect that pathologic changes to these compliances have on respiration. Specifically, the model enables one to individually vary the effective compliance of the lungs, pleural space, and abdominal cavity and subsequently measure the effects of respiratory volumes and pressures, seen in the figure below. Changes in compliance of these respiratory elements are relevant to the simulation of Fontan flow as body position, activation of abdominal muscles or food intake may vary the compliance response of the respiratory apparatus.

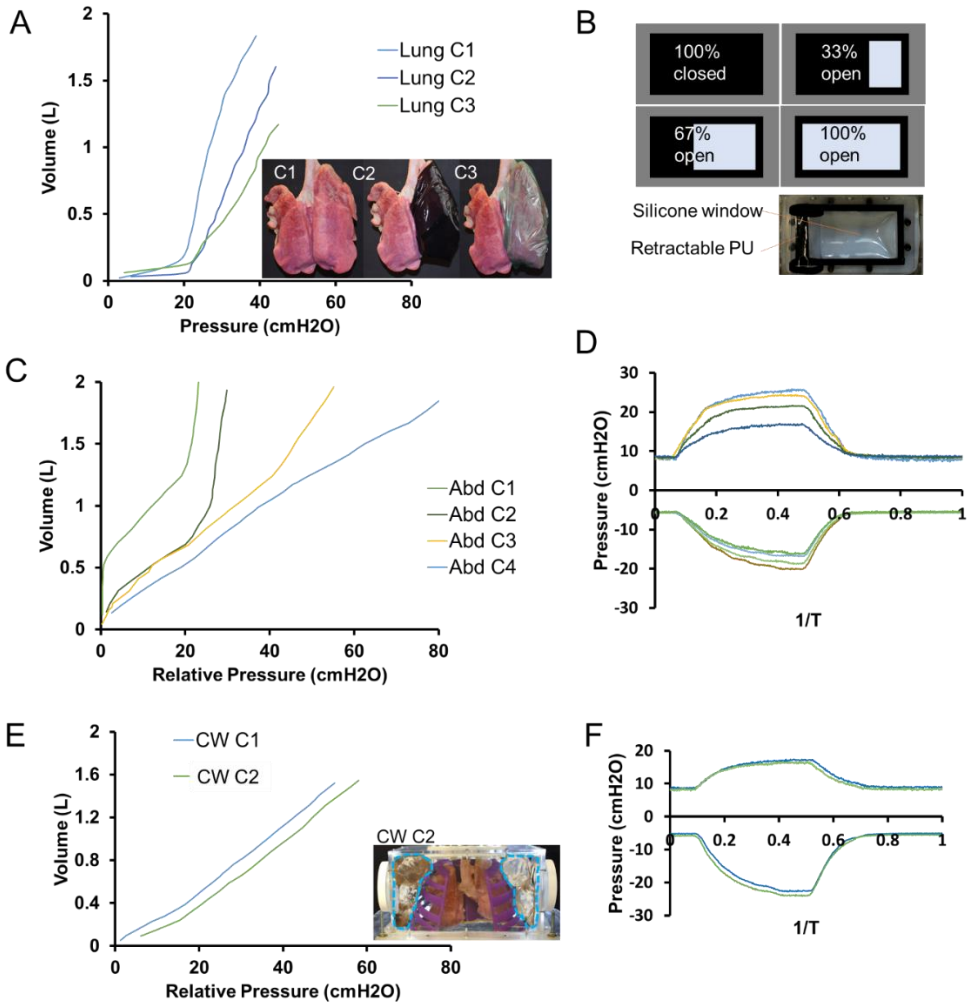

Figure 26: Modifying the compliance of different elements of the respiratory apparatus. (a) Varying lung compliance. (b) Schematic of tunable compliance of the abdominal cavity via the silicone window. (c) Varying abdominal cavity compliance. (d) Effect of variable abdominal cavity compliance on abdominal and pleural pressures during 1 cycle of respiration. (e) Varying pleural cavity compliance. (f) Effect of variable pleural cavity compliance on abdominal and pleural pressures during 1 cycle of respiration.

We use organic porcine lungs to represent the compliance of "normal lung tissue." This compliance can be decreased by wrapping the lungs in externally restrictive materials: C2 is created with a semi-distensible film around the lungs and C3 is created with a non-distensible film around the lungs (Figure 26A). The decreased compliance mimics a net stiffening of the lungs. The compliance of the abdominal cavity ultimately affects the relationship between the pleural and abdominal pressures, and thus, a silicone window with a variable non-distensible covering allows the creation of various compliances (Figure 26B-D). The variable compliance window of the abdominal cavity consists of a highly compliant silicone sheet that can be partially blocked by a stiff, polyurethane window covering to decrease the compliance: C1 is created

with the window completely open, C2 is created with the window 33% open, C3 is created with the window 67% open, and C4 is created with the window completely closed. This can be finely tuned to mimic the effect of higher abdominal muscle tone or reduction of the available volume after e.g. eating. Although we assume a rigid ribcage, we represent changes in pleural cavity compliance by modulating the volume of gas between the lungs and chest walls. Because there are no defined pleural cavities and the pressure is equal throughout the space, we modulate the space available in the pleural chamber. By filling the space with an incompressible fluid, we replace the compressible air from the pleural space: C1 is created as the air fills the volume around the lungs and C2 is created with partially filled sacs surrounding the lungs (Figure 26E,F). This decreases the overall compliance of the volume surrounding the lungs. The ability to independently control the compliance of different elements enables selective adjustment of compartment pressures in the thorax and abdomen and isolation of different mechanical phenomena.

2.3.1 Clinical validation of bench top and computational models

We conducted a prospective clinical trial of five Fontan patients with TCPC to validate the results obtained with the biomimetic cardiorespiratory bench top simulator and the organ level computation model. The objective of this pilot study was to evaluate whether the impact of varying respiratory effort and rate, as well as baseline IVC flow which were observed *in vitro* and *in silico* match clinical findings.

We successfully implemented the study workflow described in section 2.2.4 at Boston Children's Hospital (300 Longwood Avenue, Boston, Massachusetts 02115, USA). The audiovisual guide was understood well by the patients and playback during MRI recordings were frictionless. No adverse event was reported from any participants. Data recording and storage was conducted according to the IRB described in section 2.2.4.

Chest wall motion was successfully tracked and segmented from the MRI recordings as described in section 2.2.4. Figure 27 shows examples of the recorded chest wall motion for each of the analyzed breathing patterns. Study participants were able to follow the guided breathing rhythm during baseline breathing, shallow breathing, and deep breathing as shown in Figure 27A. The amplitude of the chest wall motion varied within each breathing effort, but all 5/5 participants were able to increase their chest wall motion during the study to produce statistically significant increase in respiratory efforts. Statistical analysis showed no significant fluctuations in respiratory rate for all 5/5 participants across the three distinct breathing efforts.

Figure 27B shows an example of five respiratory cycles during baseline respiratory rate (14), slow respiratory rate (9), and fast respiratory rate (28). All 5/5 participants were able to follow the audio-visual guide during the MRI study resulting in statistically significant differences for each breathing rate. Statistical analysis showed that all 5/5 participants did not increase their respiratory efforts significantly during the increase of the breathing frequency.

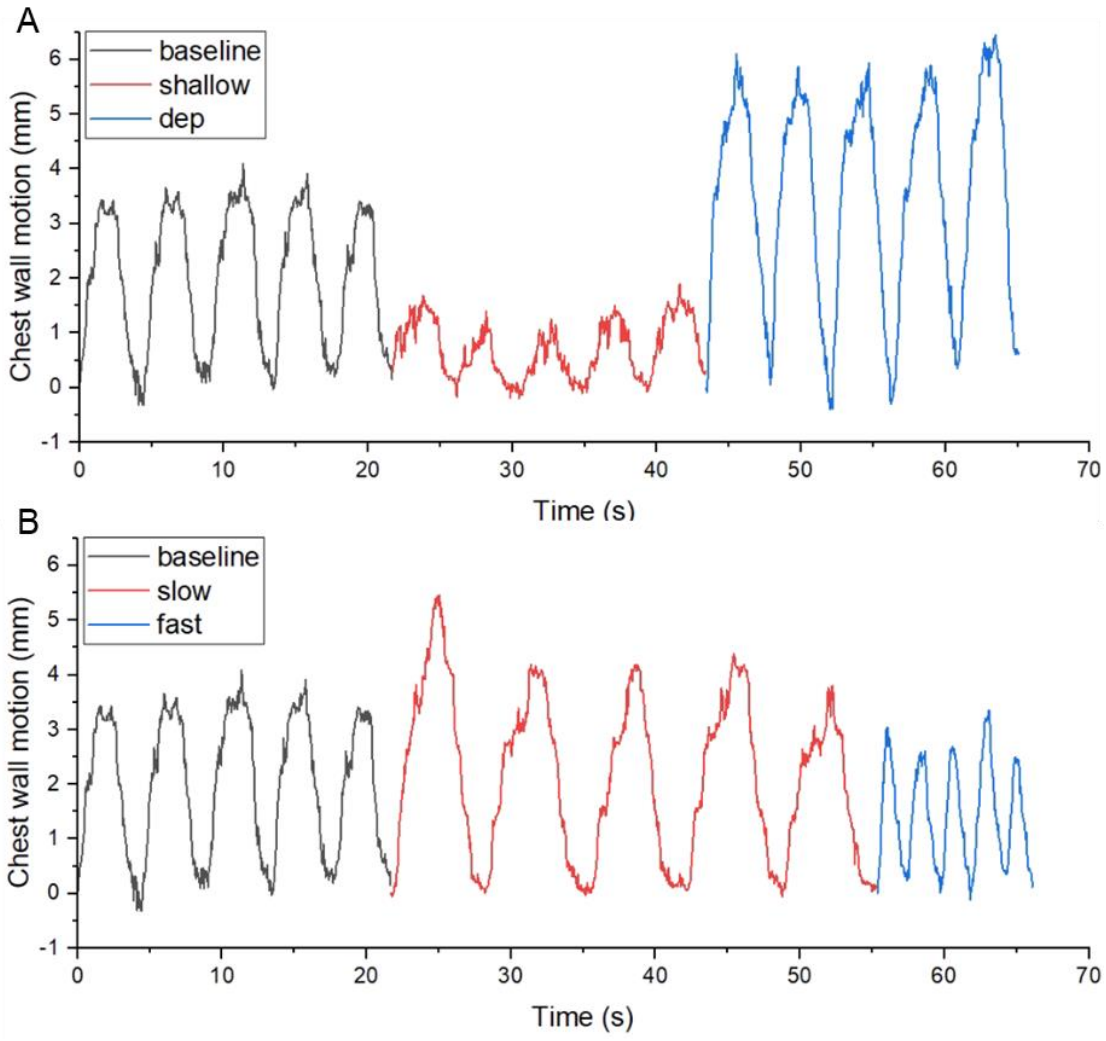

Figure 27 : Representative data of segmented chest wall motion during clinical validation trial. (A) Five respiratory cycles of baseline, shallow, and deep breathing were analyzed for each patient. (B) Five respiratory cycles of baseline (RR=14), slow (RR=9), and fast breathing (RR=28) were analyzed for each patient.

IVC flow was successfully tracked and segmented from the MRI recordings as described in section 2.2.4. Figure 28 shows examples of the recorded IVC flow pattern during different breathing efforts and breathing rates. During the increase of respiratory effort, the retrograde flow in the IVC increased for all 5/5 participants. Statistical analysis showed that during the increase of respiratory rate the per retrograde flow in the IVC also increased significantly.

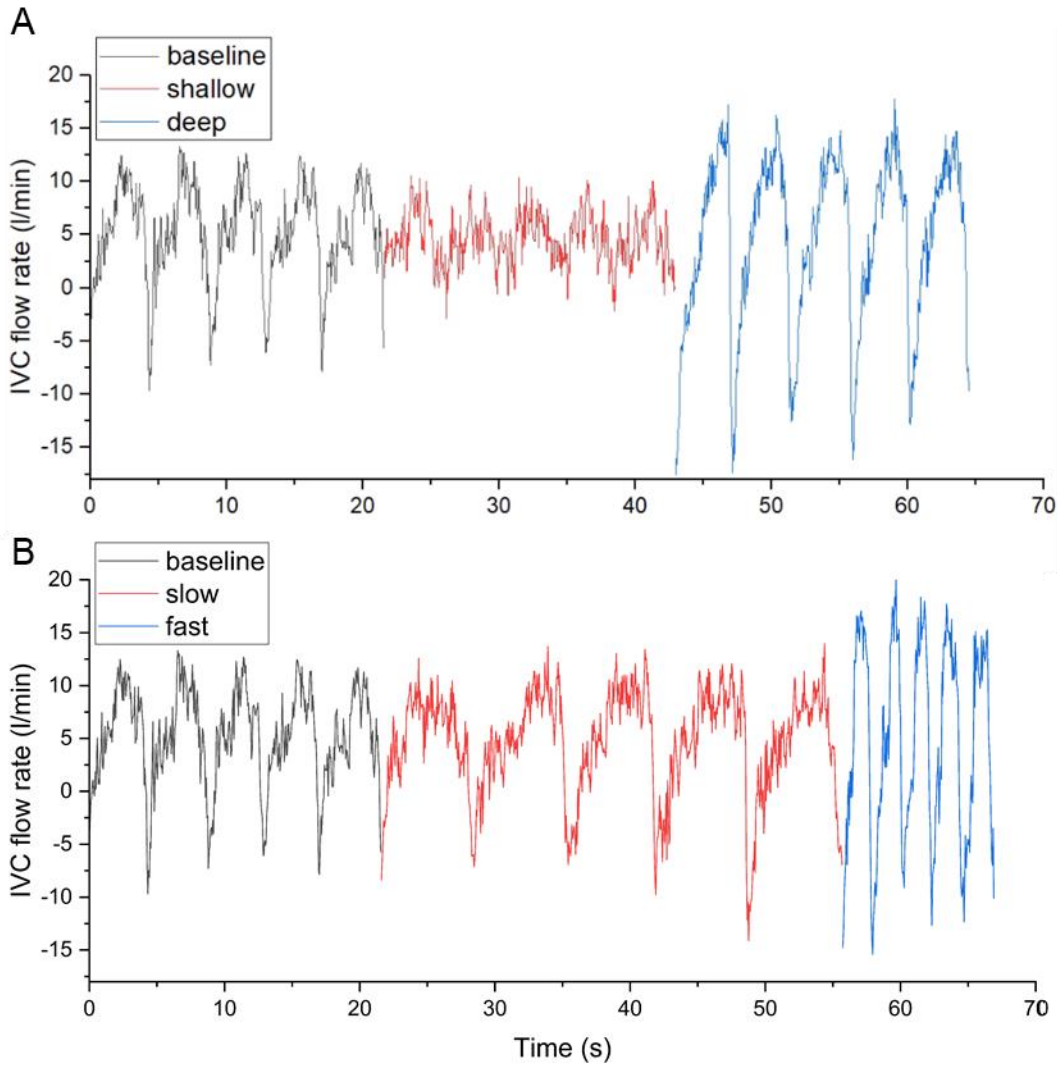

Figure 28 : Examples of clinically recorded IVC flow during different breathing patterns: Baseline breathing effort, shallow breathing, and deep breathing (A), and baseline breathing rate, slow, and fast (B).

Figure 29, Figure 30, and Figure 31 compare the hemodynamic responses of the respiratory study on the bench top as described in section 2.3.1, computationally as described in section 2.3.3 and clinically as described in section 2.2.4.

Respiratory effort

Figure 29 specifically evaluates if the flow response in the IVC due to increased respiratory efforts match *in silico*, *in vitro*, and *in vivo*. Figure 29A compared the impact of respiratory effort on the peak forward and reverse flow rate in the IVC per respiratory cycle, Figure 29B compares the impact of respiratory effort on the total forward and retrograde flow volume in the IVC per respiratory cycle, Figure 29C compares the impact of respiratory effort on the

resulting pulsatility index in the IVC, and Figure 29D compares the impact of respiratory effort on the resulting percent retrograde flow in the IVC per respiratory cycle.

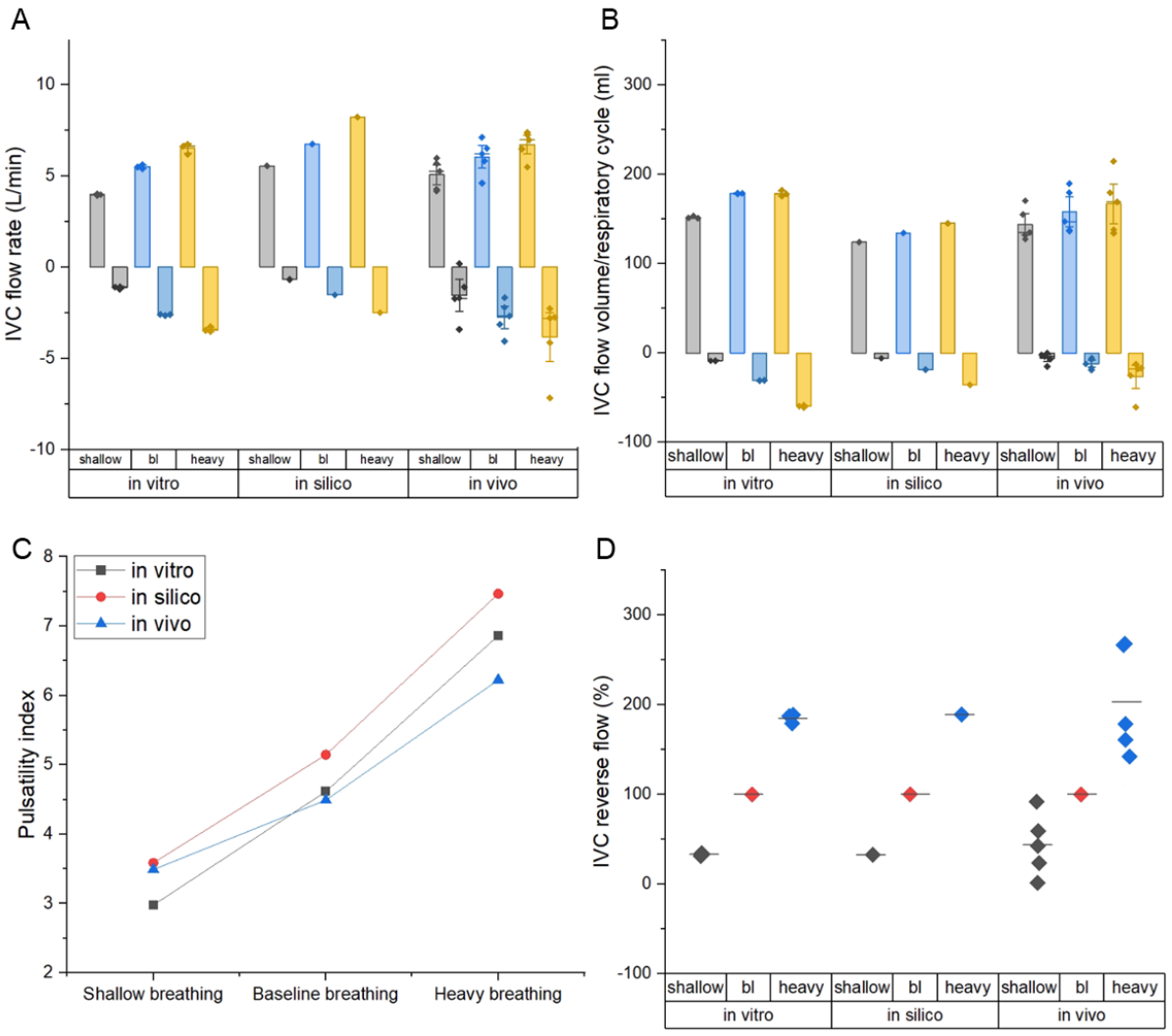

Figure 29 : Clinical, bench top, and computational results of the impact of respiratory effort on Fontan IVC hemodynamics: Resulting respiratory flow rates in the Fontan IVC (A), resulting IVC flow volumes (B), resulting pulsatility index (C), resulting percent IVC retrograde flow. Data show mean +- standard deviation. Bl=baseline

In all 5/5 clinically evaluated patients retrograde flow in the IVC decreased with shallow breathing and increased with deeper breathing. In 4/5 patients this increase in retrograde IVC flow with increased respiratory efforts was statistically significant with one patient having greater variations between values across the 5 respiratory cycles.

During increasing respiratory efforts *in vitro*, *in silico*, and *in vivo* results show an increase in IVC retrograde flow. Compared to baseline, reverse flow decreases during shallow breathing to 33.1% (±1.6%), 32.8%, and 43.6% (±34%) *in vitro*, *in silico*, and *in vivo*, respectively.

Compared to baseline, reverse flow increases during deep breathing to 184.9% (±5.1%), 189.0%, and 202.9% (±59.8%) *in vitro, in silico,* and *in vivo,* respectively.

With increased breathing efforts the pulsatility index also increased on the bench top, computationally, as well as clinically. For shallow – baseline - heavy breathing efforts the pulsatility index of the IVC flow increased 3.0 –4.6 – 6.9, 3.6 – 5.1 – 7.5, and 3.5 – 4.5 – 6.2 *in vitro, in silico,* and *in vivo,* respectively.

With increased respiratory efforts the maximal forward and reverse flow rates are augmented in all models; on the bench top, computationally, and clinically. *In vitro,* shallow, baseline, and heavy breathing efforts result in maximal positive/negative flow rates during one respiratory cycle of 4.0/-1.1 l/min (±0.04/0.1), 5.5/-2.6 l/min (±0.1/0.03), and 6.5/-3.4 l/min (±0.3/0.1). *In silico,* shallow, baseline, and heavy breathing efforts resulted in maximal positive/negative flow rates during one respiratory cycle of 5.5/-0.7 l/min, 6.7/-1.5 l/min, and 8.2/-2.5 l/min. *In vivo,* shallow, baseline, and heavy breathing efforts resulted in maximal positive/negative flow rates during one respiratory cycle of 5.1/-1.5 l/min (±0.8/1.3), 6.0/-2.7 l/min (±0.9/0.9), and 6.7/-3.8 l/min (±0.8/1.9).

An increase of respiratory efforts resulted in an augmentation of the total forward and retrograde blood volumes that flows in the Fontan IVC during one respiratory cycle. This results match on the bench top, computation, and in the clinical investigation. In vitro, shallow, baseline, and heavy breathing efforts resulted in positive/negative flow volumes during one respiratory cycle of 151.7/-8.8 ml (±1.4/0.4), 178.3/-30.9 l/min (±0.6/0.2), and 178.4/-59.8 ml (±3.5/1.2). In silico, shallow, baseline, and heavy breathing efforts resulted in positive/negative flow volumes during one respiratory cycle of 123.9/-6.0 ml, 134.2/-18.6 l/min, and 145.0/-35.8 ml. In vivo, shallow, baseline, and heavy breathing efforts resulted in positive/negative flow volumes during one respiratory cycle of 143.8/-5.7 ml (±18.2/5.8), 157.8/-12.2 ml (±24.9/5.7), and 166.9/-26.7 ml (±32.9/19.5).Respiratory rate

Figure 30 specifically evaluates if the flow response in the IVC due to increased respiratory rates match in silico, in vitro, and in vivo. Figure 30A compares the impact of respiratory effort on the peak forward and reverse flow rate in the IVC per respiratory cycle, Figure 30B compares the impact of respiratory effort on the total forward and retrograde flow volume in the IVC per respiratory cycle, Figure 30C compares the impact of respiratory effort on the resulting pulsatility index in the IVC, and Figure 30D compares the impact of respiratory effort on the resulting percent retrograde flow in the IVC per respiratory cycle.

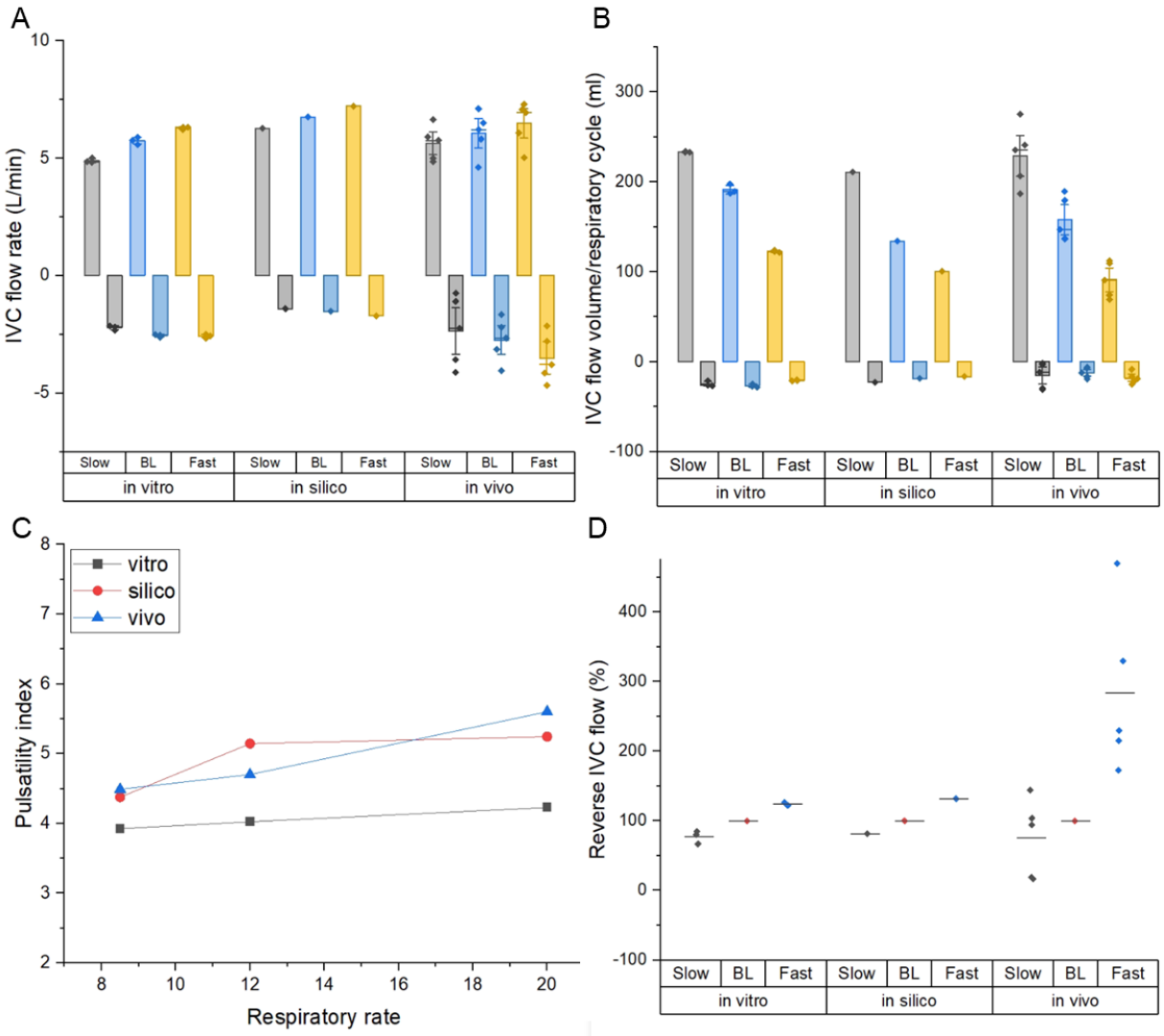

Figure 30 : Clinical, bench top, and computational results of the impact of respiratory rates on Fontan IVC hemodynamics: Resulting respiratory flow rates in the Fontan IVC (A), resulting IVC flow volumes (B), resulting pulsatility index (C), resulting percent IVC retrograde flow.

In the clinical validation trial, an increase in respiratory rate also increased retrograde IVC flow significantly for all 5/5 clinically evaluated patients as evaluated by statistical analysis.

During increasing respiratory rates *in vitro*, *in silico*, and *in vivo* results show an increase in IVC retrograde flow. Compared to baseline, reverse flow decreased during shallow breathing to 77.4% (±9.4%), 81.5%, and 75.7% (±56%) *in vitro*, *in silico*, and *in vivo*, respectively. Compared to baseline, reverse flow increased during deep breathing to 123.7% (±2.4%), 131.1%, and 283.3% (±118.8%) *in vitro*, *in silico*, and *in vivo*, respectively.

With increased breathing rates the pulsatility index also increased on the bench top, computationally, as well as clinically. For slow – baseline - fast breathing rates the pulsatility index of

the IVC flow increased 3.9 – 4.0 – 4.2, 4.3 – 5.1 – 5.2, and 4.5 – 4.7 – 5.6 *in vitro, in silico,* and *in vivo,* respectively.

With increased rates the maximal forward and reverse flow rates are augmented in all models, on the bench top, computationally, and clinically. *In vitro*, slow, baseline, and fast breathing rates resulted in maximal positive/negative flow rates during one respiratory cycle of 4.9/-2.2 l/min (±0.1/0.1), 5.7/-2.6 l/min (±0.2/0.1), and 6.3/-2.6 l/min (±0.1/0.1). *In silico*, slow, baseline, and fast breathing rates resulted in maximal positive/negative flow rates during one respiratory cycle of 6.3/-1.4 l/min, 6.8/-1.5 l/min, and 7.2/-1.7 l/min. *In vivo*, slow, baseline, and fast breathing rates resulted in maximal positive/negative flow rates during one respiratory cycle of 5.6/-2.4 l/min (±0.7/1.5), 6.0/-2.7 l/min (±0.9/0.9), and 6.4/-3.5 l/min (±0.9/1.0).

An increase of respiratory rates led to a reduction of the total forward IVC flow volumes and a slight increase of retrograde flow volumes in the Fontan IVC during one respiratory cycle. These results match on the bench top, computation, and in the clinical investigation. *In vitro*, slow, baseline, and fast breathing rates resulted in positive/negative flow volumes during one respiratory cycle of 233.3/-24.5 ml (±0.7/3.1), 1991.3/-26.6 l/min (±5.5/1.8), and 122.8/-20.7 ml (±1.3/0.7). *In silico*, slow, baseline, and fast breathing rates resulted in positive/negative flow volumes during one respiratory cycle of 210.8/-22.7 ml, 134.2/-18.6 l/min, and 100.5/-16.3 ml. *In vivo*, slow, baseline, and fast breathing rates resulted in positive/negative flow volumes during one respiratory cycle of 228.9/-15.2 ml (±33.9/14.2), 157.8/-12.2 ml (±24.9/5.7), and 91.1/-17.8 ml (±19.6/6.2).

Baseline IVC flow

Figure 31 specifically evaluates if the flow response in the IVC due to increased baseline venous IVC flow match *in silico, in vitro*, and *in vivo*. Figure 31A compares the impact of respiratory effort on the peak forward and reverse flow rate in the IVC per respiratory cycle *in silico* and *in vitro,* Figure 31B compares the impact of respiratory effort on the total forward and retrograde flow volume in the IVC per respiratory cycle *in silico* and *in vitro,* Figure 31C compares the impact of respiratory effort on the resulting pulsatility index in the IVC *in silico* and *in vitro,* and Figure 31D compares the impact of respiratory effort on the resulting percent retrograde flow in the IVC per respiratory cycle *in silico* and *in vitro*. During the clinical validation study we could not control for the baseline IVC flow of each participant, so the effects of baseline IVC flow *in vivo* are separated out in Figure 31E and Figure 31F. Figure 31E shows an inverse correlation between the pulsatility index with baseline IVC flow *in vivo* (R^2=80.5%), and Figure

31F shows an inverse correlation between baseline IVC flow and percent retrograde flow (R^2=73.4%).

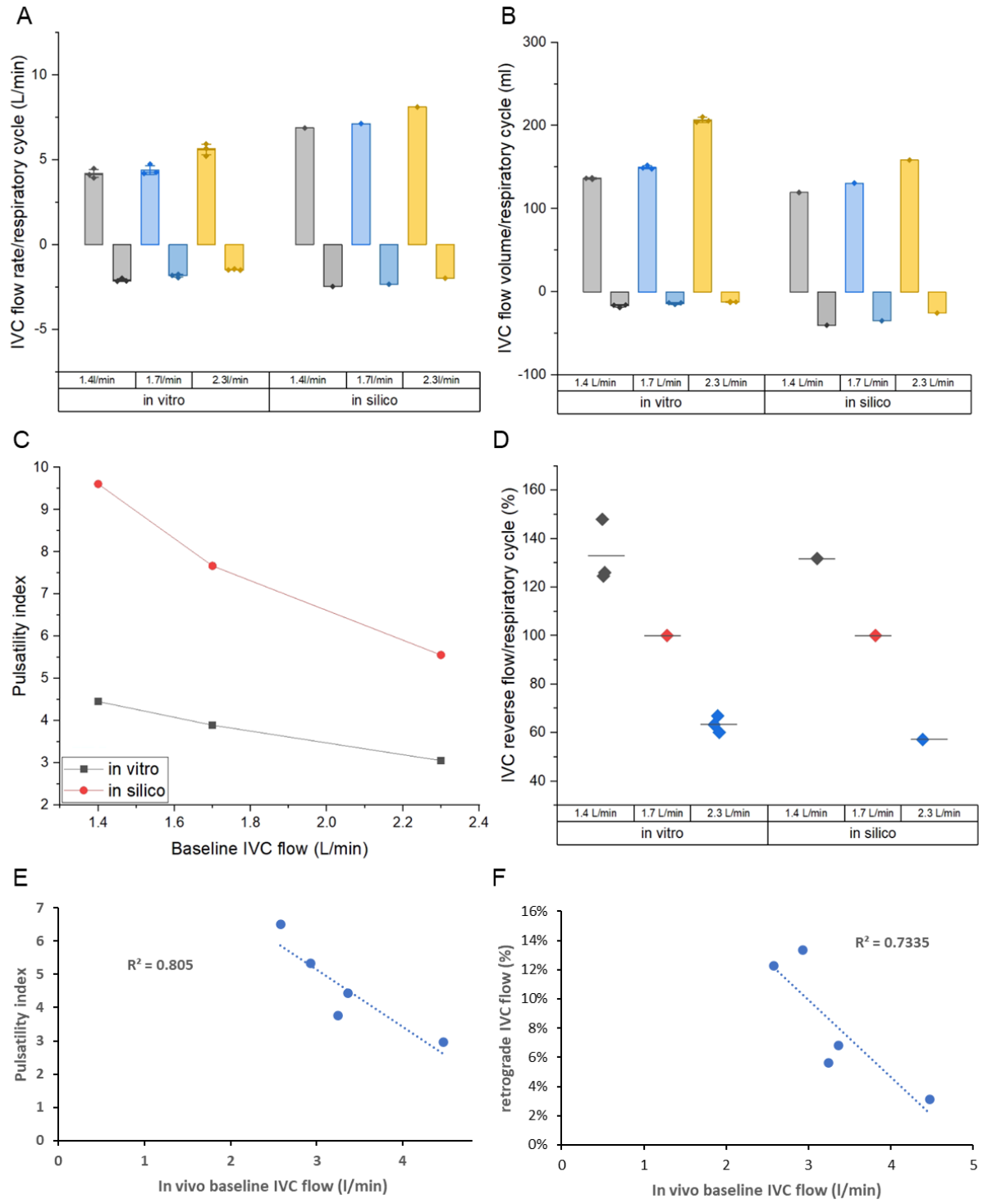

Figure 31 : Clinical, bench top, and computational results of the impact of baseline IVC flow on Fontan IVC hemodynamics: Bench top and computational results for respiratory flow rates in the Fontan IVC (A), bench top and computational results for results for IVC flow volumes (B), bench top and computational results for resulting pulsatility index (C), bench top and computational results for percent IVC

retrograde flow, clinical results for the resulting pulsatility index (E), clinical results for the resulting percent retrograde IVC flow (F).

With increasing Fontan IVC baseline flow *in vitro, in silico,* and *in vivo* results show a reduction of IVC retrograde flow during breathing. Compared to baseline IVC flow of 1.7 l/min a decrease of IVC baseline flow to 1.4 l/min increased the percent retrograde flow to 132.9% (±13.2%) and 131.8% *in vitro,* and *in silico,* respectively. Compared to baseline IVC flow of 1.7 l/min an increase of IVC baseline flow to 2.3 l/min reduced the percent retrograde flow to 63.4% (±3.4%) and 57.2% *in vitro,* and *in silico,* respectively. In the clinical study we could not control for the baseline IVC flow, so we chose the scatterplot to indicate a trend *in vivo*. In patient data the trend matches the results on the bench top and computationally indicating how an increased baseline IVC flow diminishes retrograde Fontan IVC flow (R^2=73.3%).

With increased baseline IVC flow the pulsatility index also decreases on the bench top, computationally, as well as clinically. For baseline IVC from 1.4 l/min, 1.7 l/min, and 2.3 l/min the pulsatility index drops 4.5 to 3.9, to 3.1 and 9.6 to 7.7, to 5.6 *in vitro* and *in silico,* respectively. In the clinical study we could not control for the baseline IVC flow, so we chose the scatterplot to indicate a trend *in vivo*. In patient data the trend for the pulsatility index matches the results on the bench top and computationally indicating how an increased baseline IVC flow diminishes retrograde Fontan IVC flow (R^2=80.5%).

With increased baseline IVC flow the maximal forward flow rate is increased while the maximal reverse flow rate is reduced in the bench top and computational model. *In vitro,* increasing the baseline IVC flow from 1.4 l/min to 1.7 l/min, and 2.3 l/min resulted in an increase of maximal forward flow rate during inspiration of 4.2 l/min (±0.3), to 4.4 l/min (±0.3), and 5.6 l/min (±0.4). Concurrently, the reverse IVC flow decreased during expiration from -2.1 l/min (±0.1) to -1.8 l/min (±0.1), and -1.5 l/min (±0.03). *In silico,* increasing the baseline IVC flow from 1.4 l/min to 1.7 l/min, and 2.3 l/min resulted in an increase of maximal forward flow rate during inspiration of 6.8 l/min to 7.1 l/min, and 8.1 l/min. Concurrently, the reverse IVC flow decreased during expiration from -2.5 l/min to -2.3 l/min, and -2 l/min.

With increased baseline IVC flow the forward flow volume during inspiration increased while the reverse flow volume during expiration is reduced in the bench top and computational model. *In vitro,* increasing the baseline IVC flow from 1.4 l/min to 1.7 l/min, and 2.3 l/min resulted in an increase of forward flow volume during inspiration of 136.36 l/min (±1), to 149.7 l/min (±1.7), and 5.6 l/min (±0.4). Concurrently, the reverse IVC flow decreased during expiration

from -2.1 l/min (±0.1) to -1.8 l/min (±0.1), and -1.5 l/min (±0.03). *In silico*, increasing the baseline IVC flow from 1.4 l/min to 1.7 l/min, and 2.3 l/min resulted in an increase of maximal forward flow rate during inspiration of 6.8 l/min to 7.1 l/min, and 8.1 l/min. Concurrently, the reverse IVC flow decreased during expiration from -2.5 l/min to -2.3 l/min, and -2 l/min.

With increased baseline IVC flow the forward flow volume during inspiration increased while the reverse flow volume during expiration is reduced in the bench top and computational model. *In vitro*, increasing the baseline IVC flow from 1.4 l/min to 1.7 l/min, and 2.3 l/min resulted in an increase of forward flow volume during inspiration of 136.36 ml (±1), to 149.7 ml (±1.7), and 5.6 ml (±0.4). Concurrently, the reverse IVC flow volume decreased during expiration from -16.7 ml (±1.7) to -13.8 ml (±1.2), and -12.1 ml (±0.5). *In silico*, increasing the baseline IVC flow from 1.4 l/min to 1.7 l/min, and 2.3 l/min resulted in an increase of forward flow volume during inspiration of 119.6 ml to 130.8 ml, and 158.4 ml. Concurrently, the reverse IVC flow volume decreased during expiration from -40.1 ml to -34.5 ml, and -25.4 ml.

Comprehensive flow dynamics:

Numerical simulations like computational fluid dynamics (CFD) and bench top applications like pulse image velocimetry (PIV) allow to (i) investigate velocity and shear stress information which inform hemodynamic performance, (ii) visualize potential risk for thrombogenicity, and (iii) blood damage that may occur as effects of circulatory support.

2.3.2 Bench top biomimetic Fontan flow model overlaid with respiratory simulator

Configuration of flow loop components

Compliance vessels simulate vascular beds

We investigated the compliance of non-constrained, 50% constrained and fully constrained compliance vessels i.e. totally compliant, semi-stiff, and stiff. Figure 32 shows the pressure volume curves of each configuration. The total effective compliance is the inverse of the slope of each curve. In the most compliant configuration, the fluid pressure increased from 17 mmHg to 28mmHg after the addition of 550 ml of fluid which corresponds to an effective compliance of 50 ml/mmHg. For 50% compliance, the blood pressure increased to 33 mmHg with 200 ml of added fluid corresponding to 12.5 ml/mmHg compliance. In the unconstrained configuration

pressure increased to 40 mmHg with 110 ml of additional fluid resulting in 4.8 ml/mmHg compliance.

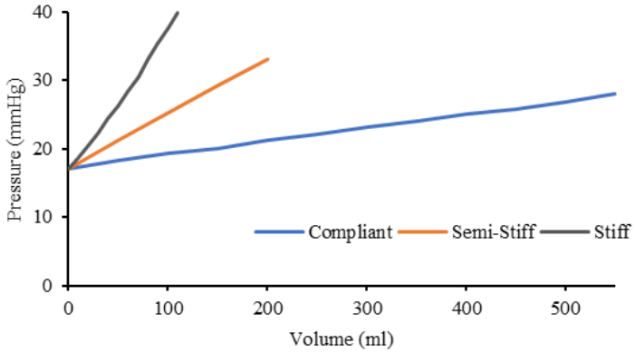

Figure 32: Characterization of the compliance vessels. Three vessel types were configured with 0%, 50%, and 100% constraints, representing compliant, semi-stiff, and stiff vessels.

Surrogate fluid mimics blood rheology

In Table 2, the results of the dynamic viscosity testing and fluid densities for the surrogate blood at room temperature are summarized.

monoethylene - glycol %vol.	**50 %**	**37.5 %**	**30 %**	**25 %**	**21.4%**	**18.75 %**
Dynamic Viscosity (mPa* s)	24.041	10.317	5.593	3.243	3.240	2.456
Density (kg/m3)	1112.5	1070.3	1045.8	1034.7	1031.1	1028.1

Table 2

To mimic hemodynamic characteristics of human blood at body temperature (viscosity ~3.5mPa*s, density ~1055kg/m^3) we chose 25 % monoethylene-glycol solution with water as the surrogate fluid.

Simulator Flow-Range and Pressure-Range Characterization

The mean flows and pressures, that can be obtained in the IVC by varying head pressures of the fluid reservoirs are shown in Table 3. Mean pressures and flows can be obtained independently of each other.

	Lower Limit	**Upper Limit**
Flow (L/min)	0	4.5
Pressure (mmHg)	10	30

Table 3

Recapitulation of clinical Fontan IVC flow

Here we aim to demonstrate that the elements of the introduced flow loop can be adjust so that simulate respiration recapitulate published clinical waveforms of Fontan IVC flow including IVC flow reversal during expiration [4]. The resulting IVC flow waveform was overlaid with the published data and closely matches it shown in Figure 33.

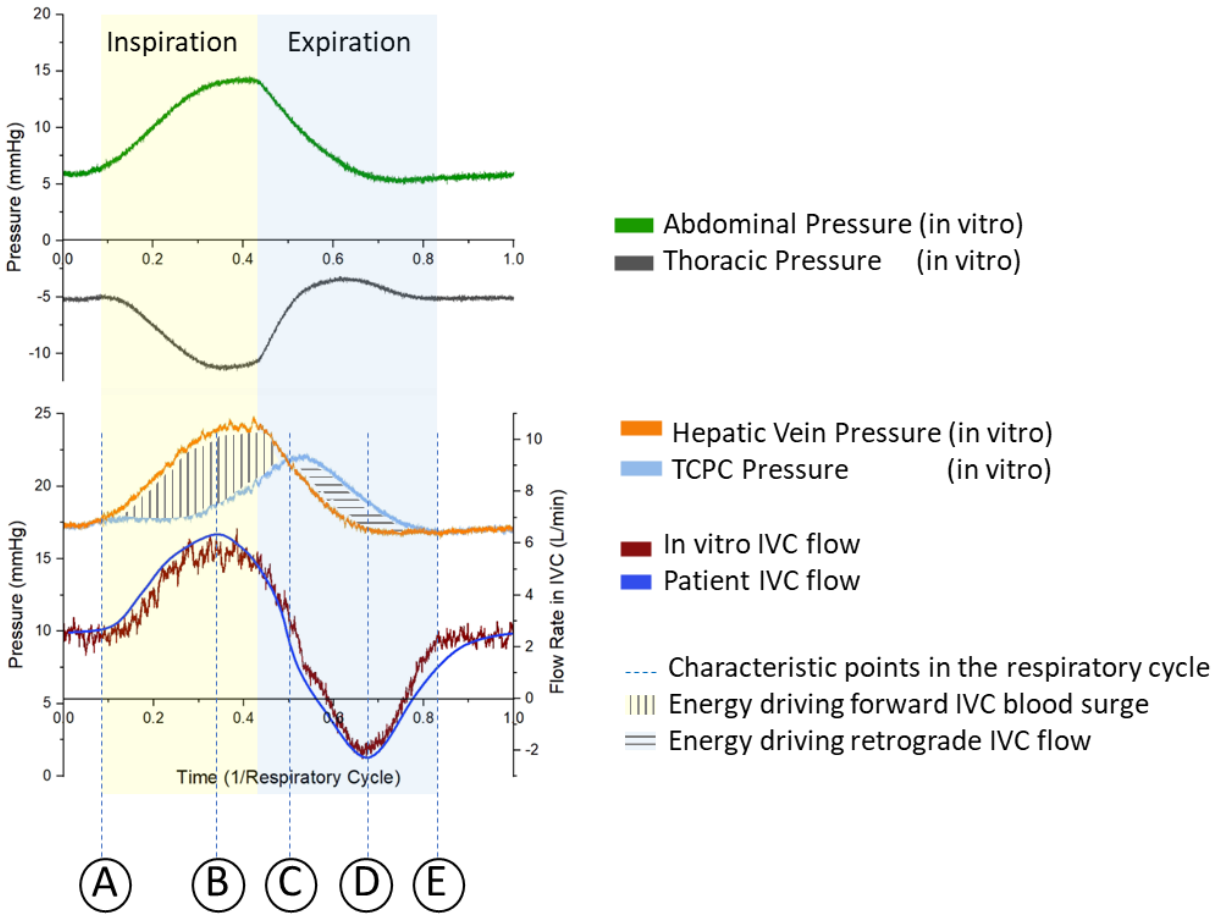

Figure 33 : Matching clinical Fontan IVC flow by receating respiratory and hemodynamic pressures in the Fontan IVC. Characteristic points throughout one respiratory cycle mark baseline flow before respiratory efforts (A), the pressure gradient between the abdominal and thoracic IVC driving peak forwrad surge of blood during inspiration (B), the reversal of the pressure gradient in the IVC (C) which drives the flow reversal of the Fontan flow to is peak values (D) before returning to the baseline flow during the end expiratory pause.

Figure 33 shows the respiratory pressure on top and the IVC flow rates as well as pressures below. The pressure graphs on top show the gas pressures in the chest and abdomen of the biomimetic simulator. They closely match the input waveform that were used from published data (Figure 4) and actuated the diaphragm motion through our pneumatic control. Inspiration and expiration are delineated in the graph and at the start of the respiratory cycle IVC flow is at baseline (point A). The simulated respiratory pressure transfer in the compliant models of the vascular beds placed in the chest and abdomen. During inspiration the lowering diaphragm increases the abdominal pressure (green line) and decreases the thoracic pressure (grey line). This causes the abdominal IVC pressure measured at the location of the hepatic vein (orange line) to rise over the thoracic IVC pressure located in the Fontan TCPC (turquoise line). This pressure gradient, marked by the vertically hatched area, drives a surge of forward flow in the IVC (red line) with the highest flow rate reached at the biggest pressure gradient between the thoracic and abdominal IVC (point B). With the start of expiration this mechanism is inverted decreasing the abdominal breathing pressure (green line) and increasing the thoracic pressure (grey line). This translates to the fluid pressure in the IVC causing the hepatic vein pressure to fall below the IVC pressure in the TCPC (orange line) at point C. The pressure gradient marked by the horizontally hatched area is now acting in the opposite flow direction of the IVC diminishing its forward flow and eventually reversing the venous flow to negative flow rates (point D). During the end-expiratory pause breathing pressure return to their baseline, the IVC pressure gradient vanished and consequently the IVC flow return to baseline (point E). The hatched area between the fluid pressure measurements in the IVC of Figure 33 represents energy which the respiratory biomechanics transfer to the Fontan flow causing its forward surge and reversal.

Parameter study to characterize Fontan flow in cardiorespiratory simulator

After showing that we can recapitulate physiological Fontan IVC flows by mimicking respiratory biomechanics we aimed to characterize the dynamic response of the biomimetic system. We explored how variations of the input parameters described in in section 2.2.2 change the IVC flow and flow reversal during different respiratory conditions. The examined parameters

and their impact on the generation of retrograde flow in the Fontan IVC are summarized in Figure 34.

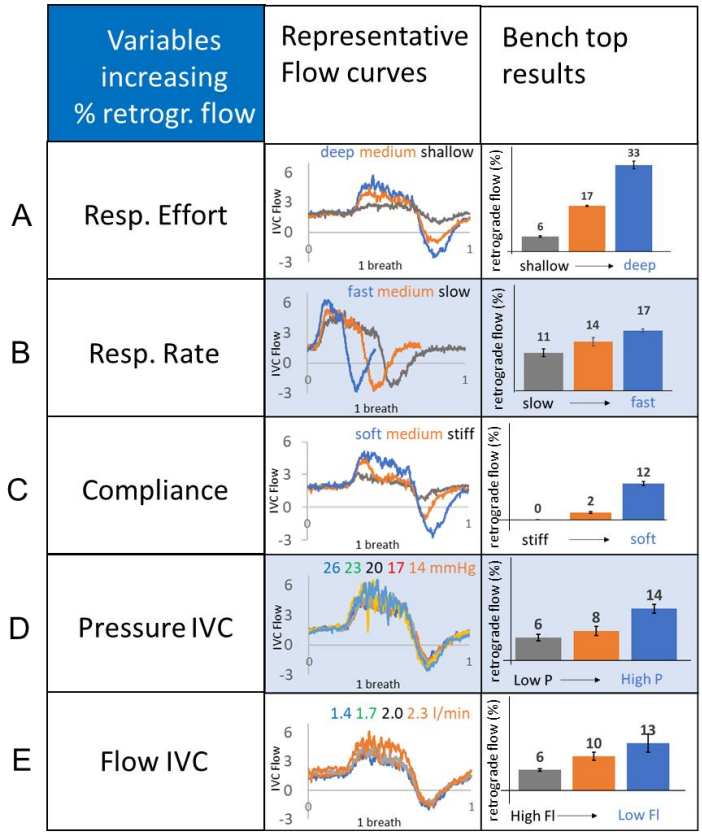

Figure 34: Characterization of the bench to cardiorespiratory simulator. The table lists the different anatomic conditions that we varied to investigate the effects on resulting retrograde IVC flow, representative flow waves of each condition and resulting histograms.

Respiratory Effort:

For shallow, baseline, and deep breathing the resulting retrograde flow in the IVC was 6 %, 17 %, and 33 % shown in Figure 34A. With increased respiratory effort the forward surge during inspiration is augmented accordingly while retrograde flow increases as well.

Respiratory Rate

With an increase of the respiratory rate, we observed an increase of the percent retrograde flow shown in Figure 34B. With increase respiratory rate from 9 to 12 to 20 breaths per minute the percent retrograde flow increases from 11 % to 14 % to 17 %. We observed a slight increase of the peak forward flow during inspiration combined with a shorter time period of elevated forward flow. The maximal flow rates of the retrograde flow remained constant during all respiratory rates and the positive flow during the end expiratory pause was shortened.

Compliance

We observed that with increased compliance from 0 to 165 ml/mmHg the resulting retrograde flow increases from 0 % to 2 % and 12 % as shown in Figure 34C. Stiff and semi-stiff vessels, wrapped in Velcro, resulted in 0 and 2% retrograde flow respectively, whereas fully compliant vessels resulted in 12 % retrograde flow. With increasing compliance, the amplitude of both the forward surge during inspiration as well as the reverse flow during expiration increase.

Baseline IVC pressure

With increasing baseline fluid pressure in the IVC we observed an increase of retrograde flow. as shown in Figure 34F. With increasing IVC pressure of 17 mmHg to 23 mmHg, and 26 mmHg retrograde flow during expiration increased from 6 % to 8 %, and 14 %.

Baseline IVC flow

With decreasing baseline flow through the IVC, resulting retrograde flow increases at constant respiratory conditions as shown in Figure 34E. With baseline IVC flows of 1.4 l/min, 1.7l/min, and 2.3l/min, retrograde resulted to 6 %, 10 %, and 13 % respectively. The representative flow waveforms show an increase in forward flow during inspiration and an increase in retrograde flow during expiration when baseline IVC flow is decreased.

2.3.3 Computational organ level lumped parameter model

Our objective with the organ level computational model was to recreate the Fontan circulation in more detail than the bench top cardiorespiratory simulator. This was to validate the functionality and dynamic response characteristics of the bench top set up which has a more simplified architecture. The approach for validation was threefold: Firstly, we chose published physiological values for all elements of the circulation, secondly, we induced breathing conditions to the *in silico* model matching the clinical flow waveforms and the bench top results for clinical Fontan flow shown in Figure 33, and thirdly, we repeated the parameter study characterizing system responses to variable physiological baseline conditions.

Figure 35 illustrates the IVC flow during a breathing cycle beginning at inspiration. Results from the *in silico* model closely match those from the clinical study of reference and from our benchtop simulator. IVC flow is seen to increase during inspiration and drop during expiration. We computed a mean IVC pressure of 18.5 mmHg on our simulation, which very closely matched that measured on the benchtop simulator.

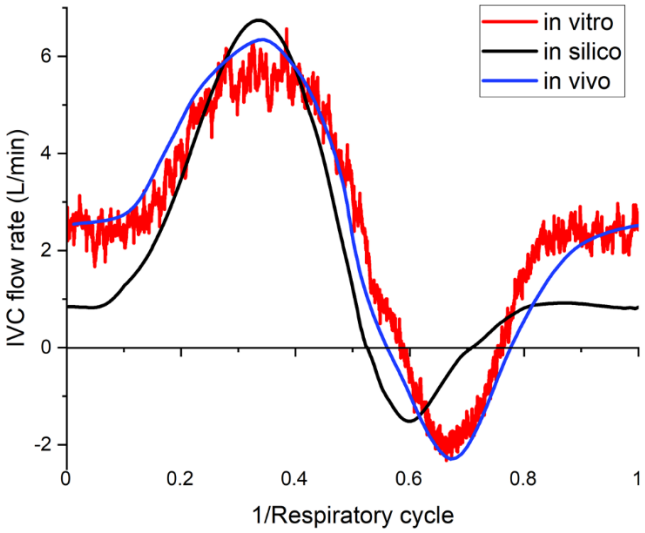

Figure 35: *In silico* and *in vitro* organ level flow models match clinical data of Fontan IVC flow during one respiratory cycle.

This validates that the simplified bench top model recreates Fontan IVC flow as the organ level lumped parameter computational model of the entire circulatory system does and both are suitable to match clinical data. Also, it shows how breathing, rather than the pumping action of the heart, governs flow characteristics observed of the IVC in the Fontan patient population.

To validate the dynamic response of the bench top system we repeated the parameter study described in section 2.2.2 and 2.2.3 to investigate the impact of variable physiological elements on the Fontan IVC flow under different breathing conditions. The results match the *in vitro* observations from section 2.3.1 and are compared in Figure 36.

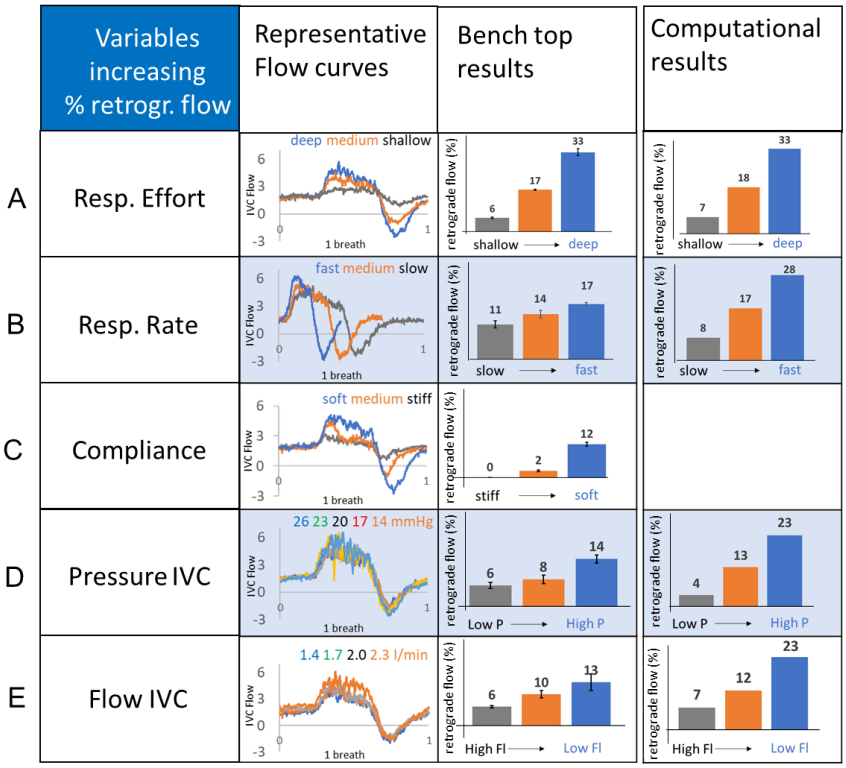

Figure 36 Computational results validate the dynamic response of the bench top cardiorespiratory simulator by matching results for the generated retrograde flow in the Fontan IVC.

Respiratory Effort

For shallow, baseline, and deep breathing the resulting *in silico* retrograde flow in the IVC was 7 %, 18 %, and 33 % shown in Figure 36A. This closely matches the bench top results and validates that an increase in respiratory effort causes in increase of percent retrograde flow in the IVC.

Respiratory Rate

For shallow, baseline, and deep breathing the resulting *in silico* retrograde flow in the IVC was 8 %, 17 %, and 28 % shown in Figure 36B. This matches the bench top results and validates that an increase in respiratory rate causes in increase of percent retrograde flow in the Fontan IVC.

Compliance

As described in section 2.2.3 it was not conducive to model variable baseline compliances with this computational model.

Baseline IVC pressure

With increasing IVC pressure of 17 mmHg to 23 mmHg, and 26 mmHg retrograde flow during expiration increased from 4 % to 13 %, and 23 % *in silico* shown in Figure 36D. This matches the bench top results and validates that increasing baseline IVC pressure leads to increasing percent retrograde flow in the Fontan IVC.

Baseline IVC flow

With baseline IVC flows of 1.4 l/min, 1.7l/min, and 2.3l/min, percent retrograde IVC flow resulted to 7 %, 12 %, and 23 % *in silico*, as shown in Figure 36E. This matches the bench top results and validates that decreasing baseline IVC flow rates lead to increasing percent retrograde flow in the Fontan IVC.

2.3.4 Computational fluid dynamics model of the Fontan IVC

The parameters of the 3-element Windkessel models were specifically tuned for the simulation to characterize the circulation profile in the IVC. The aim of the tuning procedure was to obtain experimentally measured values for the resulting flow rates and pressure waveforms at the outlet. Windkessel elements were iteratively varied to obtain the target values calculated at the outlet of the 3D fluid domain. Windkessel parameters were also iteratively varied to obtain the target pressure waveforms. The proximal resistance (Rp), compliance (C), and distal resistance (Rd) were calculated as following Rp = 0.0108 mmHg s ml^{-1}, Rd = 6.75 mmHg s ml^{-1}, C=53.3 ml $mmHg^{-1}$. A vector map of the resulting CFD Fontan IVC model is shown in Figure 37.

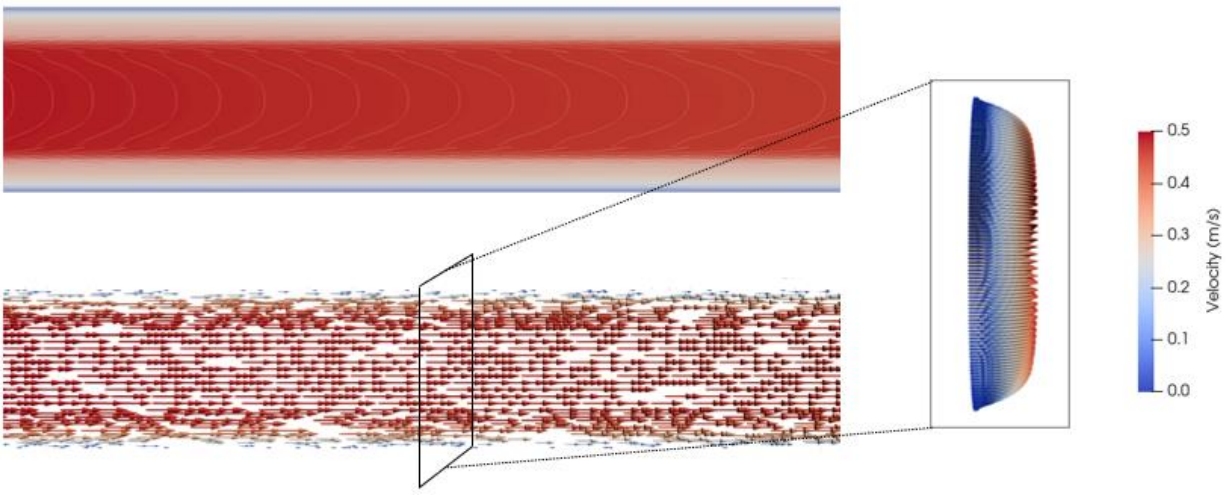

Figure 37 : Velocity vector map of the CFD simulation which models a piece of the Fontan IVC and validated by the bench top model.

Figure 38 compares the in silico and in vitro flow and pressure waveforms and flow rate amplitudes in the straight IVC flow tube. There is good agreement between the simulated and measured waveform shapes and amplitudes for both flow rate and pressure.

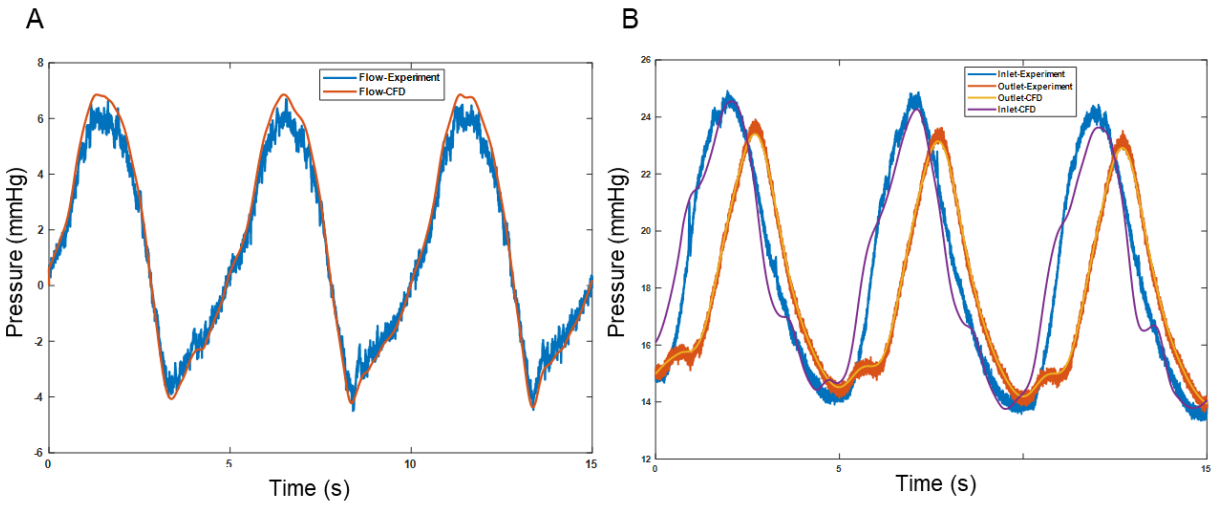

Figure 38 : Results of the study to validate the Fontan IVC computational fluid dynamic mode with the biomimetic bench top model. Prescribed flow inputs data validate pressure output data in (A), and prescribed pressure input data validate flow rate in the CFD model (B).

The average difference between the measured and simulated pressures is 0.1 mmHg which is 0.6% of the average pressure (18.56 mmHg) at the inlet and 0.19 mmHg which is 1.1% of the average pressure (17.73 mmHg) at the outlet. The maximum difference between the measured and simulated pressures is 2.3 mmHg and 0.9 mmHg at the inlet and outlet respectively. The average difference between the measured and simulated flows is 0.2 L/min which is 16% of the average flow rate (1.25 L/min).

2.4 Discussion

2.4.1 Bench top biomimetic respiratory simulator

We designed and built a respiratory simulator which mimics human respiratory mechanics to generate physiological breathing pressures of negative respiration in a modeled abdominal and chest cavity. The system design was guided by human anatomy and includes features segmented from patient MRI data and thus recapitulates the interdependence of pleural and abdominal breathing pressures and their compliances. By adjusting these physical parameters, we can imitate different patient physiologies. The electro pneumatic control system adds precise control over the diaphragm motion. Thereby the system can mimic a wide range of physiological breathing patterns. Thus, we completed aim A1 of this chapter.

2.4.2 Bench top biomimetic Fontan flow model

Integrating a lumped parameter flow loop into the biomimetic respiratory simulator creates a circulatory model which interacts with respiration in a physiological mechanism. Vascular beds serving as the venous reservoir of the body are represented with physiological compliance values. This mimics the interdependence of respiratory biomechanics and vascular compliance resulting in changes of venous flow patterns with a high physiological fidelity which has not been implanted in available bench top systems. These interdependent parameters include pressures of the negative pressure ventilation in the abdominal and chest cavities, compliance characteristics of those cavities, and compliance as well as resistive properties of the embedded vasculature.

We included patient specific vascular anatomies for key features of the Fontan circulation like the Fontan cross and implemented adjustable physiological flow parameters and respiratory patterns to provide a system for patient specific investigations. The recapitulation of Fontan biomechanics including the cardiorespiratory pump in the venous Fontan vasculature allowed us to closely recapitulate clinically published Fontan flow patterns. In addition to flow measurements the bench top model monitors respiratory pressure and resulting fluid dynamic pressure inside of the Fontan vasculature, which is not possible clinically, nor in live animal models. Exploring these fluid pressures which drive flow variations allow to understand the generation and qualities of Fontan flow patterns in more detail and estimate impact on the surrounding organ systems.

The presented parameter study shows the wide range of physiological parameters the bench top system can be used with and suggest key influencers for the generation of retrograde flow in the Fontan IVC. Our work is the first study to characterize this set of influencing parameters on Fontan retrograde flow. Also, it has not been shown that respiratory rate may impact flow reversal independently of respiratory efforts. Initial findings show that physiological parameters that increases retrograde flow on the bench top model are (i) greater respiratory effort, (ii) increased respiratory rate, (iii) greater compliance of the abdominal and lung vasculature, (iv) higher baseline pressure in the IVC, and (v) lower baseline IVC flow.

For a given set of physiological parameters the overlaid system of respiration and Fontan venous flow is only controlled by the head pressure generating the baseline IVC flow and the respiratory actions. This allows the system to dynamically adjust to any disturbances in blood flow or respiration allowing for the evaluation of support strategies in a more physiologic way.

This successfully completes aim A2 of this chapter.

We acknowledge some limitations of the bench top simulator which include the simplification of the Fontan vasculature and resistive properties, no validation of the hemodynamic findings thus far, and focusing on the venous side of the Fontan vasculature which addresses the bottleneck of the Fontan circulation as described previously but does not simulate the heart and arterial interactions with respiratory mechanics. These limitations represent a unique opportunity for future work such as: (1) The development of a computational lumped parameter model representing the interaction between respiration and Fontan venous flow similar to the bench top model but with all elements of the Fontan circulation to validate the dynamic behavior of the bench top system. (2) Conducting a clinical respiratory study to validate the hemodynamic findings on bench top findings in Fontan patients. (3) The inclusion of the arterial side into the respiratory system to simulate the full extent of the cardiorespiratory pump allowing to investigate a variety of clinical concern including biventricular diseases, right heart failure, and pulmonary diseases impacting cardiac return.

2.4.3 Computational organ level lumped parameter model

We developed a Windkessel lumped-parameter model that is based on the anatomy and biomechanics of the human cardiovascular system. This was developed using the object-oriented MATLAB-based SIMSCAPE platform in the hydraulic domain. A custom variable-compliance element was integrated to mimic cardiac contractility and compliance variations due to respiration. The model was constructed using the geometrical and mechanical characteristics of the cardiovascular anatomy and included all organ systems of the Fontan physiology. Values for local resistances were adopted from the literature when it was impractical to geometrically represent the network at various sites of the cardiovascular tree. The efficiency of traditional electrical analog lumped-parameter models and the physical intuitiveness and practical advantage associated with the hydraulic domain coalesce in the platform. This makes the proposed model suitable for creating intuitive representations of *in vitro* hydraulic mock circulatory loops, suitable to validate the hemodynamic findings on the bench top model, informing device development through the optimization of the associated geometry and material properties, and predicting patient-specific hemodynamics of clinical relevance.

Our *in-silico* results replicated a recent *in vivo* study and was successfully validated the dynamic response of the cardiorespiratory benchtop simulator discussed in the section 2.4.2. We found that, at the same respiratory rate and cardiac output, the IVC pressure and flow characteristics

were similar across the three platforms. *In silico* we observed that physiological parameters that increase retrograde flow are (i) greater respiratory effort, (ii) increased respiratory rate, (iii) higher baseline pressure in the IVC, and (iv) lower baseline IVC flow. This concurs with the findings on our bench top simulator and validates the simplified architecture of overlaid respiration and hemodynamics. Hence, we successfully completed aim A3 of this chapter.

Limitations associated with our model a lack of inertial elements that would capture the high-frequency pressure changes associated with higher order velocity changes. As the bottle neck of the failing Fontan circulation is described to be on the venous side high frequency changes of flow rates are not prevalent. Also, in our model respiration was simulated by cyclical change of the compliance values of the lungs. This didn't allow for the investigation of the impact of compliance change as shown in the bench top model.

These results which validate the findings of our overlaid respiratory and flow model by the more comprehensive computational model encouraged us to initiate a clinical trial to validate those effects of respiration on retrograde flow in the Fontan IVC clinically.

2.4.4 Clinical validation of bench top and computational models

We have shown that real time cMRI recordings can be paired with an audio-visual to guide Fontan patients from an age of 15 years through a respiratory study and evaluate the impact of breathing patterns on Fontan flow clinically. Statistical analysis showed that participants were able to follow the guide during MRI recordings and adjusted their respiratory rate and respiratory efforts independently. We were able to synchronize chest wall motion as surrogate measurement for breathing patterns to the blood flow rates in the descending aorta and IVC.

Our pilot study represents the first clinical study aimed to validate a Fontan bench top simulator as well as the first study to quantify the impact of both the respiratory effort as well as respiratory rate on venous Fontan flow dynamics to generation retrograde flow IVC flow. The results of the clinical pilot study match the results of the bench top and computational model and thus validate the dynamic response of the develop system. In the clinical results all investigated parameters concur the findings of the bench top model suggestion that greater respiratory effort, increased respiratory rate, and lower baseline IVC flow are individual contributors to more retrograde flow during expiration of the breathing cycle.

These impacting physiological parameters have not been reported in previous clinical studies of the Fontan physiology and have not been explored on other simulators thus far. The clinical

pilot trial and computational study validate all findings of the bench top model and thus show that the dynamic response of the cardiorespiratory simulator is an adequate representation of fundamental mechanisms observed in the venous Fontan hemodynamics. This successfully addresses aim A4 of this chapter.

We acknowledge some limitation of this of this clinical study which include the low number of participating Fontan patients (n=5) which does not provide the statistical power to prove that the discovered impact of respiration and physiological parameters on venous Fontan flow can be generalized for this patient population. Nonetheless, this pilot study served to validate the results of the computational and bench top models and lay the basis for a larger clinical study to investigate the effects of respiratory pattern on Fontan venous flow in greater detail.

2.4.5 Computational fluid dynamics model of the Fontan IVC

We have implemented and validated a computational fluid dynamic model of the Fontan IVC based on the biomimetic cardiorespiratory simulator described in this chapter. While CFD models of the Fontan IVC have been implemented before, we combine the system-level flow dynamics of the bench top simulator with an associated CFD model. This creates a platform of Fontan models which allows testing of the physiological impact on Fontan hemodynamics and blood interaction and detailed analysis of its interaction with support strategies.

The presented methodology has several limitations that could be improved in the future. In the numerical investigations of IVC flow, wall is considered as rigid and fluid–structure interaction (FSI) techniques have not been implemented in this study. Resistance and vascular compliance are represented using 3-element Windkessel model which is analogous to electrical resistance and compliance and can capture pressure difference and mass flow hydraulic relation. For simplicity, we utilized the Windkessel model to recreate specific benchtop simulator results for a given breathing effort. Complex flows with varying breathing dynamics, on the other hand, may need a more thorough parameter tuning strategy for individual components in the Windkessel circuit. By using the Fontan cross and other branches, such as RPA, LPA and SVC, it may be possible to depict more complicated flow dynamics.

2.5 Conclusion

We demonstrate a respiratory simulator that replicates the biomechanics of ventilation and completes aim A.1 described in section 2.1.3. Our simulator drives diaphragm displacement with soft robotic actuators mimicking physiological muscle contraction. By varying the contraction

of these actuators, we can adjust diaphragm effort to closely match physiological respiratory pressures. The system constitutes the close interdependence of thoracic and abdominal pressures which can be tuned by adjustable compliance of the respiratory chambers. It represents the first respiratory simulator to recreate breathing pressures in the thorax and abdomen simultaneously which recapitulates negative pressure ventilation with more physiological accuracy than previous systems. The bench top simulator is constructed with anatomical structures of the chest wall and diaphragm segmented from patient data and thus functions as an educational, training, and research tool. This enables the investigation of breathing effects on organ systems like the lungs, hemodynamic interactions in the chest and abdomen, and intervention strategies for both.

We introduced a lumped parameter flow loop into the respiratory simulator to create a biomimetic model of the Fontan venous hemodynamics. This circulatory model is uniquely equipped to study the interdependence of physiological breathing mechanics and Fontan flow and thus completes aim A.2 of section 2.1.3. Constant pressure heads drive flow to mimic baseline venous Fontan flow patterns, resistors and compliance elements emulate vascular characteristics, and segmented patient specific vasculature recreate the flow geometries of key features in the Fontan anatomy. Abdominal and pulmonary vascular beds made from soft materials match physiological compliance values and transfer breathing pressure to the circulation recreating characteristic Fontan flow pattern as validated with clinical data. A custom blood surrogate fluid closely matches viscous behavior of human blood which allows to investigate the interactions of breathing and Fontan flow in room temperature on the bench top. To our knowledge this demonstrates the first biomimetic cardiorespiratory simulator of the venous Fontan flow with this level of physiological fidelity. The bench top system can cover a wide range of physiological parameters by adjusting baseline respiratory efforts and rates, baseline flow rates, baseline blood pressure, flow resistances, and vascular compliance. It is instrumented to monitor breathing pressures, flow parameters of the SVC and IVC, as well as hemodynamic pressures of the abdominal and thoracic IVC simultaneously. The adjustable respiratory and hemodynamic parameters of the cardiorespiratory simulator allow the hemodynamic recapitulation of different Fontan phenotypes as well as specific patients while adding the ability to monitor intravascular pressure conditions driving the Fontan flow changes which is not feasible routinely in the clinical setting. This allows investigation of fluid pressures which drive flow variations to understand the generation and qualities of Fontan flow patterns in more detail and estimate impact on the surrounding organ systems as it is not possible in animal models or

previous bench top systems. We characterized the dynamic response of the cardiorespiratory simulator to validate its function with computational and clinical models.

We demonstrate that a computational lumped parameter model of the Fontan physiology which includes respiratory mechanisms effecting flow dynamics can reproduce clinical Fontan flow patterns. The *in-silico* model is based on hydraulic principles and mechanical deformation of cardiovascular components and includes all organ systems of the Fontan physiology. As such, it resembles a complete anatomical and physiological model of the Fontan phenotype. We characterized the dynamic response of the computational system and closely matched the results from the bench top model. This validates the dynamic response of the *in vitro* system which has more simplified hemodynamic elements and thus successfully completes aim A.3 of section 2.1.3.

With a clinical validation study of Fontan patients, we demonstrate that real time MRI recordings paired with an audio-visual guide during imaging is suitable to clinically evaluate the impact of breathing patterns on Fontan flow. To our knowledge this is the first clinical study which varies respiratory efforts and respiratory rates independently to isolate the effects on Fontan venous IVC flow. This can be a valuable tool (i) to understand physiological relationships of respiration, Fontan IVC flow, and the generation of retrograde flow in the IVC, and (ii) to generate a collection of IVC flow data at varying respiratory patterns which can be used to evaluate other clinical impact factors facilitating flow Fontan flow reversal and to evaluate the efficacy of support strategies in the IVC for different patient phenotypes. The obtained clinical data successfully validated the *in silico* and *in vitro* results and successfully completes aim A.4 of section 2.1.3.

The only input parameters during bench top simulations are respiratory patterns as the dynamic response of the system are guided by the validated overlaid biomechanics of respiration and circulation. No advanced control of each physiological element is needed so the hemodynamic responses of the bench top model to respiratory variations or circulatory support strategies are not prescribed but could indicate physiological responses more closely than available models. Animal models have been the most physiologically accurate model to test support strategies of the failing Fontan circulation. However, they are not suitable to include crucial mechanisms like respiratory interactions with Fontan flow causing flow reversal in the IVC. This simulator could be more suitable platform to explore the impact of different respiratory patterns and circulatory support strategies on Fontan flow.

We then combined the cardiorespiratory bench top model with a computational fluid dynamics model. This allows comprehensive flow analysis of the hemodynamics observed in the physiologically high-fidelity bench top system and creates a platform which allows for Fontan flow analysis on the organ system level as well as resulting blood interaction of support strategies.

3. Chapter 2:
Leveraging benchtop models and clinical imaging to investigate the effect of breathing variations on IVC hemodynamics in the Fontan physiology

3.1 Introduction

The single ventricle physiology creates atypical hemodynamics causing pathophysiological burden on many organ systems as described in section 1.1.1. A paucity of clinical trials have been reported in the Fontan population to identify the most suitable indicators for late adverse outcomes. Hence, clinical practice for this patient population varies greatly between care centers with inconsistent follow-up recommendations [47], [48]. Understanding of physiological factors which drive hemodynamic burden remain subject to research. This chapter explores aspects of how breathing impacts Fontan venous flow on the previously introduced biomimetic bench top simulator and in Fontan patients.

3.1.1 State of the field and current limitations

Clinical markers for Fontan health

The single ventricle physiology causes exceptional hemodynamics with pathophysiological burden on many organ systems. While obtaining relevant hemodynamic measurements is challenging as described in section 2.1.1 the ability to use such clinical markers to describe Fontan health remains unclear. Key features and drivers of this complex problem are still subject to research. Thus, failing of the Fontan circulation is multifaceted and can become apparent in different physiological manifestations. Also, Fontan surgery is performed in response to a variety of different congenital heart diseases with varying anatomical structures. This contributes to a highly heterogeneous patient population with specific physiologic vulnerabilities manifesting in diverse clinical markers. Therefore, analysis of clinical markers as predictors for the status of Fontan circulations is a multivariable function. The status of the heart, lungs, liver, and gastro-intestinal system can all contribute to a more accurate picture of the health of the Fontan circulation [20], [49]–[52]. Due to the rising but relatively small patient population studies to elucidate correlations between hemodynamic, physiological, and clinical markers have been limited. Clinically obtained descriptions of flow dynamics and biomarkers of the patient's physiology can contribute to understand the adaptations of the Fontan circulation in general.

Clinical relevance of retrograde flow in the Fontan IVC

In the search to identify causal elements of Fontan failure an upstream shift to place the focus on venous congestions and the attenuation of chronic venous insufficiency has been suggested [3]. This centers on flow behavior in the IVC which in turn is greatly influenced by interactions with breathing biomechanics as described in section 1.1.2. Recent studies have emphasized the clinical existence of up to 30 % retrograde venous flow in the Fontan IVC during each respiration cycle [4], [53]. No correlation between reverse flow and ventricular ejection fraction or cardiac index was found, however flow inefficiencies due to increase pulsatility, and potential long-term burden on the liver caused by retrograde flow and increased hepatic portal pressures has been suggested [4].

The impact of other physiological features has not been investigated. Consequently, suitable clinical markers have not been identified to correlate any potential impact of the retrograde flow to Fontan health.

Gravitational impact on Fontan IVC flow

Studies on the gravitational effects on the Fontan circulation and the cardio-respiratory pump have been limited. 2D doppler ultrasonic measurements were used to quantify IVC and hepatic vein flows in Fontan patients on a tilting table [25]. Results suggest that gravity enhances the deleterious effects of Fontan flow on the liver, however no flow simulator has been developed to address this issue thus far. No bench top simulator exists which allows to explore the impact of gravitation on (a) Fontan flow, (b) interactions with the cardio-respiratory pump, and (c) circulatory support strategies.

3.1.2 Limitations addressed in this chapter

Motivated by the understudied importance of retrograde flow caused by breathing biomechanics in the Fontan IVC this chapter focuses to elucidate driving mechanisms of this flow reversal. The characterization of elements causing retrograde IVC flow will be addressed in two domains: (1) on the bench top and (2) in a clinical study. The bench top simulations will allow us to investigate the impact of respiratory effort, respiratory rate, baseline flow rate, baseline blood pressure, and compliance of the pulmonary and splanchnic vascular beds. This will form the basis to distinguish individual drivers of the flow reversal. Also, the bench top set up will allow us to monitor pressure variations during flow reversal which are not available clinically. We will then modify the *in vitro* installation of the flow simulator to resemble an upright body

position. This will permit us to investigate how gravitational acceleration influences IVC flow and its flow reversal during breathing exercises *in vitro*.

The analysis of Fontan IVC flow during varying breathing conditions in patients will add clinical proof of the influencing factors of retrograde Fontan flow observed in the biomimetic bench top simulator. Additionally, it will allow us to quantify the amount of flow reversal in different patient phenotypes contributing to paint a more quantified picture of this diverse patient population. The heterogeneous nature of the study population may give insight to weather structural differences in the underlying heart conditions impact characteristics of the venous return and retrograde flow during breathing. Lastly, a review of the study population's medical history will allow us to correlate potential hemodynamic findings to physiological changes and clinical manifestations.

In this way the work helps to elucidate fundamental mechanisms acting on Fontan hemodynamics, it will help to quantify physiological effects of breathing variations, it may contribute to the understanding of the clinical relevance of flow reversal in the Fontan IVC, and it will provide flow waveforms of different patient phenotypes which can be used to evaluate performance of promising circulatory support strategies in the future.

3.1.3 Specific aims

The cardiorespiratory pump has an exaggerated effect in governing the venous flow waves in the Fontan IVC, however respiratory and physiologic contributors to this have not been characterized and are difficult to explore *in vivo*. Hence, **the goal of this chapter** is to investigate the effects of breathing variations and other contributing hemodynamic factors on the IVC flow of the Fontan physiology. To achieve this goal, I will leverage the benchtop models described and validated in chapter 2 to investigate selected key hemodynamic influencers and conduct clinical a clinical 4D MRI study to explore the effects of breathing mechanics on IVC flow dynamics *in vivo*. Also, we will explore correlations of hemodynamic findings with clinical markers for the health condition of the Fontan physiology. Towards this goal **the specific aims** are to:

1. Investigate *in vitro* hemodynamics in the IVC when subjected to various changes in breathing mechanics.

2. Perform *In vivo* 4D MRI trial to study the effect of breathing mechanics on IVC hemodynamics.

3. Correlation of hemodynamic, physiological, and clinical parameters in the Fontan study population

4. Recreate hemodynamically relevant activities of Fontan patients leading to an upright body position and erratic flow patterns.

3.2 Methods

Figure 39 shows an overview of the conducted studies including the desired outcomes for chapters 1 and 2.

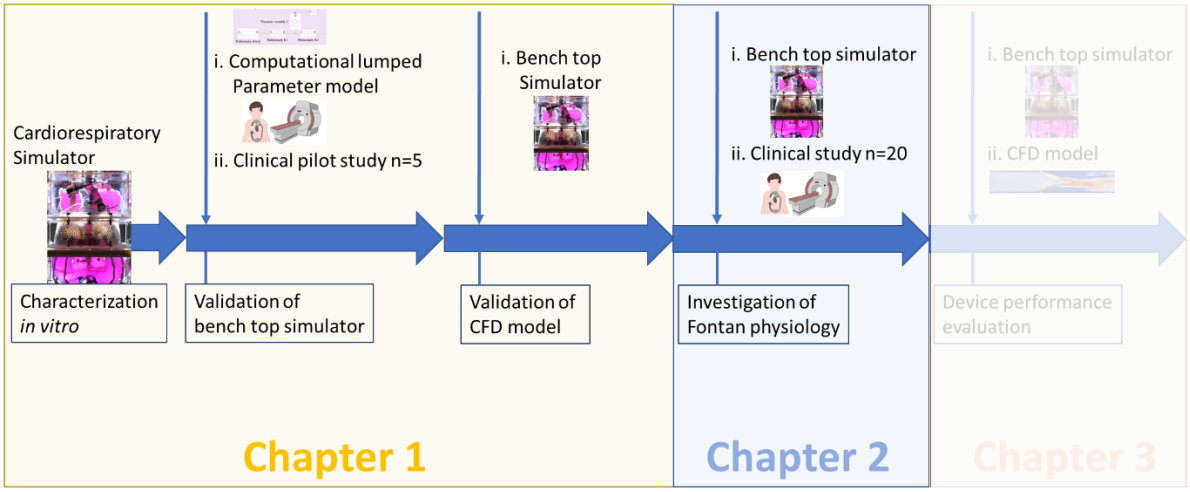

Figure 39 : Schematic showing the sequence of studies for chapter 1, and 2.

3.2.1 *In vitro* investigation of cardiorespiratory model hemodynamics

To Investigate in vitro hemodynamics in the IVC when subjected to various changes in breathing mechanics we expanded the parameter study conducted on the biomimetic bench top simulator introduced in section 2.2.2. The tested variables and evaluated physiological parameters of this bench top study are summarized in Figure 40.

A

Tested variables	
Respiratory effort (RR = 14 = const.)	Shallow breath
	Baseline breath
	Deep breath
Respiratory rate	9
	14
	28
Baseline IVC flow	1.4 l/min
	1.7 l/min
	2.3 l/min
Baseline IVC pressure	17 mmHg
	23 mmHg
	26 mmHg
Vascular compliance	Stiff
	Medium
	Soft

B

Output variables	
IVC flow curve	Respiratory cycle
IVC flow rates	Inspiration/expiration (L/min)
Pulsatility index	$\frac{Amplitude\ of\ flow\ rate}{Mean\ flow}$
IVC flow volume	Inspiration/expiration (ml)
% retrograde flow	Respiratory cycle (%)
IVC pressure curve	Respiratory cycle
IVC pressure range	Inspiration/expiration (mmHg)

Figure 40 : Tested variables (A) and evaluated output parameters (B) to investigate Fontan hemodynamics on the cardiorespiratory simulator.

Each physiological parameter was analyzed for one entire respiratory cycle. Averages and standard deviations were then calculated for three consecutive respiratory rates (OriginPro, OriginLab Corporation, USA).

3.2.2 *In vivo* 4D MRI trial to study the effect of breathing mechanics on IVC flow dynamics

After we demonstrated the feasibility of evaluating the relationship of breathing patterns with Fontan IVC flow in a pilot study described in section 2.2.4 we planned a larger clinical study targeting the same patient population. The main goal of this study was to investigate the independent impact of respiratory effort and respiratory rate on the flow dynamics of the Fontan IVC. We aimed to understand physiological relationships of respiration, Fontan IVC flow, and the generation of retrograde flow in the IVC. Further, this physiological study aimed to generate a collection of IVC flow data across varying respiratory patterns to provide hallmarks of clinically observed Fontan flow for the evaluation of circulatory support strategies.

Study design

The study design was adapted from the pilot study described in section 2.2.4. Patient screening, selection, and recruitment were identical. The workflow at the hospital was the same as well as the data collection and storage. The study was approved by the local ethical committee at Boston Children's Hospital (IRB-P00037103), and written informed consent was obtained and stored for all participants.

Study population

From April 2021 to February 2022, a total of 26 Fontan patients were enrolled and 20 of them resulted in acquired flow image data. A summary of the patient population is shown in Figure 41A.

A

Patient population	
Age (years)	23.8 (±7.4)
Fontan age (years)	20.8 (±6.7)
BSA (m2)	1.8 (±1.51)
BMI (kg/m2)	24.4 (±4.8)
Total patients	n = 20
Fontan types	HLHS (n=10)
	DILV (n=5)
	TA (n=5)
	DORV (n=3)
	RdAVC (n=1)
	Single RV (n=1)
	Critical PS (n=1)

C

Tested variables	
Respiratory effort (RR = 14 = const.)	Shallow breath
	Baseline breath
	Deep breath
Respiratory rate	9
	14
	28
Breath-hold	

C

Output variables	
% retrograde flow	
IVC flow volume	+ / - (ml)
IVC flow rates	+ / - (L/min)
Pulsatility index	$\frac{Amplitude\ of\ flow\ rate}{Mean\ flow}$

Figure 41 : Summary of study parameters for the respiratory MRI study. Characteristics of patient population (A), tested parameters (B), and output variables (C).

The study population consisted of 8 females and 18 males with an age range of 16.4 to 42.2 years (average 23.8 years ± 7.4) with completed TCPC 20.8 years ago ± 6.7, a body surface area (BSA) of 1.8 m2 ± 0.2, and body mass inex (BMI) of 24.4 kg/m2 ± 4.8. Congenital heart diseases of the patient population included hypoplastic left heart syndrome (HLHS, n=10), double inlet left ventricle (DILV, n=5), tricuspid atresia (n=5), double outlet right ventricle (DORV, n=3), right-dominant atrioventricular canal (RdAVC, n=1), single right ventricle (n=1), critical pulmonary stenosis (n=1).

MRI protocol

The MRI protocol was adapted from the pilot clinical trial. The MRI sequence, and image configurations are described in section 2.2.4.

Data analysis

Data analysis was adapted from the pilot clinical trial and adjusted as described below.

The segmentation and quantification of respiratory effort and rate was conducted as described previously in section 2.2.4.

The segmentation and quantification of flow MRI flow data was conducted as described previously in section 2.2.4.

The study variables are described in Figure 41B. During the MRI study we varied respiratory effort from baseline to shallow and heavy breathing, the respiratory rate from baseline (14 breaths/min) to slow (9 breaths/min) and fast (28 breaths/min) and compared it to the baseline venous IVC flow at breath hold. The output variables are described in Figure 41C. For each respiratory cycle we analyzed the flow rates, flow volumes, percent retrograde flow and pulsatility index during inspiration and expiration.

Statistical analyses were performed to evaluate the significant differences in breathing patterns of each patient and the resulting percentage retrograde flow. Given that the null hypothesis assumed that respiratory chest wall motion, respiratory rate, and percent retrograde flow in the IVC do not change significance of alterations for each patient were determined by a paired, double tailed, t-test with a significance level of 0.05. For each outcome five respiratory cycles were analyzed individually over five consecutive breaths. Averages and standard deviations were calculated. For the entire study cohort values were summarized and the following values were calculated (OriginPro, OriginLab Corporation, USA): Average, standard deviation, median, minimum, and maximum. Additionally, the outcome variables were normalized to baseline values.

3.2.3 Correlation of hemodynamic, physiological, and clinical parameters in the Fontan study population

The primary objective of this study was to explore the drivers of retrograde flow and mechanisms in the venous Fontan IVC modulated by respiratory pattern, intensity, and frequency.

Still, the impact of other physiological features and associated clinical markers has not been investigated. With access to one of the largest Fontan patient studies to date we use the opportunity to identify any potential impact of the retrograde flow to Fontan health.

Study design

For this investigation we collected clinical available data, divided in three main categories: (i) radiological investigations of anatomical characteristics, (ii) blood analysis, and (iii) physical examination and symptoms. We collected clinical markers retrospectively in these three categories and compared them to physiological and hemodynamic characteristics of our study population as summarized in Figure 47.

A	B	C	D
Physiological and hemodynamic characteristics	**Radiological investigation**	**Blood analysis**	**Physical exam and history**
Age	Hepatic portal vein cross section	Creatinine	Vital signs
Years after Fontan completion	Pulmonary artery cross section	Bilirubin	General discomfort
Body surface area	Liver size	Alanine transaminase (ALT)	Lung exam
Ventricular ejection fraction		Aspartate transaminase (AST)	Cardiac sounds
Baseline IVC flow rate/BSA		Gamma-glutamyl Transferase (GGT)	Oedema
Baseline % retrograde flow		International Normalized Ration (INR)	Cyanosis
Baseline pulsatility index		Blood urea nitrogen (BUN)	Abdominal exam
		Albumin	Neurological exam
		Alpha Fetoprotein (AFP)	
		Brain natriuretic peptide (BNP)	
		Hemoglobin (Hgb)	
		Hematocrit (Crit)	
		Platelet count	

Figure 42 : Summary of physiological and hemodynamic characteristics of the study population that were compared to clinical markers retrospectively taken from patient records.

The study was approved by the local ethical committee at Boston Children's Hospital (IRB-P00037103), and written informed consent was obtained and stored for all participants to review their medical history and radiological measurements.

Study patient population

In total 24 patient participated in the study which includes all 20 patients of the respiratory MRI study described in the previous section. Four patients also were part of the same study but some imaging sequences were compromised rendering their dataset unusable for the evaluation described in the previous section. All data was collected retrospectively up to a time point of 1 year prior to the MRI imaging date during which the respiratory study was performed.

Protocols for radiological measurements, blood analysis reports, and medical history

Radiological investigation of anatomical characteristics

Due to the study design only cardiac MR images were available for analysis with no specific contrast agent or imaging modalities.

Intra-hepatic portal vein cross sectional area was measured 10 mm before its bifurcation. Images were reformatted using multiplanar reformation (MPR) to create an adapted plane to fit the vessel orientation, permitting an accurate measure of the vessel's diameter.

Maximal antero-posterior liver size was measured using MPR as described in [54]. MRI acquisition sequence was based on a CMRI protocol, therefore lateral sides of the axial (approximately 50mm) images were ignored; lateral and cranio-caudal maximal size measures were not available.

To evaluate the cross-sectional area of the pulmonary arteries the Nakata index was computed using the standard formula [55] which summarizes the cross-sectional area of the left and right pulmonary artery normalized by the patient's body surface area.

Blood analysis

Blood test analysis items are summarized in Figure 47C and were collected from patient records in the medical record software Epic (Epic Systems, USA).

Physical examination and symptoms

Physical examination items are listed in Figure 47D and were collected from medical record of cardiology follow-up (Epic, Epic Systems, USA), extracted from the echocardiography reports, and stress test data reports

3.2.4 Impact of anatomical position and gravity

A Fontan patient's position may impact blood flow, whether they are lying down, standing, walking, or running. Gravitational effects on hemodynamics which occur in an upright position may alter efficacy of flow support strategies. Deleterious effects on Fontan hemodynamics by gravity due to an upright body position have been shows *in vivo* and discussed in section 3.1.1. Still, no bench top simulator exists to investigate hemodynamic effects under varying physiological conditions. We modified the biomimetic Fontan bench top simulator described in section 2 to resemble an upright body position. We designed and constructed a frame and attachment mechanisms to operate the cardiorespiratory simulator in the upright position. Our approach to simulate supine and upright body position of a Fontan patient in the vertical gravitation field is shown in Figure 43. This includes a frame construction to fix the bench top simulator in the upright position.

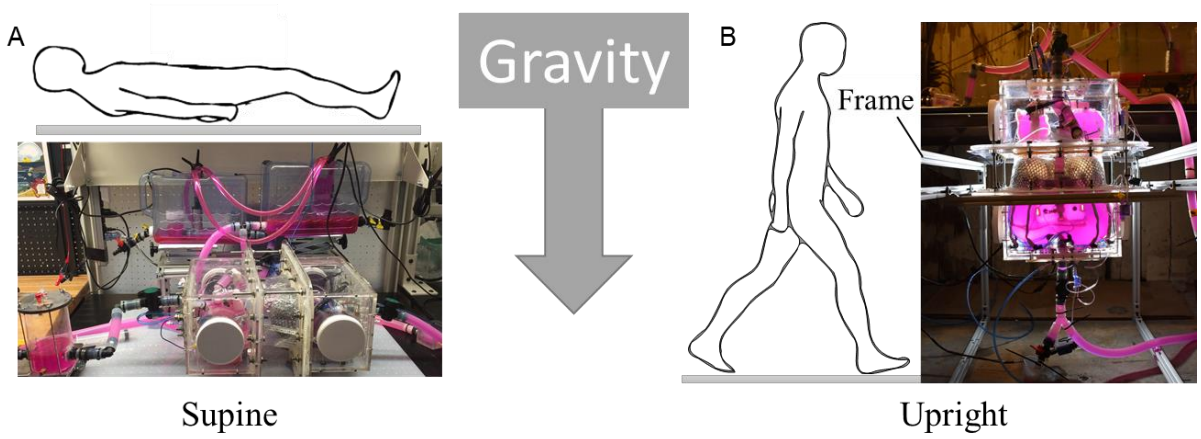

Figure 43 : Vertical positioning of the biomimetic Fontan flow model to simulate upright body position and investigate gravitational effects on the Fontan IVC flow. The direction of gravitational acceleration on fluids in the cardiorespiratory simulator changes from the supine to the upright position. Schematic of supine position represented by the horizontal orientation of the cardiorespiratory simulator (A) and upright body position seen in schematic (B) represented by the vertical positioning of the bench top model.

The system settings and instrumentation were maintained as described in section 2.2.2. To investigate gravitational effects on Fontan IVC flow we varied the respiratory efforts simulated in the system and compared results in the supine and upright orientation. To simulate increasing respiratory efforts we increased the supplied actuation pressure to the soft robotic muscles described in section 2.2.2. Input pressures ranges from 5 psi to 17.5psi in increments of 2.5 psi. Output parameters included the flow rate waveforms of the IVC, the flow volumes per

respiratory cycle, the percentage retrograde in the IVC, and the blood pressures in the abdominal IVC (location of the hepatic vein).

For each respiratory effort five consecutive breathing cycles were analyzed, for which averages, and standard deviations were calculated.

3.2.5 Erratic flow simulation

Pressures in the abdomen and thorax are sensitive to a variety of physiological variables including changes in breathing patterns as well as motions of chest and abdomen and engagement of core musculature. In daily life these influences change frequently and resulting in more erratic IVC flow conditions in Fontan patients. To recapitulate these erratic IVC flow patterns, we adapted patient data over multiple breaths [27]by scaling it to guide the input pressure of our electropneumatic control in our cardiorespiratory bench top simulator. This actuation pressure then controlled the diaphragm motion, respiratory pressures, and ultimately IVC flow changes on the benchtop. We used the instrumentation of the Fontan simulator to monitor respiratory pressures, IVC pressures and flow rates during the simulation of erratic patient flow.

3.3 Results

3.3.1 *In vitro* investigation of cardiorespiratory model hemodynamics

Physiological parameters that were investigated on the bench top model and could also be compared with clinically obtained data in the *in vivo* validation study are summarized in Figure 29, Figure 30, and Figure 31 in section 2.3.1. and are not repeated in this section. Additional findings as described in the methods are summarized here with the previously evaluated results from section 2.3.1.

Impact of respiratory effort

Figure 29 shows the resulting respiratory flow rates in the Fontan IVC (A), resulting IVC flow volumes (B), resulting pulsatility index (C), and resulting percent IVC retrograde flow(D) with increased respiratory efforts. Figure 44 shows the corresponding flow rate waveforms (A), the pressure waveforms in the IVC (B), and the pressure margins (C) generated by increased respiratory efforts.

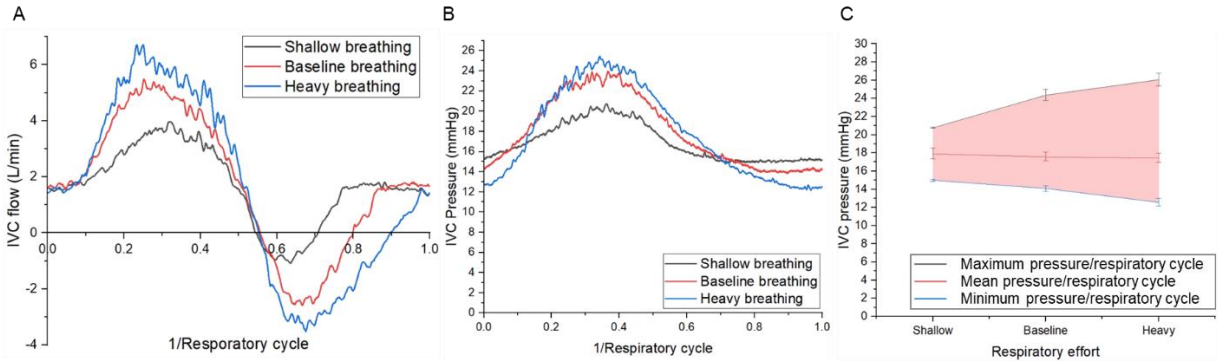

Figure 44 : Resulting flow rate waveforms (A) pressure waveforms (B) and pressure margins (C) in the Fontan IVC with increasing respiratory efforts on the biomimetic bench top model.

During greater respiratory efforts we can see the forward flow rates increase during inspiration and the retrograde flow rates also increase during expiration. This increases the forward and reverse maximum flow rates and the respective flow volumes which can be seen as the area under the flow curves in Figure 44A. The negative volume grows relatively more so the resulting percent retrograde flow in the IVC is greater when respiration is heavier. An increase in respiratory efforts also increase the pressure amplitudes as shown in Figure 44B. Despite greater maximum and minimum pressures the mean pressure in the IVC remains constant as shown in Figure 44C.

Impact of respiratory rate

Figure 30 shows the resulting respiratory flow rates in the Fontan IVC (A), resulting IVC flow volumes (B), resulting pulsatility index (C), and resulting percent IVC retrograde flow(D) with increased respiratory rates. Figure 45 shows the corresponding flow rate waveforms (A), the pressure waveforms in the IVC (B), and the pressure margins (C) generated by increased respiratory rates.

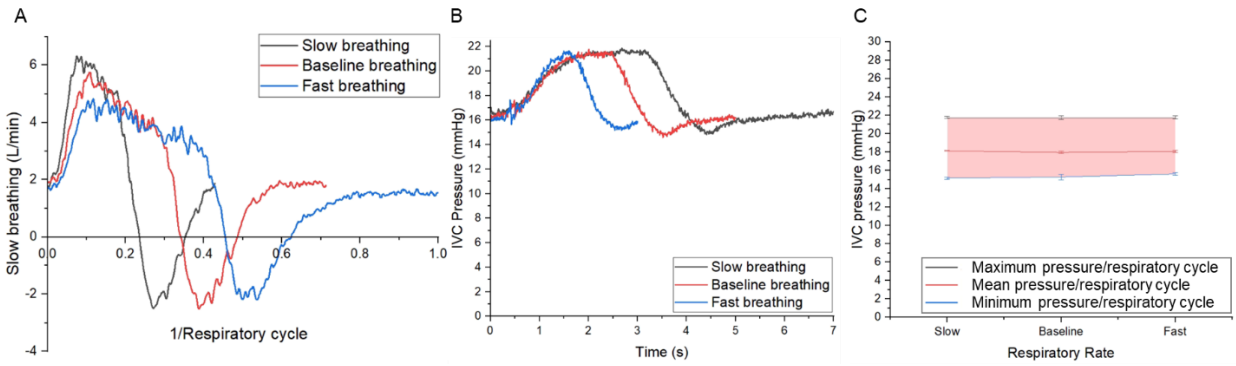

Figure 45 : Resulting flow rate waveforms (A) pressure waveforms (B) and pressure margins (C) in the Fontan IVC with increasing respiratory rates on the biomimetic bench top model.

During greater respiratory rates we can see the peak forward flow rates increase slightly during inspiration and the peak retrograde flow rates remaining constant during expiration as shown in Figure 45A. However, the overall time during which IVC flow is positive decreases more than the time during which flow is negative leading to a reduced forward flow volume compared to retrograde flow volumes and thus an increase percent retrograde IVC flow. An increase in respiratory rates did not increase the peak, mean or minimum IVC pressure as seen in Figure 45B and Figure 45C. The time at peak pressure in the IVC does decrease with higher respiratory rates as shown in Figure 45B.

Impact of baseline IVC flow

Figure 31 shows the resulting respiratory flow rates in the Fontan IVC (A), resulting IVC flow volumes (B), resulting pulsatility index (C), and resulting percent IVC retrograde flow(D) with increased baseline IVC flow. Figure 46 shows the corresponding flow rate waveforms (A), the pressure waveforms in the IVC (B), and the pressure margins (C) generated by increased baseline IVC flow.

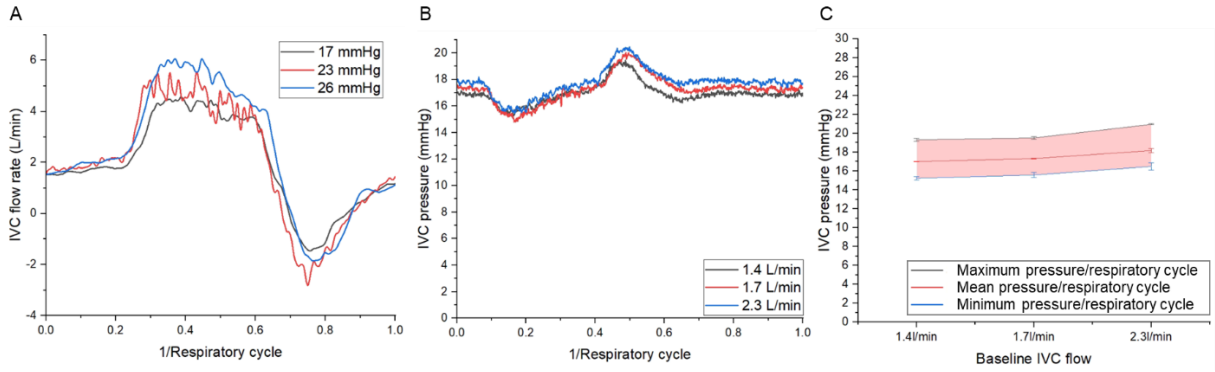

Figure 46 : Resulting flow rate waveforms (A) pressure waveforms (B) and pressure margins (C) in the Fontan IVC with baseline IVC flow on the biomimetic bench top model.

With greater IVC baseline flow rates the flow waveform is shifted upward towards higher flow rates as shown in Figure 46A. This means that the positive area under the graph increases while the negative area decreases. This illustrates the increase in forward flow volumes during inspiration, the decrease in reverse flow volume during expiration, and an increase a total decrease of percent retrograde flow in the IVC. The increase of baseline IVC flow slightly shifts the pressure curves upwards as seen in Figure 46B, similarly to the flow rate curves shown in Figure 46A. Figure 46C shows that the mean pressure does not shift significantly.

Impact of baseline IVC pressure

Figure 47 shows the resulting parameters of Fontan IVC hemodynamics when the baseline IVC pressure is increased from 17 mmHg to 23 mmHg and 26 mmHg. With increased baseline pressures the resulting flow rate waveforms are shown in (A), the pressure waveforms in the IVC are shown in (B), the pressure margins are shown in (C), forward flow rates during inspiration and reverse flow rates during expiration are shown in (D), forward flow volumes during inspiration and reverse flow volumes during expiration are shown in (E), and resulting percent retrograde flow in the IVC per respiratory cycle are shown in (F).

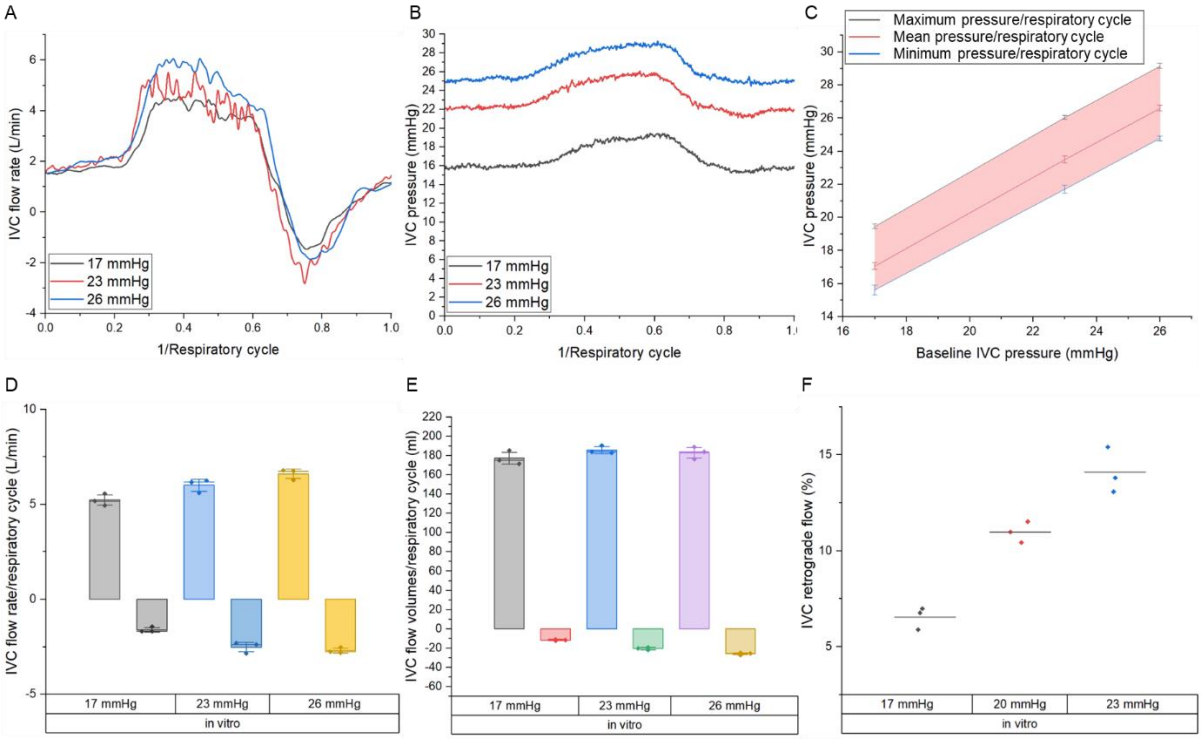

Figure 47 : Effects of increasing baseline IVC pressures on the Fontan IVC hemodynamics and flow patterns on the biomimetic bench top model. Resulting flow rate waveforms (A), pressure waveforms (B), pressure margins (C), forward and reverse flow rates during one respiratory cycle (D), forward and reverse flow volumes during one respiratory cycle (E), and resulting percent retrograde flow during one respiratory cycle (F).

With greater IVC baseline pressure the amplitude of the flow waveforms is increased as shown in Figure 47A. This is reflected by the increased peak forward flow rates during inspiration and increased peak retrograde flow rates during expiration shown in Figure 47D. The forward flow volumes are increases less compared to the retrograde flow volumes in each respiratory cycle as shown in Figure 47E. This results in a percent increase of retrograde flow in IVC with greater baseline IVC pressures as shown in Figure 47F. The amplitude of the IVC pressure curves do not change with increased baseline pressures as shown in Figure 47B. Instead, the pressure

curves are shifted up to higher pressures due to the increased baseline pressure. This corresponds to the linear increase of the pressure range shown in Figure 47C.

Impact of baseline vascular compliance

Figure 48 shows the resulting parameters of Fontan IVC hemodynamics when the baseline IVC pressure is increased from 17 mmHg to 23 mmHg and 26 mmHg. With increased baseline pressures the resulting flow rate waveforms are shown in (A), the pressure waveforms in the IVC are shown in (B), the pressure margins are shown in (C), forward flow rates during inspiration and reverse flow rates during expiration are shown in (D), forward flow volumes during inspiration and reverse flow volumes during expiration are shown in (E), and resulting percent retrograde flow in the IVC per respiratory cycle are shown in (F).

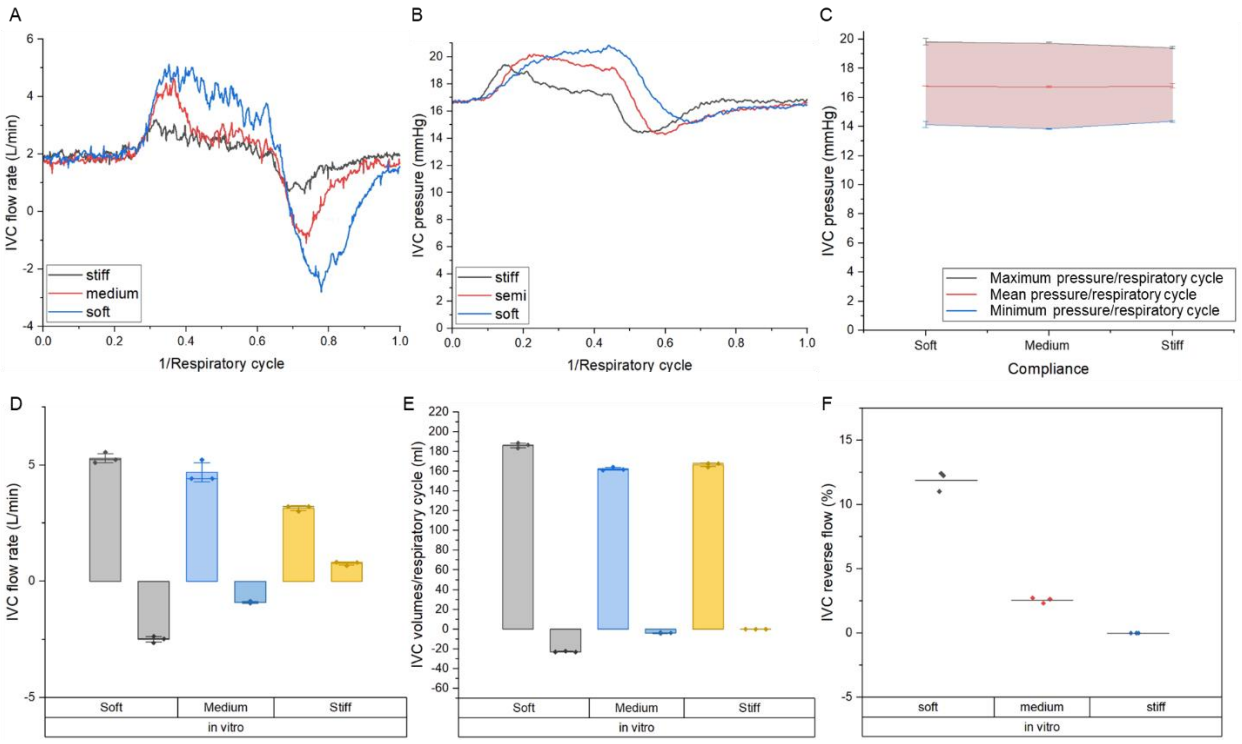

Figure 48 : Effects of simulated increased pulmonary and abdominal vascular compliance on Fontan IVC hemodynamics and flow patterns on the biomimetic bench top model. Resulting flow rate waveforms (A), pressure waveforms (B), pressure margins (C), forward and reverse flow rates during one respiratory cycle (D), forward and reverse flow volumes during one respiratory cycle (E), and resulting percent retrograde flow during one respiratory cycle (F).

With greater compliance of the simulated vascular beds, the amplitude of the flow waveforms increases as shown in Figure 48A. This is reflected by the increased peak forward flow rates during inspiration and increased peak retrograde flow rates during expiration shown in Figure 48D. This also means that less flow volumes is pushed forward during inspiration and also less

flow volume is pushed backwards in the IVC during expiration as shown in Figure 48E. When the vascular beds are stiff and not compliant no retrograde flow is observed at all as shown in Figure 48F and indicated by positive peak flow rates during expiration in Figure 48D and no negative flow volume during expiration in Figure 48E. The amplitude of the pressure curves are not increasing with increased vascular compliance as shown in Figure 48B. Consequently, the peak, mean, and minimum IVC pressure also did not change considerably as shown in Figure 48C.

3.3.2 *In vivo* 4D MRI study the effect of breathing mechanics on IVC flow dynamics

Individual results for two representative patients

Figure 49 shows representative results of two participants in the respiratory real-time MRI study described in section 3.2.2: Patient 1 (A-D) and patient 2 (E-H). Patients 1(/2) was able to increase the chest wall motion which we use as surrogate measure for respiratory effort between shallow, baseline, and heavy breathing significantly while the percent retrograde flow simultaneously increased accordingly as shown in Figure 49A(/E). Concurrently the patients kept the respiratory rate constant as shown in Figure 49B(/F). Subsequently, patient 1 (/2) the respiratory rate leading to the increase in percent retrograde flow as shown in Figure 49C(/G) while the respiratory efforts did not increase significantly (Figure 49D(/H)). Both examples show that patients were able to increase either respiratory effort or respiratory rate independently of each other and percent retrograde flow increased in either case. This comprises the first work that shows how respiratory effort as well as respiratory rate independently increase retrograde flow in the Fontan IVC. Figure 49 also shows how the same respiratory rate was achievable by both individuals, but the baseline retrograde flow and the increase in retrograde flow with greater respiratory rates vary greatly. The exemplary results show that chest wall motion while the participants subjectively increase the respiratory efforts varies between individuals. This

emphasizes the heterogeneous nature of physiological parameters in the Fontan patient population resulting in a wide variety of venous flow patterns.

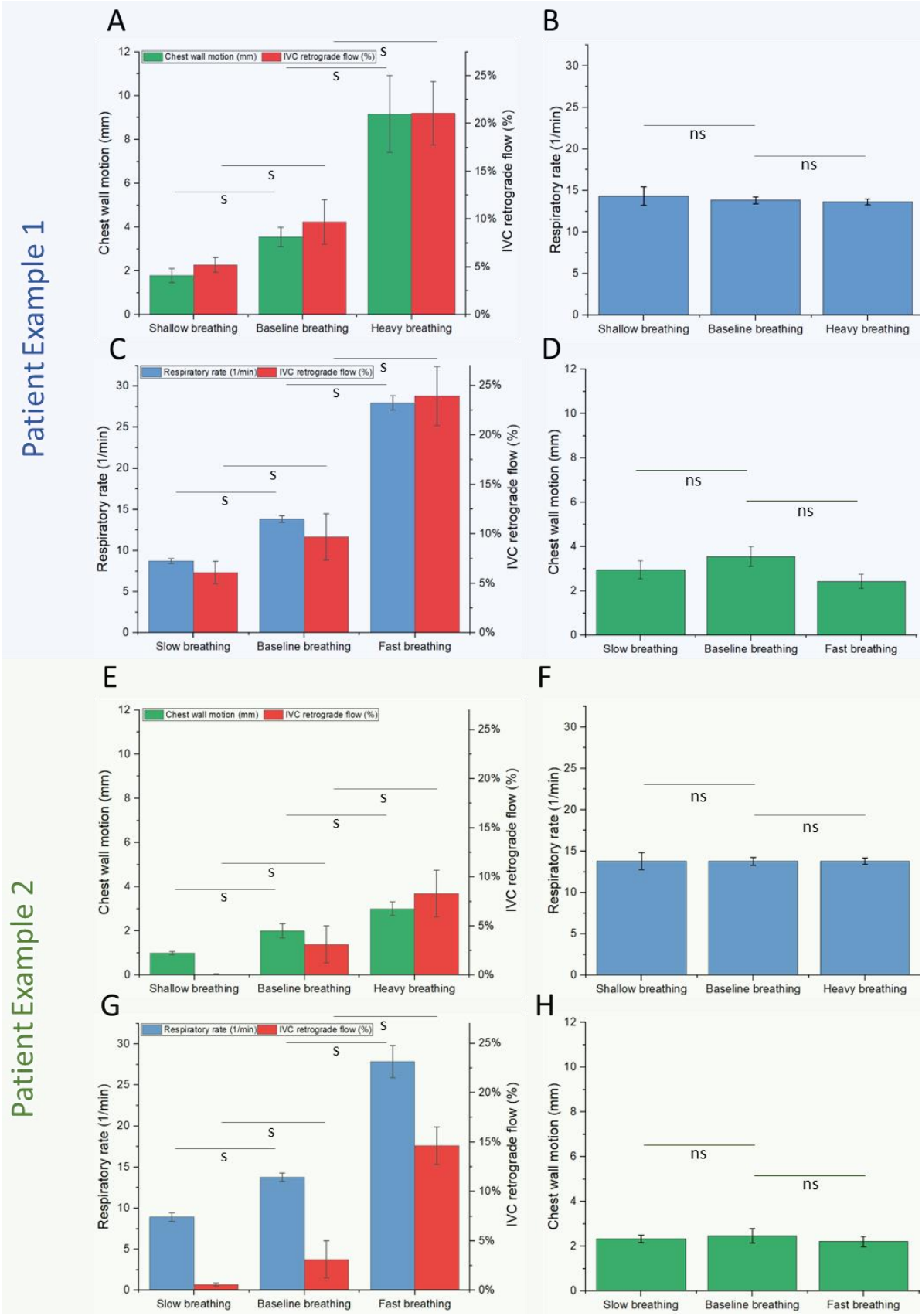

Figure 49 : Examples of respiratory efforts and rates with the corresponding effects on percent retrograde flow in the IVC for two patients: Patient 1 (A-D) and patient 2 (E-H). Patients were able to increase the respiratory effort resulting in increased percent retrograde flow while (A, E) while the respiratory rate was kept constant (B, F). Patients were also able to increase their respiratory rate leading to an increase of percent retrograde flow (C, G), while they kept the respiratory effort constant (D, H).

Effect of change in respiratory patterns to flow rates in the Fontan IVC

Figure 50A and Figure 50B show the normalized values for the peak forward and retrograde flow rates per respiratory cycle during inspiration and expiration, respectively. The dotted line indicates the mean flow that was used to normalize the data. Figure 50A shows the resulting peak flow rates during the clinical study part to increase respiratory efforts as described in section 3.2.2. Below, Figure 50C corresponds to the data in Figure 50A and indicates the number of eligible patients who showed increased forward and reverse flow during inspiration and expiration, respectively. Table 5 and Table 5 summarize the values for increasing respiratory efforts and increasing respiratory rates, respectively. Patient results were rendered not eligible if the participant failed to increase the respiratory effort (chest wall motion) significantly and thus the forward or retrograde flow did not increase. Those data points were not considered in the results. The changes of respiratory efforts were analyzed in Figure 50C for three steps: Shallow breathing to baseline breathing, baseline breathing to heavy breathing, and shallow breathing to heavy breathing. Figure 50A shows that the peak forward flow rates increase with greater respiratory efforts during inspiration and the peak retrograde flow rates also increase with greater respiratory efforts during expiration. For increased respiratory effort from shallow to baseline breathing data points of three participants were not eligible and all 17 out of 17 remaining participants showed increased peak forward flow rates during inspiration. During expiration three participants were not eligible, one participant did not increase the peak retrograde flow rates and 16 showed an increase in peak retrograde flow rates. For increased respiratory effort from baseline to heavy breathing data points of two participants were not eligible. Of the remaining participants one did not show increased forward flow rates and 16 showed increased peak forward flow rates during inspiration. During expiration one participant was not eligible, one participant did not increase the peak retrograde flow rates and 18 showed an increase in peak retrograde flow rates. For increased respiratory effort from shallow to heavy breathing data points of one participant was not eligible. Of the remaining participants one did not show increased forward flow rates and 18 showed increased peak forward flow rates during inspiration. During expiration one participant was not eligible, and all remaining 19 participants showed an increase in peak retrograde flow rates.

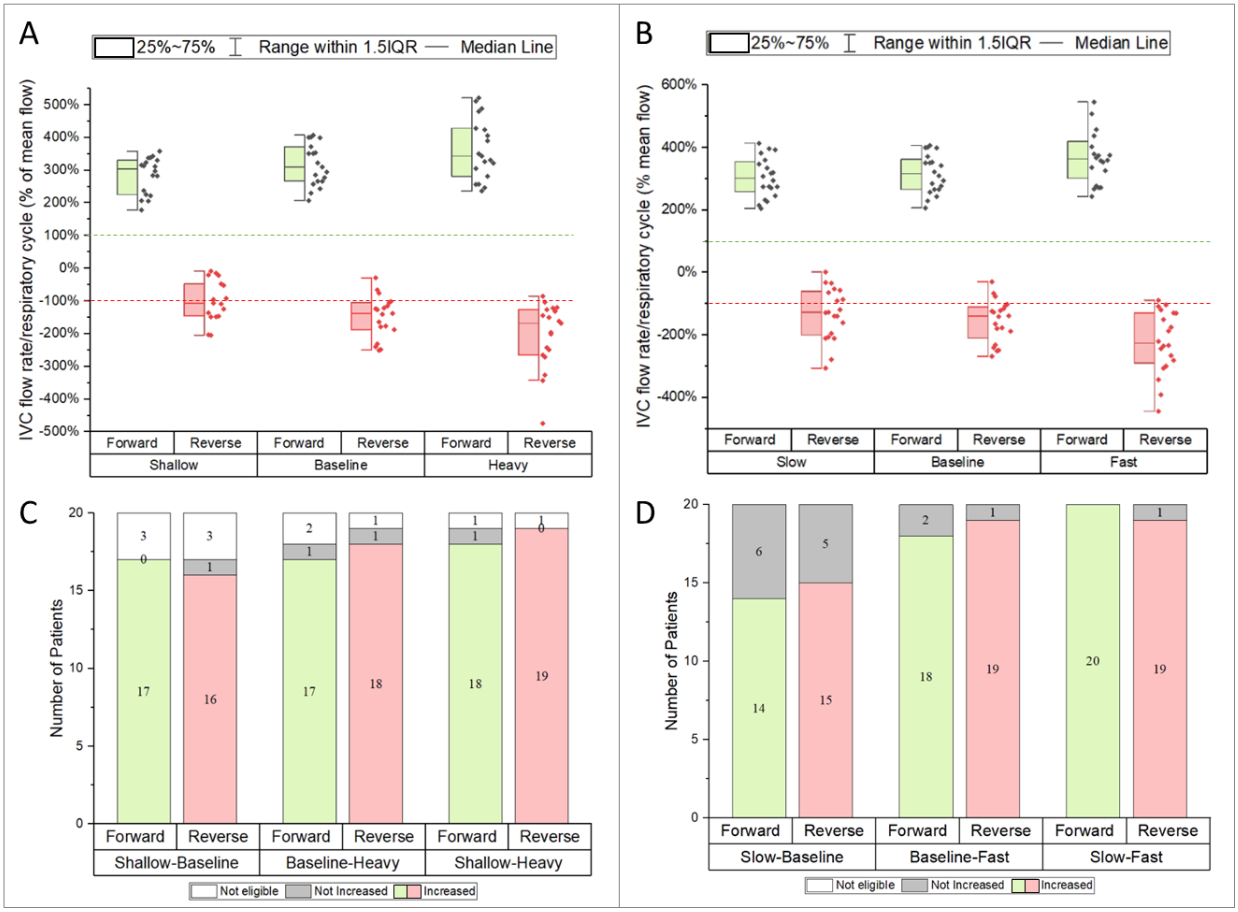

Figure 50 : Normalized flow rates from 20 patient MRI study. Forward and reverse flow in the Fontan IVC is shown normalized to average baseline (dotted lines) for increasing respiratory efforts (A) and respiratory rates (B). Number of eligible patients who showed increased forward and reverse flow during inspiration and expiration, respectively, with increasing respiratory efforts (C) and increasing respiratory rates (D).

Table 4

Breathing pattern	Flow Rate	Mean (%)	Standard Deviation (%)	Minimum (%)	Median (%)	Maximum (%)
Shallow breathing	Forward flow rate	284.18%	56.37%	178.53%	304.60%	358.31%
Shallow breathing	Reverse flow rate	-98.55%	63.08%	-204.46%	-106.34%	-8.24%
Baseline breathing	Forward flow rate	315.83%	63.47%	207.27%	310.20%	407.24%
Baseline breathing	Reverse flow rate	-148.13%	63.47%	-250.31%	-137.68%	-28.88%
Heavy breathing	Forward flow rate	363.58%	92.37%	236.82%	343.66%	521.46%
Heavy breathing	Reverse flow rate	-204.02%	99.49%	-474.10%	-167.54%	-85.21%

Table 5

Breathing pattern	Flow Rate	Mean (%)	Standard Deviation (%)	Minimum (%)	Median (%)	Maximum (%)
Slow breathing	Forward flow rate	305.05%	63.62%	205.64%	301.90%	414.13%
Slow breathing	Reverse flow rate	-131.06%	83.53%	-305.40%	-126.97%	2.41%
Baseline breathing	Forward flow rate	317.18%	62.07%	207.27%	316.49%	407.24%
Baseline breathing	Reverse flow rate	-154.10%	67.31%	-267.66%	-138.97%	-28.88%
Fast breathing	Forward flow rate	377.11%	97.65%	244.17%	363.92%	616.87%
Fast breathing	Reverse flow rate	-222.05%	100.68%	-443.49%	-226.12%	-88.07%

Figure 50B shows the resulting peak flow rates during the clinical study part to increase respiratory rates as described in section 3.2.2. Below, Figure 50D corresponds to the data in Figure 50B and indicates the number of eligible patients who showed increased forward and reverse flow rates during inspiration and expiration, respectively. Patient results were rendered not eligible if the participant failed to increase the respiratory rate significantly and the forward or retrograde flow did not increase. Those data points were not considered in the results. The changes of respiratory rates were analyzed in Figure 50D for three steps: Slow breathing (RR=9 min-1) to baseline breathing (RR=14 min-1), baseline breathing (RR=14 min-1) to fast breathing (RR=28 min-1), and slow breathing (RR=9 min-1) to fast breathing (RR=28 min-1). Figure 50B shows that the peak forward flow rates increase with greater respiratory rates during inspiration and the peak retrograde flow decreases with greater respiratory rates during expiration. For increased respiratory rates from slow to baseline breathing all patients were eligible, six did not increase peak forward flow rates and 14 showed increased peak forward flow rates during inspiration. During expiration all participants were eligible, five participants did not show increased peak retrograde flow rates and 15 showed increased peak retrograde flow rates. For increased respiratory rates from baseline to fast breathing all patients were eligible, six did not increase peak forward flow rates and 14 showed increased peak forward flow rates during inspiration. During expiration all participants were eligible, five participants did not show increased peak retrograde flow rates and 15 showed increased peak retrograde flow rates. For increased respiratory rates from slow to fast breathing all patients were eligible, and all showed increased peak forward flow rates during inspiration. During expiration all participants were eligible, one participant did not show increased peak retrograde flow rates and 19 showed increased peak retrograde flow rates.

Figure 51 shows the absolute values for the peak forward and peak retrograde flow rates in the Fontan IVC during inspiration, and expiration, as well as the resulting mean flow rates. Table 6 summarizes those values. All flow rates are normalized to the body surface area of each of the 20 participants. Figure 51A shows the flow rates during increasing respiratory efforts and Figure 51B shows the resulting flow rates during increasing respiratory rates.

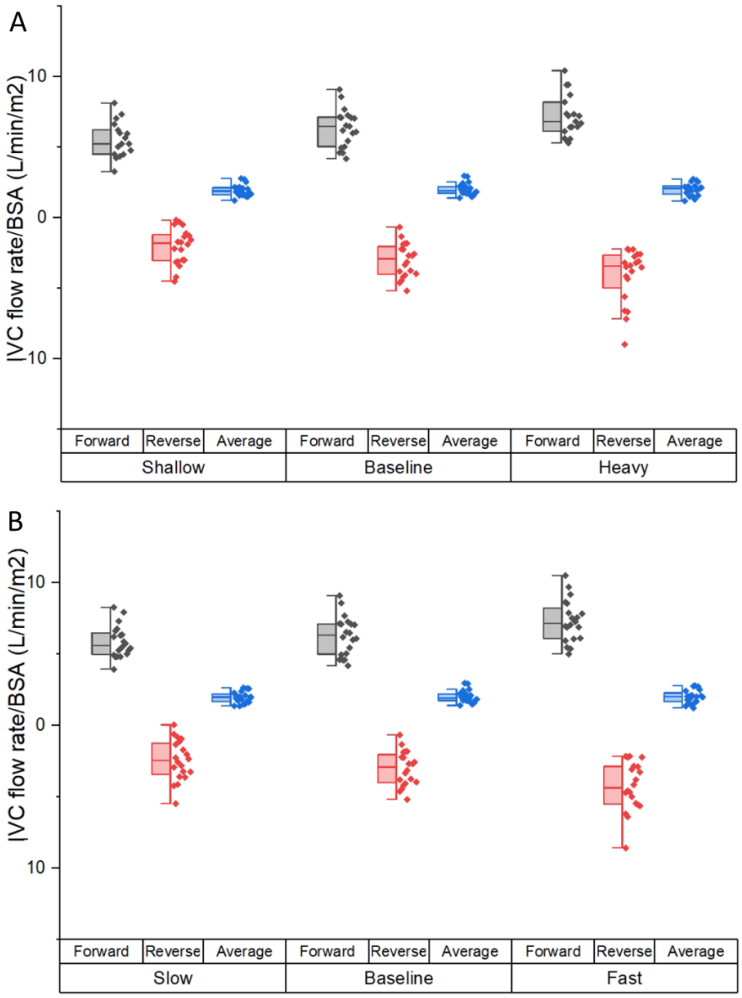

Figure 51 : Flow rates summarized from 20 patient MRI study. Absolute peak forward flow rates during inspiration, peak retrograde flow rates during expiration, and resulting mean flow rates per body surface area with increasing respiratory efforts (A), and increasing respiratory rates (B).

Table 6

Breathing pattern	Flow Rate	Mean (l/min)	Standard Deviation (l/min)	Minimum (l/min)	Median (l/min)	Maximum (l/min)
Shallow breathing	Forward flow volume	149.56	26.49	115.77	136.75	202.58
Shallow breathing	Reverse flow volume	-9.54	9.62	-39.29	-6.96	-0.06
Shallow breathing	Total flow volume	140.02	28.67	86.24	136.28	191.96
Baseline breathing	Forward flow volume	162.03	32.68	121.04	151.26	236.64
Baseline breathing	Reverse flow volume	-16.80	10.14	-35.46	-15.01	-0.67
Baseline breathing	Total flow volume	145.24	31.86	103.40	136.22	218.03
Heavy breathing	Forward flow volume	175.49	38.92	117.53	170.55	270.20
Heavy breathing	Reverse flow volume	-30.19	17.99	-72.45	-23.40	-11.10
Heavy breathing	Total flow volume	145.30	32.07	85.88	150.96	197.75

Effect of change in respiratory patterns to the flow pulsatility in the Fontan IVC

Figure 52 shows the normalized pulsatility index relative to baseline breathing in of the IVC flow in 20 patients with increasing respiratory efforts (Figure 52A) and increasing respiratory rates (Figure 52B). The analysis of the normalized values and the measured values are summarized in Table 7 and Table 8 for increasing respiratory efforts and increasing respiratory rates,

respectively. Figure 52A shows that the pulsatility index increases with greater respiratory efforts. This is coincident with the increased forward and reverse flow rates observed during higher respiratory efforts. Figure 52B shows that the pulsatility index also increases with greater respiratory rates which is coincident with the increased forward and reverse flow rates observed during higher respiratory rates.

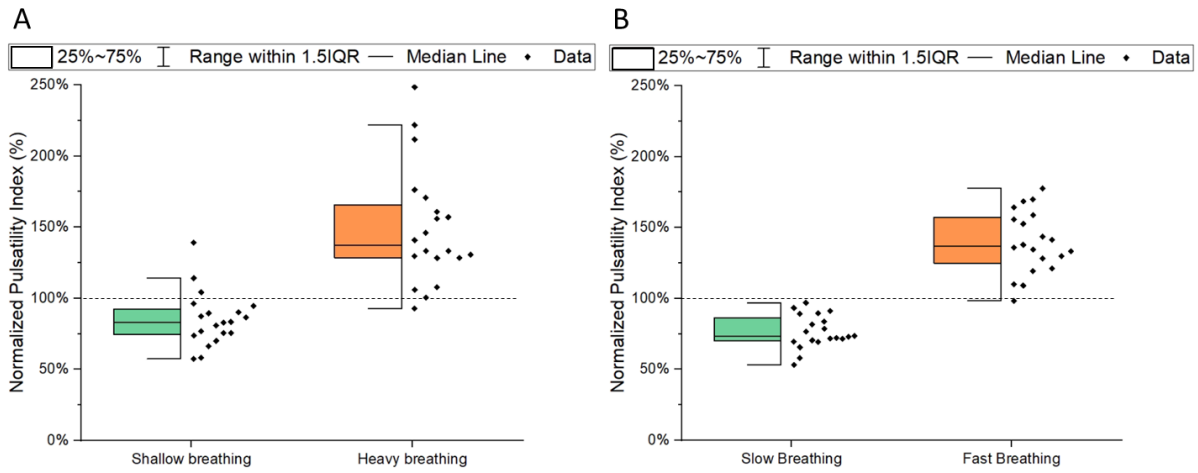

Figure 52 : Resulting pulsatility index of Fontan IVC flow in 20 patients normalized to baseline breathing. Increase of the pulsatility index with increased respiratory effort (A) and inspiratory rate (B).

Table 7

Breathing pattern	Mean	Standard Deviation	Minimum	Median	Maximum
Shallow breathing	85.22%	19.00%	57.49%	83.36%	139.23%
Heavy breathing	149.05%	40.89%	92.81%	137.15%	248.54%
Slow breathing	76.53%	11.60%	53.19%	73.45%	97.05%
Fast breathing	139.54%	21.99%	98.30%	137.02%	177.72%

Table 8

Breathing pattern	Mean	Standard Deviation	Minimum	Median	Maximum
Shallow breathing	4.05241	1.535	1.70282	4.03433	8.61881
Baseline breathing	4.71282	1.24155	2.3615	4.43982	6.51719
Heavy breathing	5.71297	1.73475	3.3196	5.6066	9.54038
Slow breathing	4.36109	1.40588	2.13286	4.24088	6.88417
Baseline breathing	4.71282	1.24155	2.3615	4.43982	6.51719
Fast breathing	5.99159	1.95676	3.32248	5.93184	10.60353

Effect of change in respiratory patterns to flow volumes in the Fontan IVC

Figure 53A and Figure 53B show the normalized values for the forward and retrograde flow volumes per respiratory cycle during inspiration and expiration, respectively. The dotted lines

indicate the mean flow volume used to normalize the data. Figure 53A shows the resulting flow volumes during the clinical study part to increase respiratory efforts as described in section 3.2.2. Below, Figure 53C corresponds to the data in Figure 53A and indicates the number of eligible patients who showed increased forward and reverse flow during inspiration and expiration, respectively. Patient results were rendered not eligible if the participant failed to increase the respiratory effort (chest wall motion) significantly and thus the forward or retrograde flow volumes did not increase. Those data points were not considered in the results. The changes of respiratory efforts were analyzed in Figure 53C for three steps: Shallow breathing to baseline breathing, baseline breathing to heavy breathing, and shallow breathing to heavy breathing. Table 9 and Table 10 summarize the values for increasing respiratory efforts and increasing respiratory volumes, respectively.

Figure 53A shows that the forward flow volumes increase with greater respiratory efforts during inspiration and the retrograde flow volumes also increase with greater respiratory efforts during expiration. Figure 53C shows that for increased respiratory effort from shallow to baseline breathing data points of three participants were not eligible, two did not increase forward volumes and 17 participants showed increased forward flow volumes during inspiration. During expiration three participants were not eligible and all the remaining 17 patients showed an increase in retrograde flow volumes. For increased respiratory effort from baseline to heavy breathing data points of two participants were not eligible. Of the remaining participants three did not show increased forward flow volumes and 15 showed increased forward flow volumes during inspiration. During expiration one participant was not eligible, all remaining 18 participants showed an increase in retrograde flow volumes. For increased respiratory effort from shallow to heavy breathing data points of two participant were not eligible. Of the remaining participants two did not show increased forward flow volumes and 16 showed increased forward flow volumes during inspiration. During expiration one participant was not eligible, and all remaining 19 participants showed an increase in retrograde flow volumes.

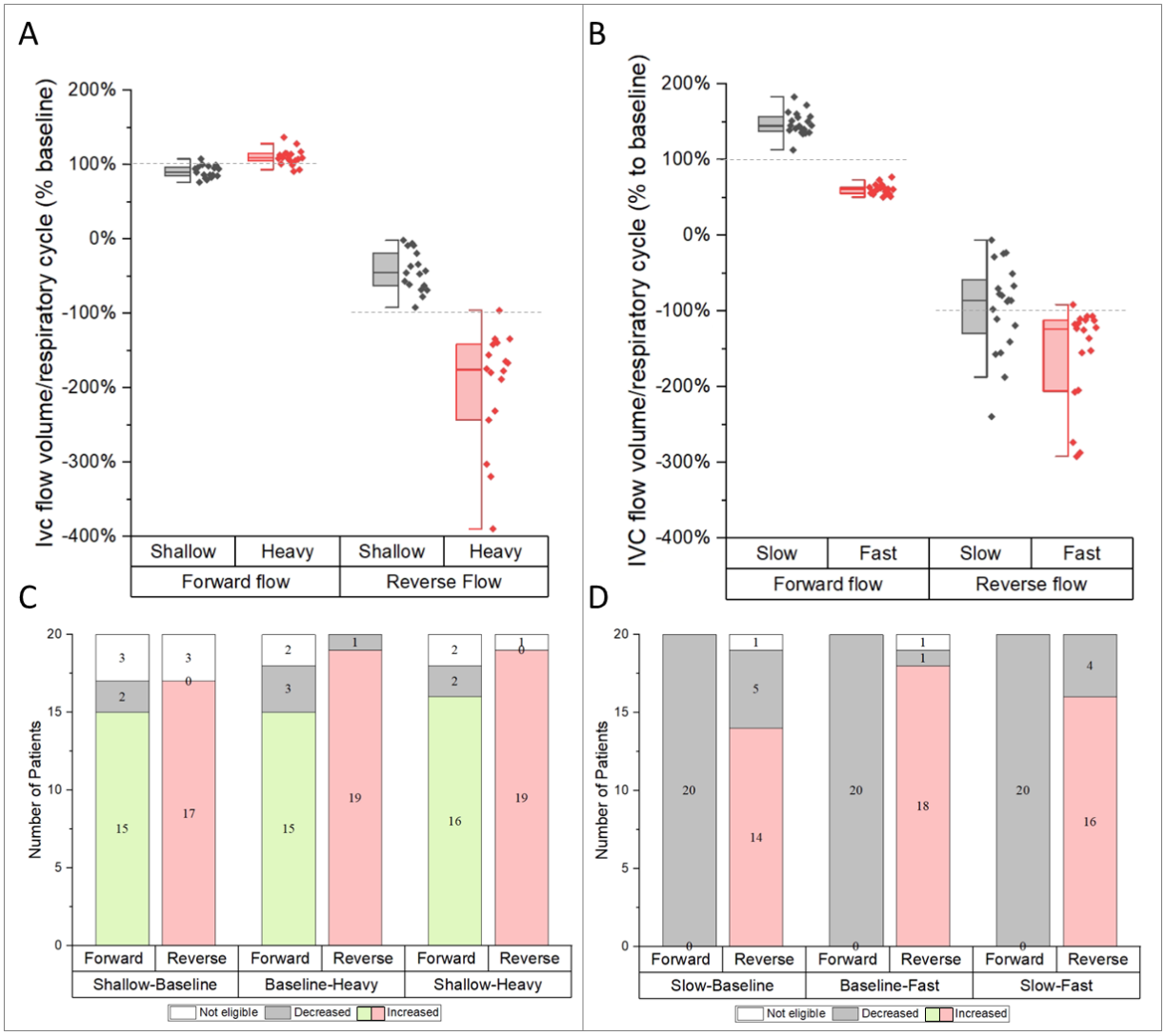

Figure 53 : Normalized flow volumes summarized from 20 patient MRI study. Forward and reverse flow volumes in the Fontan IVC are shown normalized to baseline breathing (dotted lines) for increasing respiratory efforts (A) and respiratory rates (B). Number of eligible patients who showed increased forward and reverse flow volumes during inspiration and expiration, respectively, with increasing respiratory efforts (C) and increasing respiratory rates (D).

Table 9

Breathing pattern	Flow volume	Mean (%)	Standard Deviation (%)	Minimum (%)	Median (%)	Maximum (%)
Shallow breathing	Reverse flow volume	-43.10%	27.31%	-91.68%	-45.13%	-1.39%
Shallow breathing	Forward flow volume	90.79%	8.51%	76.61%	89.81%	107.93%
Heavy breathing	Reverse flow volume	-297.18%	435.22%	-2014.92%	-175.64%	-95.81%
Heavy breathing	Forward flow volume	110.07%	11.02%	91.16%	108.94%	137.08%

Table 10

Breathing pattern	Flow volume	Mean (%)	Standard Deviation (%)	Minimum (%)	Median (%)	Maximum (%)
Slow breathing	Reverse flow volume	-94.41%	59.14%	-239.23%	-85.62%	-5.92%
Slow breathing	Forward flow volume	147.33%	15.31%	112.91%	144.90%	183.08%
Fast breathing	Reverse flow volume	-206.08%	236.61%	-1174.72%	-123.83%	-91.27%
Fast breathing	Forward flow volume	60.72%	6.79%	50.53%	61.19%	77.19%

Figure 53B shows the resulting flow volumes during the clinical study part to increase respiratory rates as described in section 3.2.2. Below, Figure 53D corresponds to the data in Figure 53B and indicates the number of eligible patients who showed increased forward and reverse flow volumes during inspiration and expiration, respectively. Patient results were rendered not eligible if the participant failed to increase the respiratory rate significantly and the forward or retrograde flow did not increase. Those data points were not considered in the results. The changes of respiratory volumes were analyzed in Figure 53D for three steps: Slow breathing (RR=9 min^{-1}) to baseline breathing (RR=14 min^{-1}), baseline breathing (RR=14 min^{-1}) to fast breathing (RR=28 min^{-1}), and slow breathing (RR=9 min^{-1}) to fast breathing (RR=28 min^{-1}). Figure 53B shows that the forward flow volumes decrease with greater respiratory rates during inspiration and the retrograde flow increases slightly with greater respiratory volumes during expiration. For increased respiratory rates from slow to baseline to fast all patients were eligible, and all patients showed decreased forward flow volumes during inspiration. For increased respiratory rates from slow to baseline breathing one participant was not eligible, five participants did not show increased retrograde flow volumes and 14 showed increased retrograde flow volumes. For increased respiratory rates from baseline to fast breathing one patient was not eligible, one did not increase forward flow volumes and 18 showed increased retrograde flow volumes during expiration. For increased respiratory rates from slow to fast breathing all patients were eligible, four did not show increased retrograde flow volumes, and 16 showed increased retrograde flow volumes during inspiration.

Figure 54 shows the absolute values for the forward and retrograde flow volumes in the Fontan IVC during inspiration, and expiration, as well as the resulting mean flow volumes per respiratory cycle. Table 11 and Table 12 summarize the values for increasing respiratory effort and increasing respiratory rate, respectively. All flow volumes are normalized to the body surface area of each of the 20 participants. Figure 54A shows the flow volumes during increasing respiratory efforts and Figure 54B shows the resulting flow volumes during increasing respiratory rates.

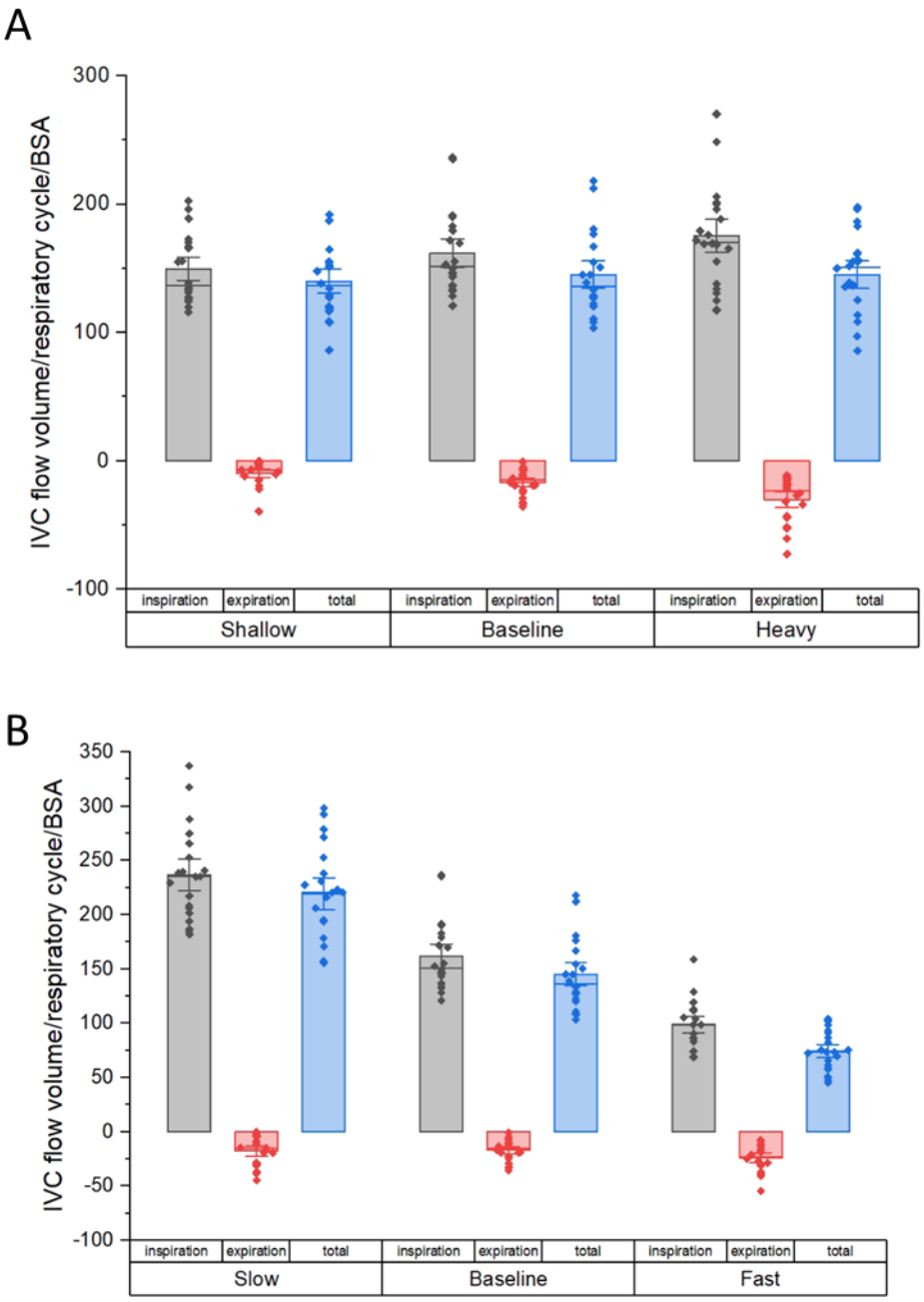

Figure 54 : Flow volumes summarized from 20 patient MRI study. Absolute total forward flow volumes during inspiration, total retrograde flow volumes during expiration, and resulting total flow volumes per body surface area with increasing respiratory efforts (A), and increasing respiratory rates (B).

Table 11

Breathing pattern	Flow volume	Mean (ml)	Standard Deviation (ml)	Minimum (ml)	Median (ml)	Maximum (ml)
Shallow breathing	Reverse flow volume	-9.54114	9.62097	-39.28546	-6.96128	-0.06472
Shallow breathing	Forward flow volume	149.55756	26.48791	115.77473	136.75059	202.58059
Shallow breathing	Total flow volume	140.01642	28.66505	86.23635	136.28033	191.96385
Baseline breathing	Reverse flow volume	-16.79678	10.14004	-35.46204	-15.01266	-0.67408
Baseline breathing	Forward flow volume	162.03461	32.68073	121.04259	151.26212	236.64185
Baseline breathing	Total flow volume	145.23783	31.85728	103.4014	136.21828	218.03277
Heavy breathing	Reverse flow volume	-30.19353	17.98758	-72.4455	-23.39606	-11.10066
Heavy breathing	Forward flow volume	175.49104	38.92284	117.52666	170.55182	270.19651
Heavy breathing	Total flow volume	145.2975	32.07295	85.87655	150.95644	197.75101

Table 12

Breathing pattern	Flow volume	Mean (ml)	Standard Deviation (ml)	Minimum (ml)	Median (ml)	Maximum (ml)
Slow breathing	Reverse flow volume	-17.58241	13.98591	-44.5177	-14.79733	-0.03993
Slow breathing	Forward flow volume	236.84497	43.12421	181.84725	235.41549	337.26634
Slow breathing	Total flow volume	219.26256	44.09139	155.78015	220.75806	298.28082
Baseline breathing	Reverse flow volume	-16.79678	10.14004	-35.46204	-15.01266	-0.67408
Baseline breathing	Forward flow volume	162.03461	32.68073	121.04259	151.26212	236.64185
Baseline breathing	Total flow volume	145.23783	31.85728	103.4014	136.21828	218.03277
Fast breathing	Reverse flow volume	-24.13801	13.05213	-54.31381	-23.0032	-7.59146
Fast breathing	Forward flow volume	98.49343	22.85038	68.80784	98.83955	158.81065
Fast breathing	Total flow volume	74.35542	17.83487	45.39175	73.58639	104.49684

Figure 55 shows exemplary chest wall motion (A – C) and IVC flow rates (D – F) of a Fontan patient who participated in the clinical study. We see that with increasing respiratory rates the end-expiratory pause marked with t1 and the end inspiratory pause marked with t2 are shortened. Simultaneously we see how the time during which the IVC flow is positive while the time during which the negative IVC occurs remains constant.

Figure 55 shows representative data of a participating Fontan patient's chest wall motion and resulting IVC flow curve during slow (RR=9min^{-1}), baseline (RR=14min^{-1}), and fast (RR=28min^{-1}) breathing. We can observe a shorter end-expiratory (t1) and end-inspiratory (t2) pause as the respiratory rate is increased. The resulting IVC flow waveforms show a large decrease in the time during which forward flow is positive (t3) during one respiratory cycle. This is an illustration of the effect how greater respiratory rates increase the percent retrograde flow

in the IVC which has been shown for the entire study population in Figure 53, on the biomimetic bench top simulator in section 2.3.1, and computational model in section 2.3.3 as well.

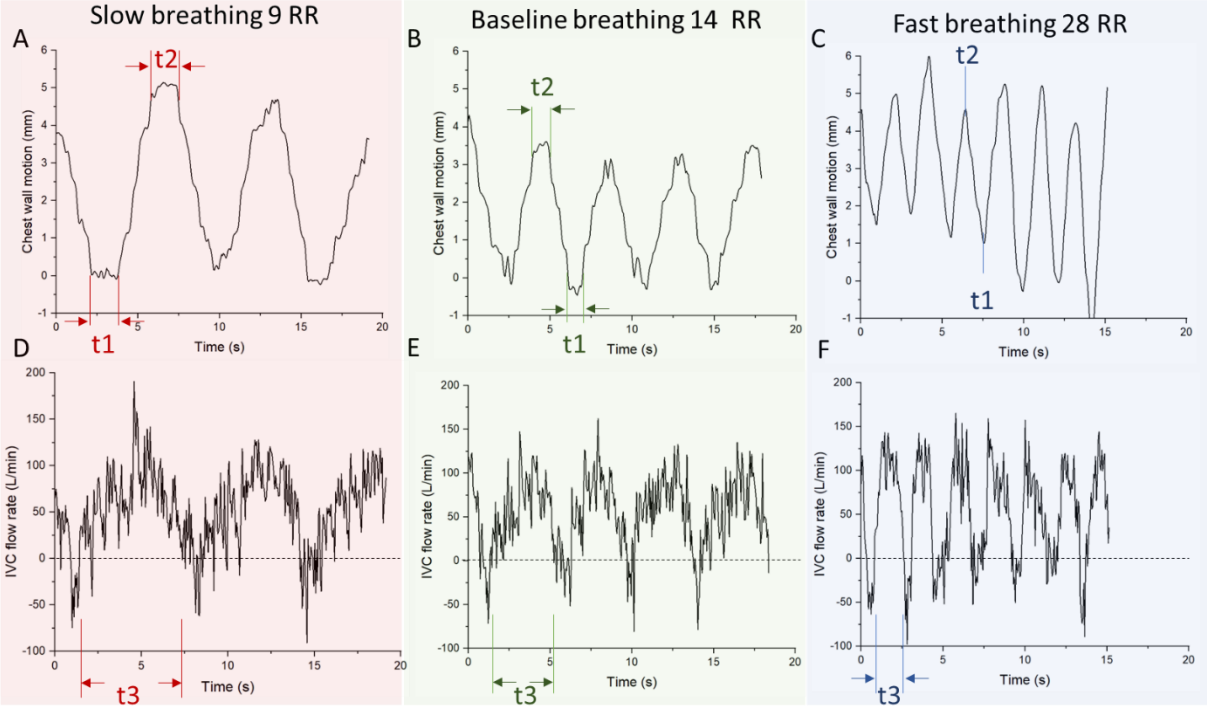

Figure 55 : Example of variations of respiratory rates during patient breathing exercise and resulting IVC flow pattern recorded by real time MR imaging. Patient data recorded during the clinical study shows the chest wall motion (A-C) and the corresponding blood flow in the IVC (D-F) during slow (A,D), baseline (B,E), and fast (C,F) breathing rhythm. During each exercise the end expiratory pause, end inspiratory paus, and the resulting time of net positive flow in the IVC is shown as t1, t2, and t3 respectively.

Effect of change in respiratory patterns to retrograde flow in the Fontan IVC

Figure 56A and Figure 56B show the resulting percent retrograde flow in the Fontan IVC during one respiratory cycle for 20 patients normalized to baseline breathing (dotted line) during increased respiratory efforts and increasing respiratory rates, respectively. This data is summarized in Table 13. Figure 56C and Figure 56D show the corresponding results of percent retrograde flow which are not normalized. This data is summarized in Table 14.

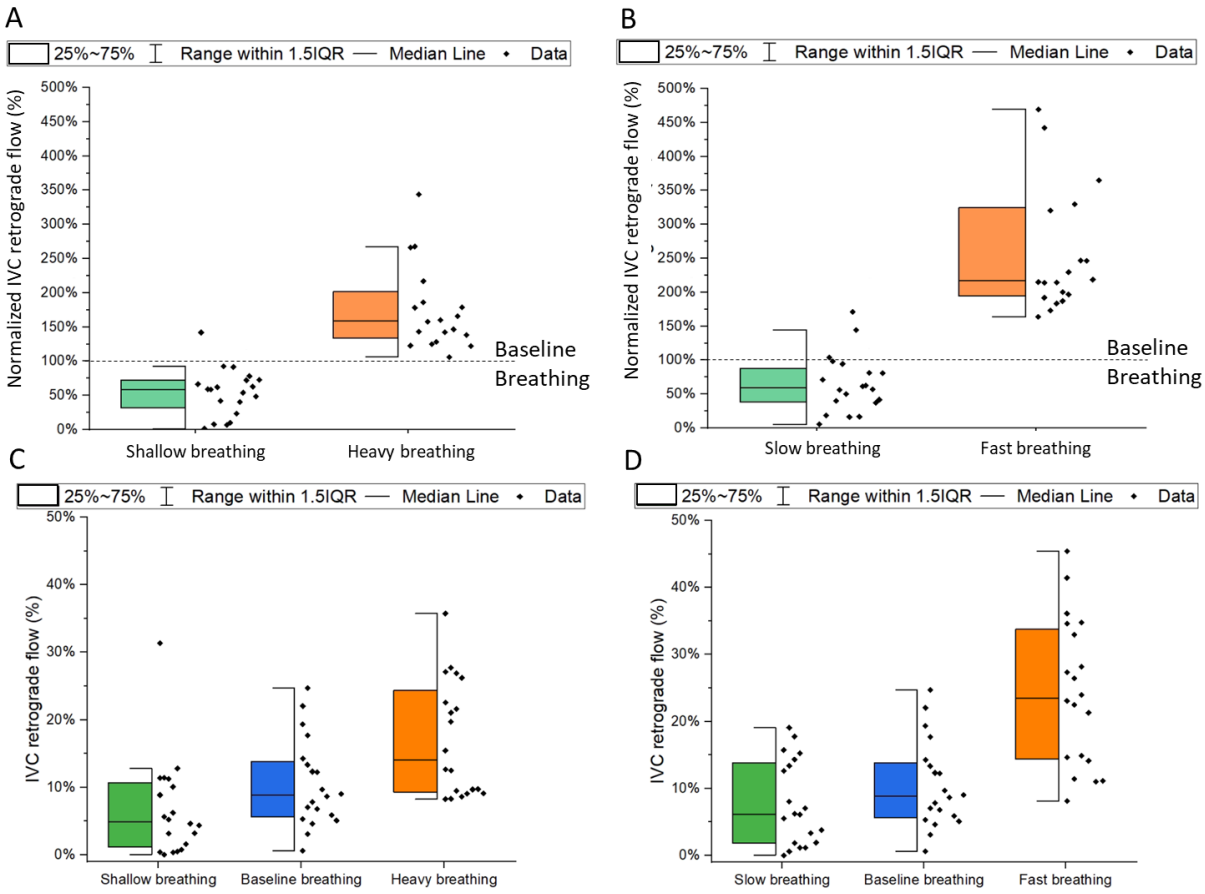

Figure 56 : Retrograde flow summarized from 20 patient MRI study. Percent retrograde flow in the Fontan IVC are shown normalized to baseline breathing (dotted line) for increasing respiratory efforts (A) and respiratory rates (B). Percent retrograde flow in each patient are summarized for increasing respiratory efforts (C), and increasing respiratory rates (D).

Figure 56A Figure 56B and Table 13 show that greater respiratory effort and higher respiratory rate increases the percent retrograde flow in the Fontan IVC independently. Figure 56C Figure 56D and Table 14 show the range of retrograde flow we have observed in the patient population. Some patients did not show any retrograde flow at baseline while others had up to 24.7% retrograde flow. Similarly, during shallow breathing some of the participants did not show any retrograde flow while others showed up to 31% retrograde flow.

Table 13 Percent retrograde flow in the Fontan IVC during one respiratory cycle for 20 patients normalized to baseline breathing.

Breathing pattern	Mean	Standard Deviation	Minimum	Median	Maximum
Shallow breathing	54.73%	34.50%	1.53%	59.01%	142.06%
Heavy breathing	263.91%	408.27%	106.05%	159.30%	1980.01%
Slow breathing	65.57%	42.43%	5.72%	59.36%	170.89%
Fast breathing	337.63%	388.14%	163.86%	216.89%	1944.31%

Table 14 : Percent retrograde flow in the Fontan IVC during one respiratory cycle for 20 patients.

Breathing pattern	Mean	Standard Deviation	Minimum	Median	Maximum
Baseline breathing	10.49%	6.48%	0.63%	8.84%	24.74%
Shallow breathing	6.67%	7.21%	0.05%	4.93%	31.32%
Heavy breathing	17.08%	8.52%	8.26%	14.06%	35.75%
Slow breathing	7.74%	6.32%	0.02%	6.15%	19.06%
Fast breathing	24.17%	10.95%	8.11%	23.51%	45.43%

Figure 57A corresponds to the data in Figure 56A and indicates the number of eligible patients who showed increased percent retrograde flow during one respiratory cycle when the respiratory efforts were increased. Patient results were rendered not eligible if the participant failed to increase the respiratory effort significantly and the retrograde flow did not increase. Those data points were not considered in the results. The changes in percent retrograde flow were analyzed in Figure 57A for three steps: Shallow breathing to baseline breathing, baseline breathing to heavy breathing, and shallow breathing to heavy breathing. Figure 57A shows that retrograde flow in the Fontan IVC increases with greater respiratory efforts. For increased respiratory effort from shallow to baseline breathing data points of one participant were not eligible, all the remaining 19 participants showed increased retrograde flow during one respiratory cycle. For increased respiratory effort from baseline to heavy all participants data was eligible and all of them increased the percent retrograde flow during one respiratory cycle. For increased respiratory effort from shallow to heavy breathing data points of one participant were not eligible and all remaining 19 participants showed increased retrograde flow during one respiratory cycle.

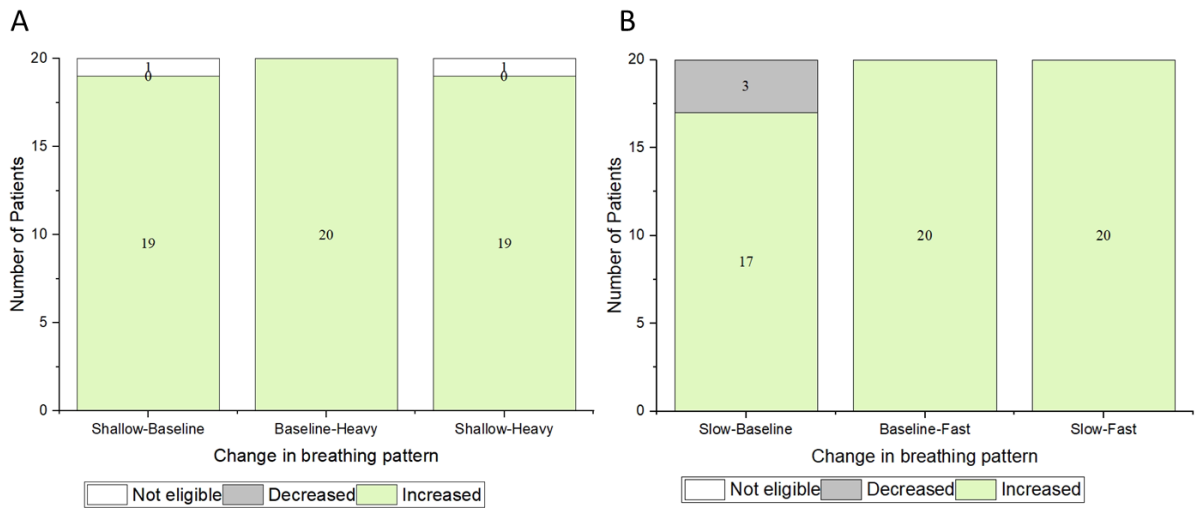

Figure 57 : Number of eligible patients who showed increased percent retrograde flow ruing one respiratory cycle with increasing respiratory efforts (A) and increasing respiratory rates (B).

Figure 57B corresponds to the data in Figure 56B and indicates the number of eligible patients who showed increased percent retrograde flow during one respiratory cycle when they increased their respiratory rates. Patient results were rendered not eligible if the participant failed to increase the respiratory rate significantly and the retrograde flow did not increase. Those data points were not considered in the results. The changes in percent retrograde flow were analyzed in Figure 57B for three steps: Slow breathing (RR=9 min^{-1}) to baseline breathing (RR=14 min^{-1}), baseline breathing (RR=14 min^{-1}) to fast breathing (RR=28 min^{-1}), and slow breathing (RR=9 min^{-1}) to fast breathing (RR=28 min^{-1}).Figure 57B shows that retrograde flow in the Fontan IVC increases with greater respiratory rates. For increased respiratory rates from slow to baseline breathing all participant were eligible, three participants did not show increased retrograde flow and 17 showed increased retrograde flow during one respiratory cycle. For increased respiratory rates from baseline to fast breathing all participant were eligible, and all of them showed increased retrograde flow during one respiratory cycle. For increased respiratory rates from slow to fast breathing all participant were eligible and all of them showed increased retrograde flow during one respiratory cycle.

3.3.3 Correlation of hemodynamic, physiological, and clinical parameters in the Fontan study population

Radiological investigation of anatomical characteristics

Table 15 shows the summary of the physiological, hemodynamic and anatomical characteristic from the radiologic investigation of the patient population. We can see that most we were able

to obtain most of the measurements for the patients. Figure 62, Figure 63, and Figure 64 show illustrations of comparing selected variables.

Table 15 : Summary of physiological, hemodynamic, and anatomical characteristics of the study population.

#	Diagnosis	Age	Years after Fontan completion	BSA	Ejection fraction	IVC flow rate at baseline	IVC flow rate/BSA at baseline	% retrograde flow at baseline	Pulsatility index at baseline	Liver size	Liver size/BSA	Hepatic portal vein size	Nakata index
1	HLHS	24.9	22.8	2.1	54%	4.6	2.2	0.4%	2.3				
2	HLHS	16.4	12.9	1.5	61%	2.7	1.8	10.6%	6.2	147.0	9.54545E-05	316.8	
3	DILV	36.7	34.4	1.5	61%	2.1	1.4	22.0%	6.2	139.1	9.21192E-05	325.5	
4	DILV	21.4	19.2	2.2	39%	4.5	2.0	3.1%	3.0	189.6	8.46429E-05	568.4	635.4
5	HLHS	19.0	17.1	1.8	37%	3.2	1.8	5.6%	3.8	149.8	8.23077E-05	341.0	559.3
6	DILV	23.4	17.9	1.8	62%	3.4	1.9	19.3%	6.1	153.0	8.64407E-05	514.7	1730.5
7	HLHS	21.4	18.0	1.8	45%	3.2	1.7	5.4%	4.1	170.8	9.38462E-05	618.0	1199.6
8	tricuspid atresia	29.4	26.6	1.9	54%	3.7	2.0	14.3%	5.2	136.5	7.26064E-05	555.8	1012.0
9	HLHS, MS, AA	16.5	14.5	2.1	57%	3.8	1.8	12.3%	6.3	161.9	7.85922E-05		499.8
10	RdAVC	20.5	20.2	1.7	35%	2.9	1.8	13.4%	5.3	135.2	8.14458E-05		
11	tricuspid atresia	23.5	19.3	1.9		4.0	2.1	11.4%	5.8	162.5	8.50785E-05	376.6	376.0
12	HLHS	16.4	13.6	1.9	57%	4.6	2.5	7.0%	3.4	157.2	8.45161E-05	284.1	635.1
13	tricuspid atresia	39.4	34.4	1.8	50%					149.9	8.19126E-05	290.5	
14	HLHS	23.6	21.6	1.7	53%					152.7	8.77586E-05	518.6	
15	DILV	16.7		1.7	35%	5.1	3.0	7.8%	3.8	153.0	8.94737E-05	542.5	
16	HLHS	18.0	15.7	1.6	46%	2.6	1.6	12.3%	6.5	137.3	8.63522E-05	428.5	504.2
17	HLHS	18.0		1.6	63%	3.4	2.1	6.8%	4.4	143.0	8.99371E-05	460.4	738.8
18	DORV	25.1	23.1	1.8	41%	2.7	1.5	24.7%	6.7	148.9	8.41243E-05	523.9	1335.1
19	DORV	17.4	15.0	1.9	46%	4.3	2.3	9.7%	4.9	158.6	8.52688E-05	451.4	976.2
20	MA, single RV	18.2	16.0	1.6	54%	2.6	1.6	6.2%	4.0	136.1	8.40123E-05	429.3	
21	DILV, TGA	20.8	18.4	1.6	46%	4.1	2.5	5.9%	3.8	163.5	0.000100926	518.0	576.0
22	DORV	42.2	32.7	1.6	52%	3	1.9	5.1%	4.4	144.0	8.9441E-05	379.0	735.6
23	tricuspid atresia	28.6	14.6	1.7	48%	3.2	1.8	9.0%	4.3	134.0	7.74566E-05		715.5
24	HLHS	25.1	23.3	2.0	45%	3.3	1.6	12.8%					2890.9
Available data:		24/24	22/24	24/24	23/24	22/24	22/24	22/24	22/24	23/24	23/24	20/24	16/24

We compared all variables with each other and combinations which are not shown in the graphs did not exhibit correlation in this patient population. Figure 62A and Figure 62B shows that in this study population there was no correlation between the time after completion of the Fontan physiology and percent retrograde flow or observed ventricular ejection fraction. Also, we could not observe any correlation between the time after Fontan completion and anatomical characteristics like size of the pulmonary arteries (Figure 62C), liver size (D), or size of the hepatic portal vein (Figure 62E).

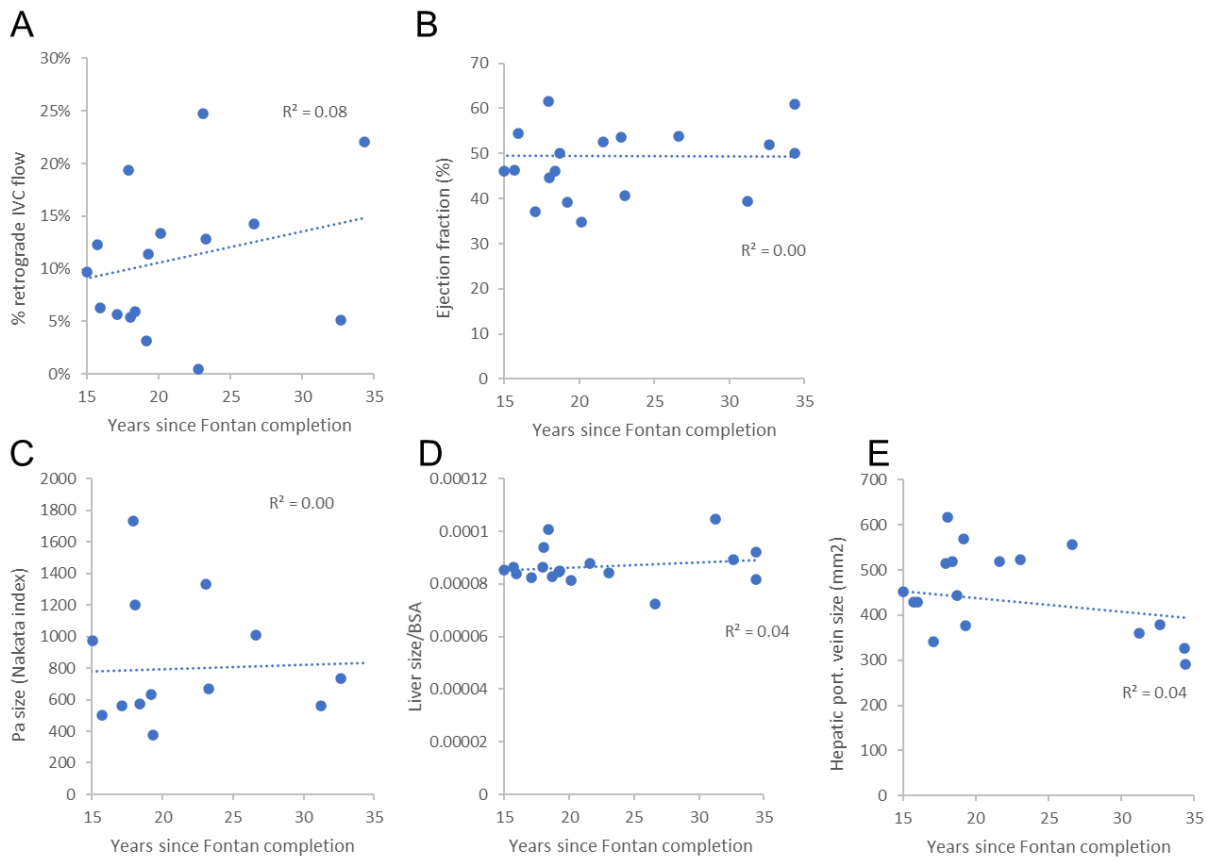

Figure 58 : Illustration of the recorded impact of years living with the Fontan physiology in this study population on percent retrograde IVC flow (A), ventricular ejection fraction (B), Pulmonary artery size as described by the Nakata index (C), Liver size normalized by BSA (D), and cross-sectional area of the hepatic portal vein (E).

Figure 63 shows the comparison of selected hemodynamic characteristics. We observed that there is a negative correlation between the baseline forward flow in the IVC and the pulsatility index shown in Figure 63A (R^2=0.35) as well as with the percent retrograde flow in the IVC as shown in Figure 63B (R^2=0.25). This corroborates our findings on the biomimetic bench top model. We could not observe a correlation between percent retrograde flow in the IVC and the ventricular ejection fraction as shown in Figure 63C (R^2=0.02).

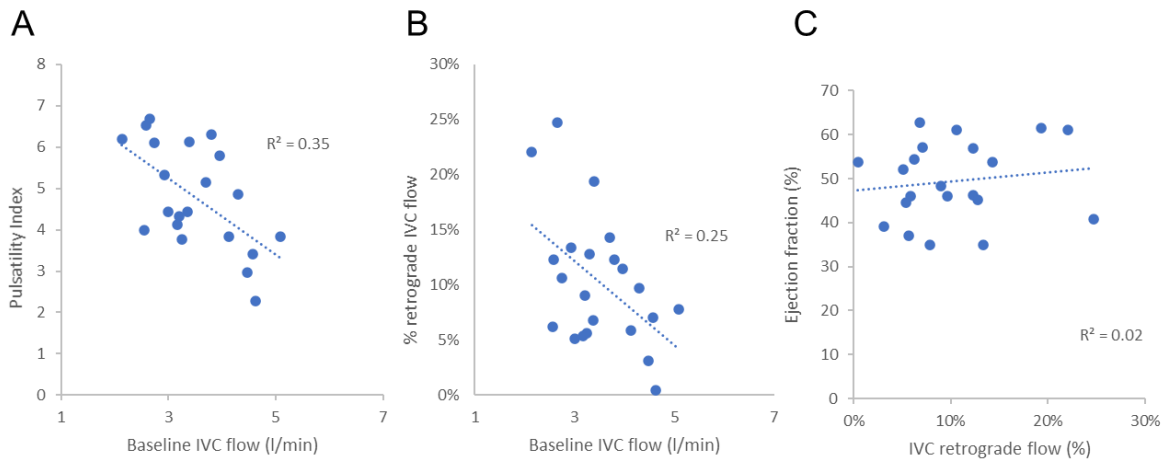

Figure 59 : Illustration of the recorded impact selected hemodynamic parameters in this study population. Baseline IVC flow on the flow pulsatility (A), baseline IVC flow on the percent retrograde flow (B), and percent retrograde flow in the IVC on the ventricular ejection fraction (C).

Figure 64 shows the comparison of percent retrograde flow with anatomical characteristics from the radiologic investigation. We observed that there is a positive correlation between the percent retrograde flow in the IVC the pulmonary artery cross sectional area as calculated with the Nakata index as shown in Figure 64A (R^2=0.32). Figure 64B and Figure 64C show that there was no observable correlation between the percent retrograde flow in the IVC and Liver size (R^2=0.35) and size of the hepatic portal vein (R^2=0.00).

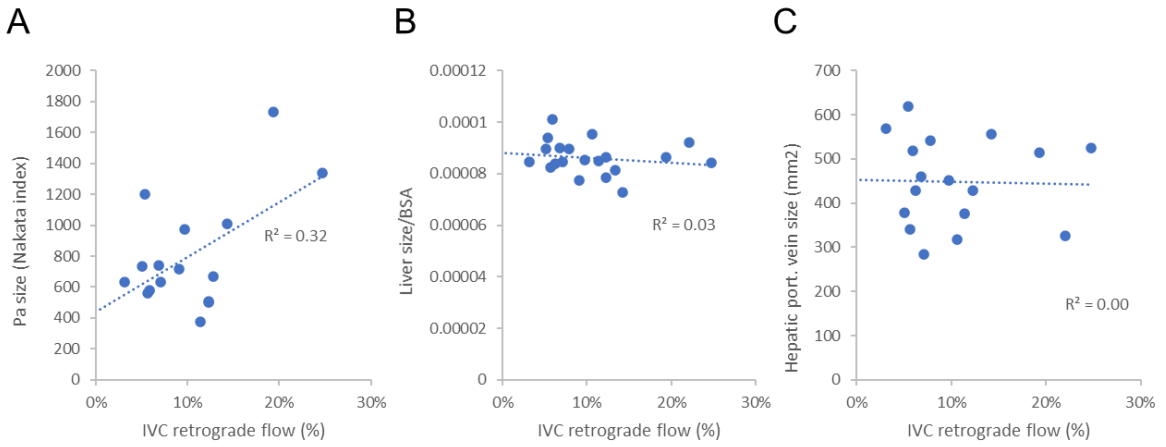

Figure 60 : Illustration of the recorded impact of percent retrograde flow in the IVC on anatomical characteristics from the radiological investigation. Correlations with Pulmonary artery size as described by the Nakata index (A), Liver size normalized by BSA (B), and cross-sectional area of the hepatic portal vein (C).

Blood analysis

Table 16 summarizes the results from the blood analysis conducted for the study participants. Only approximately half or less of participants had blood analysis recorded within the previous year which we could access for this retrospective study. Within the reported blood analysis the majority of participants did not show any pathological values. Less than half did exhibit pathological values in the evaluated tests as shown in Table 16.

Table 16 : Summary of the obtained blood analysis results for the study population.

Prospective clinical correlatives (<=1 year)					
	Blood analysis	**n/all**	**Normal range**	**Median (range)**	**Out of normal range/available**
Labs	Creatinine	**12/24**	M 0.74 to 1.35 mg/dL W 0.59 to 1.04 mg/dL	0.8 (0.6-1.02)	**0/12**
	Bilirubin	**12/24**	0.1 to 1.2 mg/dL	0.8 (0.4-11.6)	**4/12**
	ALT	**12/24**	7-55 U/L	22 (13-92)	**1/12**
	AST	**12/24**	10-40 U/L	23.5 (15-52)	**2/12**
	GGT	**8/24**	0-40 U/L	42 (23-73)	**4/8**
	INR	**9/24**	<1.1 or 2-3	1.2 (1.03-1.8)	**0/9**
	BUN	**12/24**	6-24 mg/dL	15.5 (9-21)	**0/12**
	Albumin	**12/24**	3.4-5.4 g/dL	4.7 (4.-5.3)	**0/12**
	AFP	**6/24**	10-20 ng/ml	3 (1-3)	**0/6**
	BNP	6/24	<100 pg/ml	43 (12-78)	**0/6**
	Hgb	14/24	11.6-16.6 g/dL	16.1 (14.4-19.8)	**5/14**
	Hct	14/24	35.5-48.6 %	46.2 (42.6-58.4)	**5/14**
	Platelets	**14/24**	150k-450k	178.5 (130-337)	**4/14**

We compared all variables of the blood analysis with the physiological, hemodynamic, and anatomical characteristics evaluated in the radiological investigation of this study population and could not observe clinically relevant correlations.

Selected correlations can be seen in Figure 65. Figure 65A shows a positive correlation of the years after Fontan completion with BNP values (R^2=0.79) but only five datasets were available to analyze, and BNP values of all participants were in the normal range. Figure 65B shows a positive correlation of the percent retrograde IVC flow with BNP values (R^2=0.65) but only five datasets were available to analyze, and BNP values of all participants were in the normal range.

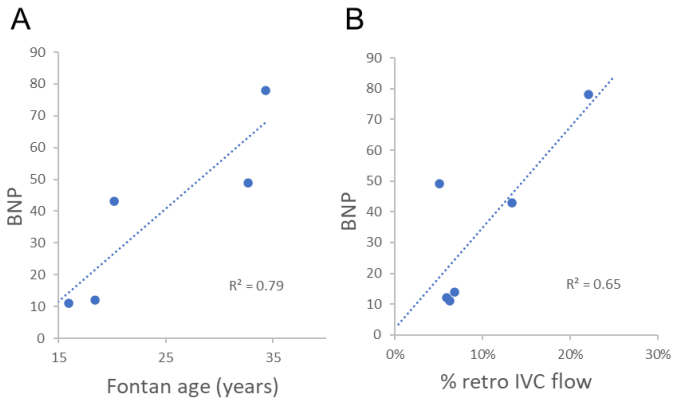

Figure 61 : Illustration of selected correlations of years since Fontan completion (A) and percent retrograde flow in the IVC (B) on BNP levels.

Physical examination and symptoms

Table 17 shows the review summary of the physical examination and reported symptoms of the study population. Only one patient completed an exercise study during the previous year, most patients did not report acute distress or symptoms, 8 were diagnosed with FALD or alterations in the liver texture or size, and description of the general status were good and very heterogeneous. Pressure evaluations of the venous side were nearly completely absent for the study population.

Table 17 : Summary of the study population's review of medical records.

	Variable	Reported /24 patients	Pathologic finding
Vital signs	BP systolic	10	0
	BP diastolic	10	0
	SpO2	9	1
	HR	10	0
General	Perfusion	8	0
	Resp. distress	8	0
	Pain	8	0
Lungs	Breath sound	9	1
Cardiac	Cardiac rhythm	9	1
	Jugular distension	9	0
	Cardiac sounds	8	0
	Oedema	8	0
	Cyanosis	7	0
Abdominal	Hepatomegaly	9	1
	Splenomegaly	8	1
	Liver border	7	2
Vascular	Vascular	6	0
Nuerological	Neurologic	7	0
Skin	Skin	2	2
Liver	FALD or liver abnormalities	8	8
Patient reported symptoms	Dyspnea	9	0
	Cough	3	0
	Hemoptysia	2	0
	Wheezing	2	0
	Oedema	6	0
	Orthopnea	4	0
	Chest pain	9	0
	Palpitations	9	0
	Syncope	8	0
	Dizziness	4	0
	Appetite	2	0
	Vomiting	3	0
	Diarrhea	4	0

3.3.4 Impact of anatomical position and gravity

Figure 62A shows the waveforms of the IVC flow rates during upright body orientation which show the same flow characteristics as described for the supine position in Figure 33 and changes similarly during increasing respiratory efforts compared to the supine position.

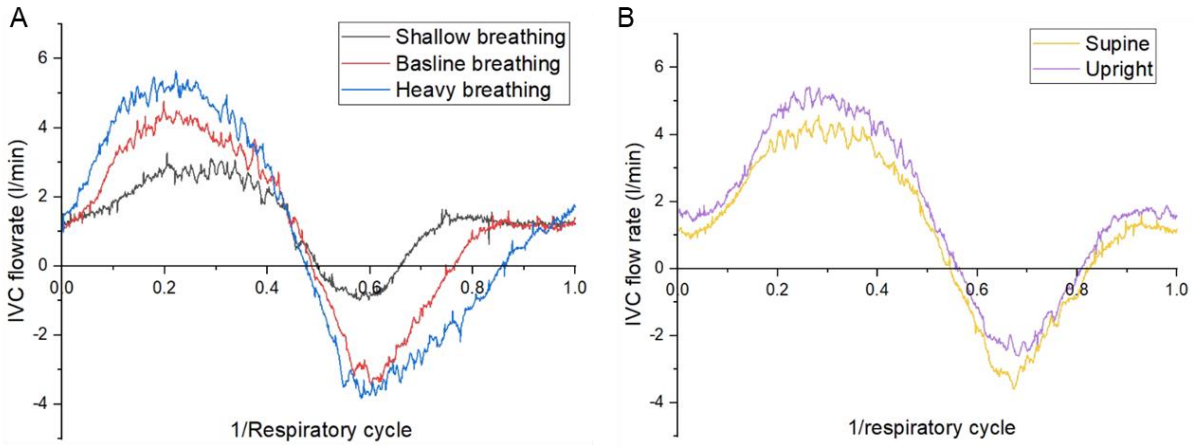

Figure 62 : Resulting flow waveforms during upright body positioning of the biomimetic cardiorespiratory simulator during increased breathing efforts (A) and a comparison of gravitational effects on the flow waveforms in the Fontan IVC at constant breathing efforts (B).

During inspiration forward flow during shallow to baseline, and heavy breathing increased to 3.3 l/min, 4.8 l/min, and 5.6 l/min. During expiration flow reversal in the IVC also increased with respiratory effort from shallot to baseline, and heavy breathing from -1 l/min to -3.4 l/min, and -3.8 l/min. Figure 62B shows the resulting IVC flow-waveforms comparing supine and upright body position with the same input conditions. The characteristics of the flow are similar while the waveform appears shifted downwards towards smaller values in the direction of the gravitational acceleration. During inspiration the surge of forward flow was less and the peak retrograde flow during expiration increased when comparing supine to upright position.

Figure 63A shows the gravitational effects during upright position as the forward flow volumes during increasing respiratory efforts are lower in upright compared to the supine position.

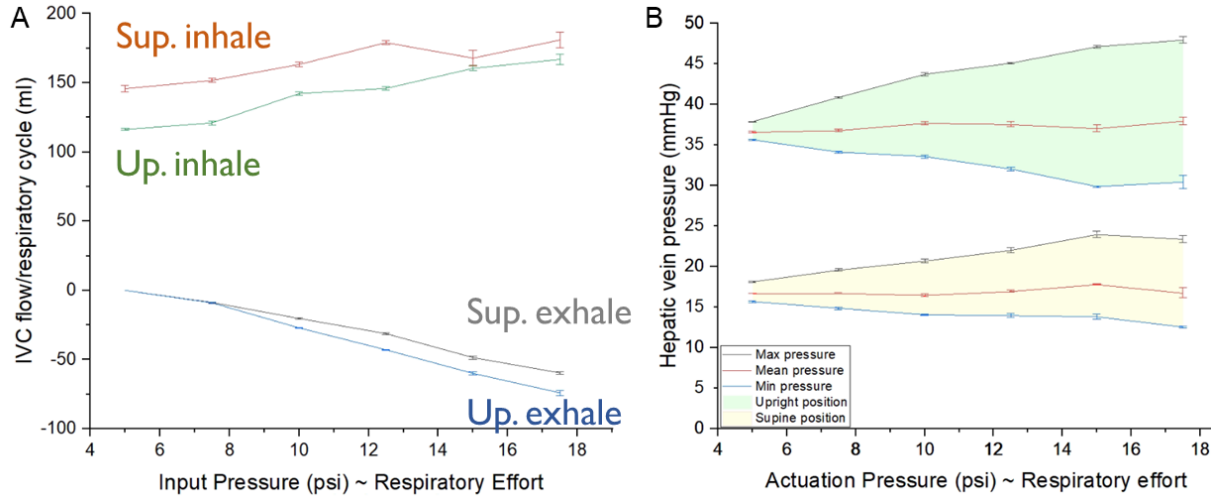

Figure 63 : Results comparing gravitational effects on Fontan hemodynamics during supine and upright body positioning. IVC flow volumes with standard deviations during inspiration and expiration of one

respiratory cycle (A), and hepatic vein pressure with standard deviations during one respiratory cycle (B).

The lowered peak flow rates are mirrored in the total flow volumes per respiratory cycle which decrease because of the upright position. During expiration the total retrograde flow volume increased compared to the supine position. The gap of less forward flow volume and more retrograde flow volume in the upright versus supine position is boosted with greater respiratory efforts. Values of the describes volume changes are summarized in Table 18.

Table 18

Input pressure (psi) ~ Respiratory effort	Supine negative volume (ml)	Supine positive volume (ml)	Upright negative volume (ml)	Upright positive volume (ml)
5	0	145.77	0	116.32
7.5	-8.78	151.73	-9.04	121.09
10	-20.26	163.23	-27.11	142.19
12.5	-31.26	179.02	-42.97	145.96
15	-48.54	167.86	-59.94	160.43
17.5	-59.63	180.89	-74.06	166.86

Figure 63B shows hepatic vein pressure in the abdominal IVC during increased respiratory efforts in the supine (yellow) and upright (green) position. The upper bound of the colored area shows the peak pressure values, the lower bound of the colored area shows the minimum pressure values and the center line indicates the average pressures in the IVC. The baseline pressure in the hepatic vein increases increased during the upright position shifting all pressure up. We can also appreciate how the amplitude between the minimum and maximum pressure values increases with greater respiratory effort. Additionally, the increase of the peak maximum and minimum pressures between each step of respiratory effort is larger in the upright position compared to the supine position. Pressure values are summarized in Table 19.

Table 19

Input pressure (psi) ~ Respiratory effort	Supine max. pressure (mmHg)	Supine mean pressure (mmHg)	Supine min. pressure (mmHg)	Upright max. pressure (mmHg)	Upright mean pressure (mmHg)	Upright min. pressure (mmHg)
5	18.11	16.68	15.66	37.87	36.61	35.65
7.5	19.56	16.71	14.84	40.87	36.83	34.14
10	20.68	16.47	14.03	43.72	37.73	33.59
12.5	22.01	16.97	13.94	45.1	37.58	32.04
15	23.95	17.83	13.78	47.14	37.07	29.88
17.5	23.38	16.75	12.52	47.96	38	30.44

Figure 64 shows the resulting percent retrograde IVC flow per respiratory cycle. At very low respiratory effort there is no retrograde flow and with increasing respiratory effort the percent retrograde flow in the IVC also increases. This is consistent with our previous findings and the clinical results in section 3.3.2. In the upright position the retrograde flow increases more than in the supine position.

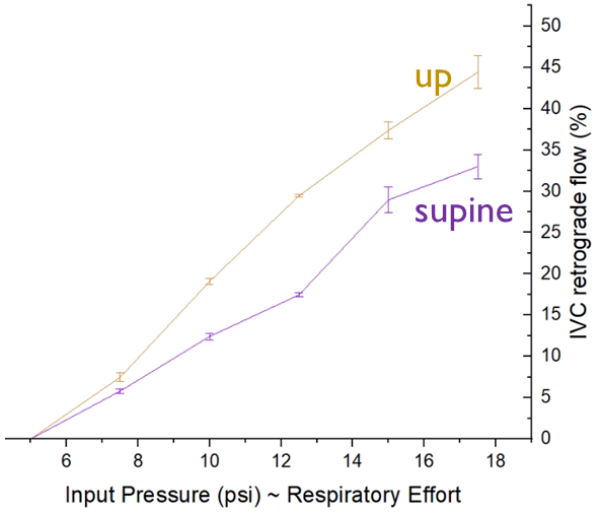

Figure 64: Percent retrograde flow in the Fontan IVC in the upright (yellow) and supine (violet) body position.

The values of the generated percent retrograde flow are summarized in Table 20. Retrograde flow ranged from 0% to 33% and 0% to 44.4% in the upright position, respectively. Retrograde flow was within the range of clinically recorded values in section 3.3.2.

Table 20

Input pressure (psi) ~ Respiratory effort	Supine % retro. Flow	Upright % retro. Flow
5	0	0
7.5	5.79	7.47
10	12.41	19.07
12.5	17.46	29.44
15	28.96	37.37
17.5	33	44.42

3.3.5 Erratic flow simulation

Figure 65 shows the recreation of erratic venous IVC flow from Fontan patient data. Figure 65A shows the IVC flow rate taken from patient data which served as the input waveform to control the contraction of the diaphragm in the cardiorespiratory simulator. Figure 65B shows the resulting IVC flow in the bench top simulator. Even though small differences in the absolute values flow values can be observed the bench top simulator recapitulates important flow characteristics like large forward surge of blood during inspiration and retrograde flow during expiration, the time distribution of the fluctuations in flow and the range of the resulting flow rates. It can be observed that the forward and backward flow in the IVC is not regular which is recreated on the bench top. Figure 65C shows the IVC blood pressure in the Fontan shunt, the IVC pressure in the location of the hepatic vein, the abdominal cavity, and thoracic cavity pressure pressures. Which drive the resulting IVC flow shown in Figure 65B.

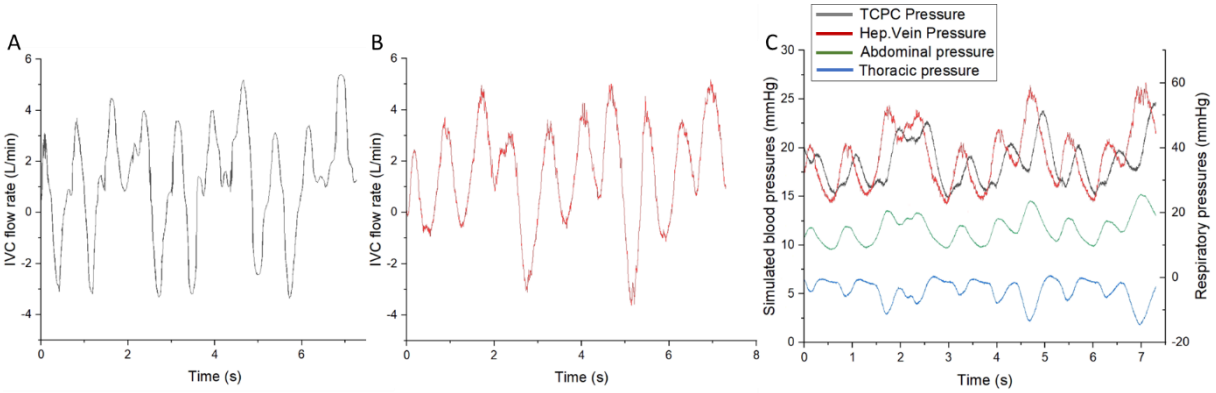

Figure 65 : Erratic Fontan IVC flow during spontaneous breathing from patient ultrasound recordings (A), recapitulation of Fontan IVC flow characteristics from patient data on the bench top simulator (B), respiratory and IVC pressure values that recreate the patient flow data on the Fontan cardiorespiratory bench top model (C).

3.4 Discussion

3.4.1 *In vitro* investigation of cardiorespiratory model hemodynamics

Impact of respiratory effort

We showed that greater respiratory effort increases the peak forward and peak reverse flow rates during inspiration and expiration, respectively. This manifests in an increase of the waveform amplitudes and a pronounced increase of the IVC pulsatility index. It also causes a boost of the forward and backward flow volumes in the IVC during inspiration and expiration. Compared to baseline the forward flow volumes increases less than the retrograde flow volume which leads to an overall increase of the percent retrograde flow in the IVC. Similar to the IVC flow rates the amplitude of the pressure waveform in the IVC is boosted during greater respiratory efforts. This manifests in greater peak pressure during inspiration and slightly lowered minimum pressure during expiration while the mean pressure in the IVC remains constant.

Impact of respiratory rate

With increased respiratory rate the peak forward flow rates during inspiration increase slightly while the peak retrograde flow during expiration does not change. This contrasts flow waveforms during variable respiratory efforts. Accordingly, the pulsatility index only increases very slightly compared to the jump in pulsatility during greater respiratory efforts. This increase in peak forward flow rate during inspiration but little change to the peak retrograde flow rate during expiration does not indicate a greater percentage retrograde flow in the IVC during one respiratory cycle. However, with augmented breathing rates the forward flow volume during inspiration decreases significantly while the retrograde flowing volume cause by expiration stays constant. The area under the flow waveforms (Figure 45A) marks the flow volumes and we can appreciate that the amount of positive area decreases much more during faster breathing rates than the negative flow area. This result in the observed overall increase of percent retrograde flow in the Fontan IVC when breathing rates are increased. Physiologically, baseline flow in the IVC is positive during the end-inspiratory and end-expiratory pause which diminishes the relative retrograde flow. The flow waveforms on the bench top indicate that with increased breathing rates, the positive impact of forward flow during the respiratory pauses get shortened augmenting the overall retrograde flow in the Fontan IVC.

The amplitude of the pressure waveforms do not increase during greater respiratory rates. This was expected as the respiratory efforts which would translate into the venous vasculature were

kept constant for this study. We do observe a that with greater breathing rates the time at peak IVC pressures decreases. Overall, the peak maximum pressure during inspiration, the minimum pressures during expiration and the average pressures are not greatly impacted by the respiratory rate.

Impact of baseline IVC flow

We showed that on the benchtop an increased baseline IVC flow at constant breathing effort and rate leads to less overall percent retrograde flow during expiration. The peak forward flow rate during inspiration increases while the peak reverse flow in the IVC does not decrease significantly during expiration. Similarly, the overall forward flow volume increases during inspiration and the reverse flow volume decreases slightly with higher baseline IVC flow. This can be explained by greater flow inertance of the IVC flow. Flow inertance can be described as the pressure difference in a fluid required to cause a unit change of volumetric flow-rate with time and is defines as [19]:

$$I = \frac{\Delta P}{\dot{Q}}$$

With inertance I, pressure difference $\Delta P$and the flow rate $\dot{Q} = \frac{dQ}{dt}$. This effect can also be described as the flow inertia of the blood. Higher baseline flow rates in the IVC carry greater flow energy in the forward direction so more energy is required to reverse this flow. At the same time the surge of forward flow is supported by the greater forward flow inertia, thus less retrograde flow is produced. The pressure waveforms are slightly shifted upward but the mean IVC pressure is not increased greatly.

Impact of baseline IVC pressure

We showed that increase baseline IVC pressure slightly increases peak forward flow rates during inspiration as well as peak reverse flow rates during expiration. IVC flow volumes behave similarly but the increase in forward flow volume is less than the increase in retrograde flow volume during expiration so the overall percent retrograde flow increases. With greater baseline IVC pressures have shown that the pressure curves during one respiratory cycle are shifted upwards by the amount of higher baseline pressure but the waveform characteristic and the relative amplitude of the pressure curve remains constant.

Impact of baseline vascular compliance

We have shown that decreased vascular compliance diminishes the forward peak flow rates and flow volumes during inspiration and decreased the retrograde flow rates and flow volumes. We have shown that the surge of forward flow diminishes less relative to the decrease in retrograde flow volume resulting in less retrograde flow. Non-compliant vasculature does not allow for any retrograde flow volume during expiration at all and shows how instrumental the compliance of the vascular beds is in the generation of retrograde flow in the Fontan IVC. The amplitude of the pressure curves is also diminished with less compliant vascular beds, however, the mean pressure in the IVC remains constant.

Contribution to the state of the art, limitations, and future opportunities

This is the first Fontan bench top model that characterized the impact of respiratory patterns as well as basic hemodynamic conditions on the generation of retrograde flow in this detail. This allows us to describe mechanisms how retrograde flow is generated and allows us to create hypotheses how respiratory interventions can help or harm a Fontan patient. For example, breathing exercises that were reported previously which include greater respiratory efforts would be counterproductive as they also increase the generated retrograde flow. Our bench top analysis suggests that a calm breathing with low respiratory effort and low respiratory rate would be the desirable breathing pattern to mitigate retrograde flow. All analysis includes pressure readings which are not easily available in the clinical setting.

Moreover, this study is the first bench top simulation which showed that respiratory effort and respiratory rates are two separate drivers of the generation of retrograde flow. Flow rate, flow volume and pressure measurements elucidated what factors contribute to the different mechanisms increasing retrograde flow in each case.

We acknowledge some limitations of this study which include that not comprehensive changes in flow resistance were investigated, and these findings are not validated with clinical data. Holds great opportunity to include the variation of flow resistors in the Fontan bench topo model. Also, a clinical study is required to validate the findings and confirm the bench top results.

3.4.2 *In vivo* 4D MRI study the effect of breathing mechanics on IVC flow dynamics

We have shown that patients in this clinical study were able to increase respiratory rate and respiratory effort (chest wall motion) independently of each other (Figure 49). This provides

the foundation to evaluate the impact of respiratory effort and rate on the Fontan IVC flow. Figure 50 and Figure 53 show how increased respiratory effort and increased respiratory rate augment the retrograde flow in the Fontan IVC and concur the finding on the bench top. Greater respiratory effort boosts the peak forward and reverse flow rates and flow volumes in the IVC which indicates that the greater pleural and abdominal breathing pressures drive more blood forward during inspiration and backward during expiration. As the breathing efforts increase the forward flow increase less than the retrograde flow which results in a greater percent retrograde flow during each respiratory cycle. We have also shown that respiratory rates increase the retrograde IVC Flow in the Fontan physiology in a different mechanism than breathing efforts do. Even though the flow rates slightly increase during higher respiratory rates as shown in Figure 50, the forward flow volumes decrease significantly during inspiration while the retrograde flow volumes remain constant during expiration (Figure 53). We have shown that these details concur the finding on the bench top model and increases overall retrograde flow in the Fontan IVC during higher respiratory rates. Figure 55 illustrates this effect qualitatively in clinical data of a single participant: As the respiratory rates increase, we observe shorter end-expiratory and end-inspiratory pauses in the chest wall motion. Simultaneously, the overall time during which IVC flow is positive decreases while the time during which retrograde flow in the IVC occurs remains similar.

This study presents the first work to analyze Fontan the IVC flow rate, flow volume, flow pulsatility, and resulting retrograde flow in the Fontan population during individually increased respiratory rates and respiratory efforts.

This is the first work that shows how respiratory rates impacts venous hemodynamics in the Fontan IVC. To our knowledge, it is the first time that respiratory effort and respiratory rate are identified as independent mechanisms to increase retrograde flow in the Fontan IVC.

In this work we also show that baseline flow patterns of Fontan patients and resulting fluctuations due to respiratory efforts vary greatly. We showed that the sensitivity of Fontan IVC flow to respiratory impact is very patient specific and we have documented a wide range of retrograde flow values that patients have developed. In our study we have shown that retrograde flows of up to 45 % is achieved in supine position which surpasses reported peak retrograde flow of 30 % [4] by over 15 %. This emphasizes the heterogeneous nature of physiological parameters in the Fontan patient population resulting in a wide variety of venous flow patterns and underscores the necessity to evaluate support strategies in physiological flow patterns including the effects of respiration. This work is one of very few clinical studies which included

20 or more Fontan patients at all. We have aggregated a variety of patient specific Fontan flow data and different flow patterns which in the future can be used to evaluate efficacy of circulatory support devices for different patient phenotypes. Thereby we completed aim 2 of this chapter.

Impact: The Fontan circulation is the resulting physiology for several different rare congenital heart diseases. Therefore, very few clinical studies including as many as 20 Fontan patients exist so far. Still, the low patient number is a limitation of this study, and a larger number of participants would increase the statistical power of the new hemodynamic findings of this study. Additionally, important parameters like exercise, body posture, and status of meal ingestion could be relevant to detail more specifics of the respiratory effects on Fontan venous flow. Towards this goal a new IRB has been approved at Boston Children's hospital which may include the investigation of these effects.

3.4.3 Correlation of hemodynamic, physiological, and clinical parameters in the Fontan study population

Overall, the results do show little correlation between IVC retrograde flow and the clinical parameters, whether they are clinical examination, symptoms, radiological investigations, or lab examinations. This finding does not allow to isolate clinical parameters which could either show the impact of retrograde flow on organ systems or indicate physiological boundary conditions leading to more retrograde flow. Several considerations might help understanding these findings.

The protocol of the present respiratory study required a high level of participation during the cMRI, including synchronized breathing exercises. This implies (1) an acceptable cardiopulmonary condition, and (2) the ability to understand, follow, and apply the breathing protocol. This inevitably led to a selection bias, excluding patients with poor cardiopulmonary condition, as well as those suffering neuro-cognitive disorders preventing the correct protocol application. Also, patient selection was confined to scheduled MRI examinations which were part of the yearly or bi-yearly follow-up protocol of Fontan patients. This implied that the patients did necessarily suffer from acute symptoms. Hence, the present cohort is limited to a narrow spectrum of the disease, including mostly patients with no severe functional limitation. This observation is reflected by the very limited availability of blood analysis, almost complete absence of exercise tests, imaging abnormalities, clinical symptoms, venous pressure measurements,

and clinical signs. This small degree of variation in dependent parameters significantly impact the ability to show any clinical correlations.

Regarding secondary analysis of MRI parameters, the following points might impact our analysis, on top of those mentioned above. Firstly, pulmonary artery size has been positively correlated in the adult population without cardiac congenital anomaly with the risk of pulmonary hypertension. We see a positive correlation of percent retrograde flow in the IVC and pulmonary artery cross sectional area. This could imply that greater venous congestion occurs with increased retrograde flow elevating IVC pressures which distends the pulmonary arteries in the Fontan physiology. Central venous pressure readings would be essential to understand effects of retrograde flow but there were not available for this study population. Also, it is not clear if the relationship of pulmonary artery size and risk of hypertension in bi-ventricular physiology is true for the Fontan physiology since pulmonary artery size is highly dependent on the developmental status and might present some degree of hypoplasia. A previous study [50] has shown that the Nakata index is negatively correlated with survival. Those two opposite trends might be simultaneously present and affect the statistical analysis. Secondly, the evolution of liver size during hepatic disease is not linear, and usually a first period with augmentation is followed by a reduction of size. Therefore, a single measure is not appropriate to identifying the stage of disease and require complementary investigation.

We acknowledge some limitations of this study. (1) Although we sought to correlate retrograde flow with clinical data, its retrospective nature does not allow to infer any causal relationship, but only an association. Moreover, the analysis of a single value for each clinical marker does not reflect evolution of disease over time, which might provide critical information. (2) The number of subjects included was not high enough to reach the minimal requirement for statistical power. In addition, we observed a high proportion of missing values, which reduces statistical power even more. (3) For each patient, data were collected over a predetermined interval of time around the intervention (within 1 year) to increase their availability. If the medical condition of the patient changed in this time interval, considering them on a single timepoint would not truly reflect a single condition, and rather induce a chronological bias. Unfortunately, the scarcity of data and their heterogeneity does not allow us to identify such bias. (4) Because the primary goal of the clinical study was to investigate IVC flow dynamics the used MRI sequences were dedicated to cMRI, not hepatic nor abdominal analysis. Therefore, the measurement of portal vein dimensions is affected by low spatial resolution of the images, and hepatic size evaluation is impeded by truncated images, which both affect accuracy of results.

Although this study presents with strong limitations which prevent the definition of clinical markers to the effect of retrograde flow in the Fontan IVC it represented a unique opportunity to pave the way for future works. With the aim of correlating the IVC retrograde flow to clinical markers the following points might be taken into account for future studies: (1) The study design should be prospective aimed to follow the hemodynamic changes in the IVC alongside clinical markers ideally over years (2) The study protocol should include standardized clinical and symptoms recording, as well as organ specific investigations, e.g. IVC pressure readings, liver specific MRI recordings to evaluate organ health (hepatic fibroscans), abdominal MRIs. (3) Ideally those clinical measurements should be obtained within a reasonably short time span. (4) Most importantly, investigators should widen the inclusion criteria to encompass the entire spectrum of the disease, especially including patient with more compromised health conditions.

3.4.4 Impact of anatomical position and gravity

We designed and constructed a frame and attachment mechanisms to operate the cardiorespiratory simulator in different body orientations. We presented a modified configuration of our biomimetic respiratory and flow simulator which positions the entire bench top system in a vertical orientation to recreate the gravitational impact on the Fontan hemodynamics. Clinical ultrasound studies have shown that upright position of Fontan patients has negative impact on flow dynamics in the venous vasculature and this is the first *in vitro* system which recreates this interaction with gravitational acceleration on Fontan hemodynamics. This is important because forward and reverse flow in the Fontan IVC is either against or in the direction of these gravitational forces. We then demonstrated that flow reversal in the Fontan IVC is impacted by the addition of the gravitational forces.

The waveforms showing the IVC flow rates during one respiratory cycle are shifted downwards (Figure 62) indicating a diminished forward surge of IVC flow during inspiration and a increased retrograde flow rates during expiration. During inspiration the respiratory pump pressurizes the abdominal vasculature and depressurized the pulmonary vasculature which introduces additional flow energy in the IVC towards the lungs. Constant gravitational acceleration of the blood towards the ground and abdomen counteracts this forward flow energy due to the approximately vertical orientation of the IVC. This diminishes the forward flow rates and conversely increases the retrograde flow rates during expiration when the flow energy of the blood in the IVC and the acceleration of gravitation point in the same direction and thus add up.

Flow volume in the IVC is the time integral of the flow rate so we see the diminished flowrates impact the overall flow volume during each respiratory cycle in Figure 63A. Forward flow volume going against the gravitational field is lower than during supine position while the reverse flow volume directed with the gravitational forces increased. Here we also showed the impact of increasing respiratory efforts in the supine and upright body position. Figure 63A indicates that the difference in forward flow volume decreases, and the augmentation of retrograde flow volumes increases during greater breathing efforts when comparing horizontal and vertical orientation of the IVC. This is explained by a larger amount of flow energy introduced by the respiratory pump which counteracts the downward pull of gravity during forward flow but enhances the retrograde flow during expiration. To our knowledge these findings are the first analysis of Fontan flow rates and flow volumes during different respiratory patterns comparing supine and upright body position.

In Figure 63B we show the impact of body position on the blood pressure in the IVC during increasing respiratory efforts. Clinical evaluation of the effect of body position on Fontan flow reversal have been made with ultrasound modalities. This does not include pressure readings which are the main drivers of organ damage in the Fontan vasculature. This is the fist study to evaluate effects on IVC pressure in the hepatic vein location. Congestion of hepatic vasculature and chronic elevated pressures are main drivers of Fontan associated liver disease and protein losing enteropathy with fatal outcomes (section 1.1.1) so a detailed understanding of the effect of position and respiration is crucial. In Figure 63B we see that hepatic vein pressure is shift to greater values with the upright position of the body. During supine position the abdominal and pulmonary vasculature are in approximately the same level. During upright position the pulmonary vasculature is raised above the abdominal vasculature introducing a static fluid pressure generated by gravitation and the height difference as explained in Equation 2. With the direct connection of the pulmonary and abdominal vasculature in Fontan physiology this static pressure translates directly to the hepatic veins and is responsible for the pressure increase seen in Figure 63B. During the increasingly oscillatory IVC flow at greater breathing efforts the mean pressure in the abdominal IVC stays constant as indicated by the red line in Figure 63B. We also show how the upper and lower pressure limits during increased respiration increase. The increasing amplitude of the maximum and minimum pressure is greater in the upright compared to the supine position.

3.4.5 Erratic flow simulation

We have shown that we can recreate IVC flow waveforms obtained from clinical patient data. By adapting patient IVC flow rate data we can actuate the respiratory mechanism of the biomimetic bench top simulator such that the resulting IVC flow rates match the original flow waveforms. This shows that we can recreate patient specific hemodynamic conditions *in vivo* and analyze the underlying pressures associated with these flow changes. This allows us to recreate patient flow characteristics on the bench top to then evaluate efficacy of specific circulatory support devices for the patient specific hemodynamics. The day-to-day impact of support strategies can be simulated in a typical situation that cause these erratic flow profiles.

3.5 Conclusion

In summary we leveraged the biomimetic cardiorespiratory bench to simulator to investigate hemodynamics and the generation of retrograde IVC flow when subjected to changes in breathing mechanics, baseline flow rates, baseline central venous pressures, and vascular compliance. We characterized the impact of those physiological parameters on Fontan hemodynamics by evaluating flow rates, flow volumes, flow pulsatility, generated pressures and resulting forward and retrograde flow. This work is the first to describe these relationships on the bench top and helped to identify respiratory rate and respiratory effort as separate drivers of retrograde flow in the Fontan IVC. We then conducted a clinical study of 20 Fontan patients with TCPC physiology to investigate the impact of breathing patterns on the IVC flow. We analyzed Fontan IVC flow rates, flow volumes, flow pulsatility, and retrograde flow and found that increased respiratory effort and increased respiratory rates boost the percent retrograde flow in Fontan patients. The clinical study concurred with the bench top findings that respiratory rate and respiratory effort are independent drivers of flow reversal in the IVC and we considered the different mechanisms of action. The in vivo trials also affirmed the bench top findings that increased baseline flow rates mitigate the generation of retrograde flow in Fontan IVC. We conducted a review study of patient history, blood work, and anatomical features to identify potential clinical markers correlating to the hemodynamics found in the respiratory study. Available data was incomplete and thus didn't allow for conclusive findings but informed the study design of a subsequent clinical study to investigate end organ effects of retrograde flow in the Fontan physiology. Increased retrograde flow was correlated with the size of the pulmonary artery which may indicate greater venous congestion but needs further pressure analysis in future studies.

We then investigated the effect of upright compared to supine position on the bench top and found that the addition of gravitational forces exacerbates the flow reversal as well as peak pressures in the Fontan IVC. The negative effect of the upright position is boosted by greater respiratory efforts. It was reported that chronic IVC pressures above 20 mmHg are difficult to tolerate for the Fontan physiology and lead to end organ failure. Our bench top evaluations can estimate additional impact of gravitation and respiration on Fontan pressures and indicate harmful pressure levels. Further, the bench top model can simulate flow and pressure conditions to evaluate support strategies in a more physiological environment. This represents the first reported bench top model with these characteristics. Lastly, in this chapter we showed that we can use clinically recorded flow data as input waveforms to our bench top simulator to recreate flow characteristics and generate erratic flow patterns which may address hemodynamic fluctuations in the patient's life outside of the clinically controlled setting. This provides the platform to evaluate the efficacy of specific circulatory support devices for the patient specific hemodynamics.

In conclusion, the bench top simulations in different body positions paired with the clinical respiratory study characterized physiological parameters driving the generation of retrograde flow which have not been published previously. The clinical implications of retrograde flow in the Fontan physiology will be explored in a follow up study but current finding indicate that calm breathing with shallow respiratory efforts, slow breathing rates, supine position and decreasing abdominal compliance for example favoring chest breathing over stomach breathing mitigate the increase of flow reversal in the Fontan IVC.

4. Chapter 3: Development and characterization of Fontan circulatory support strategies

4.1 Introduction

The permanent hemodynamic burden in Fontan physiology leads to a variety of fatal effects as described in chapter 1. Multiple attempts to support the Fontan circulation have not addressed the challenge and no assist device developed for the Fontan circulation has been approved for use to date.

4.1.1 State of the field and current limitations

Ventricular assist devices

To mechanically assist the failing human circulation, ventricular assist devices (VADs) are commonly used as a life-prolonging therapy, either as a bridge-to-transplant or, in some cases, as a "destination therapy", meaning that the device remains implanted for the rest of the patient's life. For current VADs, the heart and one, or both, of the great vessels are cannulated, blood is removed from the heart, and then pumped into the aorta or pulmonary artery. VADs are developed to support circulation during heart failure. In this scenario, the VAD takes over the function of one, or both, of the ventricles. Initially, VADs used pulsatile pumps and valve technology before continuous, valveless, axial-flow technology became the gold standard. Subsequently, magnetic levitation technology for contactless bearings was introduced [56], [57]. Still, all commercially available VADs directly contact blood resulting in a risk of thromboembolic events requiring anti-coagulation treatment.

Limited available technologies for pediatric applications

Availability of VADs for the pediatric patient population is limited (Heartware, Heartmate3, Jarvik infant, EXCOR Berlin Heart) and with these systems children are at even greater risk for bleeding and thrombotic complications. VAD models are traditionally developed and sized for the adult population, which limits their use for pediatric purposes. The size of VADs with dimensions suitable for adult patients contribute to their robustness[58], and as such, does not allow for simple downsizing for pediatric patients. Management of congenital defects of the heart and great vessels constitutes the largest part of pediatric cardiology practice. Nowadays, most of the young patients require surgical interventions for complex lesions, with suboptimal clinical outcomes, especially in small patients[58]. Nonetheless, surgical approaches are

considered to be superior, based on the presumed durability of the repair in small children, who are still growing. Additionally, VADS are designed for the adult population and the high pressure, high flow environment of the arterial side. The use of the commercially available pumps for the Fontan physiology required modifications which lie outside of the optimal operation point of systems. The case load of patients with congenital heart defects is small compared to developed heart failure, which results in lower revenues and lack of investments and research for failing Fontan. The resulting limited revenues also keep major health care companies from investing in intervention technologies, deeming it a favorable field for academic research.

Presently, no circulatory support strategy developed specifically for the single ventricle physiology is approved and commercially available. The size and age of the Fontan patient population is increasing and the need for reliable circulatory support for the failing physiology sparks the development and testing of a wide variety of support strategies [59]:

Ventricular assist devices for Fontan physiology

Many different approaches have been explored to support the failing Fontan circulation and mitigate pathophysiological effects on the patients without leading to any approved devices thus far. Figure 66 shows a summary of devices tested in the Fontan physiology.

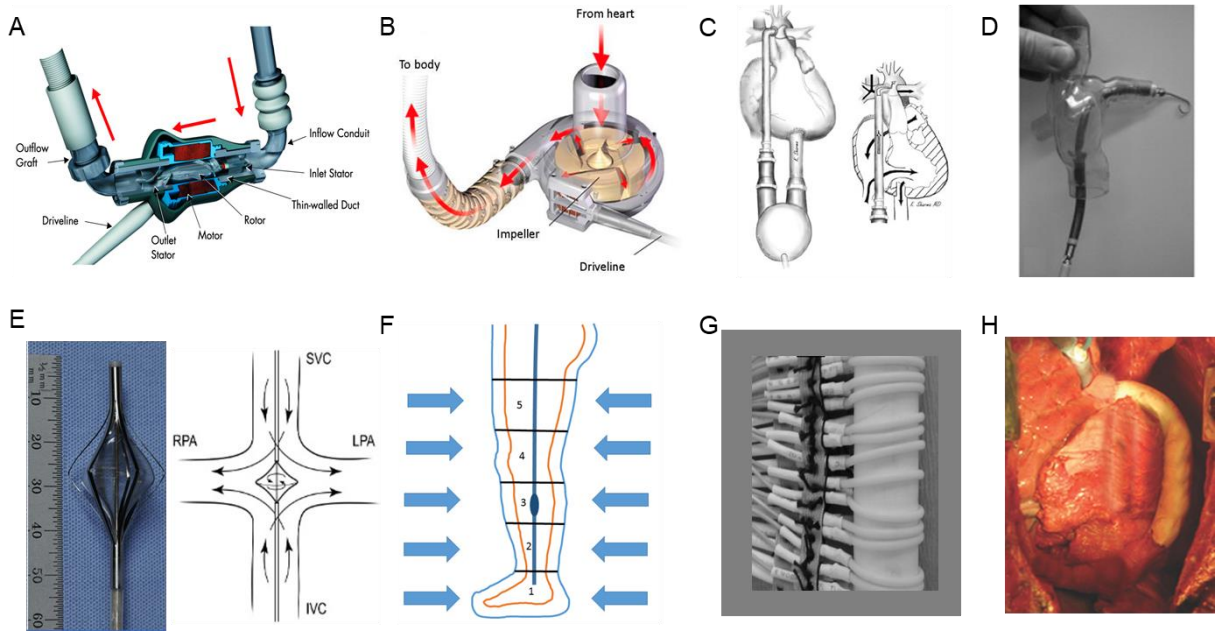

Figure 66 : Examples of different approaches to support the single ventricle physiology. Ventricular assist devices (A-D) including the HeartMate2 (A) and HeartWare (B) [60], BerlinHeart pulsatile pump (C) [61], catheter based Abiomed Impella (D) [41], and alternative Fontan specific support strategies including van Karaman impeller(E) [62], compression trousers (F) [63], thermoelectric extravascular

compression of the Fontan shunt (G) [64], and skeletal muscle pump as extravascular compression (H) [6].

Facing the absence of available treatment, apart from transplantation, commercially available VAD systems are implanted in patients with failing Fontan physiology. This includes Thoratec's axial flow pump HeartMate2[65] (Figure 66A), HeartWare's centrifugal pump HVAD[66] (Figure 66B) and Berlin Heart's diaphragm pump EXCOR23 (Figure 66C) showcasing that the use of VADs in univentricular patients is increasing. Nevertheless, applications of these systems are almost always relegated to support the heart and arterial circulation [65], [67]–[71]. Venous congestions, diminished flow energy through the TCPC, and impaired pulmonary flow contribute greatly to the failing of univentricular circulation shifting the focus of support to the venous side. Even though the available devices are not designed for the venous side, VAD support of blood flow through the TCPC has been investigated numerous times and across different VAD models [59], [72]–[74]. These experiments included computational, bench top, and animal models but even though some results included improvements in cardiac output and venous hypertension, non could be translated to clinical use thus far. There are several reasons why established circulatory support devices can't simply be implanted in the Fontan circulation. Axial and centrifugal flow pumps, developed mainly for left ventricular support, are pre-configured to have operation points for the high pressure (80-120mmHg) and high flow condition seen on the arterial side which differ greatly from the low pressure (10-20mmHg), high flow condition on the venous side. Challenges also include cannulation of the frail small pediatric venous vessels. Axial flow pumps must compensate for the smaller diameter by increasing the rotation speed which increases hemolysis through high shear forces. All available pumps have large artificial areas contacting the blood which poses an increased risk for thromboembolic complications. This exacerbates physiological vulnerabilities which the Fontan circulation faces inherently.

Fontan specific Intravascular Pumps

Venous flow conditions, heterogeneous hemodynamics in Fontan patients, and varying anatomical implementations of the Fontan circulation demand for support strategies specifically designed for this patient population. Most of the venous return is distributed to the IVC (~75%) over the SVC and a majority of pathophysiological complications leading to the failing of the Fontan circulation are based on venous congestion in the IVC. This makes the IVC the preferred therapeutic target for the development of support strategies. The Fontan paradox describes the relative increase in central venous pressure and concomitant decrease of pulmonary arterial

pressure diminishing trans-pulmonary blood flow [75], [76]. In this context, it was suggested that a support strategy which could provide a 2-5 mmHg pressure boost would reduce systemic venous pressure and increase pulmonary arterial pressure meaningfully reversing negative effects of the single ventricle physiology [73], [77].

The adaptation of design principles from VADs to develop axial pumps has been a popular approach for intravascular Fontan pumps [62], [75], [78]–[81]. Like VADs, these axial flow pumps consist of a propeller-type of impeller driven to rotate axially inside of a tube-like casing. The design of the impeller blades pushes the blood forward generating head pressure. Initial device testing revealed that intravascular axial pump systems need an obstructed separation between the inflow and outflow of the pump to prevent recirculation and retrograde flow [62]. Concerns were also raised about the collapse of the venous vasculature due to device inlet suction. As the caval veins are much more compliant than arterial vessels the device suction may cause such vessel collapse causing flow obstruction and vessel tissue damage [62]. Axial pump designs are often a last resort in Fontan treatment when the implant replaces the vasculature of the IVC, SVC and the pulmonary arteries, the so-called Fontan cross and introduce large areas of foreign material surface which increases the risk of thromboembolic complications.

Smaller axial pump systems include catheter-based devices which have been investigated for usage in the Fontan circulation [41], [82]. These devices like the Impella (Abiomed, Danvers, Mass) shown in Figure 66D are tethered through catheter system and can only be administered for shorter time periods. Impella devices have shown to improve Fontan hemodynamics, however, like other axial flow pumps, they require a barrier between inflow and outflow completely altering inherent Fontan flow patterns. Additionally, it was noted that two catheter-based devices were necessary to prevent systemic hypertension in the SVC.

Alternate design concepts to support the venous caval flow of the Fontan circulation include turbine-based assist system. One proposed device uses the elevated arterial blood pressure to drive a venous pump through a turbine-like mechanism [83]. The van Karaman impeller pump is shown in Figure 66E aims to avoid large flow barriers through vessel ligation, hemolysis, and the potential collapse of the caval veins by placing a flat spinning disk in the center of the Fontan cross [62]. The disk rotates to pull blood from the caval veins and push it in the x-axis towards the pulmonary arteries. Efficacy of such devices has not been proven to date and the introduction of additional devices in the Fontan flow constitutes additional flow obstructions and origins for thrombus formation.

Generally, Fontan assist strategies should minimize flow obstruction to preserve the notoriously low flow energy. This is especially important during high flow periods caused by the respiratory pump. Any implanted pumps in the IVC come with great risks as they increase resistance in the already compromised venous flow. Any support strategy must be tailored in terms of flow resistance and actuation timing to the flow pattern of the hemodynamic Fontan phenotype. Hence, current research with available circulatory support systems has only shown promising results as short-term bridge-to-transplant application.

Potential benefits of pulsatile flow support in the IVC

Venous return through the Fontan shunt exhibits lower levels of pulsatility generated by ventricular pumping resulting in a more continuous flow though the lungs and detrimental physiological effects of the lower pulse wave pressures have been underscored. Elevated PVR is a hallmark of failing Fontan physiology. The lack of a sub-pulmonary pump results in chronic low pulsatile flow to the lungs and in conjunction with the absence of high flow and pressures during normal exercise it can lead to endothelial dysfunction and increase PVR of up to four-fold[84], [85]. After heart transplantation and restoration of pulsatile flow, this elevated PVR was shown to be reversible. Additionally, the non-pulsatile flow dynamics of the Fontan circulation predisposes patients to thromboembolic events[14].

Both mechanisms underscore the potential benefits of pulsatile support of the Fontan physiology. Skeletal muscle contraction and respiration are two biomechanical factors that greatly influence venous return in the Fontan circulation. Skeletal muscles in the lower limbs contract around the vasculature and propel blood towards the lungs in conjunction with bileaflet venous valves[86]. It has been reported that weight training to augment muscle mass and strength improves Fontan hemodynamics[87]. This mechanism underscores the efficacy of tubular contraction in combination with valves and ought to serve as guidance in the development of support strategies for the Fontan flow.

Fontan specific extravascular pumps

A support strategy based on the existing cavopulmonary shunt that minimizes flow obstruction during forward flow but propels blood towards the lungs through an extra-vascular contraction during retrograde flow could be incorporated in the current treatment of Fontan patients. The system would aim to establish higher pulmonary flow, decreasing systemic hypertension and could thereby mitigate the adverse pathophysiological consequences.

Autologous skeletal muscle wrapped around the Fontan shunt was suggested to create an external compression pump. Latissimus dorsi muscle from the patient could be paced by an electrical impulse generator to create an untethered system as shown in Figure 66H [88], [89]. In previous studies physiologically normal pressure in the IVC failed to provide a suitable preload to the conduit after muscle transplantation. Moreover, enthusiasm for use of autologous muscle to create a pulsatile Fontan pump waned due to patient morbidity at the excision site, overstimulation of the skeletal muscle leading to muscle injury, and harmful remodeling of contractile muscle into fibrofatty tissue [90], [91].

Still, the potential benefits of non-blood contacting, non-flow obstructing designs are driving recent development of extravascular pumps. As such, the c-pulse system (CHF Solutions, Inc. Eden Prairie, Minnesota) was designed as an extra-aortic balloon pump and was tested in combination with valves to provide directional flow in the Fontan IVC [92]. Synthetic shape memory fibers were placed around the model of a Fontan shunt to create a peristaltic compression pump and augment venous flow [64]. A bio-engineered pump uses decellularized urinary bladder material to create a biologic reservoir which can be combined with valves and an adjacent compression device aiming to support forward flow in the venous Fontan circulation [93]. Advancements in stem cell research have fueled the approach of a tissue engineered pulsatile conduit to serve as sub-pulmonary pump in the Fontan circulation [94]. A non-invasive approach to augmenting venous return was suggested by applying external compression therapy to the limbs using compression trousers shown in Figure 66F. Support reduced patient's mobility, yet a pilot study of two patients showed encouraging results for further investigations [63].

Overall extravascular pump systems targeting a peristaltic support of the Fontan IVC are promising approaches in current research. Even though multiple technological solutions are suggested computational simulations and any proof of efficacy in a physiologically relevant Fontan flow model are lacking.

Valves as passive support strategies

With recent emphasis on the abnormal venous flow patterns including large amounts of retrograde flow in the Fontan IVC passive support strategies have been suggested. Valve usage in the correction of vessel flow anomalies is robustly incorporated in modern medical workflows and generally presents with risks which Fontan hemodynamics are inherently challenged by already: 1) increased propensity for driving thromboembolic events and 2) flow disturbance which diminishes flow energy [95], [96]. Clinically available mechanical valves are designed

for use in a high pressure, high flow environment and implanting them in a low flow environment such as the Fontan venous flow may make render them even more susceptible to thrombus formation [97].

Unidirectional valves positioned in the venous Fontan flow have been suggested both in combination with compression devices or skeletal muscle pumps [89], [92], [93] and as standalone strategies to improve univentricular hemodynamics [53], [98]. Even though directional blood flow was achieved, energy loss was diminished, and temporary alleviation of hepatic pressure were reported, no improvements of overall flow or pressure were achieved. Previous exploration of valve performance did not include effects of respiratory biomechanics on pulmonary and systemic vascular beds. It was underscored that the positive effect of valve placement in the Fontan IVC increases with more baseline retrograde IVC flow. During previous investigations valves performance was tested up to a reverse flow of 10% [37] however, recent clinical studies revealed that reverse flow varies greatly in the Fontan patients and can reach over 30 % of the total IVC flow [4]. A trileaflet, distal bovine venous valve positioned in the Fontan shunt was tested in a bench top flow loop and showed promising results, suggesting that a valve more closely linked to a low flow-high pressure system could improve hemodynamics by lowering hepatic pressures and minimizing energy loss within the shunt [98]. These studies pave the way to designing a valve specific for low flow-high pressure environments (i.e. Fontan IVC). Del Nido et al. suggested that modelling venous valve designs with a bileaflet fabrication offers superior versatility to vessels of different sizes by preserving coaptation height, coaptation area, and normalised valve orifice area as opposed to tricuspid valve designs[99], [100].

4.1.2 Limitations addressed in this chapter

Circulatory assist devices introduce turbulence and cause flow obstructions which may lead to decrease flow energy and increased risk of thromboembolic events. The high pressure and low flow circulation of the venous Fontan physiology is inherently vulnerable to those disturbances and hence focus should lie on minimizing both. This requires support strategies particularly designed for the Fontan flow and performance evaluation in physiologically similar test environments. This chapter addresses the aforementioned shortcomings by designing two of the most promising Fontan specific support strategies and evaluating them in the previously clinically validated biomimetic cardiorespiratory flow simulator (Chapter 1). Active and passive support strategies will be designed, manufactured, and tested for their potential to improve Fontan hemodynamics.

Firstly, an extravascular peristaltic pump system will be developed due to its decreased blood contact and flow obstruction, as well as the potential benefits of pulsatile support for the Fontan venous vasculature. The actuation method will be chosen to allow for adequate power transmission to the flow and peristaltic motion to create the pump function will be achieve in a compressing manner, as suggested previously. An expanding configuration of a peristaltic extravascular pump will be explored to further minimize flow obstructions.

Secondly, a unidirectional valve will be designed specifically for the hemodynamic requirements of the Fontan IVC flow. The bioinspired bench top and computational models described in chapter 1 will be used to compare available valve designs and optimize the most suitable approach based on minimal flow obstruction and thromboembolic risk. The efficacy of such a valve will be evaluated in varying breathing patterns and physiological positions. To further decrease blood contacting and flow obstruction the feasibility of an extravascular occluder device triggered by flow reversal in the IVC which functions as a unidirectional valve will be investigated.

Lastly, active and passive support strategies will be combined on the bench top to explore their potential efficacy to support the Fontan circulation.

4.1.3 Specific aims

To date, no circulatory support strategy has been approved to remedy the adverse hemodynamics of the Fontan IVC flow. Approaches focus on the support of the sub-pulmonary venous return but simple adaptation of existing systems developed for bi-ventricular physiology failed. Also, the lack of testing devices on physiologically relevant test platform which include respiratory biomechanics and validated computational models hamper advancement. This demands for strategies specifically tailored to address the hemodynamic conditions of Fontan flow to minimizing flow obstruction and turbulence formation.

The goal of this chapter is to develop support strategies that are most promising according to the current state of the field and evaluate their performance in the aforementioned simulator platform. Towards the end, **the specific aims** are to

1. Design, manufacture, and evaluate an active extravascular circulatory support strategy using soft robotic techniques at the existing Fontan shunt.

2. Design, manufacture, and evaluate a passive circulatory support strategy in the existing Fontan shunt to prevent retrograde flow.

3. To combine and evaluate the active and passive circulatory support strategies.

4.2 Methods

Figure 67 shows an overview of the conducted studies including the desired outcomes for chapters 1, 2, and 3.

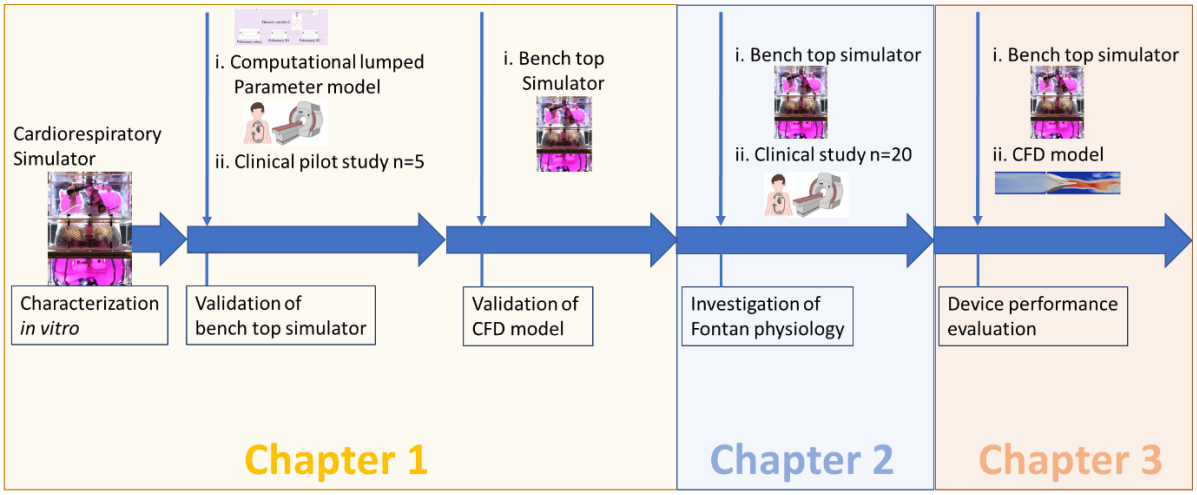

Figure 67 : Schematic showing the sequence of studies for chapters 1,2, and 3.

4.2.1 Extravascular compression pump around the existing Fontan shunt

Actuation sleeve design and manufacturing

The targeted impedance pump must generate enough axial pressure on the Fontan conduit to displace blood even in elevated blood pressures of the congested Fontan IVC. Figure 68 shows a schematic of the relationship between the pressure inside a vessel and the hoop stress which act around the circumstance of the vessel. A device which wraps around the conduit circumferentially needs to overcome this this hoop stress to achieve compression.

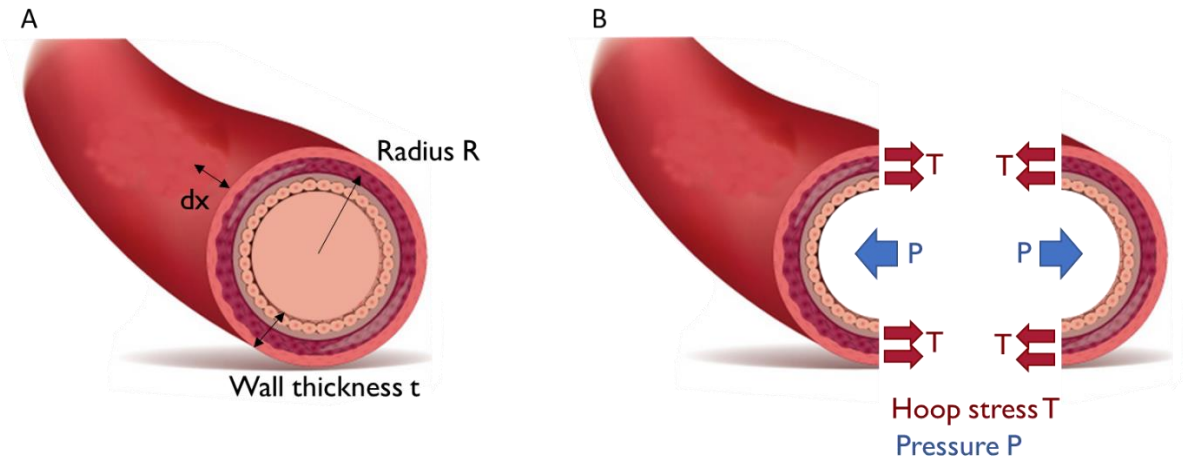

Figure 68 : Schematic of relationship between intravascular pressure and hoop tension of the vessel walls. For thin-walled vessels (A) we see the hoop stress T which is caused by the blood pressure P inside of the vessel (B).

Hoop stress defined for rotationally symmetric objects as vessels, pipe, or tubing like the Fontan shunt as mechanical stress. For a vessel it can be illustrated as the tension applied to the vessel walls to hold together the blood pressure inside. It is the force equilibrium between the fluid forces acting to push out the vessel walls and the circumferential counterforces. The classic equation for hoop stress created by an internal pressure on a thin wall cylindrical is given in Equation 8 [101]:

$$T = \frac{P * R}{t}$$

Equation 8

where T, the hoop stress, P the internal pressure; *t*, the wall thickness; *R*, the radius of the cylinder or vessel. For elevated physiological IVC pressure of 25 mmHg this would result in a compression force of 3 N which a compression element needs to exert on the vessels to generate compression. To ensure rapid actuation capabilities, and a wide range a possible force generation we used circumferentially designed McKibben pneumatic actuators as described previously [42]. We manufactured these actuators using soft robotic manufacturing techniques as described in section 2.2.1 and manufactured different sized as seen in Figure 69. We used the custom pneumatic control box described in section 2.2.1 to actuate the pneumatic actuators. Two versions design were made: (1.) a smaller starting diameter of 20 mm (Figure 69A) which fits the outer dimension of a standard Fontan TCPC conduit, starts at a non-inflated resting positing and occludes the inner diameter upon actuation(Figure 69B), and (2.) a larger diameter

of 45 mm (Figure 69), which starts in a resting configuration around the 20 mm Fontan conduit and expands actuated by vacuum (Figure 69C).

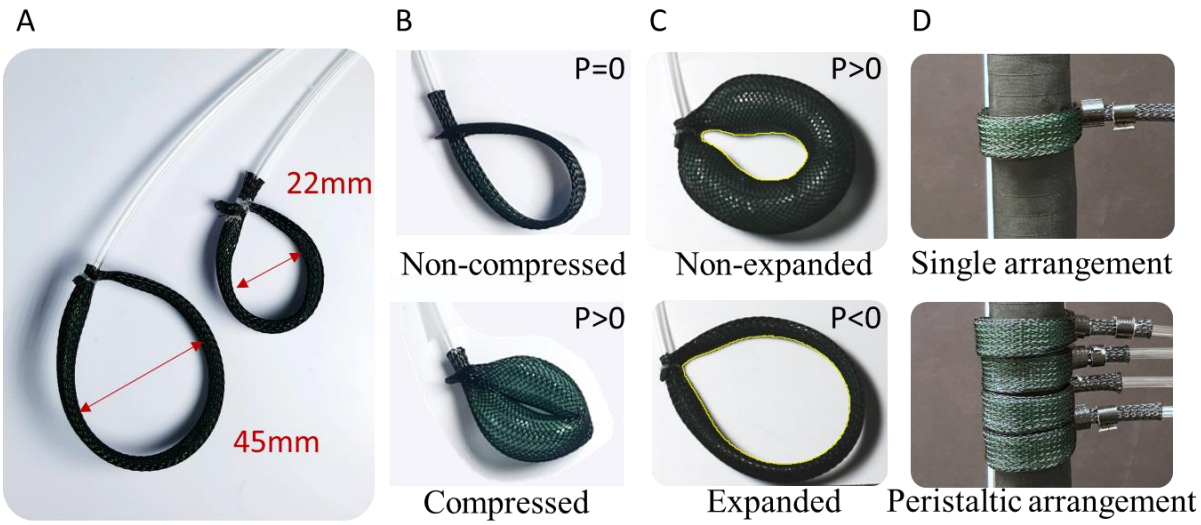

Figure 69 : McKibben bases pneumatic actuation elements. Different designs with variable inner diameter (A) realize either compression (B) or expansion (C) motion and can be assembled individually or in a group to allow for peristaltic motion (D).

Device characterization

With this design both compression and expansion could be achieved with the soft actuators. Either actuation element could be positioned around the Fontan conduit individually or as a group to allow for sequential actuation to generate a peristaltic compression or expansion motion (Figure 69D).

We assembled the pneumatic actuation units in a 50mm long sleeve around a “Dacron” shunt material which simulated the Fontan TCPC shunt as shown in Figure 70A.

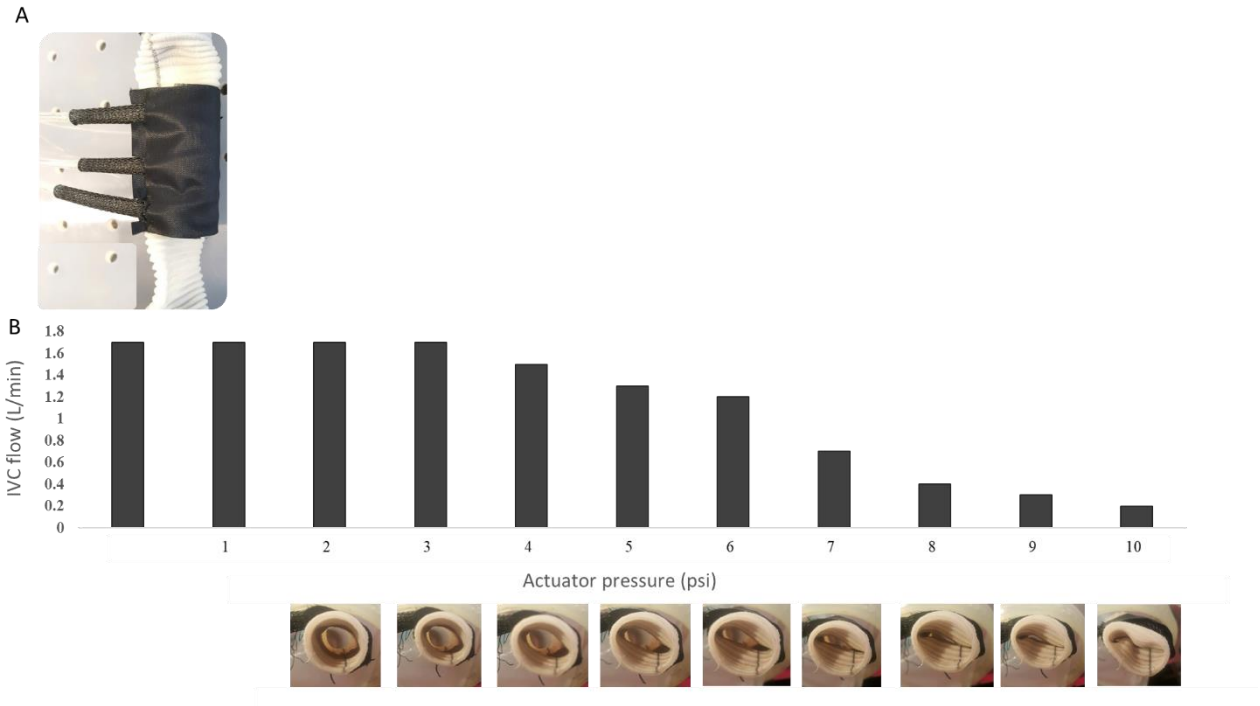

Figure 70 : Assembly of compression sleeve (A) and characterization of the compression deformation of the TCPC shunt (B).

We then characterized the compression sleeve in the bench top simulator. For this we set the IVC flow rate to a physiological level (1.7 L/min) and gradually increase the actuation pressure provided to the pneumatic compression elements using the pneumatic control system described in section 2.2.1. The inflating elements gradually diminished the IVC flow as shown in Figure 70B. We were able to achieve complete occlusion of the shunt lumen at 10 psi which was set as the actuation pressure during following testing in the flow loop.

Figure 71 shows a schematic of the mechanism of action of the peristaltic compression pump consisting of three pneumatic elements. Before the first compression the flow resistance is similar on both sides of the first contracting pneumatic element so during the first contraction fluid volume is displaced forward as well as against the baseline flow direction. When the second compression element contract the first contraction element increased the flow resistance for the generation of retrograde pushed volume. Hence, the displaced volume from the actuator contraction is pushed forward. This is repeated for the third compression actuator creating a peristaltic motion and displacing volume forward. Device relaxation is also performed in a peristaltic manner to draw upstream fluid into the pump instead of sucking downstream volume back.

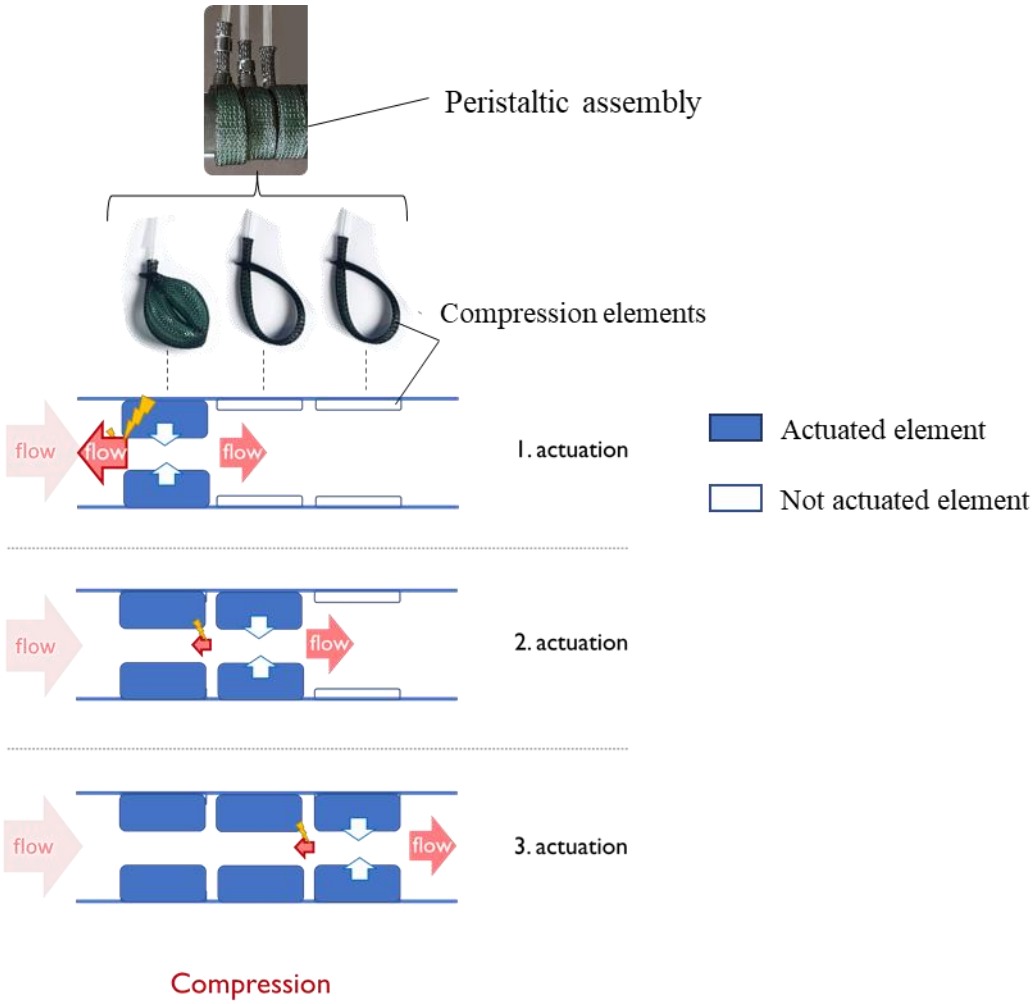

Figure 71 : Schematic explaining the mechanism of action for the extravascular compression pump with peristaltic motion. Sequential compression drives flow volume forward and sequential expansion of draws fluid into the pump lumen.

We then determined the forward flow which can be achieved by such a peristaltic compression pump dimensioned to fit a commonly sized Fontan shunt. We analytically simulated the a Fontan shunt with 50 mm length and a diameter of 20 mm in software Matlab (MathWorks, USA). The results of this the compression model is shown in Figure 72. With contraction of the first element, we see a peak in the forward and backward displacement of volume. This if followed by the contraction of the second and third element which displace volume more to forwards as explained in Figure 71. During relaxation of the first element, we see that fluid is drawn inside of the pump from upstream of the pump while the contracted second and third element block the backward suction of fluid volume downstream of the pump. This backward draw of fluid is increased as the last element relaxed.

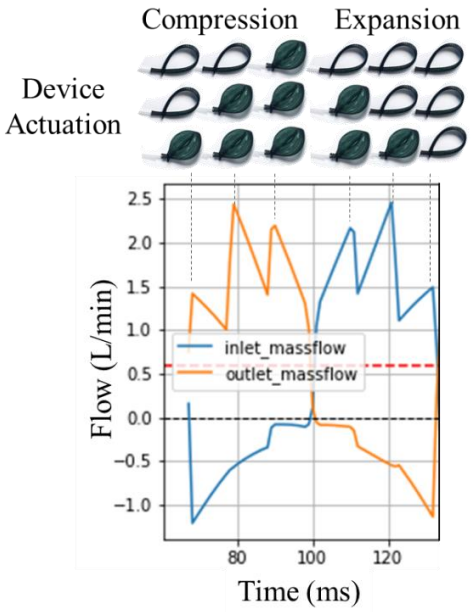

Figure 72 : Analytical evaluation of displaced volume during one actuation cycle of the extravascular compression pump. The blue line indicated the flow rate at the pump inlet while the orange line indicates the simultaneous flow rate at the pump outlet and the red dotted line indicates the average flow rate.

Figure 72 illustrates important characteristics to optimize actuation patterns for forward displaced volume which include: (1) each compression element should contract or relax when the previous element has just finished contraction or relaxation and the time delay should be minimized to the inflation time of one pneumatic element. (2) Delay between each actuation cycle should be minimized to create a continuous peristaltic motion displacing fluid forward. (3) More forward flow can be achieved by adding a greater number of pneumatic elements. Due to the average length of the Fontan shunt to be 50 mm we were limited to three pneumatic elements in the sleeve. Because the inflation time of one pneumatic element was measured to be 80 ms the time delay between each actuation ring was set to 80 ms resulting in a actuation cycle time of 240 ms with a relaxation cycle time of 240 ms and a resulting total actuation period of 480 ms which was repeated continuously for device testing. With this actuation setting a mean forward flow rate of 0.6 L/min was calculated for the performance of the compression pump alone.

Device testing in cardiorespiratory simulator

We then installed the compression pump in the biomimetic cardiorespiratory simulator described in section 2.2.2. For this purpose, we removed a portion of the thoracic IVC and

replaced it with the compression pump shown in Figure 70A. Additional ports in simulated thoracic cavity of the bench top simulator served to connect each individual compression element with a pressure port of the custom electropneumatic control box. The cardiorespiratory simulator was actuated at a respiratory rate of 14 min^{-1} and an input pressure of 12 psi, a baseline IVC pressure of 17 mmHg and baseline flow rate of 1.7 L/min. We tested two actuation configurations with the compression pump: (i) continuous actuation, and (ii) actuation during retrograde flow periods. For (i) we set the device settings as described above on a continuous cycle. For (ii) we aimed to actuate the pump only during the time when the IVC flow reverses due to expiration. To sense the initiation of retrograde flow and start actuation we developed a trigger mechanism based on the IVC flow rates. When the IVC flow dropped beneath the positive flow rate values the pump was started and stopped actuation when the trigger mechanism showed forward flow during inspiration again. The trigger mechanism was implemented as follows: An Arduino that controlled the pressure regulators (ITV1031-21N2BL4, SMC Corporation) in the pneumatic control box received the analog signal from the IVC flow. The signal output from the flow meter, in the range of -5 to 5V, was passed through a differential amplifier circuit with gain of 0.5 and DC voltage offset of 2.5V to convert the signal into the 0-5V range needed for the Arduino analog input. Before connection to the Arduino, the output of the differential amplifier was connected to a passive low-pass filter (a resistor and capacitor in series) to help eliminate signal noise. A schematic of this circuity is shown in Figure 73.

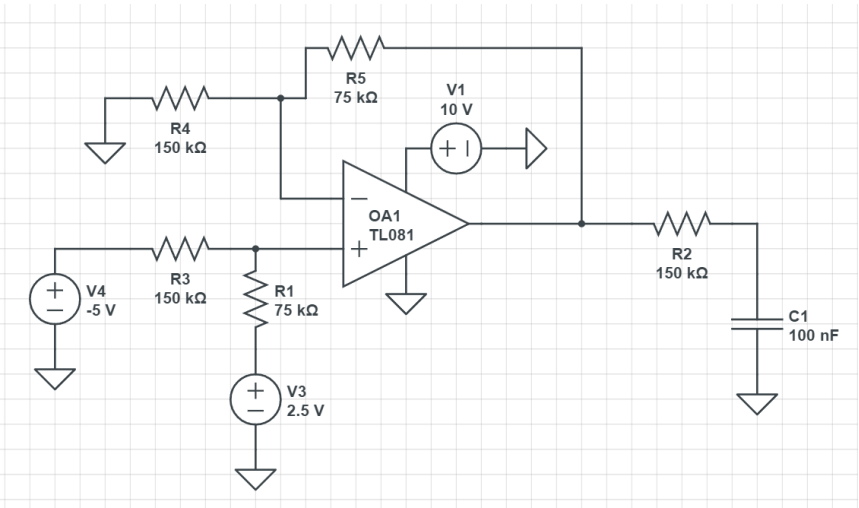

Figure 73 : Schematic of the differential amplifier to convert the flow signal into an analog range between zero and five volts.

4.2.2 Extravascular expansion pump around the existing Fontan shunt

To reduce flow obstruction in the IVC due to the narrowing of the IVC lumen by the extravascular compression device described in section 4.2.1 we developed an extravascular expansion

device using the same manufacturing methods as described in section 4.2.1. The expansion device was designed to fit the same section of the Fontan shunt made from Dacron material (three actuation elements on a 50 mm long shunt which has a 20 mm diameter). The actuators were resting at an actuation pressure of 10 psi which reduced the inner diameter to 20 mm as shown in Figure 69C. During actuation the inside of the pneumatic elements is vacuumed to pull the shunt material outwards to a diameter of 45 mm. We assembled three of these expansion elements in series which each underwent the oscillatory motion from inner diameter 20 mm to 45 mm and back during one actuation cycle. By triggering each expansion element sequentially, we generated a peristaltic pump motion without diminishing the baseline lumen and hence increasing flow resistance in the IVC. This actuation principle is illustrated in Figure 74.

Before the first expansion the flow resistance is similar on both sides of the first expanding pneumatic element so during the first expansion fluid volume is drawn into the generated volume from upstream and downstream of the expanding element. When the second expansion element is pulls out more volume the first element decreased the flow resistance upstream so the second expansion draws more volume from the upstream direction compared to the downstream direction. This is repeated for the following expansion element. Contraction back to the 20 mm diameter follow same principle as illustrated in Figure 72. Thus, cyclical actuation acts as a peristaltic pump with a minimum diameter of the inner lumen of 20 mm and a maximum diameter of 45 mm.

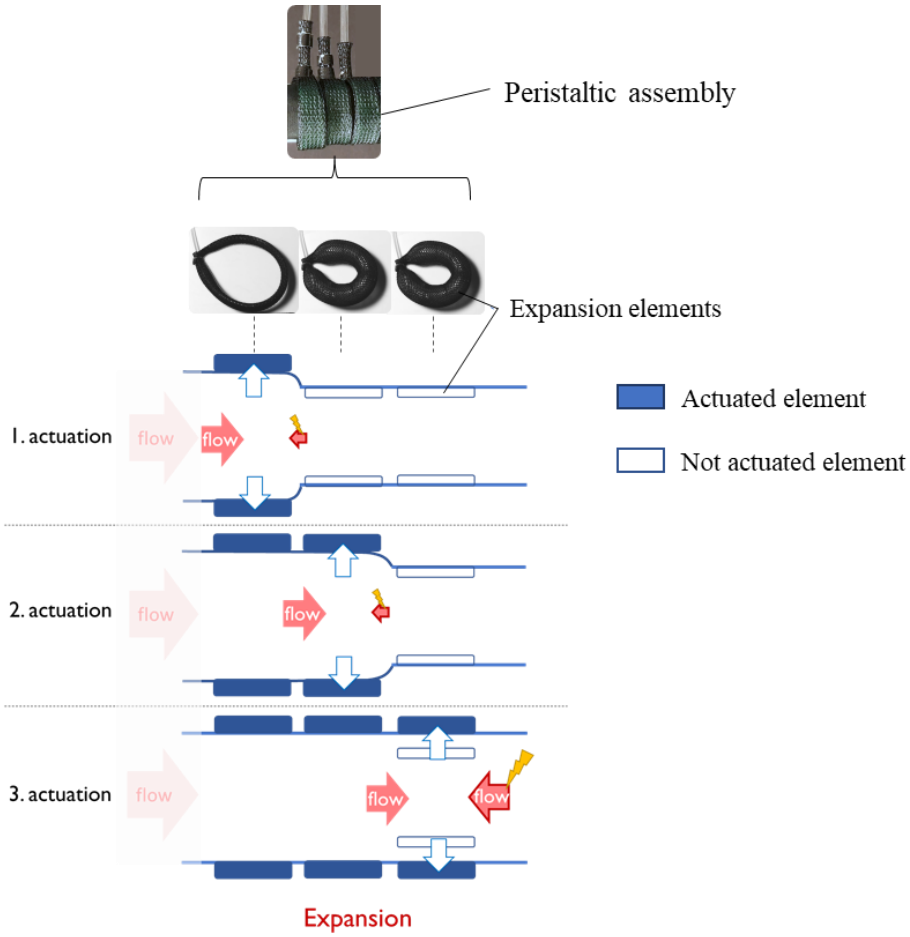

Figure 74 : Schematic explaining the mechanism of action for the extravascular expansion pump with peristaltic motion. Sequential expansion from the starting diameter drives flow volume forward.

The main purpose of the extravascular pump, as any pump, is to add energy, also called head gains, to the flow. A pump is defined by its characteristic curve, which relates the pump head, to the flow and is indicative of the ability of the pump to add head at different flow rates. This characteristic curve remains constant but may shift depending on the ability of the pump to propel fluid forward. In the case of an impeller-based pump this shift is mainly due to impeller size and speed.

To test the functionality of this peristaltic expansion pump simplified our bench top flow model to create programmable pressure or flow conditions between two fluid reservoirs which are connected through a segment including the extra vascular pump (Figure 75A). To ascertain the ability of the pump design to generate head pressure, we adjusted the two reservoirs at the same height resulting in zero initial flow and pressure gradient. We expected the pump to generate a pressure head and gradient between the two fluid reservoirs which corresponds to the point on the far left of its characteristic pump curve shown in Figure 75B. We varied the actuation regime to evaluate the amount of generated head pressure which will be indicative of the effectiveness of the pump design.

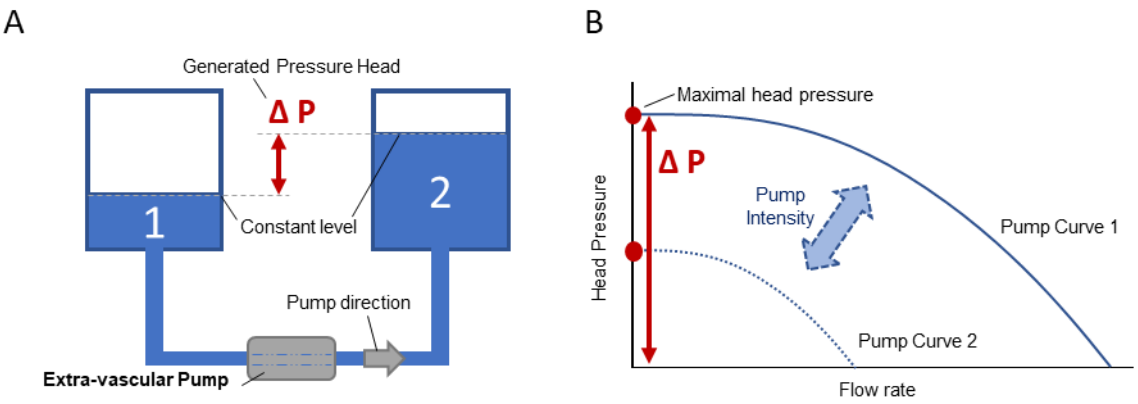

Figure 75 : Experimental setup to test the generated pressure head of the extravascular expansion pump and a schematic of a characteristic fluid pump curve.

We actuated the peristaltic expansion pump at a expansion and contraction time of a single element of 80ms, delay between each actuated segment of 80 ms, and total cycle time of 480 ms. Holding pressure was set to 10 psi and vacuumed for device expansion. We successfully generated a head pressure of 14 mmHg. If this pressure gradient could be transferred to the Fontan IVC it could generate the previously described 6 mmHg alleviation of IVC pressure which was deemed to have clinically relevant end-organ effects to mitigate venous congestion.

We then installed the expansion pump in the biomimetic cardiorespiratory simulator described in section 2.2.2. For this purpose, we removed a portion of the thoracic IVC and replaced it with the expansion pump. Additional ports in simulated thoracic cavity of the bench top simulator served to connect each individual compression element with a pressure and vacuum port of the custom electropneumatic control box. The cardiorespiratory simulator was actuated at a respiratory rate of 14 min^{-1} and an input pressure of 12 psi, a baseline IVC pressure of 17 mmHg and baseline flow rate of 1.7 L/min. We tested two actuation configurations of the expansion pump: (i) continuous actuation, and (ii) actuation only during retrograde flow periods. For (i) we set the device settings as described above on a continuous cycle. For (ii) we triggered the actuation only during negative flow rates in the IVC and used the IVC flow trigger mechanism described in section 4.2.1.

4.2.3 Passive support strategies in existing Fontan shunt

One way valve evaluation in the Fontan IVC

Valve placement in the Fontan IVC has been suggested as discussed in section 4.1.1 but characterization in a physiologically relevant bench top model was limited. We leveraged our clinically validated cardiorespiratory Fontan simulator to test the placement of a one-way valve in

the already existing Shunt of the Fontan TCPC. Towards this end we placed a mechanical St. Jude valve in the simulated Fontan shunt as shown in Figure 76.

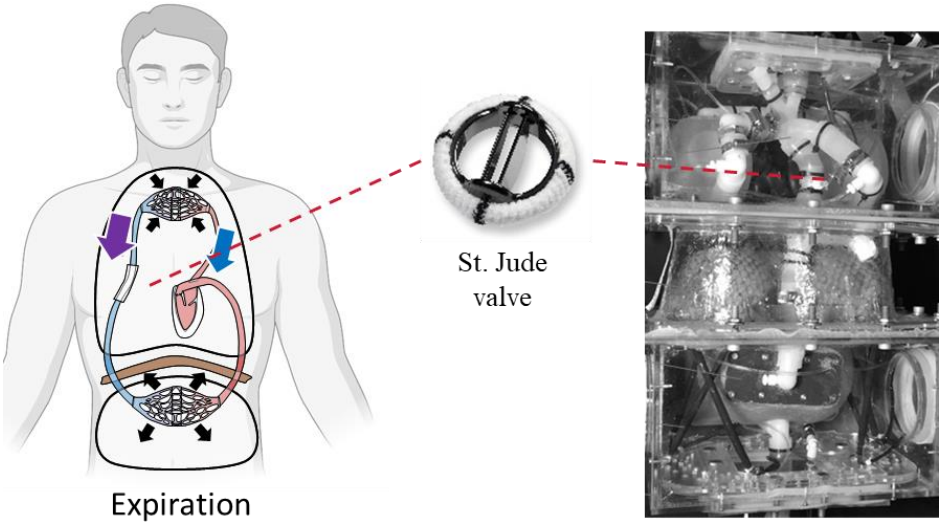

Figure 76 : Mechanical valve placement in the Fontan IVC. Schematic of the physiological placement and the positioning in the cardiorespiratory bench top model.

The valve size matched the Fontan shunt size with an inner diameter of 20 mm. The goal was to evaluate if the mechanical valve can top the retrograde flow in the Fontan IVC during expiration and improve hemodynamics throughout the respiratory cycle. We tested the valve performance in a parameter study of increasing respiratory rates. This would allow us to compare the hemodynamic impact of valve placement with increased amounts of retrograde flow and pressure conditions. For all testing of the valved and valve-less Fontan shunt the baseline parameters were as follows: 1.7 L/min baseline flow, 17 mmHg baseline IVC pressure, -4 mmHg baseline thoracic pressure, 7 mmHg abdominal pressure, 14 min^{-1}respiratory rate, and increasing respiratory effort with 12.5 psi, 15 psi, and 17.5 psi pressure provided to the contraction elements of the diaphragm. To evaluate valve performance we monitored IVC flow rates, SVC flow rates, thoracic, and abdominal pressures, IVC fluid pressures in the location of the hepatic vein in the abdomen, and IVC fluid pressures in the location of the TCPC in the thorax as described in section 2.2.2.

Feasibility study of extravascular occluder device functioning as one-way valve

Because of the low energy flow conditions minimal flow obstruction in the IVC is a key feature of potential Fontan circulatory support strategies as described in section 4.1.1. Mechanical valves can be optimized for specific flow conditions but are inherently intravascular. To lower the flow obstruction extravascular approaches of peristaltic pump systems have been described in section 4.1.1 and section 4.2.1. Here we suggest using concepts of extravascular actuation

but with the target of recreating the functionality of a one-way valve. This extravascular occluder device would be placed around the Fontan shunt in the IVC and occluder IVC retrograde flow but provide no flow obstruction during forward flow. Toward this concept we used a single-element configuration of the compression actuator as shown in Figure 69D paired with the flow sensing and triggering software describe in section 4.2.1.

We compared the ability of the extravascular occluder device to stop retrograde flow in the Fontan IVC to the performance of the intravascular mechanical valve. For this experiment the baseline parameters were as follows: 1.7 L/min baseline flow, 17 mmHg baseline IVC pressure, -4 mmHg baseline thoracic pressure, 7 mmHg abdominal pressure, 14 min^{-1}respiratory rate, and 12.5 psi pressure supply to contract the diaphragm. To evaluate device performance, we monitored IVC flow rates to compare the resulting flow waveform, calculated the flow volume and the percent retrograde flow as described in section 2.2.2.

4.2.4 Combination of active and passive support strategies in existing Fontan shunt

As described in section 4.2.1 extravascular compression in combination with the placement of an intravascular one-way valve to act as like the lacking sub-pulmonary has been suggested for decades and is subject of current research. Still, reported characterization of such an approach in a physiologically relevant bench top model is limited. We leveraged our clinically validated cardiorespiratory Fontan simulator to test the placement of this combination of an active compression pump and a one-way valve in the already existing Fontan shunt.

To evaluate the feasibility of the combination of active and passive support strategies we repeated the analytic evaluation of the compression pump described in section 4.2.1. For this purpose, we changed the boundary conditions to include a one-way wave in the shunt inlet and an additional one-way valve in the shunt outlet as indicated in Figure 77.

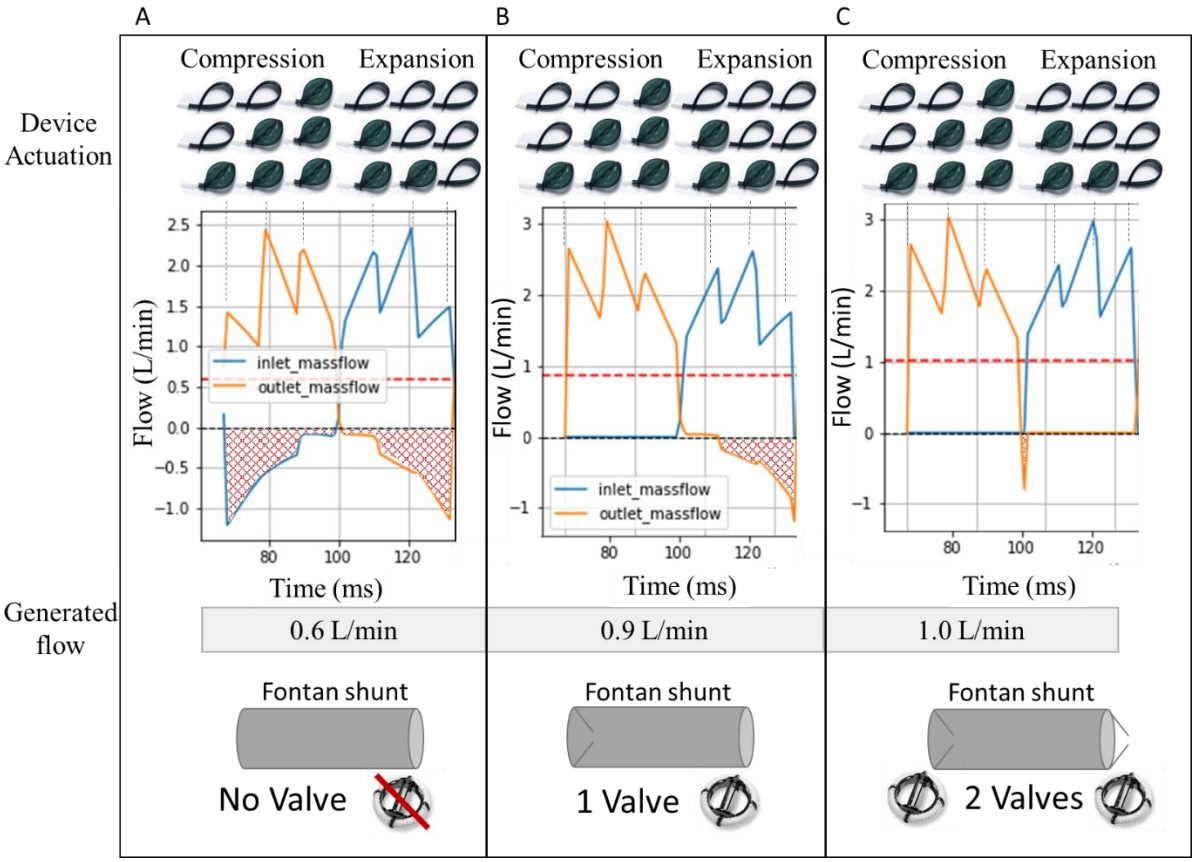

Figure 77 : Analytical evaluation of displaced volume during one actuation cycle of the extravascular compression pump with no (A), one (B), and two valves (C). The compression sequence of each actuator in the compression sleeve is indicated on top, the blue line indicates the flow rate at the pump inlet, the orange line indicates the flow rate at the pump outlet, the red dotted line indicates the average flow rate, and the red shaded area indicates the flow rate pushed against the baseline IVC flow direction.

Forward and reverse flow generation by the individual contractions of the three compression elements in the pump sleeve without the combination of a one-way valve are shown in Figure 77A and were explained in section 4.2.1. With the placement of a one-way valve at the inlet of the pump reverse flow volume against the baseline IVC flow direction is stopped during device compression as seen in Figure 77B which increases forward flow. At an actuation period of 240 ms this resulted in an elevated forward flow rate generated by the pump alone of 0.9 L/min compared to 0.6 L/min without the combination with a valve. With the addition of another one-way valve at the outflow of the pump the backward draw of blood during device relaxation is also blocked resulting in a total forward flow rate of 1 L/min.

To test the functionality of the combined active and passive flow support strategy on our cardiorespiratory simulator, we placed the passive support device in from of a mechanical St. Jude valve in series with the active soft compression pump. We investigated the combination of both (i) the compression pump described in section 4.2.1 and (ii) the expansion pump described in section 4.2.2 with the one-way valve in the IVC.

For all tests we set the baseline parameters as follows: 1.7 L/min baseline flow, 17 mmHg baseline IVC pressure, -4 mmHg baseline thoracic pressure, 7 mmHg abdominal pressure, 14 min^{-1}respiratory rate, and 12.5 psi pressure supply to contract the diaphragm. To evaluate device performance, we monitored IVC flow rates, and pressures as described in section 2.2.2.

4.2.5 Optimization of valve design for the Fontan IVC

To develop a valve specifically for the Fontan IVC we chose an optimization cycle illustrated in Figure 78. Starting with the performance of the mechanical St. Jude valve in the Fontan bench top simulator we made computational models of the mechanical valve and other promising approaches to evaluate the most suitable geometries for the loading cycles in the Fontan IVC flow. Subsequently, we used the most suitable designs and tested them in the computational fluid dynamics (CFD) model which was validated with the biomimetic bench top simulator as is described in section 2. We then developed manufacturing techniques, fabricated prototypes, and performed initial performance characterization compared with the commercially available mechanical valve. We explored different design parameters of (i) trileaflet like they are found in the heart and (ii) bileaflet valves like they are found in the venous vasculature.

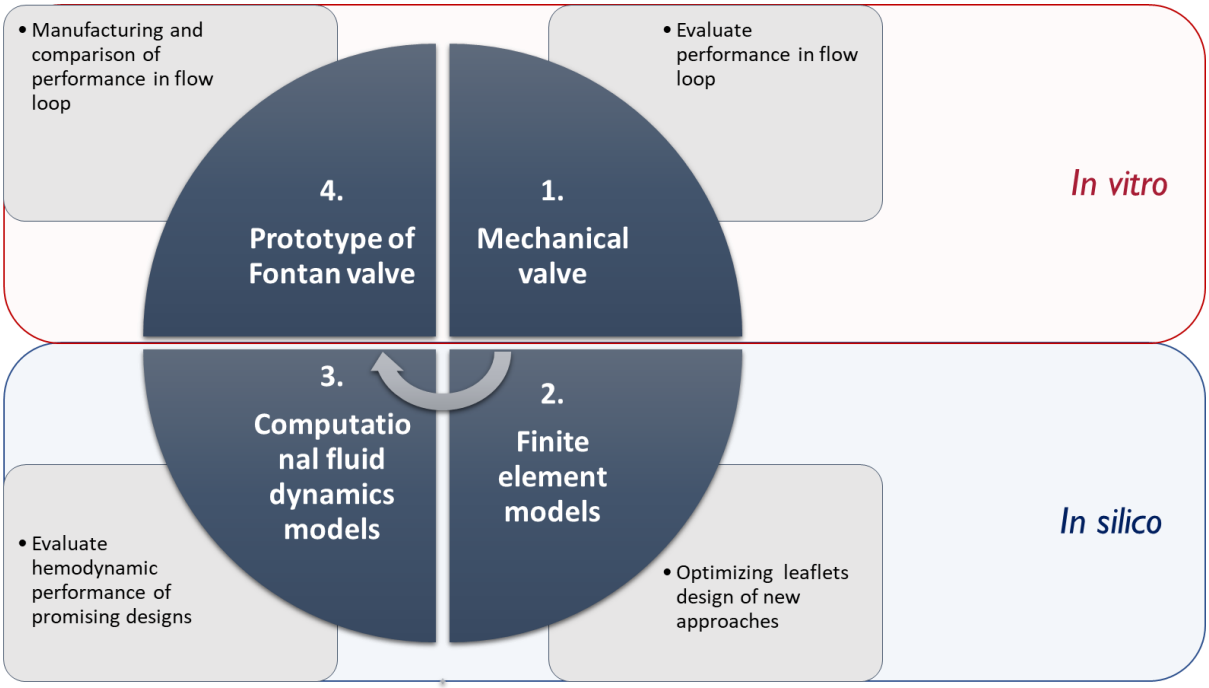

Figure 78 : Optimization cycle to develop a valve specifically for the Fontan IVC.

Finite element (FE) modelling

Finite element analysis (FEA) was conducted to characterize valve closure profiles and evaluate the stress/strain distribution on the leaflet surface. The valves were constructed using computer aided design (CAD) software SolidWorks (Dassault Systèmes) and imported into Abaqus 2018

software (Simulia, Dassault Systèmes). Loading states were derived from fluid dynamic measurements in the Fontan cardiorespiratory simulator during the following baseline values: 1.7 L/min baseline flow, 17 mmHg baseline IVC pressure, -4 mmHg baseline thoracic pressure, 7 mmHg abdominal pressure, 14 min^{-1}respiratory rate, and 12.5 psi pressure supply to contract the diaphragm. Nonlinear explicit dynamic analysis was performed to simulate the mechanical characteristics of valve in closed position. The leaflets were modelled as 3-node triangular shell elements (S3R) and assigned isotropic Marlow hyperelastic ePTFE material properties with 0.1 mm thickness. Uniaxial test data was used as an input source for the hyperelastic model. The transvalvular pressure gradient waveform obtained from the in-vitro test was then used as the dynamic pressure loading boundary condition to simulate realistic valve closure and quasi-static deformation was achieved. These studies were performed using Abaqus/Explicit solver and each model was completed in approximately 2 hours on a desktop PC with a 3.0 GHZ i7-9700 processor with 8 cores and 32 GB RAM.

Computational fluid dynamic (CFD) modelling

In this study, XFlow 2020 (Dassault Systèmes) was used to model the blood flow through bileaflet valves and simulating flow patterns after implantation. Traditional numerical techniques are based on approaches that use finite volumes and finite elements, which are applied to Navier-Stokes equations. Despite Navier-Stokes solvers having been broadly employed in the literature, they suffer from several disadvantages, including inaccurate meshing and extremely empirical turbulence simulations (e.g., RANS)[102], [103]. The lattice Boltzmann formulation used was utilized to overcome these limitations.

A Large-Eddy Simulation (LES) turbulence model was utilized in XFlow 2020 software (Dassault Systèmes). A fully coupled fluid-structure interaction model was created to capture the local flow hemodynamics with the valve motion. Two-way coupling computation was applied between the structural and the fluid flow domain to simulate the dynamic flow features. The blood was modeled as an incompressible Newtonian fluid with 1050 kg/m3 density and 0.0035 Pas dynamic viscosity. The inlet and outlet ports were extended to facilitate convergence. The inlet was defined as a pressure input source imposing *in vitro* pressure measurements, and using the difference between the upstream and downstream. Outflow boundary condition was set to constant pressure of 0 mmHg allowing to monitor the outflow rate. The total simulation time was set to 10 seconds (~2 cycles) and the time step $\Delta t = 1x10\text{-}5s$ was applied for each simulation to ensure numerical stability. Grid independence is checked using three different grid sizes (the lattice resolution of 1.0mm, 0.6mm and 0.4mm). The convergence of the stability parameter

was achieved with a gap of 0.92% between the medium quality grid and the fine grid, hence the medium grid (0.6 mm resolution, ~530,000 elements) was considered grid independent. The refinement method with 0.3 mm resolution was applied near the walls to ensure enough lattice elements at the wall as a boundary layer. Analysis was completed in ~24 hours on a desktop PC with a 3.0 GHZ i7-9700 processor with 8 cores and 32 GB RAM.

Valve Design

We used venous valve designs as an input generate geometries for valve optimization study. Several valve characterization parameters, valve height (H), the valve diameter (D) and geometric area ratio (GOA) were utilized to determine the optimal valve geometry. Computer aided design (CAD) software SolidWorks (Dassault Systèmes) was used to perform solid modeling of valves. The leaflet profile geometry was first defined as a 2D sketch and then projected on the cylindrical or conical shapes to obtain different geometrical orifice area ratio. The valve height (H) and the leaflet mid-height (LH) were parametrically adjusted to perform commissure and coaptation profile assessment. The fundamental component of leaflet profile optimization was the varying aspect ratio between the valve diameter (D), valve height (H) and the leaflet mid-height (LH). The valve diameter was fixed at 19 mm throughout the leaflet optimization. Figure 79 shows the workflow for creating the primary valve shape and adjusting its geometrical parameters for optimization.

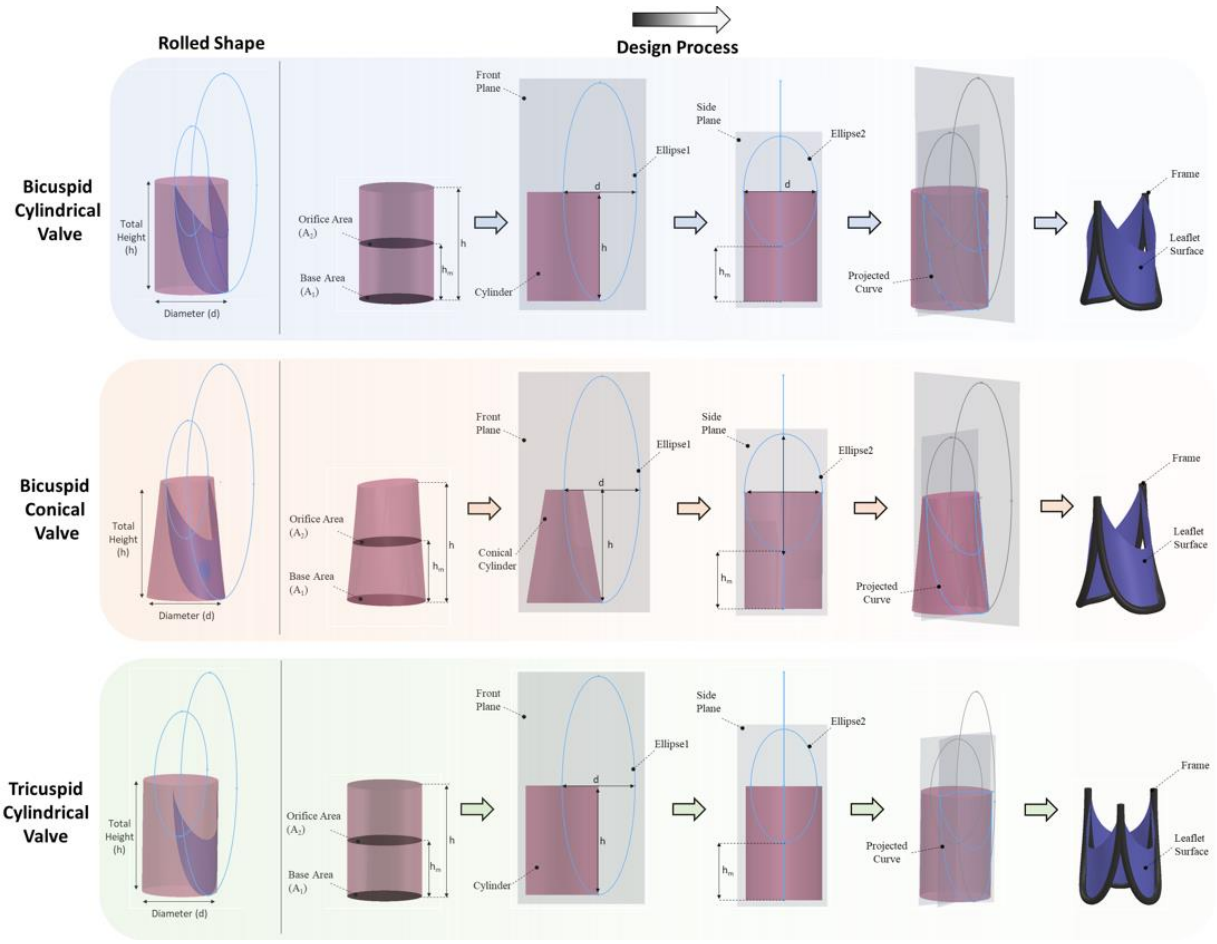

Figure 79 : Methodology for creating valve geometries

In silico hemodynamic index

Thromboembolism has been the most common adverse effect associated with Bileaflet mechanical valves, affecting around 0.1% to 5.7% per patient-year. [104], [105]. Over the last several decades, much emphasis has been paid to describing the effects of various hemodynamic stimuli on endothelial cell gene expression, which results in either pro-atherosclerotic or pro-thrombogenic phenotypes [106]. Numerous indices based on wall shear stress (WSS) and its temporal and spatial fluctuations have been presented with varying degrees of effectiveness.

The endothelial cell activation potential (ECAP) hemodynamic index was computed using fluid simulations to determine regions with low blood flow velocities and complicated flow patterns. It was initially created to characterize blood flow patterns derived from CFD simulations and identify pro-thrombotic regions in the LAA. [107]. This approach was used to improve the localization of endothelial areas exposed to low and oscillatory shear flows around the valve surface, both of which promote a pro-thrombogenic phenotype. The ECAP was calculated to

capture the mechanobiological effects in different valve designs [106]. It is calculated by combining the Time-Averaged Wall Shear Stress (TAWSS) and the Oscillatory Shear Index (OSI).

The time-averaged wall shear stress magnitude (TAWSS) was defined as:

$$TAWSS = \frac{1}{T}\int_0^T |WSS| dt$$

Equation 9

As low flow rates are associated with blood stasis and an increased risk of clotting, the TAWSS index were defined to measure the mechanobiological effects of the WSS on the wall surface [106]. To capture the WSS field direction changes due to complex flow patterns, OSI parameter is defined as:

$$OSI = \frac{1}{2}\frac{\int_0^T WSS dt}{\int_0^T |WSS| dt}$$

Equation 10

Finally, ECAP value is defined as the ratio between the OSI and the TAWSS:

$$ECAP = \frac{OSI}{TAWSS}$$

Equation 11

Using this algorithm to calculate ECAP values, it is possible to identify low-velocity areas with small TAWSS values and complex blood flows with large OSI values that are at risk of thrombus formation.

Valve Manufacturing

Frame

Frames were generated using SOLIDWORKS 2019. Frame dimensions were 2.5 mm thick, 28.5 mm high and 19 mm in luminal diameter and followed an ellipse-on-cylinder 3D projection. Frame holes were generated along the contour of the ellipse on cylinder projection, beginning at the tallest leaflet attachment edge (1 mm from the apex of the frame) and continuing around the frame following the leaflet attachment geometry. These holes were facing between lumen of the valve and eventual vessel wall and were created with a diameter of .6 mm were spaced 2 mm apart. The frame was 3D printed using an OBJET30 (Stratasys, Israel) 3D printer.

Leaflet

Leaflets were generated in SOLIDWORKS 2019 and were 75% of the total valve height (21.375 mm) at the free-leaflet edge midheight. These leaflets matched the ellipse-on-cylinder projection described above and followed the cylindrical contour to ensure maximum opening luminal diameter. Unrolling these leaflets to the 2d profile allowed us to generate templates. Templates were printed and used to cut out leaflets from .1 mm thickness ePTFE.

Assembly

6-0 non-resorbable prolene sutures (Medtronic) were used in the assembly process. Leaving the top hole at the apex of the valve on both sides free, the next hole was used to fasten the leaflet to the frame. Six knots were instrument tied in the following fashion: forward, forward, back, forward, back, forward. Across the lumen of the frame, the opposite leaflet edge was attached to the frame using the same knot at the second highest hole with respect to the frame apex. Then, following the curvature of the frame and with the leaflet guided to the open position, the same 6-part knot was tied at each hole along the curvature of the valve paying attention to not over-distending the material or overtightening the knots. The knots were tied in a fashion such that the bulk of their size was hidden within the frame hole. This process was repeated for the second leaflet.

Commissural Stitch

To ensure proper closing, a commissural stitch was used to adhere the luminal faces of the leaflets to each other and the frame. 6-0 prolene was used to tie this knot tied in the forward, forward, back, forward, back, forward fashion. At the empty hole at the apex of the frame (left unoccupied in the attachment process), the suture was guided through the leaflets (placed in a position to where the free leaflet edges were in the closed position to ensure geometric accuracy) then around the frame and back through the frame hole. The knot was embedded in the frame hole. This allowed the leaflets to remain in contact with each other and the frame.

4.3 Results

4.3.1 Extravascular compression pump around the existing Fontan shunt

Continuous peristaltic pump motion

Figure 80 shows the results of continuous actuation of the compression pump during physiologic Fontan flow simulated on our cardiorespiratory bench top model. Upon actuation the

graph shows the pulsatile peaks of flow during device compression on the flow rates. We see a resulting impairment of forward as well as retrograde flow in the IVC and no beneficial circulatory support.

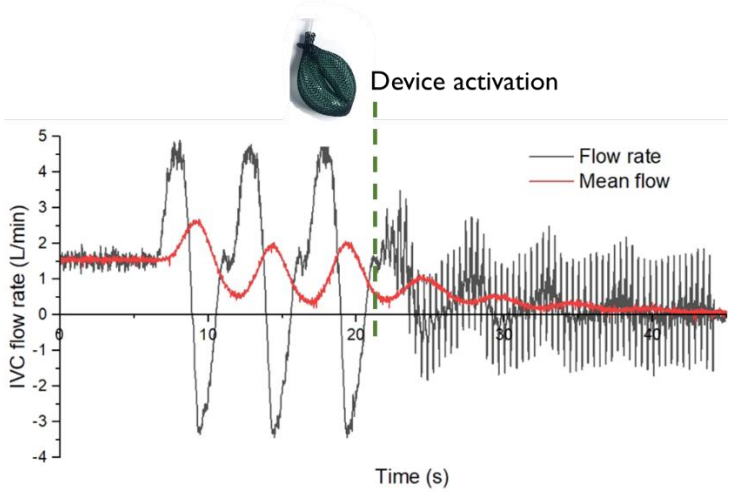

Figure 80 : Impact of continuous compression pump motion on bench top IVC flow. IVC flow rate data of baseline flow rate (black) and mean flow (red) during baseline respiration and after device activation.

Triggered compression pump during retrograde flow in the IVC

Figure 81 summarizes the hemodynamic effects of the compression pump which is activated only by retrograde flow. Figure 81A shows the quantitative results (Figure 81E) of the forward and reverse IVC flow. With active pump function the resulting forward IVC flow and reverse IVC flow are diminished during inspiration and expiration, respectively. Each peristaltic compression cycle is visualized in the pressure readings in the IVC TCPC location. Average pressure in the abdominal and thoracic IVC decrease slightly as shown in Figure 81F. Due to lower IVC pressures and flows the SVC flow increases as visualized qualitatively in Figure 81B and summarized compared to baseline in Figure 81E. In aggregate the total venous return consisting of the combined flow in the IVC and SVC is diminished during device actuation as visualized in Figure 81C and summarize in Figure 81E.

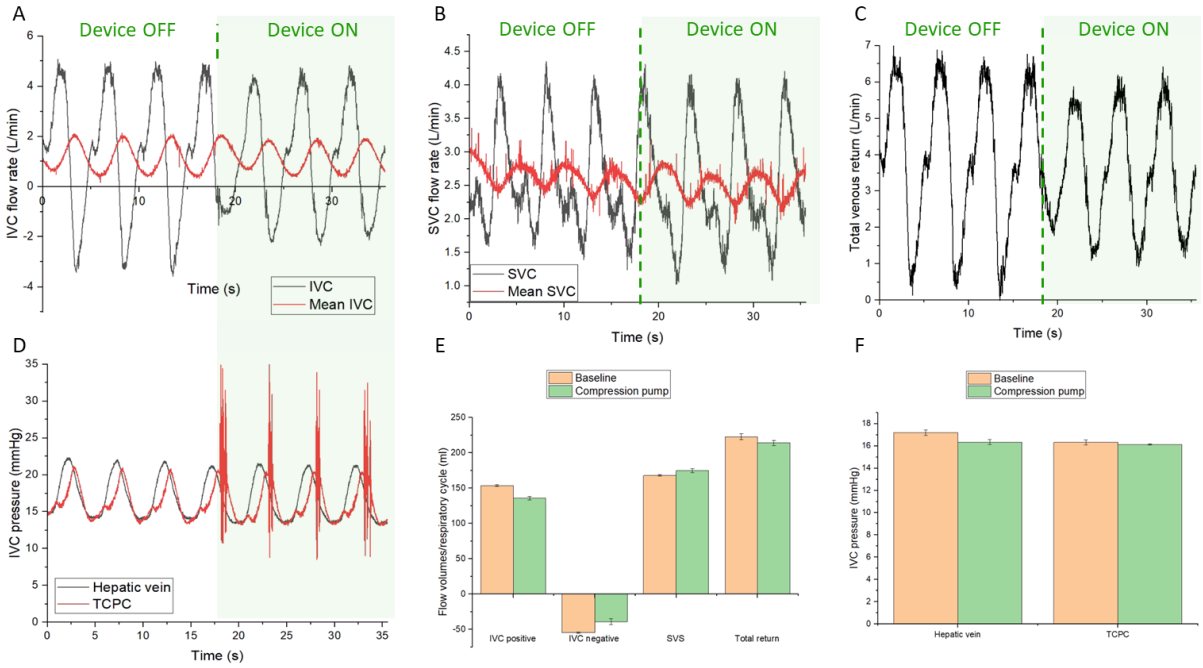

Figure 81 : Hemodynamic impact of peristaltic compression pump on bench top IVC flow when triggered during retrograde flow periods. IVC flow rate (black) and mean flow rate (red) during baseline Fontan flow and during device activation (A). SVC flow rate (black) and mean flow rate (red) during baseline Fontan flow and during device activation (B). Total venous return during baseline Fontan flow and during device activation (C). IVC pressure at the hepatic vein (black) and TCPC (red)location during baseline Fontan flow and during device activation (D). Flow volumes (E) and IVC pressure (F) results during baseline Fontan flow and during device activation.

4.3.2 Extravascular expansion pump around the existing Fontan shunt

Figure 82 summarizes the hemodynamic effects of the peristaltic expansion pump on the bench top Fontan IVC flow during two actuation modes. Resulting pressures and IVC flow during continuous peristaltic actuation (Figure 82A and Figure 82C) and with device activation only during retrograde flow in the IVC (Figure 82B and Figure 82D). Increase oscillatory flow rates in the pressure readings of the TCPC indicate the continuous and intermittent actuation in Figure 82A and Figure 82, respectively. While increase oscillatory motion in the IVC flow rates can be observed in both actuation modes the mean forward and retrograde flow does not change in either case.

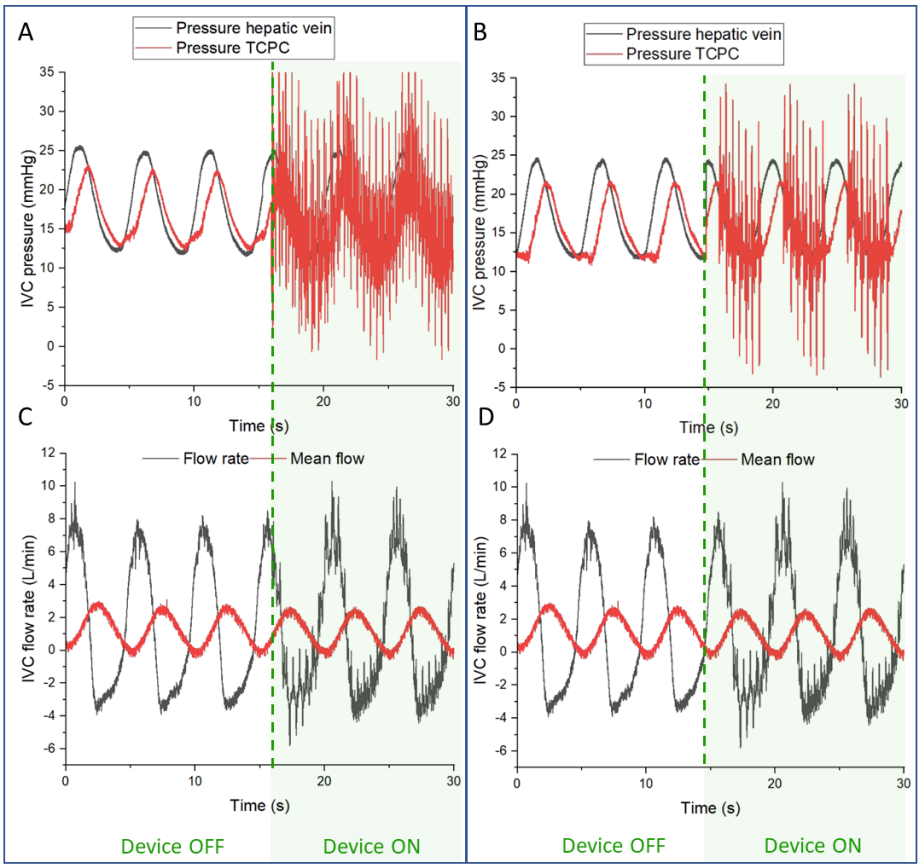

Figure 82 : Hemodynamic effects of the peristaltic expansion pump on the bench top Fontan IVC flow. IVC pressures in the hepatic vein location (black) and TCPC location (red) for baseline and continuous pump activation (A), and triggered pump activation during retrograde flow in the IVC (B). IVC flow rates (black) and mean flow (red) for baseline and continuous pump activation (C), and triggered pump activation during retrograde flow in the IVC (D).

4.3.3 Passive support strategies in existing Fontan shunt

One way valve evaluation in the Fontan IVC

Figure 83 shows the effects of the integration of a one-way mechanical valve into the IVC of the validated Fontan bench top model and potential angles to improve the performance of this support strategy. With expiration the IVC flow decreases so far that the flow reverse direction. At this point we see the valve closes (1.) and and diminishing the retrograde flow volume marked with a violet area in Figure 83A. The valve does not immediately close resulting in some retrograde flow which is marked with the shaded red area in Figure 83B. Potential valve characteristics that should be optimized in a dedicated valve design for the Fontan IVC include minimized (i) closing pressure, (ii) opening pressure, and (iii) flow resistance during open configuration. The closing volume is generated because valve closure is initiated by the rising pressure gradient across the valve which is characteristic for each valve design. The required pressure across the valve to re-open it is also valve specific and should be minimized. Finally, we see that peak forward flow rates are decreased with the valve placement compared to no device

implantation. Hence a Fontan IVC valve should minimize flow obstructions and created turbulence.

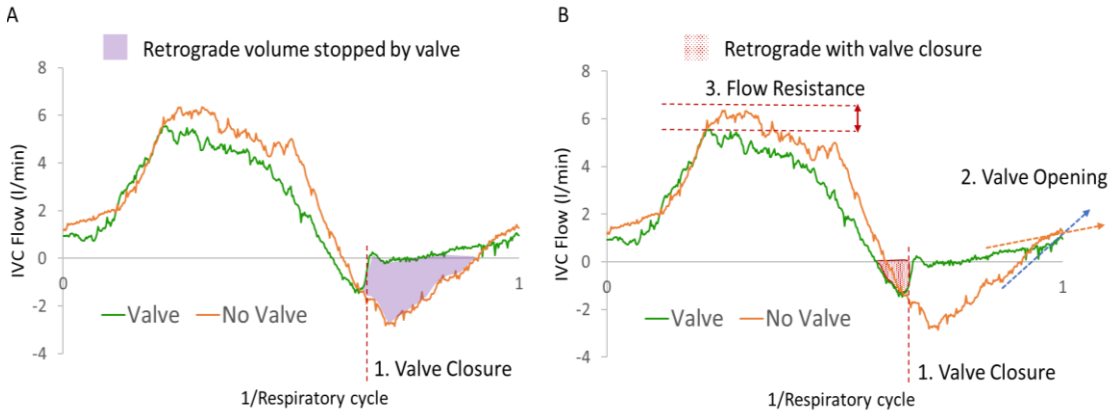

Figure 83 : Comparison of IVC flow with and without an implanted mechanical one-way valve on the bench top. Valve closure is indicated by the red dashed line. IVC flow rates over one respiratory cycle showing the retrograde flow volume which is prevented by valve closure (violet area) in (A). Hemodynamic indicators that could be optimized for an implanted valve in the Fontan IVC are shown in (B): 1. early valve closure to prevent retrograde flow volume (red dotted area), 2. Easy valve opening to allow for forward flow increase, and 3. Minimizing forward flow resistance to allow for maximum peak flows.

The hemodynamic effects of valve placement in the Fontan IVC are summarized in Figure 84. We can see that the implanted valve decreases retrograde flow to around 2% of the flow rate consistently even during increasing backward flow volumes at baseline (Figure 84A). This means that a one-way valve successfully reduces IVC retrograde flow by more than 90%. Mean IVC pressure before the valve in the location of the hepatic vein decrease with valve placement as shown in Figure 84B. This effect increases with greater baseline retrograde flow. Conversely, the IVC pressure after the valve increases towards the TCPC and pulmonary artery. This can be observed for greater baseline retrograde flow of 40% and 50%. At 23% retrograde flow TCPC mean pressures are unchanged. This is accompanied by a change of total venous return (combined IVC and SVC flow) at high retrograde flow rates if a valve is implanted. Without a valve total venous return decreased from with increase retrograde flow from 23% to 40%, and 50%. This effect is mitigated by valve placement (Figure 84D). Similarly, the total IVC flow decreases without a valve when greater percent retrograde flows are achieved but remain constant with an implanted valve (Figure 84E). The underlying forward and negative flow volumes in the IVC during inspiration and expiration, respectively, are shown in Figure 84F. Here we see that without valve placement the forward as well as the reverse flow volumes increase during one respiratory cycle. The placement of a valve prevents the retrograde flow volume which leads to a steady forward flow volume during increase respiratory efforts.

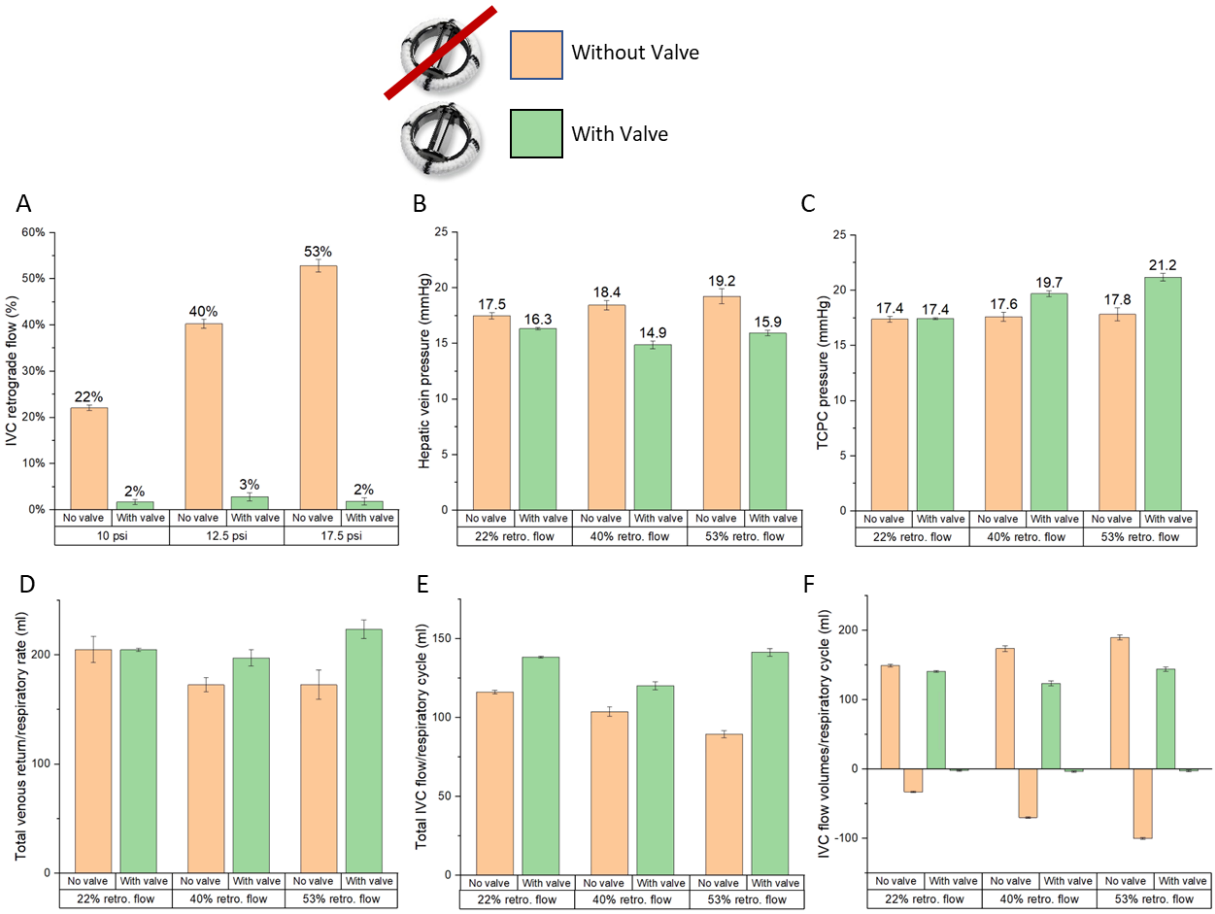

Figure 84 : Hemodynamic impact of an implanted one-way valve in the Fontan IVC in the cardiorespiratory bench to simulator are summarized during increasing respiratory efforts and resulting greater retrograde baseline retrograde flow. Results at baseline are indicated with orange while results with the implanted valve are indicated with green. Resulting retrograde flows (A), IVC pressures in the location of the hepatic vein (B) and TCPC (C), total venous return volumes of the combined IVC and SVC (D), total IVC flow volumes (E), and forward and backward IVC flow volumes (F) during one respiratory cycle are summarized.

Feasibility study of extravascular occluder device functioning as one-way valve

To decrease the amount of flow obstruction an implanted device presents in the Fontan IVC we investigated the feasibility of an external occluder device which is triggered by retrograde flow and thereby act like a one-way valve. Figure 85A shows the resulting IVC flow during baseline and during triggered device actuation. During inspiration the device is open, so there is no additional flow obstruction as it can be seen in the same peak flow rate. During expiration the flow reverses when the extravascular occluder device is triggered and contracts resulting in a forward flow and no retrograde flow during expiration. The SVC flow is not impacted by the actuation of the device and prevention of retrograde flow as shown in Figure 85B. IVC pressure remain similar to baseline measurements with pressure peaks in the TCPC location during device contraction and release.

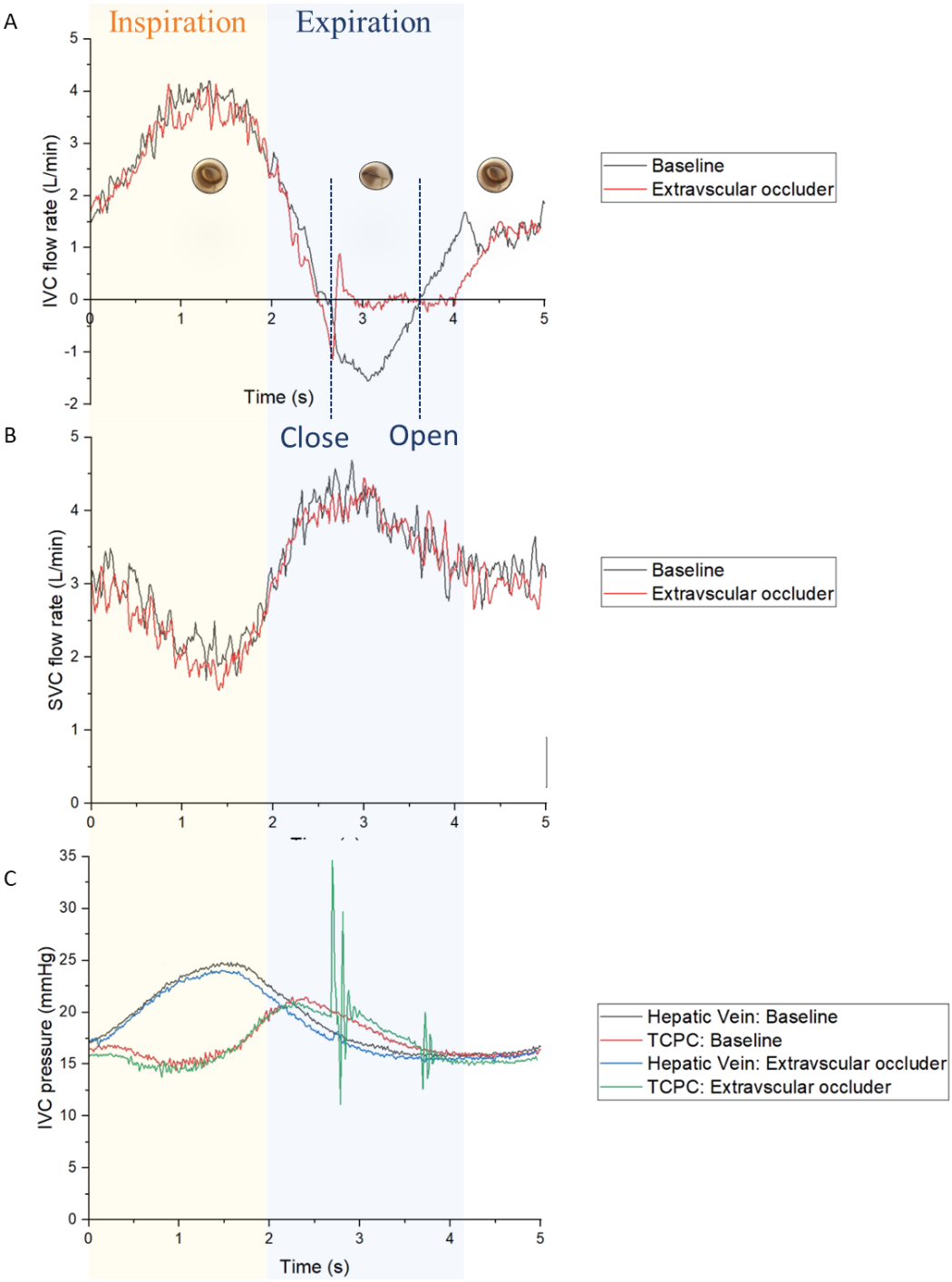

Figure 85 : Function of an extravascular occluder device as a one-way valve triggered by retrograde IVC flow on the bench top. Baseline and active device values are compared during inspiration (yellow) and expiration (blue) of one respiratory cycle. IVC flow rate (A), IVC flow volume (B) and abdominal as well as chest IVC pressures (C) are compared.

Figure 86 shows the resulting percent retrograde at baseline without a device and with the actuation of the extravascular occluder device. IVC percent retrograde flow decreases 83% with the active device.

for baseline measurements with pressure peaks in the TCPC location during device contraction and release.

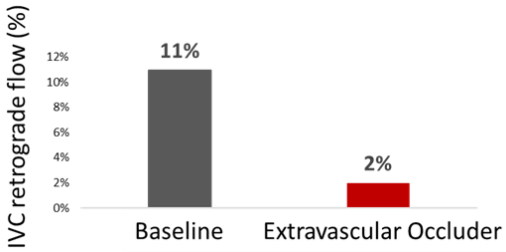

Figure 86 : Resulting reduction in retrograde flow with usage of the flow triggered extravascular occluder device in the Fontan simulator.

4.3.4 Combination of active and passive support strategies in existing Fontan shunt

Figure 87 shows the combination of an active compression pump and a one-way valve integrated with the IVC Fontan vascular shunt.

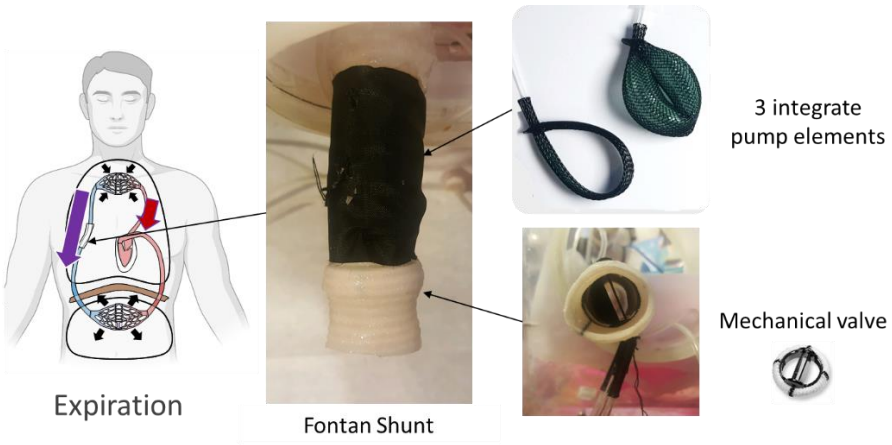

Figure 87 : Integration of the peristaltic compression pump around a Fontan shunt with an implanted mechanical one-way valve.

Figure 88 compares the IVC flow curves during one respiratory cycle at baseline without device integration (Figure 88A), with integrated one-wavy valve (Figure 88B), and the combination of a valve with the extravascular compression device which was triggered by with the valve closure (Figure 88C). We see that the valve placement inhibits the retrograde IVC flow in Figure 88B which is marked with the violet area in Figure 88A. The device was successfully triggered to as shown by the forward flow peak marked with the red circle in Figure 88C.

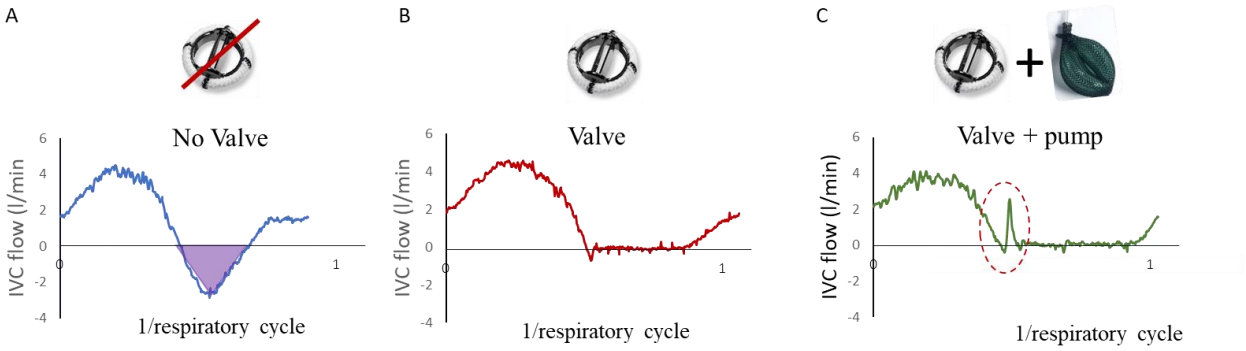

Figure 88 : Comparing IVC flow rates during one respiratory cycle at baseline breathing (A), with an implanted one-way flow valve (B), and with a combination of an implanted one-way valve and extracardiac compression pump around the TCPC shunt (C). The retrograde flow in the IVC is indicated by the violet marked area and the impact of a single contraction is circled in red.

The hemodynamic effects of the combination of support devices are summarized in Figure 89 for 5 consecutive respiratory cycles. The single triggered actuation which is visualized in Figure 88C results in no change of the forward IVC flow, a slight reduction in the retrograde flow during expiration, a slight increase in the SVC flow and overall venous return as shown in Figure 89A. IVC flow rate curves during baseline breathing and during multiple actuation cycles of the device combination during expiration are visualized in Figure 89B. We can see increase forward and reverse flow during device actuation and the overall peak flow rates are increased with device activation. This is concurred by the analytical results summarized in Figure 89C where IVC forward flow during inspiration increases but not significantly, and overall retrograde flow during one respiratory cycle increases. The SVC flow increases slightly but the total venous return decreases. So no improvement of the IVC flow hemodynamics can be observed.

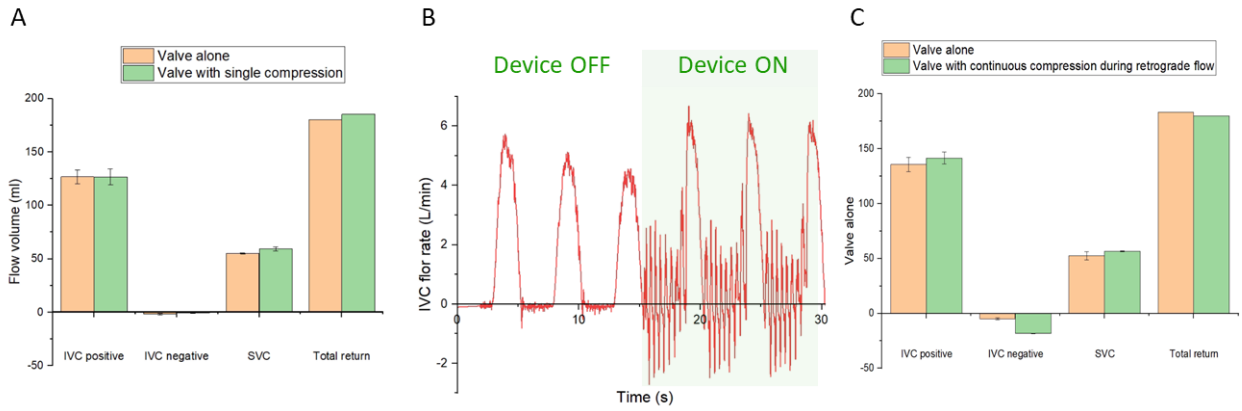

Figure 89 : Results of a combination support strategy including a one-way valve and extravascular compression pump. Flow volumes during one single actuation triggered after valve closure during expiration

(A), exemplary flow waveforms (B) and flow volumes (C) of multiple device actuation cycles during retrograde flow of the expiration period.

4.3.5 Optimization of valve design for the Fontan IVC

Mechanical Characteristics

Different valve leaflets ranged from 1:1 to 2:1 of diameter to height ratio, 0.5 to 0.9 of the valve height to mid-height ratio and 100% to 50% of geometric orifice area were designed and characterized using finite element modeling. Figure 90 shows the deformation and the maximum principal strain distribution of these leaflets in a quasi-static loaded condition. The peak strain was observed along the leaflet attachment line, with a peak value around 15%. During the valve closing phase, large strains were concentrated in the middle region of the leaflet attachment line, followed by the commissure regions. The lowest strain regions were located at the commissures region where leaflets meet, specifically during the presence of an excessive coaptation.

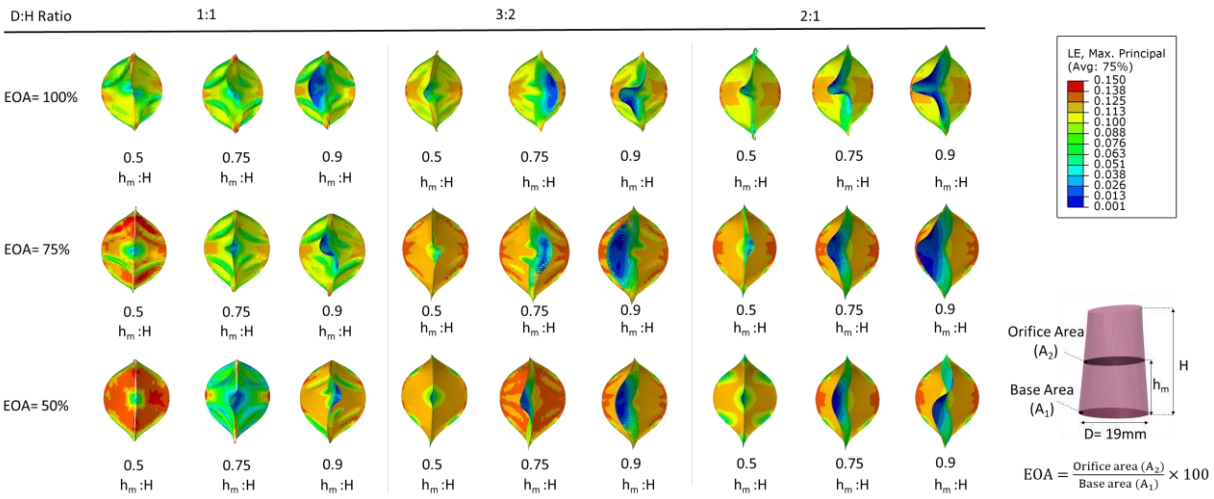

Figure 90 : Finite Element model of bileaflet valve geometries showing maximum principal strains distribution under physiological pressure load. Leaflet geometries varied the valve height(H) and the valve mid-height ($H_{m)}$. Geometric orifice area (GOA) was ranged between 100% to 50%.

The coaptation zone of the valve is crucial for valve competence so coaptation depth and length are often used to measure the valve performance. In human venous valve anatomy, venous valve leaflets meet over a length (coaptation length) equating to up to half the vessel diameter and this coaptation maintain the contact under the pressure built-up [100].

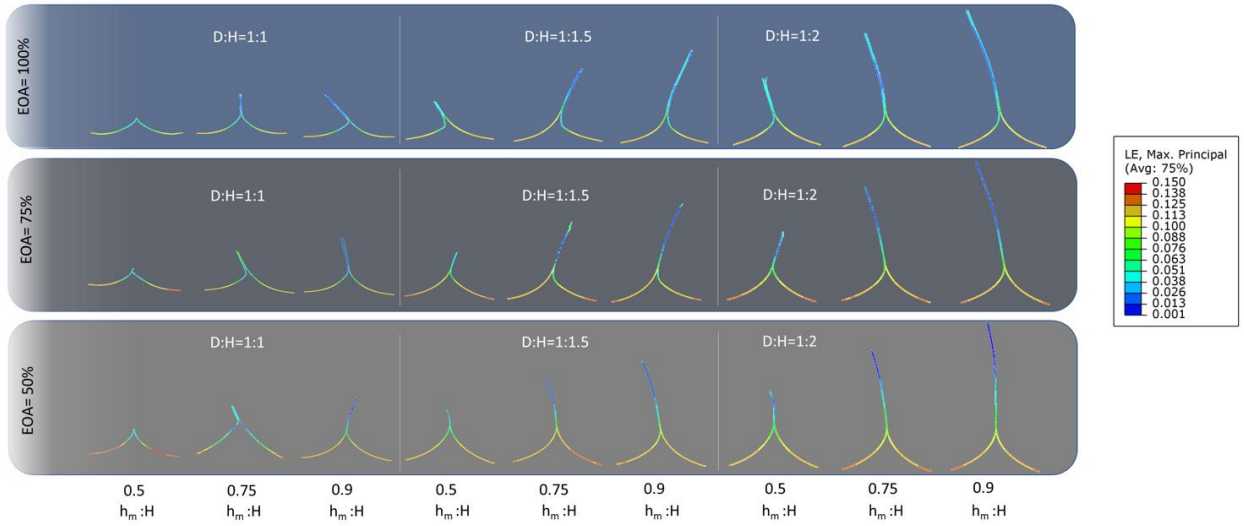

Figure 91 shows the coaptation profile of varying bileaflet valves during the closing phase. Results indicated that the lowest strain regions were concreted at the coaptation areas. As seen in Table 21, coaptation length depends on valve height. Coaptation length increases greatly when the valve height(H) to the valve mid-height (H_m) ratio is higher than 0.5 and the ratio of diameter to the height (D:H) is increased.

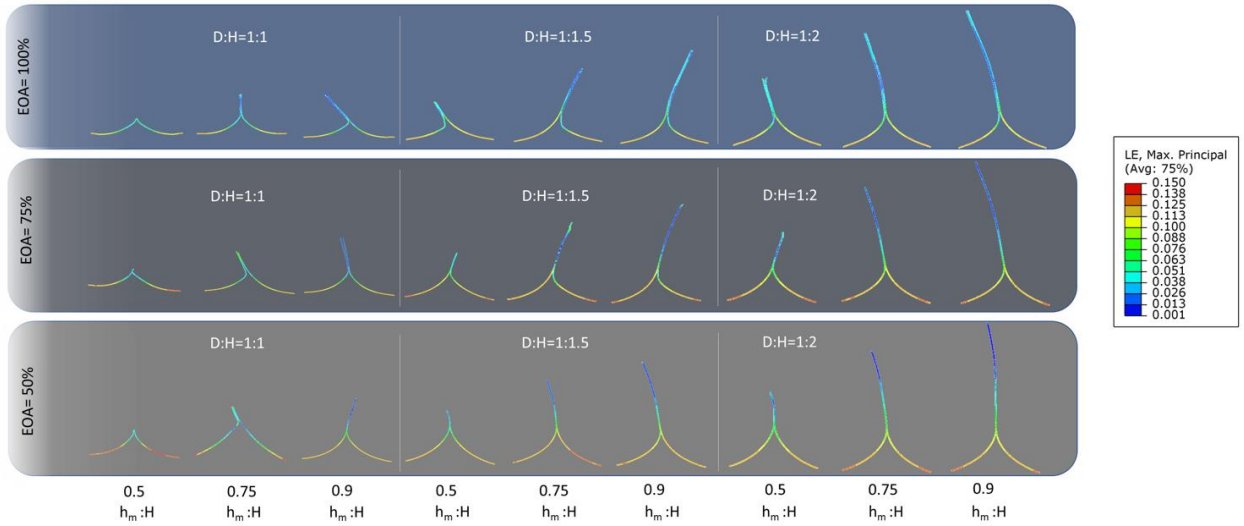

Figure 91 : Coaptation profile of bileaflet valves during the closing phase, colored by the maximum principal strain.

Table 21 : Comparison of coaptation length between valve leaflet geometries.

			h_m:H Ratio = 0.5	h_m:H Ratio = 0.75	h_m:H Ratio = 0.9
		D:H Ratio	Coaptation Length		
Bileaflet	EOA =100%	1:1	0mm	4.42mm	7.13mm
		3:2	4.36mm	9.31mm	15.15mm
		2:1	7.22mm	17.18mm	24.57mm
	EOA =75%	1:1	0.4mm	3.58mm	5.99mm
		3:2	3.85mm	7.44mm	17.8mm
		2:1	7.58mm	16.97mm	24.62mm
	EOA =50%	1:1	0.9mm	5.8mm	11.38mm
		3:2	4.69mm	12.78mm	21.38mm
		2:1	7.72mm	17.9mm	25.9mm
Trileaflet	EOA =100%	1:1	0mm	0.1mm	2.5mm
		3:2	0mm	0.4mm	3mm
		2:1	0mm	2.8mm	3.9mm

The trileaflet valve geometries were subjected to a similar deformation evaluation. The FE model was used to determine mechanical characteristics of the valve with diameter-to-height ratios ranging from 1:1 to 2:1 and valve height-to-mid-height ratios ranging from 0.5 to 0.9. Maximum principal logarithmic strain (LE) contours of the leaflets during closing are shown in Figure 92. Similarly, the peak strain was observed along the leaflet attachment line mostly concentrated on the top edges. During the closing phase, trileaflet-shaped valves demonstrated a more homogeneous strain distribution than bileaflet valves, which might be due to geometric asymmetry produced by excess contact area at the bileaflet commissure. The presence of isolated, high stress zones in trileaflet bioprosthetic valves has been linked to early device failure,

making stress distribution pattern critical for the life cycle of an implanted valve device [100], [108], [109]. There were no areas of significant strain concentration that may have induced early valve degeneration due to failure stress.

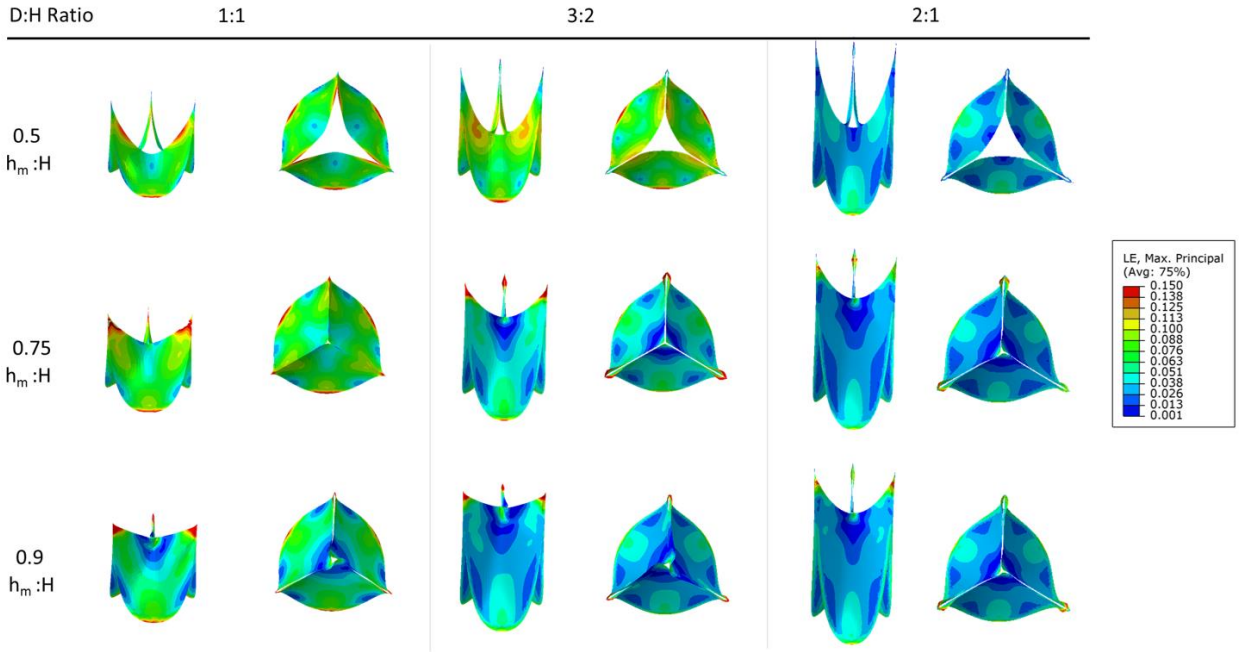

Figure 92 : Finite Element model of trileaflet valve geometries showing maximum principal stress distribution under physiological pressure load. The leaflet geometries varied the valve height(H) and the valve mid-height ($H_{m)}$. Geometric orifice area (GOA) was ranged between 100% to 50%

Valve Hemodynamics

A fully coupled two-way fluid structure interaction approach was implemented in the CFD model to simulate the detailed flow structure. The contours of the flow velocity magnitude as well as the stream traces at a time instance during the valve opening and closing are presented in Figure 93.

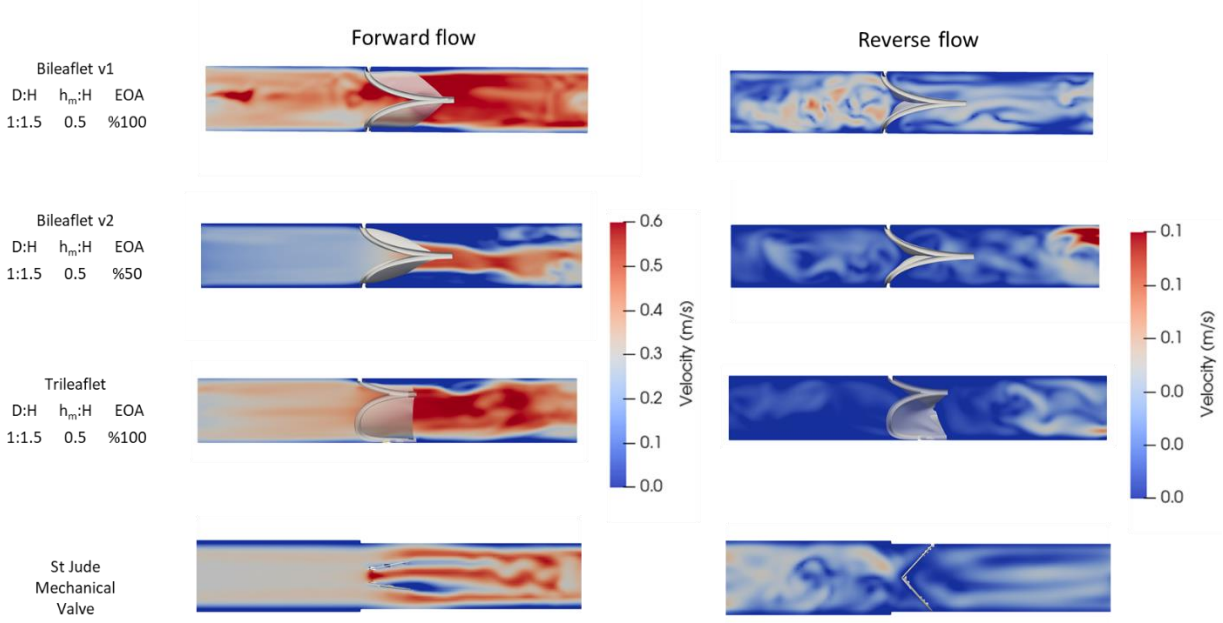

Figure 93 : The contours of the flow velocity magnitude during forward and reverse flow in the Fontan IVC.

The velocity vectors and vorticity contours between leaflets and the wall are shown in Figure 94 at various time periods throughout the flow cycle. Vortex fields highlighted significant differences between the valve designs.

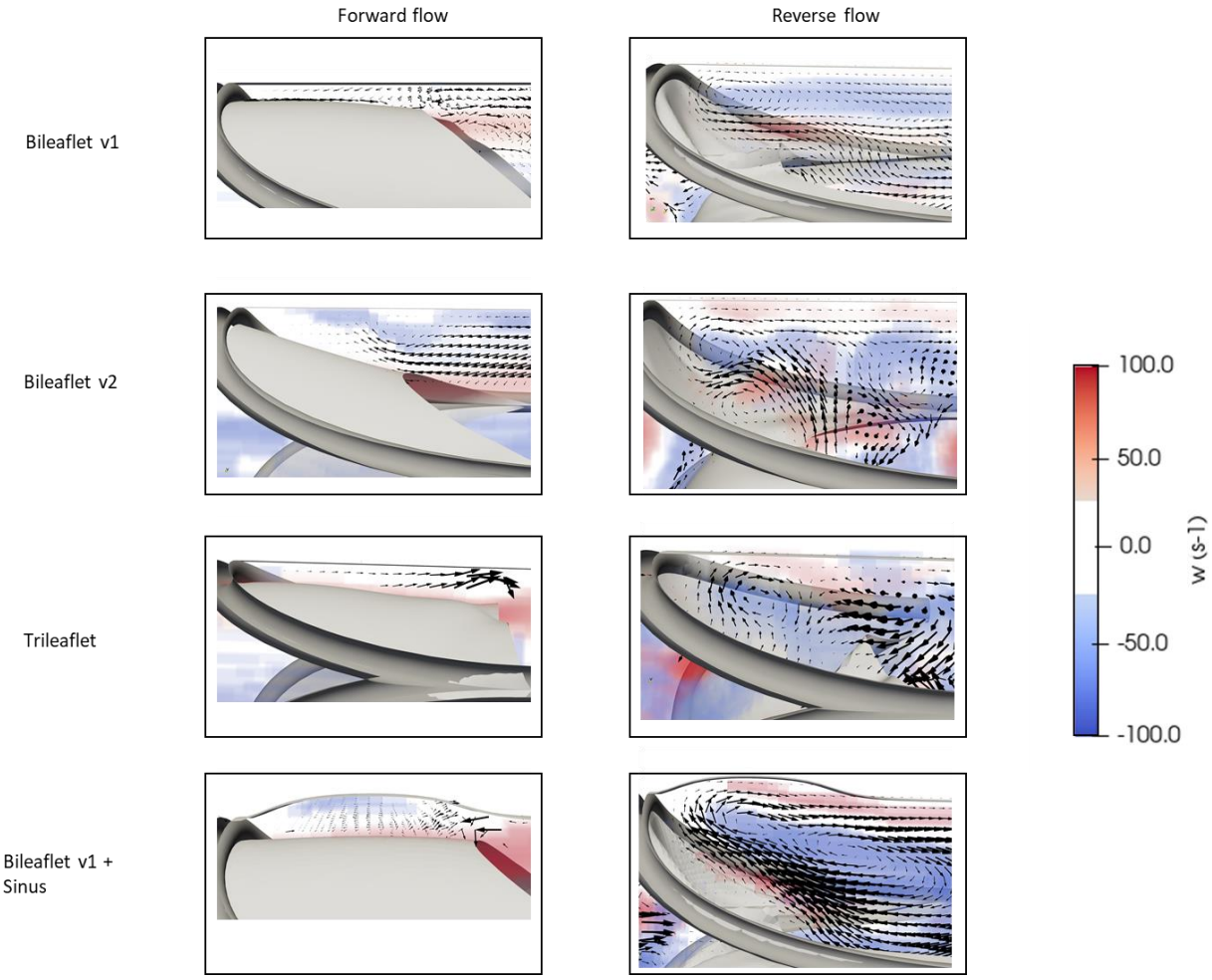

Figure 94 : Velocity vectors and vorticity contours within the representative valve designs during forward and reverse flow in the Fontan IVC.

During peak systole, no significant vortex formation was observed in the straight vessel configuration except for the design includes sinus shape. This clearly indicates the distance between leaflet and the wall has important role. During the reverse flow phase, vortex onset is clearly visible in all designs. It is obvious though that vortex in Bileaflet v2 and Bileaflet v1+Sinus are well conserved in terms of strength and size compared to other versions.

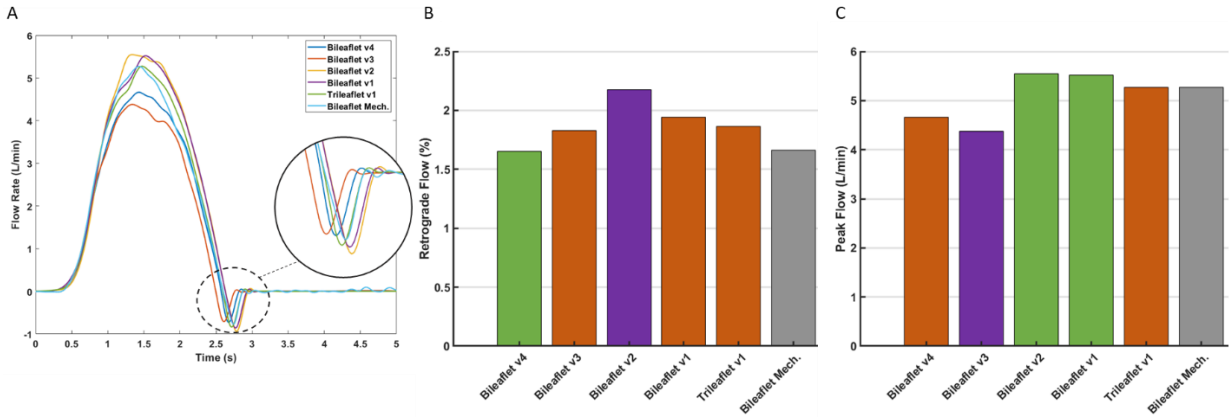

Figure 95 : The volumetric flow rates in the IVC during the flow cycle. B) Comparison of peak volumetric flow rate of valve designs C) Percentage of the retrograde flow.

We evaluated and compared the volumetric flow rates across the valve designs during a single flow cycle as shown in Figure 95 The interaction between the flow field and the leaflets during opening and closing is represented by flow acceleration-deceleration, peak systole, and closed phases. The flow rate profiles of Bileaflet designs varied from 4.66 L/min to 5.55 L/min. Bileaflet v1 and v2 had the greatest peak flow rates (5.55 L/min), indicating that they are pose less flow obstruction in the IVC. Smaller orifice areas (v3 and v4) reduced the forward peak flow to 4.66 L/min and 4.38 L/min, respectively. In terms of valve closing performance, EOA had a significant impact on the valve closing phase. The designs with large orifice areas (v1 and v2) were closed at the same time (2.616s), but 50ms later than Bileaflet v4, which showed the shortest closing time. Bileaflet v1 demonstrated the optimal performance, with the minimum flow resistance and an acceptable retrograde flow of 1.94%. This is comparable to the mechanical valve's (St. Jude Valve) capacity of 1.66% retrograde flow and 5.27 L/min peak volumetric flow rate.

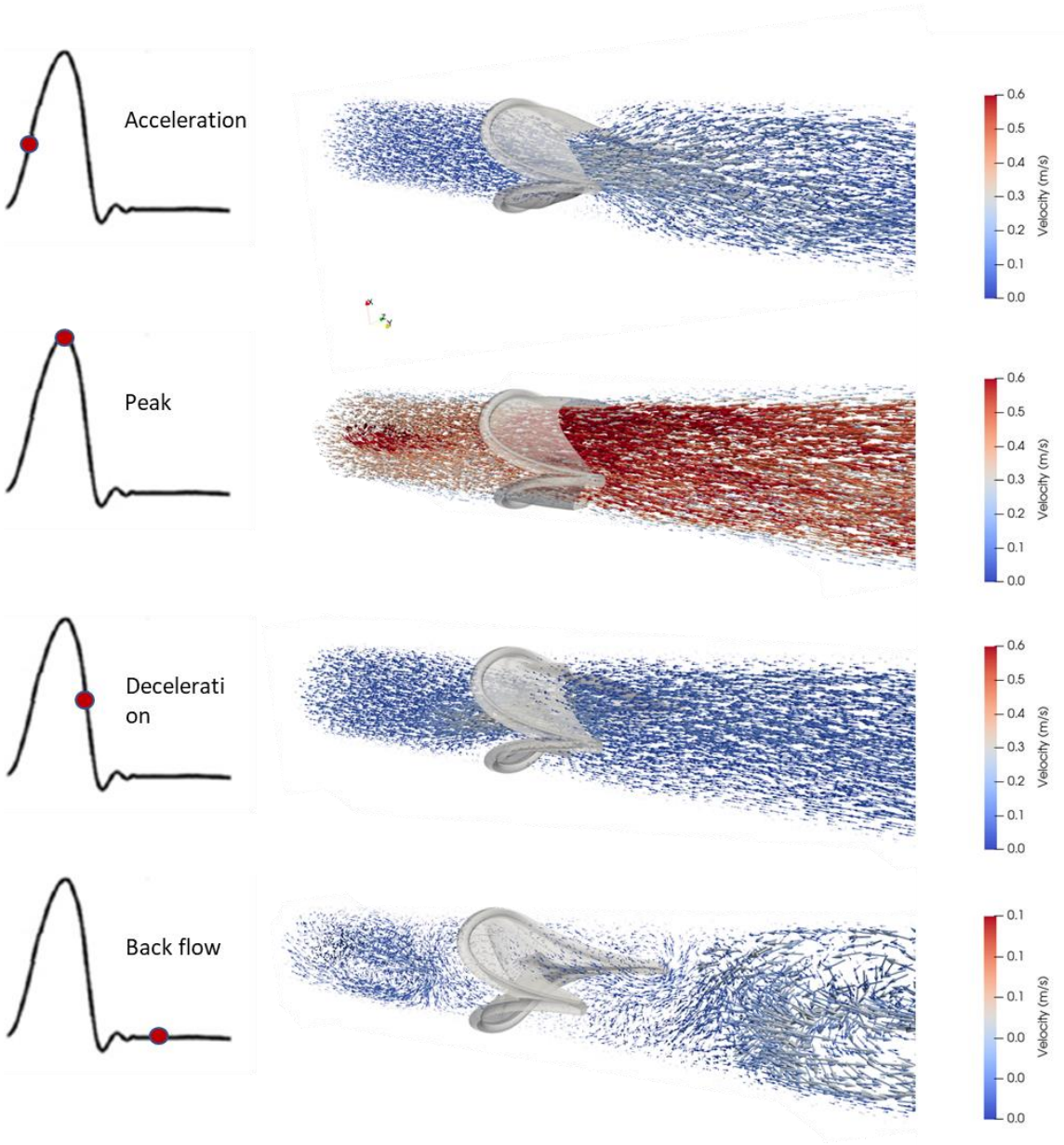

Figure 96 : Velocity vector map of Bileaflet valve (v1) at different phases in the cardiac cycle.

The velocity vectors of the best performing valve are presented in Figure 96 at different points in the forward and reverser Fontan IVC flow during one respiratory cycle . With optimal valve design (Bileaflet v1), velocity vector fields characterizing blood flow patterns in the IVC were analyzed. At mid-acceleration, the IVC flow increases by reaching the velocity of 0.3 m/s. The highest velocity occurs as the result of flow entering the valve region, with velocity magnitude in this region at approximately 0.6 m/s. Towards the mid-deceleration, recirculating flow pattern begins to develop. The peak vorticity occurs when the valve is closed. This triggers increased vortex formation before and after the valve region, as well as increased recirculation between the leaflet and the wall.

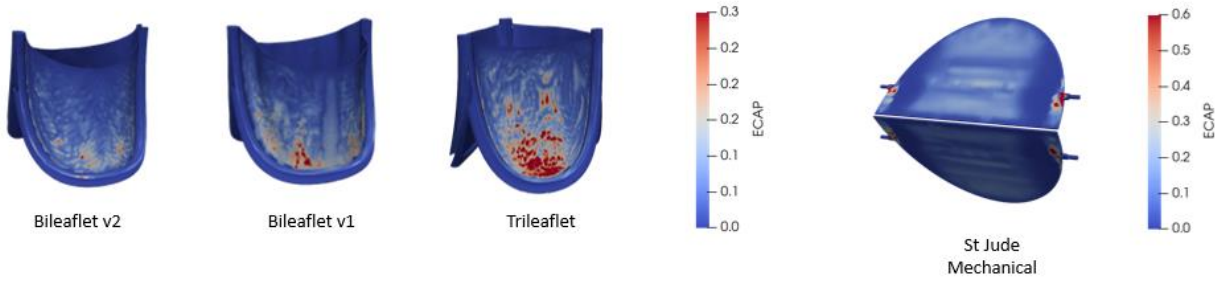

Figure 97 : ECAP (endothelial cell activation potential) map on the leaflet surfaces as a hemodynamic in silico index.

Simulated ECAP results are shown in Figure 97 .The ECAP was computed based on Equation 11. High ECAP values were mostly concentrated around the leaflet edges at the frame connection. Regions of high ECAP were similarly located between soft Bileaflet designs, but slightly higher values were observed in the Trileaflet design. Although the mechanical bileaflet design has a smooth structure and orientation, significant ECAP values were observed around the valve pivots indicates a high suspicion of valve thrombosis. This finding is also consistent with existing clinical findings [110]. Bileaflet v1 and v2 case showing smaller ECAP values due to its highly flexible leaflet orientation, leading to larger blood flow velocity magnitudes in most regions. For Bileaflet designs, the likelihood of having high ECAP near the leaflets decreases drastically (<0.3 1/Pa), however, the mechanical valve yields higher values (up to 0.6 1/Pa) compared with the trileaflet valve (up to 0.3 1/Pa).

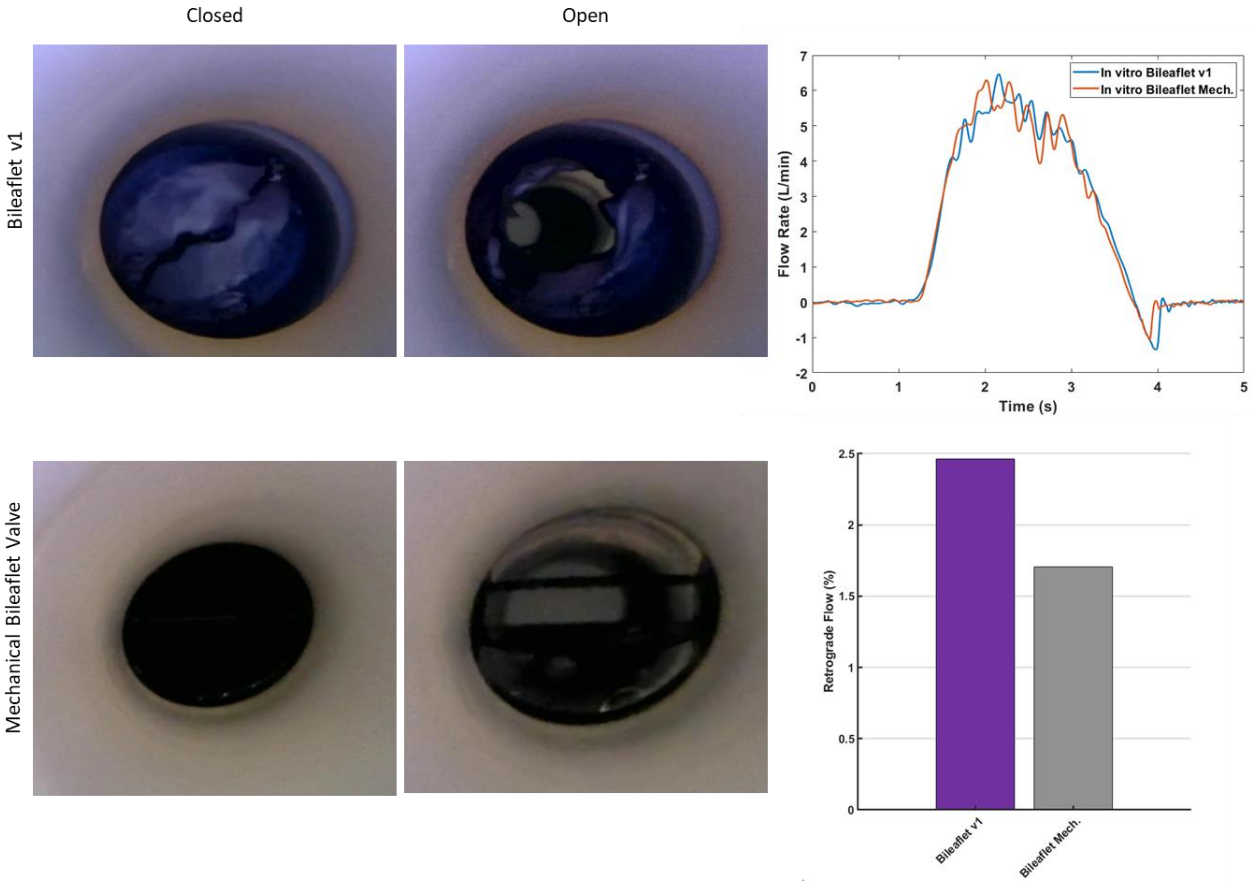

Figure 98 : Experimental Results, The volumetric flow rates in the IVC during the flow cycle. B) Percentage of the retrograde flow.

Experimental results of the opening and closing of the mechanical and soft bileaflet valves are shown in Figure 98. These are preliminary results of the first soft bileaflet prototype. Both valve designs were tested in the cardiorespiratory Fontan simulator, fully closed during reverse IVC flow and were able to reduce retrograde flow in the IVC during expiration. Peak forward flow was the same with both valves indicating similar resistance to flow and the commercially available mechanical valve closed slightly before the soft bileaflet valve.

4.4 Discussion

4.4.1 Extravascular compression pump around the existing Fontan shunt

We have designed and manufactured an extravascular compression device which can be actuated in a peristaltic manner to create forward flow as shown in computational simulations. We manufactured the compression pump with sufficient force to act on the pressure seen in the Fontan IVC. We evaluated device performance on our clinically validated cardiorespiratory

simulator and showed that continuous peristaltic compression diminishes IVC flow and hurts the Fontan hemodynamics. Pump actuation during expiratory phases was able to decrease the amount of retrograde flow but did not increase the overall flow and hence also failed to improve Fontan hemodynamics. This work is the first to implement the broadly suggested approach of an extravascular compression pump to support Fontan circulation including the device evaluation in physiologically relevant flow conditions. It shows that any narrowing of the IVC increases flow resistance greatly. This impedes forward as well as retrograde flow but fails to increase venous return in the Fontan physiology. Our results may present valuable information for other approaches of compression pumps around the IVC showing how the characteristic Fontan flow pattern which is highly impacted by respiration must be considered and addressed in the development of a circulatory support device.

We acknowledge limitations to this study which include a limited number of contractile elements in the pump sleeve.

4.4.2 Extravascular expansion pump around the existing Fontan shunt

We have designed and manufactured an extravascular expansion device which can be actuated in a peristaltic manner to create forward flow as shown under zero flow conditions. We manufactured the expansion pump with sufficient force to act on the physiological pressures in the Fontan IVC. We evaluated device performance on our clinically validated cardiorespiratory simulator and showed neither continuous actuation, nor triggered pumping during expiratory phases and retrograde flow in the IVC increase IVC flow or improve hemodynamic conditions. This work is the first to suggest and explore such pumping motion in an expanding manner to not increase flow resistance of the baseline flow. It shows that even though the peristaltic expanding motion may work as a pump in zero flow conditions the open lumen in the center of the device allows for the flow fluctuations during the respiratory cycle. Forward flow surge and retrograde flow during inspiration and expiration, respectively, were not impacted and hence no improvement of the Fontan hemodynamics was established. This underscored how powerful the impact of respiratory pressure is on the venous return of the Fontan physiology and that it is paramount to address these flow patterns to support the circulation effectively.

We acknowledge limitations to this study which include a limited number of contractile elements in the pump sleeve.

We addressed aim 1 of this chapter by evaluating extravascular compression and expansion pumps with peristaltic motion in the cardiorespiratory simulator. We analyzed the implications on the hemodynamics during inspiration and expiration in the IVC and the results underscore the need to tailor device design and performance to the flow patterns in the Fontan IVC.

4.4.3 Passive support strategies in existing Fontan shunt

We tested a mechanical one-way valve in the clinically validated bench top Fontan simulator and showed that it successfully prevents retrograde flow during expiration in the Fontan IVC. Percent retrograde flow is reduced over 90% at all respiratory efforts and baseline reverse flow volumes. We can appreciate that IVC pressure before the valve at the location of the hepatic veins drop with greater respiratory efforts and baseline retrograde flows while IVC pressure after the valve towards the pulmonary arteries increase. The total venous return consisting of the combined IVC and SVC flow is increasing at high baseline retrograde flows with valve implantation compared to no valve placement in the IVC. This is due to the decrease retrograde flow volume in the IVC but constant forward surge of blood during inspiration. The shown hemodynamic effects are positive for the Fontan physiology. A lowered hepatic vein pressure could mitigate venous congestion which can lead to fatal outcomes including liver failure and protein losing enteropathy. Greater pressure after the valve in the TCPC increases the transpulmonary pressure to drive blood through the lungs, help the oxygenation of the venous blood and ultimately increase cardiac return. Overall increase of the venous return is beneficial for the Fontan physiology. This work represents one of the first studies of mechanical valve placement in the Fontan IVC and the first study to test the hemodynamic impact in a clinically validated cardiorespiratory simulator. It shows promising results in hemodynamic circumstances of large retrograde flow volumes and no detrimental effects during hemodynamic conditions of little retrograde flow. We also compared the IVC flow curves with and without valve placement and identified key parameters to optimize a valve dedicated for the Fontan IVC flow. This includes low opening and closing pressures, minimal flow obstruction during the open valve configuration, low blood shearing, and good washout of the artificial surfaces to minimize thromboembolic risks. To avoid flow obstruction during forward flow in the IVC we designed and evaluated a new kind approach of an extravascular occluder device. This device is triggered by retrograde flow in the IVC to compress the IVC during flow reversal and thus function like a one-way valve without implantation of materials into the blood stream. We proved the feasibility of the device in the cardiorespiratory Fontan simulator by reducing retrograde flow by over 80%.

We acknowledge limitations of this study which include the evaluation of the valve performance in the supine position and variations of physiological parameters. The promising results of these studies pave the way for future work to include evaluation of the implanted valve and extravascular device on the bench top with adjusted orientation of the IVC to include gravitational effects. Different physiological parameters may impact the performance of both device types and increase valve efficacy. These investigating will include different baseline flow rates, increases IVC baseline pressures, and decreases vascular compliance of the failing Fontan physiology.

We completed aim 2 of this chapter by evaluating an implanted mechanical valve in the cardiorespiratory simulator under increasing baseline retrograde flow conditions and showing functionality of an extravascular occluder device to work as a one-way valve in the Fontan IVC.

4.4.4 Combination of active and passive support strategies in existing Fontan shunt

We successfully designed and fabricated a prototype of a contracting ventricle paired with a one-way flow valve to give the flow from the pump directionality, we integrated the active and passive device combination into the Fontan shunt and evaluated its performance in our Fontan bench top model. We showed that the combination device works when the pump is triggered for one actuation cycle during expiration and retrograde flow. This displaces the volume of one pump stroke forward in the IVC. The overall effects of one stroke per respiratory cycle are limited. We also evaluate device performance of multiple actuation cycles during expiration and retrograde flow in the IVC. We showed that multiple subsequent pump cycles open the valve during the relaxation of the pump to draw in more fluid. After opening the of the valve there is some backflow in the valve until the valve is closed again during device contraction. The volume that is pushed backwards in the IVC due to repeated opening and closing with device actuation is greater than with only an implanted valve. Hence, hemodynamic benefits were not achieved.

Combination devices including a one-way valve and adjacent ventricle which contract periodically have been suggested and are evaluated in recent literature. Our work is the first to test such an approach in a physiologically relevant bench top model to expose the limited efficacy.

We acknowledge limitation of this work which include the maximal volume of the current contraction pump being the volume of the Fontan shunt (20 mm). A greater volume of the

compression chamber could displace more volume during a single stroke and hence increase beneficial volume flow in the IVC. Greater volumes of the compression sleeve, the addition of a second valve at the sleeve outflow, and rigorous pumping in synchrony with the heart the missing sub-pulmonary ventricle may be recapitulated more closely to recreate bi-ventricular characteristics of the venous return to mitigate the hemodynamic burden in the Fontan IVC.

We completed aim 3 of this chapter by designing, manufacturing, and testing of a combination device that included a one-way valve in the IVC and a compression sleeve to replace the function of the sub pulmonary ventricle.

4.4.5 Fontan IVC valve optimization

This study provides an approach to better understand the prospective hemodynamic effects of implanting a valve in the Fontan IVC. We primarily explored how incorporating a soft bileaflet valve into the IVC alters Fontan hemodynamics and its possible importance to avoiding retrograde flow and leaflet opening in the context of understanding the risk of leaflet thrombosis. The flow dynamic differences between mechanical and soft bileaflet valves, as well as the Trileaflet shapes were also emphasized.

Valve thrombosis has been widely observed in explanted valves and in retrospective analysis of transesophageal echocardiograms (TEEs) [111]–[113]. The calculation of ECAP values on the leaflet surfaces served for assessing the thrombogenic potential of each valve design and we compared our findings with the clinically available mechanical valve design, St Jude valve. Our results suggest that soft Bileaflet valves are less prone to thrombus formation (e.g., low velocities and complex flow). Our findings suggests that the flow resistance is minimal when the effective orifice area is the largest (100%). To minimize retrograde flow and enhance forward flow efficiency, we believe that having a valve design with the lowest flow resistance is critical. Thus, by enhancing thrombogenic performance, the Bileaflet v1 design may be a good alternative to the mechanical valve design. Thrombus formation is more commonly associated with mechanical valves and can lead to patient mortality as well as valve dysfunction or obstruction anytime. This risk is increased in the low flow environment of the venous Fontan circulation. Our findings also indicate that there is a higher risk of thrombus formation around the pivots that can lead to limited mobility of the rigid leaflets. Overall, the thrombosis potential findings of this study do not necessarily suggest an absolute value rather serves as hemodynamic index to compare the design in terms thrombogenic performance. It should also be noted that the evaluation of the accuracy and credibility of the presented ECAP calculation is beyond

the scope of this study. This estimation method was adopted from the existing studies and implemented as *in silico* tool for developing a valve prosthesis for Fontan circulation.

The study demonstrates that a clinical rationale to interventional methods that can limit the retrograde flow in the IVC which is a very critical problem for Fontan patients. We also fabricated the first prototype of the optimized valve design and tested them in our biomimetic Fontan simulator. Preliminary results showed similar hemodynamic impact of the prototypes valve and the commercially available mechanical valve on the Fontan IVC flow during forward and retrograde phases.

4.5 Conclusion

In this chapter we designed, manufactured, and tested some of the most promising circulatory support strategies for the Fontan circulation. We leveraged our clinically validated bench top and computational test platform to evaluate and optimize support devices.

We realized an extravascular peristaltic pump in two configurations: a compression and an expansion pump and showed pump functionality at zero flow conditions. Our results suggest that active flow support should be tailored to the IVC flow patterns which are governed by the respiratory biomechanics. Asynchronous actuation resulted in flow obstruction and diminished Fontan flow energy in lieu of increasing blood flow.

We demonstrated the impact of a unidirectional valve implanted in the Fontan IVC. The observed benefits to the Fontan circulation include lowered hepatic vein pressure, greater transpulmonary driving pressure and increased total venous return. Beneficial effects can be observed for physiologic conditions of high retrograde flow while circulations with low percent retrograde flow are not impacted negatively by valve placement. This suggests that valve placement is most efficacious in Fontan patient population which high retrograde flow characteristics. Positive impact of a one-way valve may also be boosted by activities performed by the patient which may include increased respiratory rate, increased respiratory effort and an upright body position. We have also demonstrated that other passive flow support strategies like an extravascular occluder device which is triggered by retrograde flow in the IVC may serve to prevent retrograde flow without device implantation in the blood stream and hence mitigate thromboembolic risks. We then optimized the design of a soft-bi-leaflet valve that is tailored to the physiological flow conditions of the Fontan IVC. We have minimized the negative effects of blood interactions on the valve leaflets as shown in our validated CFD Fontan model,

manufacture a prototype of the valve and successfully conducted initial bench top testing to compare performance with the commercially available mechanical valve in physiologic flow conditions.

Finally, we combined the active peristaltic pump sleeve with an implanted valve in the Fontan sunt and demonstrated that single actuation cycles during retrograde flow can increase the forward flow but continuous pump motion which opens and closes the single inflow valve increases retrograde flow compared to valve usage alone.

These findings inform the further design of active and passive support strategies and show promising approaches to supporting the Fontan flow in the light of great flow fluctuations characteristic for the Fontan IVC.

5. Conclusion and future direction

Conclusion

Forty-five years after its first description, we are still uncertain about the exact mechanisms why the Fontan physiology fails. The Fontan surgery is the final stage palliative treatment for a variety of congenital heart diseases that result in a single ventricle. The remaining ventricle pumps blood to the body resulting in the passive venous return through the lungs. This establishes unique hemodynamic circumstances that are still poorly understood. The physiological changes lead to end organ damage in the entire body including fatal liver, lung, and heart disease. Developmental and neurocognitive impairments increase the burden on this patient population and contribute to severely impaired quality of life. This results in high mid-to long term mortality rates which could not have been improved for the last two decades. The failure of the Fontan circulation has not been well characterized, suitable approaches to mechanically support these patients are still undetermined, and indications for heart transplantation, which remains the only curative treatment, are deficient. To date, circulatory support strategies which have been developed for biventricular physiologies failed to be translated into the Fontan circulation. At the core of this clinical problem lies a limited understanding of the underlying interactions of respiration, hemodynamics, and tissue damage. During inspiration breathing pressure drive a surge of blood from the abdominal vasculature into the lungs. During expiration the reversed breathing pressures invert this flow and through the direct connection of the lungs with the abdominal vasculature blood is pushed backward into the abdomen establishing a retrograde flow.

There are several impediments to research these interactions in the Fontan population resulting in stagnating progress in this field. Low numbers of patients are followed by each individual center, only few clinical trials of 15 or more patients even exist, and the Fontan population is by essence extremely heterogeneous which renders study endpoints illusive. Recently, the venous return has been identified as potential bottleneck of the single ventricle circulation and respiratory impact has been recognized to govern flow pattern in the Fontan IVC. Still, bench top models lack physiological fidelity to recreate the effects of respiratory biomechanics on the Fontan flow. Additionally computational and bench top models lack clinical validation. Comprehensive flow and pressure measurements are difficult to obtain clinically, animal models which would allow for more invasive measurements miss the anatomical fidelity of the Fontan

circulation and inherently fail to recreate the impact of negative pressure respiration on the venous flow. This contributes to our limited understanding of the Fontan venous flow, and suitable bench top platforms to test and develop circulatory support strategies.

To address these challenges, we developed a biomimetic respiratory model with an integrated single ventricle circulation to reproduces the impact of respiratory biomechanics on the Fontan venous flow. We used this system to accurately recreate clinically observed flow data on the bench top. We then validated the simplified physiology of the bench top system with a computational lumped parameter model of the entire body. Subsequently, we conducted a clinical trial to validate the findings from the bench top and computational models. We included patient specific vascular anatomies of key features in the Fontan anatomy segmented from patient MRI data into the bench top model and can recreate patient specific venous flow curves. The cardiorespiratory Fontan simulator is instrumented with flow and pressure sensors which allow us to make hemodynamic measurements which we cannot obtain during standard clinical examinations.

We then expanded the simulator platform with a computational fluid dynamics model of the Fontan shunt and used physiological flow data from the bench top model to validate the comprehensive flow model. The computational and bench top Fontan simulators provide a multiscale platform that serves two main goals: (A) to characterize respiratory impact on Fontan IVC flow and its physiological drivers and (B) to evaluate support strategies in hemodynamic conditions which mimic the Fontan physiology more closely than previous systems. Towards these goals, the bench top and computational lumped parameter models provide hemodynamic insights on the organ systems level while the validated computational fluid dynamics model enables the comprehensive study of acting forces on the blood flow, risk evaluation of thromboembolic events, and flow patterns. As such, this platform is a tool to broaden and deepen the lacking physiological understanding of the Fontan circulation and support the stagnating development of circulatory support strategies specifically tailored to the needs of this patient population.

Subsequently, we expanded the functionality of the biomimetic cardiorespiratory Fontan model to recreate hemodynamics frequently established in the Fontan IVC but which are not constricted to clinically controlled settings. This included the reconfiguration of the bench top model to simulate the upright body position. We characterized resulting flow dynamics and showed that the impact of gravity on the Fontan flow exacerbates the hemodynamic burden on the Fontan patient as retrograde flow and IVC pressures increased. Additionally, we recreated

IVC flow from clinical patient data including erratic flow patterns which can serve as tool to study the impact of support strategies in typical situation of daily life.

We leveraged the bench top and computational model to investigate the impact of respiration on the venous Fontan flow and characterized the effects of physiological parameters. We identified respiratory effort, respiratory rate, decreased baseline IVC flow, increased IVC baseline pressure and high vascular compliance as drivers of IVC retrograde flow. We characterized IVC pressure, flow pulsatility, peak forward and backward flow rates as well as flow volumes for each of the mentioned physiological parameters. Consequently, we repeated the respiratory study in a clinical trial with 20 Fontan patients using real time MRI to quantify respiration and Fontan flow. The clinical results corroborate our simulated findings. In the clinical evaluation we recorded great variability of the impact of respiration on Fontan venous flow with up to 45% retrograde flow in the IVC. We summarized a database of IVC flow patterns resembling a wide variety of IVC flow phenotypes which will serve to determine suitable support strategies for each group. No clinical study has characterized Fontan venous flow in such detail before. We identified baseline IVC flow, respiratory efforts, and respiratory rates as independent drivers of retrograde flow clinically. In summary, quiet, and slow breathing in a supine position with preferred chest breathing reduce the retrograde flow in the Fontan IVC.

We investigated clinical markers to correlate retrograde flow with the health status of the investigated study group. Towards this goal we analyzed anatomical features of the pulmonary and hepatic vasculature, patient health records, as well as available blood work. This serves as important information to guide the design of subsequent clinical study to investigate the impact of retrograde flow to the Fontan health.

We designed and manufactured recent and commonly suggested approaches as well as new concepts for circulatory support in the Fontan IVC which try to minimize flow obstruction and re-establish pulsatile flow in the pulmonary vasculature. These support strategies included extravascular compression and expansion pumps, one-way flow valves, and combinations of these active and passive systems. We evaluated characteristics of device function and identified the need for circulatory flow strategies to be closely tailored to the flow patterns created in the Fontan IVC. Our results underscore how circulatory support pumps can perform well in simplified flow conditions but may impede patient specific flow in the Fontan IVC and result in inferior flow dynamics. Standardized evaluations for each patient must be coupled with individualized phenotype-specific therapies and circulatory support. Support devices should address the underlying hemodynamics and highlight the importance of phenotype-specific

hemodynamic models for the testing of device efficacy. Support strategies should thus work together with and not against the respiratory effects found in the Fontan venous flow.

After promising results of valve implantation for Fontan hemodynamics with high retrograde flows we designed and optimized a bi-leaflet valve inspired by the native venous valve architecture. We leveraged the validated CFD model to evaluate device performance, risk of blood damage and coagulation compared to commercially available mechanical valves. We then manufactured a valve prototype and conducted preliminary testing on the cardiorespiratory bench top flow model showing valve competency.

Limitations

We acknowledge some limitations of this work: (1) The Simulator platform focused on the venous circulation of the Fontan physiology. Thus, the single ventricle heart was not modeled, and interactions of increased cardiac return and cardiac output were incorporated. (2) Flow resistance in the Fontan models were not recreated in a physiological way as the imitation of flow resistors remains subject of current research. (3) Anatomical structures that influence respiration and compliance of respiratory organs as well as of the Fontan vasculature were simplified into lumped parameters. (4) Vascular anatomies were only recreated for key features like the Fontan cross and not detailed for the pulmonary or abdominal vasculature. (5) Even though our clinical study enrolled a relatively large participation number (n=20) for clinical studies with Fontan patients, the overall numbers of study subjects was not high and great heterogeneity between each patient increased the variability in the results. (6) The clinical study self-selected for a patient population with relatively stable health status and the lack of available clinical information impeded the successful correlation of clinical markers to the impact of retrograde Fontan flow. (7) Only preliminary testing of the optimized Fontan valve has been concluded and device evaluation under variable hemodynamic conditions and improved manufacturing techniques will be part of future work.

Future work

Future work includes advancements in three areas: (1) Clinical exploration of Fontan flow in the upright body position and the evaluation of clinical impacts triggered by increased retrograde flow in the Fontan IVC. (2) Improvement to the cardiorespiratory simulator. (3) Improved manufacturing of the Fontan specific bi-leaflet vale and advance device testing.

Next clinical steps include a respiratory study to evaluate retrograde flow behavior in Fontan patient during upright body position. This can be achieved with special MRI machines or

ultrasound studies. We are currently exploring the opportunity to collaborate with clinicians at Boston Children's Hospital to conduct such an ultrasound guided respiratory study. Additionally, next clinical steps are to explore the impact of retrograde flow on the health status of Fontan patients. Towards this goal two clinical studies have been initiated at Boston Children's Hospital. One is a retrospective study aimed to use a large patient dataset to correlate retrograde flow in the IVC with health progression in Fontan patients. The second initiated study aims to evaluate IVC hemodynamics and retrograde flow during exercise. Furthermore, our clinical collaborators are evaluating the possibility to include a shortened version of the respiratory study to record retrograde flow in the IVC as part of the standard follow-up MRI procedure for every patient to facilitate future studies.

The cardiorespiratory simulator will be improved by integrating a ventricle and physiological flow resistors. This includes the possibility to add the arterial side into the lumped parameter flow loop and will allow to investigate effects of ventricular filling and cardiac output. Additional examinations of the impact of flow resistors in the arterial and venous side of the Fontan circulation will contribute to a more detailed understanding of the Fontan hemodynamics. Furthermore, our concept can be translated into a biventricular physiology to investigate respiratory effects and explore right heart failure in the biventricular physiology.

We will revise the manufacturing of the Fontan specific venous IVC valve placed in the TCPC shunt to match the improved hemodynamics seen in the computational modeling. We will then investigate the effects of the Fontan venous valve in different hemodynamic baseline conditions, physiological parameters, and body positions. To visualize flow effects and validate the computational findings in the Fontan IVC we are currently planning a 4D MRI examination of the developed valve. We have also established the possibility to conduct PIV measurements of the Fontan circulation including PIV visualization of the Fontan cross. This allows us to evaluate valve placement in the IVC as well as the impact flow variations to the blood mixing in the Fontan cross.

Moreover, we will test commercially available circulatory support devices like ventricular assist devices to elucidate benefits and challenges in device usage for this patient population. For these studies we will use the gather patient specific flow profiles which will help to evaluate device efficacy for a certain individual.

References

[1] Y. d'Udekem and J. Rychik, "Towards the goal of achieving a normal duration and quality of life after Fontan operation: Creation of the International Fontan Interest group (I-FIG), an international collaborative initiative dedicated to improving outcomes," *International Journal of Cardiology*, vol. 245, pp. 131–134, 2017, doi: 10.1016/j.ijcard.2017.05.027.

[2] C. Schilling *et al.*, "The Fontan epidemic: Population projections from the Australia and New Zealand Fontan Registry," *International Journal of Cardiology*, vol. 219, pp. 14–19, 2016, doi: 10.1016/j.ijcard.2016.05.035.

[3] M. Gewillig, S. C. Brown, A. van de Bruaene, and J. Rychik, "Providing a framework of principles for conceptualising the Fontan circulation," *Acta Paediatrica, International Journal of Paediatrics*, vol. 109, no. 4, pp. 651–658, 2020, doi: 10.1111/apa.15098.

[4] D. D. Gabbert *et al.*, "Heart beat but not respiration is the main driving force of the systemic venous return in the Fontan circulation," *Nature Scientific Reports*, vol. 9, no. 1, pp. 1–10, 2019, doi: 10.1038/s41598-019-38848-5.

[5] J. Rychik, "The Relentless Effects of the Fontan Paradox," *Seminars in Thoracic and Cardiovascular Surgery: Pediatric Cardiac Surgery Annual*, vol. 19, no. 1, pp. 37–43, 2016, doi: 10.1053/j.pcsu.2015.11.006.

[6] A. F. Corno, C. Vergara, C. Subramanian, R. A. Johnson, and T. Passerini, "Institutional report - Congenital Assisted Fontan procedure : animal and in vitro models and computational fluid dynamics study˚ ,˚," vol. 10, pp. 679–684, 2010, doi: 10.1510/icvts.2009.223024.

[7] G. R. Veldtman *et al.*, "Cardiovascular adaptation to the Fontan circulation," *Congenital Heart Disease*, vol. 12, no. 6, pp. 699–710, 2017, doi: 10.1111/chd.12526.

[8] P. Khairy *et al.*, "Long-term survival, modes of death, and predictors of mortality in patients with Fontan surgery," *Circulation*, vol. 117, no. 1, pp. 85–92, 2008, doi: 10.1161/CIRCULATIONAHA.107.738559.

[9] K. N. Pundi *et al.*, "40-Year Follow-Up after the Fontan Operation Long-Term Outcomes of 1,052 Patients," *J Am Coll Cardiol*, vol. 66, no. 15, pp. 1700–1710, 2015, doi: 10.1016/j.jacc.2015.07.065.

[10] R. J. Dabal *et al.*, "The modern Fontan operation shows no increase in mortality out to 20 years: A new paradigm," *Journal of Thoracic and Cardiovascular Surgery*, vol. 148, no. 6, pp. 2517-2524.e1, 2014, doi: 10.1016/j.jtcvs.2014.07.075.

[11] Y. D'udekem *et al.*, "Redefining expectations of long- Term survival after the fontan procedure twenty-five years of follow-up from the entire population of Australia and New Zealand," *Circulation*, vol. 130, no. 11, pp. S32–S38, 2014, doi: 10.1161/CIRCULATIONAHA.113.007764.

[12] T. Downing, K. Allen, D. Goldber, L. Rogers, and A. Glatz, "Surgical and Catheter-Based Reinterventions Are Common in Long-Term Survivors of the Fontan Operation," *Congenital Heart DiseaseCongenital Heart Disease*, vol. 10, no. 9, 2017.

[13] NIH and FDA, "Executive Summary: Unmet Medical Device Needs for Rare Diseases." 2017.

[14] C. R. Broda, T. E. Downing, and A. S. John, “Diagnosis and management of the adult patient with a failing Fontan circulation,” *Heart Failure Reviews*, 2020, doi: 10.1007/s10741-020-09932-0.
[15] M. Mori *et al.*, “Beyond a broken heart: Circulatory dysfunction in the failing Fontan,” *Pediatric Cardiology*, vol. 35, no. 4, pp. 569–579, 2014, doi: 10.1007/s00246-014-0881-y.
[16] P. Clift and D. Celermajer, “Managing adult Fontan patients: Where do we stand?,” *European Respiratory Review*, vol. 25, no. 142, pp. 438–450, 2016, doi: 10.1183/16000617.0091-2016.
[17] A. M. Valente *et al.*, “The CALF (Congenital Heart Disease in Adults Lower Extremity Systemic Venous Health in Fontan Patients) Study,” *J Am Coll Cardiol*, vol. 56, no. 2, pp. 144–150, 2010, doi: 10.1016/j.jacc.2010.02.048.
[18] W. M. Book, J. Gerardin, and A. Saraf, “Clinical Phenotypes of Fontan Failure: Implications for Management,” *Congenit Heart Dis.*, vol. 11, pp. 296–308, 2016.
[19] R. M. Berne and M. N. Levy, *Physiology*, 6th ed. 2010.
[20] T. Kogiso and K. Tokushige, “Fontan-associated liver disease and hepatocellular carcinoma in adults,” *Scientific Reports*, vol. 10, no. 1, Dec. 2020, doi: 10.1038/s41598-020-78840-y.
[21] G. A. G. Mark D Rodefeld, Steven H Frankel, “Cavopulmonary assist: (Em)powering the univentricular Fontan circulation,” *Semin Thorac Cardiovasc Surg Pediatr Card Surg*, pp. 1–20, 2011, doi: 10.1053/j.pcsu.2011.01.015.Cavopulmonary.
[22] H. B. Panitch, “The pathophysiology of respiratory impairment in pediatric neuromuscular diseases,” *Pediatrics*, vol. 123, no. SUPPL. 4, 2009, doi: 10.1542/peds.2008-2952C.
[23] R. S. Kuzo, R. A. Pooley, J. E. Crook, M. G. Heckman, and T. C. Gerber, “Measurement of caval blood flow with MRI during respiratory maneuvers: Implications for vascular contrast opacification on pulmonary CT angiographic studies,” *American Journal of Roentgenology*, vol. 188, no. 3, pp. 839–842, 2007, doi: 10.2214/AJR.06.5035.
[24] A. van de Bruaene and S. Kutty, “The peculiar challenges of breathing and exercising with a Fontan circulation,” *American Journal of Physiology - Heart and Circulatory Physiology*, vol. 316, no. 2, pp. H311–H313, 2019, doi: 10.1152/ajpheart.00762.2018.
[25] T. Y. Hsia, S. Khambadkone, J. E. Deanfield, J. F. N. Taylor, F. Migliavacca, and M. R. de Leval, “Subdiaphragmatic venous hemodynamics in the Fontan circulation,” *Journal of Thoracic and Cardiovascular Surgery*, vol. 121, no. 3, pp. 436–447, 2001, doi: 10.1067/mtc.2001.112527.
[26] A. L. Marsden, I. E. Vignon-Clementel, F. P. Chan, J. A. Feinstein, and C. A. Taylor, “Effects of exercise and respiration on hemodynamic efficiency in CFD simulations of the total cavopulmonary connection,” *Annals of Biomedical Engineering*, vol. 35, no. 2, pp. 250–263, Feb. 2007, doi: 10.1007/s10439-006-9224-3.
[27] O. Dur *et al.*, “Pulsatile venous waveform quality affects the conduit performance in functional and failing Fontan circulations,” *Cardiology in the Young*, vol. 22, no. 3, pp. 251–262, 2012, doi: 10.1017/S1047951111001491.
[28] L. Huntsman, D. Stewart, S. Barnes, S. Fanklin, J. Colocousis, and E. Hessel, “Noninvasive Dopplerdetermination of cardiac output in man clinical validation,” *Circulation*, vol. 67, no. 3, 1983.
[29] R. Bastkowski, R. Bindermann, K. Brockmeier, K. Weiss, D. Maintz, and D. Giese, “Respiration Dependency of Caval Blood Flow in Patients with Fontan

Circulation: Quantification Using 5D Flow MRI," *Radiology: Cardiothoracic Imaging*, vol. 1, no. 4, p. e190005, 2019, doi: 10.1148/ryct.2019190005.

[30] Z. Wei and A. Yoganathan, "Respiratory Effects on Fontan Circulation during Rest and Exercise Utilizing Real Time Cardiac Magnetic Resonance Imaging," *Ann Thorac Surg.*, vol. 176, no. 10, pp. 139–148, 2016, doi: 10.1016/j.physbeh.2017.03.040.

[31] V. E. Hjortdal, T. D. Christensen, S. H. Larsen, K. Emmertsen, and E. M. Pedersen, "Caval Blood Flow During Supine Exercise in Normal and Fontan Patients," *Annals of Thoracic Surgery*, vol. 85, no. 2, pp. 599–603, Feb. 2008, doi: 10.1016/j.athoracsur.2007.08.062.

[32] J. A. Dixon and F. G. Spinale, "Large animal models of heart failure; A critical link in the translation of basic science to clinical practice," *Circulation: Heart Failure*, vol. 2, no. 3. pp. 262–271, May 2009. doi: 10.1161/CIRCHEARTFAILURE.108.814459.

[33] M. Granegger *et al.*, "Approaches to Establish Extracardiac Total Cavopulmonary Connections in Animal Models — A Review," vol. 10, no. 1, pp. 81–89, 2019, doi: 10.1177/2150135118802788.

[34] T. Senage *et al.*, "A mock circulatory system to assess the performance of continuous-flow left ventricular assist devices (LVADs): Does axial flow unload better than centrifugal LVAD?," *ASAIO Journal*, vol. 60, no. 2, pp. 140–147, 2014, doi: 10.1097/MAT.0000000000000045.

[35] D. V. Telyshev, A. A. Pugovkin, and S. V. Selishchev, "A Mock Circulatory System for Testing Pediatric Rotary Blood Pumps," *Biomedical Engineering*, vol. 51, no. 2, pp. 83–87, 2017, doi: 10.1007/s10527-017-9689-4.

[36] A. Petrou, M. Granegger, M. Meboldt, and M. Schmid Daners, "A Versatile Hybrid Mock Circulation for Hydraulic Investigations of Active and Passive Cardiovascular Implants," *ASAIO J*, vol. 65, no. 5, pp. 495–502, 2019, doi: 10.1097/MAT.0000000000000851.

[37] M. Vukicevic, J. A. Chiulli, T. Conover, G. Pennati, T. Y. Hsia, and R. S. Figliola, "Mock circulatory system of the fontan circulation to study respiration effects on venous flow behavior," *ASAIO Journal*, vol. 59, no. 3, pp. 253–260, 2013, doi: 10.1097/MAT.0b013e318288a2ab.

[38] M. Tree *et al.*, "Using a Novel In Vitro Fontan Model and Condition-Specific Real-Time MRI Data to Examine Hemodynamic Effects of Respiration and Exercise," *Annals of Biomedical Engineering*, vol. 46, no. 1, pp. 135–147, 2018, doi: 10.1007/s10439-017-1943-0.

[39] A. Baretta *et al.*, "Respiratory effects on hemodynamics in patient-specific CFD models of the Fontan circulation under exercise conditions," *European Journal of Mechanics, B/Fluids*, vol. 35, pp. 61–69, Sep. 2012, doi: 10.1016/j.euromechflu.2012.01.012.

[40] S. W. Day and J. C. McDaniel, "PIV measurements of flow in a centrifugal blood pump: Time-varying flow," *Journal of Biomechanical Engineering*, vol. 127, no. 2, pp. 254–263, Apr. 2005, doi: 10.1115/1.1865190.

[41] C. M. Haggerty *et al.*, "Experimental and numeric investigation of Impella pumps as cavopulmonary assistance for a failing Fontan," *Journal of Thoracic and Cardiovascular Surgery*, vol. 144, no. 3, pp. 563–569, 2012, doi: 10.1016/j.jtcvs.2011.12.063.

[42] E. T. Roche, M. A. Horvath, K. C. Galloway, and D. J. Mooney, "DESIGN AND FABRICATION OF A SOFT ROBOTIC DIRECT CARDIAC COMPRESSION DEVICE," *Proceedings of the ASME 2015 International Design Engineering*

Technical Conferences & Computers and Information in Engineering Conference IDETC/CIE 2015, pp. 1–11, 2015.

[43] C. J. Payne *et al.*, "An Implantable Extracardiac Soft Robotic Mechanical Coupling and Synchronization," *Soft Robotics*, vol. 4, no. 3, pp. 241–250, 2017, doi: 10.1089/soro.2016.0076.

[44] B. Suki, R. H. Habib, and A. C. Jackson, "Wave propagation, input impedance, and wall mechanics of the calf trachea from 16 to 1,600 Hz," *Journal of Applied Physiology*, vol. 75, no. 6, pp. 2755–2766, 1993, doi: 10.1152/jappl.1993.75.6.2755.

[45] S. L. Jones, *Respiratory Physiology: The Essentials*, vol. 55, no. 5. 1975. doi: 10.1093/ptj/55.5.563a.

[46] L. Rosalia, C. Ozturk, D. van Story, M. A. Horvath, and E. T. Roche, "Object-Oriented Lumped-Parameter Modeling of the Cardiovascular System for Physiological and Pathophysiological Conditions," *Advanced Theory and Simulations*, vol. 4, no. 3, Mar. 2021, doi: 10.1002/adts.202000216.

[47] G. K. Gnanappa *et al.*, "The Long-Term Management of Children and Adults with a Fontan Circulation: A Systematic Review and Survey of Current Practice in Australia and New Zealand," *Pediatric Cardiology*, vol. 38, no. 1, pp. 56–69, Jan. 2017, doi: 10.1007/s00246-016-1484-6.

[48] P. A. W. Anderson *et al.*, "The fontan patient: Inconsistencies in medication therapy across seven pediatric heart network centers," *Pediatric Cardiology*, vol. 31, no. 8, pp. 1219–1228, Nov. 2010, doi: 10.1007/s00246-010-9807-5.

[49] S. S. M. Bossers *et al.*, "Long-Term Serial Follow-Up of Pulmonary Artery Size and Wall Shear Stress in Fontan Patients," *Pediatric Cardiology*, vol. 37, no. 4, pp. 637–645, Apr. 2016, doi: 10.1007/s00246-015-1326-y.

[50] F. J. S. Ridderbos *et al.*, "Pulmonary artery size is associated with functional clinical status in the Fontan circulation," *Heart*, vol. 106, no. 3, pp. 233–239, Feb. 2020, doi: 10.1136/heartjnl-2019-314972.

[51] G. E. Assenza *et al.*, "MELD-XI score and cardiac mortality or transplantation in patients after Fontan surgery," *Heart*, vol. 99, no. 7, pp. 491–496, Apr. 2013, doi: 10.1136/heartjnl-2012-303347.

[52] J. Emamaullee *et al.*, "Fontan-associated liver disease: Screening, management, and transplant considerations," *Circulation*, vol. 142, no. 6. Lippincott Williams and Wilkins, pp. 591–604, Aug. 11, 2020. doi: 10.1161/CIRCULATIONAHA.120.045597.

[53] M Vukicevic, "Control of respiration-driven retrograde flow in the subdiaphragmatic venous return of the Fontan circulation," vol. 60, no. 4, pp. 391–399, 2014, doi: 10.1097/MAT.0000000000000093.Control.

[54] D. Seppelt *et al.*, "Simple diameter measurement as predictor of liver volume and liver parenchymal disease," *Scientific Reports*, vol. 12, no. 1, Dec. 2022, doi: 10.1038/s41598-022-04825-8.

[55] S. Nakata *et al.*, "A new method for the quantitative standardization of cross-sectional areas of the pulmonary arteries in congenital heart diseases with decreased pulmonary blood flow," *Journal of Thoracic and Cardiovascular Surgery*, vol. 88, no. 4, pp. 610–619, 1984, doi: 10.1016/s0022-5223(19)38300-x.

[56] A. S. Go *et al.*, "Heart disease and stroke statistics-2013 update: A Report from the American Heart Association," *Circulation*, vol. 127, 2013, doi: 10.1161/CIR.0b013e31828124ad.

[57] L. E. Rodriguez, E. E. Suarez, M. Loebe, D. Ph, and B. A. Bruckner, "Ventricular Assist Devices (VAD) Therapy : New Technology , New Hope ?," vol. 2012, no. 1, pp. 32–37, 2013.

[58] A. Sizarova, “Novel materials and devices in the transcatheter management of congenital heart diseases — the future comes slowly,” vol. 109, no. 4, pp. 278–302, 2016.
[59] F. Gandolfo *et al.*, “Mechanically Assisted Total Cavopulmonary Connection With an Axial Flow Pump: Computational and In Vivo Study,” *Artificial Organs*, vol. 40, no. 1, pp. 43–49, 2016, doi: 10.1111/aor.12641.
[60] A. Singhvi and B. Trachtenberg, “Left ventricular assist devices 101: Shared care for general cardiologists and primary care,” *Journal of Clinical Medicine*, vol. 8, no. 10. MDPI, Oct. 01, 2019. doi: 10.3390/jcm8101720.
[61] D. B. Sanders *et al.*, “The failing Fontan: What’s NEXT...?,” *Perfusion (United Kingdom)*, vol. 29, no. 1, pp. 89–93, Jan. 2014, doi: 10.1177/0267659113495913.
[62] M. D. Rodefeld *et al.*, “Cavopulmonary assist for the univentricular Fontan circulation: Von Kármán viscous impeller pump,” *Journal of Thoracic and Cardiovascular Surgery*, vol. 140, no. 3, pp. 529–535, 2010, doi: 10.1016/j.jtcvs.2010.04.037.
[63] J. Hernandez, S. G. Chopski, S. Lee, W. B. Moskowitz, and A. L. Throckmorton, “Externally applied compression therapy for Fontan patients,” 2017, doi: 10.21037/tp.2017.08.01.
[64] A. Yamada *et al.*, “Peristaltic Hemodynamics of a New Pediatric Circulatory Assist System for Fontan Circulation using Shape Memory Alloy Fibers,” pp. 683–686, 2013.
[65] D. L. S. Morales, I. Adachi, J. S. Heinle, and C. D. Fraser, “A new era: Use of an intracorporeal systemic ventricular assist device to support a patient with a failing Fontan circulation,” *Journal of Thoracic and Cardiovascular Surgery*, vol. 142, no. 3, pp. e138–e140, 2011, doi: 10.1016/j.jtcvs.2011.05.018.
[66] M. Tree, P. M. Trusty, T. C. Slesnick, A. Yoganathan, S. Deshpande, and K. Maher, “In Vitro Examination of the HeartWare CircuLite Ventricular Assist Device in the Fontan Connection,” *ASAIO Journal*, vol. 63, no. 4, pp. 482–489, 2017, doi: 10.1097/MAT.0000000000000521.
[67] O. H. Frazier, I. D. Gregoric, and G. N. Messner, “Total Circulatory Support with an LVAD in an Adolescent with a Previous Fontan Procedure,” 2005.
[68] R. A. Niebler *et al.*, “Use of a HeartWare ventricular assist device in a patient with failed fontan circulation,” *Annals of Thoracic Surgery*, vol. 97, no. 4, 2014, doi: 10.1016/j.athoracsur.2013.11.075.
[69] “calvaruso_2007_Implantation_of_a_Berlin_Heart_as_Single_Ventricle.30”.
[70] D. M. Hoganson, U. S. Boston, A. Z. Gazit, C. E. Canter, and P. Eghtesady, “Successful bridge through transplantation with Berlin heart ventricular assist device in a child with failing Fontan,” *Annals of Thoracic Surgery*, vol. 99, no. 2, pp. 707–709, Feb. 2015, doi: 10.1016/j.athoracsur.2014.04.064.
[71] S. Weinstein *et al.*, “The use of the Berlin heart EXCOR in patients with functional single ventricle,” *Journal of Thoracic and Cardiovascular Surgery*, vol. 147, no. 2, pp. 697–705, Feb. 2014, doi: 10.1016/j.jtcvs.2013.10.030.
[72] G. Derk *et al.*, “Novel techniques of mechanical circulatory support for the right heart and Fontan circulation,” *International Journal of Cardiology*, vol. 176, no. 3, pp. 828–832, Oct. 2014, doi: 10.1016/j.ijcard.2014.08.012.
[73] R. K. Riemer, G. Amir, S. H. Reichenbach, and O. Reinhartz, “Mechanical support of total cavopulmonary connection with an axial flow pump,” *Journal of Thoracic and Cardiovascular Surgery*, vol. 130, no. 2, pp. 351–354, Aug. 2005, doi: 10.1016/j.jtcvs.2004.12.037.
[74] S. Tsuda, T. Sasaki, K. Maeda, R. K. Riemer, S. H. Reichenbach, and O. Reinhartz, “Recovery during mid-term mechanical support of fontan circulation in

sheep," *ASAIO Journal*, vol. 55, no. 4, pp. 406–411, Jul. 2009, doi: 10.1097/MAT.0b013e3181a0a570.

[75] K. Pekkan, D. Frakes, D. de Zelicourt, C. W. Lucas, W. J. Parks, and A. P. Yoganathan, "Coupling pediatric ventricle assist devices to the Fontan circulation: Simulations with a lumped-parameter model," *ASAIO Journal*, vol. 51, no. 5, pp. 618–628, 2005, doi: 10.1097/01.mat.0000176169.73987.0d.

[76] M. R. de Leval, "The Fontan Circulation: What Have We Learned? What to Expect?"

[77] A. L. Throckmorton, S. S. Bhavsar, S. G. Chopski, and W. B. Moskowitz, "Pneumatically-driven external pressure applicator to augment Fontan hemodynamics: preliminary findings.," *Transl Pediatr*, vol. 2, no. 4, pp. 148–14853, 2013, doi: 10.3978/j.issn.2224-4336.2013.10.02.

[78] F. G. Lacour-Gayet *et al.*, "An Artificial Right Ventricle for Failing Fontan: In Vitro and Computational Study," *Annals of Thoracic Surgery*, vol. 88, no. 1, pp. 170–176, 2009, doi: 10.1016/j.athoracsur.2009.03.091.

[79] A. di Molfetta *et al.*, "Use of Ventricular Assist Device in Univentricular Physiology: The Role of Lumped Parameter Models," *Artificial Organs*, vol. 40, no. 5, pp. 444–453, 2016, doi: 10.1111/aor.12583.

[80] S. G. Chopski, O. M. Rangus, E. A. Downs, W. B. Moskowitz, and A. L. Throckmorton, "Three-Dimensional Laser Flow Measurements of a Patient-Specific Fontan Physiology With Mechanical Circulatory Assistance," *Artificial Organs*, vol. 39, no. 6, pp. E67–E78, Jun. 2015, doi: 10.1111/aor.12426.

[81] M. Granegger, M. Schweiger, M. Schmid Daners, M. Meboldt, and M. Hübler, "Cavopulmonary mechanical circulatory support in Fontan patients and the need for physiologic control: A computational study with a closed-loop exercise model," *International Journal of Artificial Organs*. 2018. doi: 10.1177/0391398818762359.

[82] J. Zhu *et al.*, "Cavopulmonary support with a microaxial pump for the failing fontan physiology," *ASAIO Journal*, vol. 61, no. 1, pp. 49–54, 2015, doi: 10.1097/MAT.0000000000000162.

[83] K. Pekkan *et al.*, "In vitro validation of a self-driving aortic-turbine venous-assist device for Fontan patients," *Journal of Thoracic and Cardiovascular Surgery*, vol. 156, no. 1, pp. 292-301.e7, 2018, doi: 10.1016/j.jtcvs.2018.02.088.

[84] H. Ishida *et al.*, "Overexpression of endothelin-1 and endothelin receptors in the pulmonary arteries of failed Fontan patients," *International Journal of Cardiology*, vol. 159, no. 1, pp. 34–39, 2012, doi: 10.1016/j.ijcard.2011.02.021.

[85] E. H. Johnson, S. H. Bennett, and B. W. Goetzman, "The influence of pulsatile perfusion on the vascular properties of the newborn lamb lung.," *Pediatr Res*, vol. 31, no. 4 Pt 1, pp. 349–53, 1992, doi: 10.1203/00006450-199204000-00009.

[86] Shafer, Garcia, Babb, and Levine, "The Importance of the Muscle and Ventilatory Blood Pumps During Exercise in Patients Without a Subpulmonary Ventricle (Fontan Operation)," *J Am Coll Cardiol*, 2012.

[87] C. 2013, "Resistance training imporves cardiac output, exercise capacity and tolerance to positive airway pressure in Fontan physiology.pdf."

[88] JohnA. Macoviak *et al.*, "Myoventriculoplastyand neoventriclemyograftcardiacaugmentationto establishpulmonarybloodflow," *Journal of Thoracic Cardiovascular Surgery*, 1987.

[89] A. F. Corno *et al.*, "Assisted Fontan procedure: animal and in vitro models and computational fluid dynamics study☆☆☆," *Interactive CardioVascular and Thoracic Surgery*, vol. 10, no. 5, pp. 679–684, May 2010, doi: 10.1510/icvts.2009.223024.

[90] E. Monnet, E. Christopher Orton, G. Jacobs, and L. Metelman, “Fluoroscopic Determination of Latissimus Dorsi Muscle Shortening Fraction after Dynamic Cardiomyoplasty.”
[91] S. Salmons, “Cardiac assistance from skeletal muscle: Should we be downhearted?,” *Annals of Thoracic Surgery*, vol. 79, no. 4. Elsevier USA, pp. 1101–1103, 2005. doi: 10.1016/j.athoracsur.2004.10.009.
[92] J. Valdovinos, E. Shkolyar, G. P. Carman, and D. S. Levi, “In vitro evaluation of an external compression device for fontan mechanical assistance,” *Artificial Organs*, vol. 38, no. 3, pp. 199–207, 2014, doi: 10.1111/aor.12152.
[93] D. Taylor *et al.*, “Construction and Evaluation of a Bio-Engineered Pump to Enable Subpulmonary Support of the Fontan Circulation: A Proof-of-Concept Study,” *ASAIO Journal*, 2021, doi: 10.1097/MAT.0000000000001617.
[94] J. Park *et al.*, “Modular design of a tissue engineered pulsatile conduit using human induced pluripotent stem cell-derived cardiomyocytes,” *Acta Biomaterialia*, vol. 102, pp. 220–230, Jan. 2020, doi: 10.1016/j.actbio.2019.10.019.
[95] R. Roudaut, K. Serri, and S. Lafitte, “Thrombosis of prosthetic heart valves: Diagnosis and therapeutic considerations,” *Heart*, vol. 93, no. 1. pp. 137–142, Jan. 2007. doi: 10.1136/hrt.2005.071183.
[96] G. Marom and S. Einav, “New insights into valve hemodynamics,” *Rambam Maimonides Medical Journal*, vol. 11, no. 2. Rambam Health Care Campus, Apr. 01, 2020. doi: 10.5041/RMMJ.10400.
[97] L. P. Dasi, H. A. Simon, P. Sucosky, and A. P. Yoganathan, “Fluid mechanics of artificial heart valves,” *Clinical and Experimental Pharmacology and Physiology*, vol. 36, no. 2. pp. 225–237, Feb. 2009. doi: 10.1111/j.1440-1681.2008.05099.x.
[98] A. Santhanakrishnan, K. O. Maher, E. Tang, R. H. Khiabani, J. Johnson, and A. P. Yoganathan, “Hemodynamic effects of implanting a unidirectional valve in the inferior vena cava of the Fontan circulation pathway: an in vitro investigation,” *American Journal of Physiology - Heart and Circulatory Physiology*, vol. 305, no. 10, pp. H1538–H1547, 2013, doi: 10.1152/ajpheart.00351.2013.
[99] P. E. Hammer, E. G. Roberts, S. M. Emani, and P. J. del Nido, “Surgical reconstruction of semilunar valves in the growing child: Should we mimic the venous valve? A simulation study,” *Journal of Thoracic and Cardiovascular Surgery*, vol. 153, no. 2, pp. 389–396, 2017, doi: 10.1016/j.jtcvs.2016.08.019.
[100] S. C. Hofferberth *et al.*, “A geometrically adaptable heart valve replacement,” *Science Translational Medicine*, vol. 12, no. 532, pp. 1–13, 2020, doi: 10.1126/scitranslmed.aay4006.
[101] Laurence W. McKeen, *Fatigue and Tribological Properties of Plastics and Elastomers*, 3rd ed. William Andrew Applied Science Publishers, 2016.
[102] D. M. Holman, R. M. Brionnaud, and Z. Abiza, “SOLUTION TO INDUSTRY BENCHMARK PROBLEMS WITH THE LATTICE-BOLTZMANN CODE XFLOW,” 2012.
[103] F. Ducros, F. Nicoud, and T. Poinsot, “Wall-Adapting Local Eddy-Viscosity models for simulations in complex geometries,” 2014.
[104] D. W. Murphy, L. P. Dasi, J. Vukasinovic, A. Glezer, and A. P. Yoganathan, “Reduction of procoagulant potential of b-datum leakage jet flow in bileaflet mechanical heart valves via application of vortex generator arrays,” *Journal of Biomechanical Engineering*, vol. 132, no. 7, Jul. 2010, doi: 10.1115/1.4001260.
[105] H. Hatoum, P. Maureira, and L. P. Dasi, “A turbulence in-vitro assessment of ON-X and St. Jude Medical prostheses HHS Public Access,” 2020.
[106] P. di Achille, G. Tellides, C. A. Figueroa, and J. D. Humphrey, “A haemodynamic predictor of intraluminal thrombus formation in abdominal aortic aneurysms,”

Proceedings of the Royal Society A: Mathematical, Physical and Engineering Sciences, vol. 470, no. 2172, Dec. 2014, doi: 10.1098/rspa.2014.0163.
[107] G. García-Isla *et al.*, "Sensitivity analysis of geometrical parameters to study haemodynamics and thrombus formation in the left atrial appendage," *International Journal for Numerical Methods in Biomedical Engineering*, vol. 34, no. 8, Aug. 2018, doi: 10.1002/cnm.3100.
[108] C. Martin and W. Sun, "Simulation of long-term fatigue damage in bioprosthetic heart valves: Effects of leaflet and stent elastic properties," *Biomechanics and Modeling in Mechanobiology*, vol. 13, no. 4, pp. 759–770, 2014, doi: 10.1007/s10237-013-0532-x.
[109] W. Sun, A. Abad, and M. S. Sacks, "Simulated bioprosthetic heart valve deformation under quasi-static loading," *Journal of Biomechanical Engineering*, vol. 127, no. 6, pp. 905–914, Nov. 2005, doi: 10.1115/1.2049337.
[110] S. Zain, C.-L. Cian O', M. David, and L. Bryan, "Acute Mechanical Valve Thrombosis in the Setting of Unusual Aetiology," *International Journal of Clinical Cardiology*, vol. 5, no. 2, Jun. 2018, doi: 10.23937/2378-2951/1410119.
[111] E. de Marchena *et al.*, "Thrombus Formation Following Transcatheter Aortic Valve Replacement," 2015.
[112] A. C. Egbe *et al.*, "Bioprosthetic Valve Thrombosis Versus Structural Failure Clinical and Echocardiographic Predictors," 2015.
[113] P. A. Midha *et al.*, "The fluid mechanics of transcatheter heart valve leaflet thrombosis in the neosinus," *Circulation*, vol. 136, no. 17, pp. 1598–1609, Jul. 2017, doi: 10.1161/CIRCULATIONAHA.117.029479.

Table of figures